

**Tomographic Studies of Pulsar Radio Emission Cones
And
Searches for Radio Counterparts of Gamma-ray Pulsars**

A THESIS
SUBMITTED FOR THE DEGREE OF
Doctor of Philosophy
IN THE FACULTY OF SCIENCE

by

Yogesh Maan

UNDER THE SUPERVISION OF

Avinash A. Deshpande
(Raman Research Institute)



Astronomy And Astrophysics
Indian Institute of Science

Bangalore – 560 012

INDIA

(Submitted: July 2013)

Synopsis

Radio emission from pulsars is believed to originate from charged particles streaming along the open magnetic field lines, radiating within a narrow cone at each of the two magnetic poles. In each rotation of the star, the emission beam sweeping across the observer’s line of sight, is seen as a pulse of radio emission. Average pulse profiles integrated over several hundreds of individual pulses, along with polarization information, reveal the viewing geometry and various emission properties (e.g., emission in multiple cones, frequency dependence of the emission altitude, notches in the average profiles, etc.), and provide some clues about the possible emission mechanisms. The sequence of individual pulses generally exhibit richer details, e.g., pulse-nulling, variety of subpulse drifting, polarization mode-changing, micro-structure and giant pulse emission, etc., and seem to be more crucial and promising in probing the underlying physical processes. The physical understanding of many of the above properties and phenomena is still far from complete. In first two parts of this thesis, we address a few of these aspects, and probe related details by mapping the pulsar polar emission patterns, while in the last part, we present our searches for dispersed signals (periodic as well as transient) at very low frequencies. More specifically, Part-I makes use of the present understanding of drifting subpulses phenomenon to reconstruct the emission patterns in nearly complete polar cap region of the pulsar B1237+25, and addresses the origin of emission in multiple cones using these reconstructed emission maps. In Part-II, we discuss a need for new instrumentation primarily motivated by the need for tomographic studies of pulsar polar emission regions. We report the consequent design and development of a novel, self-contained multi-band receiver (MBR) system, intended for use with a single large aperture to facilitate sensitive and high time-resolution observations simultaneously in 10 discrete frequency bands sampling a wide spectral span (100–1500 MHz) in a nearly log-periodic fashion. Part-III presents our deep searches designed to detect radio transient as well as periodic signals from the (so far) “radio-quiet” gamma-ray pulsars — a population of radio silent pulsars recently discovered using the Large Area Telescope on the *Fermi*-satellite. Brief descriptions of the issues addressed in the three parts of the thesis, along with a summary of respective results, is as follows.

1. *Origin of Radio Emission in Multiple Cones*

Many pulsars exhibit systematic variations in position and intensity of their subpulses, a phenomenon now well known as “subpulse drifting”. Ruderman & Sutherland (1975) suggested this regular modulation to be a manifestation of a carousel of “spark” discharges in the acceleration zone of the star, circulating around the magnetic axis because of the $E \times B$ drift. In the qualitative framework of the above *carousel model*, the coherent modulation in a subpulse sequence can be

mapped back to the underlying pattern of sub-beams/emission-columns (see, for example, Deshpande & Rankin, 1999). However, the completeness with which the underlying configuration of sub-beams can be sampled depends on how close our line of sight approaches the magnetic axis. The bright pulsar B1237+25 has a special viewing geometry where the sightline traverses almost through the magnetic axis, thus providing an excellent opportunity to map and study the underlying patterns across the full transverse slice of its polar emission region. However, the rich variety in pulse-to-pulse fluctuations in this pulsar makes this task challenging. In Chapter 2, we present our analysis of a number of pulse-sequences from this star observed with the Arecibo telescope, wherein we search for, and use, coherent modulation in sub-sequences, to map the underlying emission patterns. The reconstructed maps provide a convenient way to study the details in multiple emission cones, and any inter-relationship between them. More specifically, we have utilized these maps to explore whether the multiple cones of this pulsar originate from a common seed pattern or not.

A summary of results

The results obtained from our study of B1237+25 are summarized below:

1. The underlying carousel of sparks for this pulsar appears to lack stability over long durations. The circulation period, deduced using smaller length sub-sequences, appears to vary over a large range (about 18 to 34 times the rotation period).
2. The emission patterns corresponding to the outer and the inner cones are found to be significantly correlated with each other, implying that the emission in the two cones share a common seed pattern of sparks. This main result is consistent with the same radio frequency emission in the two cones, originating from a common seed pattern of sparks at two different altitudes.
3. The emission patterns corresponding to the outer and the inner cones are found to be offset from each other, consistently across various sub-sequences, by about 10° in magnetic azimuth. This large offset indicates certainly a twist in the emission columns, and most likely in the magnetic field geometry, between the two different emission altitudes.
4. The core component also seems to share its origin with the conal counterparts. Presence of a compact, diffuse and *further-in* carousel of sub-beams is consistent with the observed modulation in the core component of this pulsar. The featureless spectrum observed for many core-single pulsars can be explained readily when the diffuse pattern approaches uniformity.

2. Tomography of the Pulsar Magnetosphere: Development of a Multi-band Receiver

Although drifting subpulses are now routinely interpreted in the qualitative framework of the carousel model, estimation of circulation time associated with the system of emission columns has been possible so far in only a handful of pulsars, and the important details determining such configurations, their evolution across the magnetosphere, and the pattern circulation are yet to be understood. Radius-to-frequency mapping in pulsars suggests that the lower frequency emission originates farther away from the surface of the star than the higher frequency emission. Hence, the sub-beam configuration mapped at a particular frequency provides a view of a single slice of the polar emission region at the corresponding emission altitude. Mapping of the underlying emission patterns simultaneously at a number of frequencies would amount to viewing a “tomograph” of the pulsar magnetosphere. Such tomographic studies would reveal not only the evolution of sub-beams across the magnetosphere but can also provide much needed clues about the generation of the sub-beam patterns, and their possible connection with the profile/polarization mode changes observed in various pulsars.

Simultaneous multi-frequency observations, which are required for many other interesting astronomical studies as well, are usually carried out by using several telescopes, each observing at different frequency. Such an approach has inherent complexity in coordinating various telescopes, in addition to numerous other difficulties which limit the desired advantages of such observations. Some of these difficulties, which we faced in our attempt of carrying out simultaneous multi-frequency observations using five different telescopes, are discussed in Chapter 3. We suggest an optimum approach to carry out simultaneous multi-frequency observations, using a single large aperture. In Chapter 4, we present the design of a novel, “self-contained” multi-band receiver (MBR) system developed for this purpose. The MBR system includes a suitable feed, broadband front-end, parallel analog and digital receiver pipelines, along with appropriate monitoring, synchronization and data recording systems. When used with a large aperture, the MBR facilitates high time-resolution observations simultaneously in 10 discrete frequency bands sampling a wide spectral span (100–1500 MHz) in a nearly log-periodic fashion. The raw voltage time sequences corresponding to each of the two linear polarization channels for each of the 10 spectral bands are simultaneously recorded, each sampling a bandwidth of 16 MHz at the Nyquist rate.

The dual-polarization multi-band feed, a key component of the MBR, is designed to have good responses only over the 10 discrete bands pre-selected as relatively RFI-free, and hence provides preliminary immunity against RFI. The MBR also offers significant tunability of the center frequencies of each of the 16-MHz sub-bands separately, within the spectral spans of respective bands. Similarity of the 10 sub-band receiver chains provides desired compatibility, in addition to

an easy inter-changeability of these units, if required, and an overall modularity to the system.

The MBR was used with the 110 meter Green Bank Telescope to conduct test observations on a few bright continuum sources, and about 20 hours of observations on a number of bright pulsars. Using these observations, we have constructed a preliminary tomograph of the polar emission region of B0809+74, and studied the spectral evolution of emission altitudes and flux density of B0329+54 (Chapter 5). Although the MBR system design is optimized for tomographic studies of pulsar polar emission regions, the simultaneous multi-frequency observations with such a system offer particular advantages in fast transient searches. The MBR is also suitable for several other astronomical investigations, e.g., studying the spectral evolution of average properties of pulsars and propagation effects, single-dish continuum studies and surveys/studies of recombination lines.

3. Searches for Decameter-wavelength Counterparts of Radio-quiet Gamma-ray Pulsars

Before the launch of the *Fermi gamma-ray space telescope*, the “radio-quiet” gamma-ray pulsar population consisted of only one pulsar, i.e., Geminga (for example, see Bignami & Caraveo, 1996; Abdo *et al.*, 2009). High sensitivity of the Large Area Telescope (LAT) on the *Fermi*-satellite made it possible, for the first time, to perform blind searches for pulsars in γ -rays. Since the *Fermi*-operation started, the number of pulsars known to emit in γ -rays has seen an extraordinary increase — from less than 10 to 117 pulsars. About one-third of these pulsars have been discovered in blind searches of the LAT data. Despite deep radio searches, only 4 of these LAT-discovered pulsars could be detected, suggesting the rest of these to be “radio-quiet” gamma-ray pulsars.

One of the possible explanations for the apparent absence of radio emission from these pulsars is that their narrow radio beams miss the line of sight towards earth (Brazier & Johnston, 1999), and hence appear as “radio-quiet”. The radius-to-frequency mapping in radio pulsars suggests that the emission beam becomes wider at low frequencies, increasing the probability of our line of sight passing through the beam. However, all of the deep searches mentioned above were carried out at higher radio frequencies (~ 1 GHz and above, and some at 300 MHz, Ray *et al.*, 2011; Pletsch *et al.*, 2012), and the lower frequency domain ($< \approx 100$ MHz) has remained relatively unexplored. Given the expected widening of emission beam, follow-up searches of the radio-quiet pulsars at low radio frequencies could also be revealing. With this view, we searched the archival data of the pulsar/transient survey at 34.5 MHz, carried out using the Gauribidanur telescope during 2002-2006, for any periodic or transient dispersed signal along the direction of many of the LAT-discovered pulsars. Motivated by an intriguing possible detection of the pulsar J1732–3131 from the above search, we carried out further extensive follow-up observations and *deep* searches for pulsed (periodic as well as transient) radio emission from a selected sample of radio-quiet pulsars. Chapters

6 and 7 present details of our observations, detection strategies and methodologies, and interesting results obtained in a few of the target directions. The results obtained from these searches include:

1. A possible detection of periodic radio pulses from J1732–3131 was made, using the archival data, at a dispersion measure (DM) of 15.44 ± 0.32 pc/cc. We also detected 10 individual bright pulses in the same observing session, although marginally above the detection threshold, at a DM consistent with that associated with the periodic signal. The apparent brightness of these single pulses, and similarity of their apparent distribution in pulse-longitude with that of giant pulses in J0218+4232, suggest that these might be giant pulses. Our DM-based distance estimate, using Cordes & Lazio electron density model (2002), matches well with earlier estimates based on gamma-ray emission efficiency.
 2. In our follow-up deep searches, we could not detect any readily apparent pulsed radio signal (neither periodic nor single pulses) from J1732–3131, i.e., above a detection threshold of 8σ . However, when we time-aligned and co-added data from observing sessions at 21 different epochs, and dedispersed using the DM estimated from the candidate detection, the average profile shape is found to be completely consistent with that from the candidate detection. Finding the same profile shape after 10 years of the original detection suggests that the signal is unlikely to be due to RFI or a mere manifestation of random noise.
 3. In a couple of the observing sessions towards the telescope pointing direction of RA=06:34:30, DEC=10°, we detected a few ultra-bright pulses at two different DMs of about 2 pc/cc and 3.3 pc/cc, respectively. However, when dedispersed at the DMs suggested by the bright single pulses, no significant signal was found at the expected periodicities of our target pulsars J0633+0632 and J0633+1746, which would be in the telescope beam centered at above coordinates. Energies of these strong pulses in the two observing sessions are comparable to typical energies of giant pulses from the Crab pulsar at decameter wavelengths.
 4. No significant pulsed signal (periodic or transient), above a detection threshold of 8σ , was found towards the directions of other selected radio-quiet gamma-ray pulsars. Time-aligning and combining of observations at different epochs allowed us to carry out deep searches for signals at the expected periodicities of these pulsars. Despite the large background sky-temperature at decameter wavelengths, the minimum detectable flux density in our deep searches are comparable with those from previous searches at higher frequencies, when scaled using a spectral index of -2.0 and assuming no turn-over in the spectrum.
-

Acknowledgments

I am grateful to Desh, my thesis supervisor, for the scientific and personal support he has provided at numerous stages of the thesis work, for exemplifying a great scientific temper, and for his contributions in developing various scientific ideas explored in this thesis. I am also thankful to him for providing the space and encouragement to explore my own ideas.

I am thankful to my family, specially my parents and sister, for their patient support and encouragement throughout the period of this work.

Nishant's enthusiasm for scientific discussions has always been encouraging. Its a pleasure to thank Harsha and Nishant for various useful discussions, and for being such wonderful friends. It will be a crime if I fail to acknowledge that the writing of this thesis got benefited a lot from Harsha's promptness and enthusiasm towards *learning latex for others*. I am also thankful to Renu for her support in various ways during busy times of this thesis work.

Life at the Astro-floor would have been different had Vidya not been around. Thank you Vidya, for keeping us at a safe distance from the messy administrative work at times, and for your friendly support throughout.

I would like to thank all the library staff at RRI, for their active and consistent support. I am also thankful to Tarun for providing his active support in academic and administrative matters at IISc. I would also like to thank all the colleagues on the Astro-floor for their contributions in various scientific as well as non-scientific discussions and activities which I perceive as knowledge-cum-fun packages.

I am grateful to Aswathappa, Anand, Venu and other members of their team, at the Gauribidanur observatory, for their immense and successful efforts in again bringing life to the huge dipole array, and for their prompt support whenever it was required. The pulsar/transient survey and the follow-up observations would not have been possible without the immense efforts from Aswathappa and the staff at the Gauribidanur observatory. I gratefully acknowledge help from Indrajit, Hariharan, Rajalingam and several other friends at crucial stages of our follow-up observations of J1732-3131 and other gamma-ray pulsars. I am also thankful to the observatory staff for their generous support during my prolong stays there.

I sincerely thank Paul Ray, and the other members of the LAT-team for providing up-to-date timing models of several radio-quiet gamma-ray pulsars.

I am grateful to Wasim, Prabu, Venkatesh, Manoharan, Aswathappa, Rajendra, Manan, Jayanth and many more colleagues who helped in carrying out our simultaneous multi-frequency observations using the GMRT, ORT, Gauribidanur telescope and the MST Radar facility. Thanks to Wasim for various (quite long) discussions about radio astronomy and signal processing which have been useful at times.

Single pulse sequences analyzed in Chapter 2 were observed using the Arecibo telescope. We are thankful to Joanna Rankin for making these data sets available to us.

MBR could be realized due to significant efforts from Vinutha, Jayanth, Raghavendra (KBR), Som, Arasi, Sujatha, Kasturi, Sandhya, Durai, Shahram, Aswathappa, Indrajit, Sarabagopalan, Ananda, Deepa, Krishnamurthy, Nikhil, Nagaraja, Narayanaswamy, Wasim, Harshad, Srivani, Venugopal, and Salna from RRI and Gary, Jonah, Carla, Marty, Dennis, John, Anthony, Karen, and Amy from GBT. Working with the MBR-team and interacting with the team members, directly or indirectly, was really a fruitful learning experience. I am also thankful to various other colleagues from RRI, IIA, GBT and to the GMRT operation team, for their generous support and help at various stages of the MBR project.

Work presented in this thesis has made use of observations carried out using the Arecibo Telescope, Green Bank Telescope (GBT; operated by the National Radio Astronomy Observatory), Gauribidanur Radio Telescope, MST Radar Facility, Giant Metrewave Radio Telescope (GMRT) and Ooty Radio Telescope (ORT).

1. The Arecibo Observatory is operated by SRI International under a cooperative agreement

with the National Science Foundation (AST-1100968), and in alliance with Ana G. Mendez-Universidad Metropolitana, and the Universities Space Research Association.

2. The National Radio Astronomy Observatory is a facility of the National Science Foundation operated under cooperative agreement by Associated Universities, Inc.
3. The Gauribidanur radio telescope is jointly operated by the Raman Research Institute and the Indian Institute of Astrophysics.
4. MST radar facility is operated by the National Atmospheric Research Laboratory (NARL) which is an autonomous Research Institute funded by the Department of Space of the Government of India.
5. GMRT is an international facility run by the National Centre for Radio Astrophysics of the Tata Institute of Fundamental Research. ORT is run by the National Centre for Radio Astrophysics of the Tata Institute of Fundamental Research.

This thesis has made use of various useful resources, available freely on the web, like ADS, ArXiv, ATNF, EPN, Google, etc. I also wish to acknowledge Council for Scientific and Industrial Research, India for financial support during initial stages of the work.

Contents

Synopsis	ii
Acknowledgments	vii
Table of Contents	x
List of Figures	xiii
List of Tables	xvi
1 Introduction	1
1.1 A brief introduction to pulsars	1
1.2 Average properties of pulsars	3
1.2.1 Pulse shape and morphology	3
1.2.2 Flux density spectra	5
1.2.3 Polarization	7
1.2.4 Profile evolution with frequency	9
1.3 Characteristics of single pulses	11
1.3.1 Giant pulses and micro-structures	11
1.3.2 Subpulse drifting	11
1.3.3 Pulse nulling	17
1.3.4 Profile mode changing	18
1.4 Pulsar searches	19
1.4.1 Periodicity searches	19
1.4.2 Single pulse searches	20
1.5 Structure of the thesis	21
I Origin of Radio Emission in Multiple Cones	23
2 The multiple emission cones of the pulsar B1237+25	24
2.1 Introduction	24
2.2 The polar magnetosphere emission patterns	26
2.2.1 Analysis procedure	26
2.2.2 The emission maps	30
2.3 The modulation-phase and the carousel model	34
2.4 The emission in the two cones	39
2.4.1 The correlation properties	39

2.4.2	The emission altitudes	44
2.5	Discussion	46
2.6	Conclusions	49
 II Tomography of the Pulsar Magnetosphere: Development of a Multi-band Receiver		51
3	Multi-band receiver: Motivation	52
3.1	An approach using many telescopes simultaneously	53
3.2	Towards a superior alternative	56
4	Multi-band receiver : Design and development	57
4.1	The MBR system design: An overview	58
4.2	Multi-band feed: A design study	58
4.2.1	New multi-band feed designs: An overview	60
4.2.2	Further characterization of the second design	62
4.2.3	The bottom line	65
4.3	Description of the MBR system in its present form	65
4.3.1	Multi-band feed	67
4.3.2	RF front-end	67
4.3.3	Sub-band receiver chains	68
4.3.4	Monitoring and control software	69
4.3.5	Tests and performance	71
4.4	Summary	74
5	Synoptic Results	75
5.1	Synchronization and data quality	75
5.2	Spectral evolution of average properties	76
5.2.1	Analysis procedure	76
5.2.2	Spectral evolution of the emission altitude	78
5.2.3	The radio emission spectrum	85
5.3	Tomography of the pulsar magnetosphere	87
5.3.1	Subpulse modulation properties and the emission maps	87
5.3.2	A preliminary tomograph	89
5.4	A multi-band search for fast transients	91
5.5	Summary	92
 III Searches for Decameter-wavelength Counterparts of Radio-quiet Gamma-ray Pulsars		94
6	Motivation, observations, and detection methods	95
6.1	Introduction	95
6.2	Gauribidanur radio telescope	97
6.3	Reactivation of the telescope	99
6.3.1	Phasing of the dipole-array	99
6.3.2	The acquisition setup	100
6.3.3	The monitoring setup	103
6.4	Observations and pre-search data processing	104

6.4.1	The archival data	104
6.4.2	Deep search observations	104
6.4.3	Pre-search data processing	107
6.5	Single pulse search	110
6.5.1	Methodology	110
6.5.2	Challenges at low frequencies	115
6.6	Search for periodic signal	118
6.7	Deep search for periodic signals	120
6.7.1	Methodology	121
6.8	Summary	126
7	A possible detection and other results	127
7.1	A candidate detection of J1732–3131	128
7.1.1	Search for periodic pulsed signal	128
7.1.2	Search for single bright pulses	130
7.1.3	Confirmatory Checks	133
7.1.4	Discussion	133
7.2	Deep follow-up observations of J1732–3131	136
7.3	Upper limits on pulsed radio emission	138
7.4	Giant radio pulses/flares from unknown source(s)	142
7.5	Summary	144
8	Conclusions and future perspectives	146
A	Emission geometry: A few useful expressions	153
A.1	Polarization position angle	153
A.2	Magnetic azimuth	155
A.3	Subpulse modulation phase	155
B	MBR: Supplementary Material	157
B.1	MBR hardware block diagrams	157
B.2	MBR software details	162
B.3	Synoptic results: Supplementary material	164
C	Radio counterparts of gamma-ray pulsars	167
C.1	Profile significance measure: Figure of merit	167
C.2	Estimation of the clock drift rate	169
	Bibliography	171

List of Figures

1.1	A toy model for pulsar and its magnetosphere.	2
1.2	Average profiles for a sample of 12 pulsars.	4
1.3	Origin of different number of pulse components in two competing beam models.	5
1.4	Examples of typical pulsar radio spectra.	6
1.5	Full polarimetric average profile of the pulsar B0525+21.	7
1.6	An illustration of the “Magnetic pole model” (or “Rotating vector model”).	8
1.7	Profile shape evolution with frequency.	9
1.8	An illustration of radius-to-frequency mapping.	10
1.9	Examples of sub-pulse drifting phenomenon.	12
1.10	Longitude-resolved fluctuation spectrum for pulsar B0943+10.	13
1.11	A schematic illustration of the carousel model.	14
1.12	Reconstructed emission map of B0943+10.	17
1.13	Average profiles of B1237+25 in three different modes.	18
2.1	A typical longitude-resolved fluctuation spectrum of the pulsar B1237+25.	28
2.2	Sliding Fluctuation Spectrum (SFS).	29
2.3	Component-resolved fluctuation spectrum and longitude-longitude correlation map of B1237+25.	31
2.4	A reconstructed image of the accessible emission region of B1237+25.	33
2.5	Polar emission maps constructed for various sub-sequences.	34
2.6	Modulation amplitude and phase as a function of pulse longitude, computed for various sub-sequences.	36
2.7	Relative pulse-energy histograms of various pulse sequence.	38
2.8	The Polar Correlation and Azimuthal-Shift maps computed using the sub-sequence A ₁	40
2.9	The Polar Correlation maps for all the sub-sequences.	41
2.10	The Polar Azimuthal-Shift maps for all the sub-sequences.	42
2.11	Polar maps of the emission corresponding to the two OPMs.	45
2.12	Cross-correlation function of fluctuations in the outer and inner emission patterns.	48
3.1	A cartoon illustrating tomography of the polar emission region.	53
3.2	Average profiles of the bright pulsar B1237+25 obtained from observations using the GMRT and the ORT.	54

4.1	The basic design of the MBR.	59
4.2	Multi-Band Feed (MBF) Design-1: Mechanical model and return-loss measurements.	60
4.3	MBF Design-2: Mechanical model and return-loss measurements.	61
4.4	MBF Design-2: Details of the feed-line connections.	62
4.5	An optimum grid pointing scheme to sample beams across wide frequency range.	63
4.6	The azimuthally-averaged radial illumination function.	64
4.7	Overall block diagram of the MBR.	66
4.8	Ethernet data packet structure.	69
4.9	A snapshot of spectra as well as total power time-sequences being monitored in quasi-real-time.	70
4.10	An example test scan performed through the accessible spectral spans.	71
4.11	Beam-width estimates corresponding to the 10 frequency bands.	73
5.1	Dynamic spectra for each of the nine MBR bands stacked together, across a 2 seconds span.	77
5.2	The system gain for each of the two polarization channels, and nine frequency bands.	79
5.3	Average Stokes-I, linearly polarized intensity, position angle, and Stokes V profiles of the bright pulsar B0329+54, observed simultaneously in the nine bands.	80
5.4	Summary of the fitted parameters, and the profile-shift, of B0329+54 as a function of frequency.	81
5.5	Period-averaged and conal & core component peak flux density spectrum of the pulsar B0329+54.	85
5.6	Raw single pulse sub-subsequences (period-stacked) of B0809+74 at 4 of 10 MBR frequency bands.	88
5.7	Longitude resolved fluctuation spectra of B0809+74 at 233 and 330 MHz.	89
5.8	Cartographically mapped emission patterns of B0809+74 at 4 frequency bands.	90
5.9	A preliminary tomograph of the polar emission region of B0809+74.	91
5.10	Dedispersed single pulses corresponding to the dynamic spectra shown in Figure 5.1.	93
6.1	Configuration within each of the EW array groups.	97
6.2	Combination of outputs from the 10 groups in the EW array.	98
6.3	Quasi-real time monitoring of total power sequence.	103
6.4	Typical system gain variations while tracking the source.	106
6.5	Optimum time resolution as a function of dispersion measure.	108
6.6	A typical mapping of trial DM-channel number to DM.	112
6.7	Diagnostic plots presenting single pulse search output.	114
6.8	Optimal detection of single pulses by matched filtering using a truncated exponential template.	116
6.9	Swept frequency RFI resulting in a spurious detection.	117
6.10	Spectral characteristics of the spurious detection in Figure 6.9	117
6.11	Simultaneous detection of bright pulses from the pulsars B0943+10 and B0950+08.	119
6.12	Search for periodic signal in the DM–pulse-width, and the DM–P0 domains.	120
6.13	Deep search for periodic signal by combining multi-epoch observations.	123
6.14	Phase-aligned stack of average profiles of the pulsar B1919+21.	124
6.15	Detection of an high DM pulsar: B0525+21 with a DM of 50.94 pc/cc.	125
7.1	Results of search for periodic signal from J1732–3131 in the <i>DM, pulse-width</i> space.	128
7.2	Results of search for periodic signal from J1732–3131 in the <i>DM, Period</i> space.	129
7.3	Average pulse profile of J1732–3131 at 34.5 MHz.	130

7.4	A stack of partially averaged profiles of J1732–3131, along with the positions of 10 bright single pulses.	131
7.5	Dynamic spectrum of the 10 single pulses of J1732–3131, aligned and averaged together.	132
7.6	Multi-epoch average radio profiles of J1732–3131.	137
7.7	Minimum detectable pulse energies for our single pulse searches.	139
7.8	Search results presenting detection of ultra-bright dispersed pulses.	143
7.9	Dedispersed dynamic spectra of brightest single pulses from two sessions.	143
A.1	A schematic view of the pulsar emission geometry.	154
B.1	Block diagram of the band-reject filter unit.	157
B.2	Block diagram of the MBR front-end.	158
B.3	Block diagram of the up-converter unit.	158
B.4	Block diagram of the down-converter unit.	159
B.5	Block diagram of the RF-unit.	159
B.6	Block diagram of the IF-chain.	160
B.7	Block diagram of the ADC-module.	160
B.8	Block diagram of the Virtex-5 FPGA Board.	161
B.9	Block diagram of the clock-generation and distribution board.	161
B.10	Software architecture of the MBR system.	164
B.11	Summary of modeling the average profiles as a sum of individual Gaussian components: The fitted Gaussian components	165
B.12	Summary of modeling the average profiles as a sum of individual Gaussian components: Fitted profiles and residuals	166
C.1	Comparison of two different realizations of sum-of-squares as a function of pulse duty cycle.	169
C.2	Estimation of the clock drift rate using multi-epoch observations of the bright pulsar B0834+06.	170

List of Tables

2.1	Modulation parameter summary of various sub-sequences.	30
2.2	Correlation between the <i>outer</i> and <i>inner</i> conal emission patterns: Summary of parameters.	43
2.3	Emission-altitude estimates.	44
4.1	Summary of the edge-tapers and G/T for 9 bands	64
4.2	RF Filter Specifications	68
5.1	Summary of estimated component positions and emission altitudes.	84
6.1	Decameter Wavelength Observations of Radio-quiet Gamma-ray Pulsars	105
6.2	Decameter Wavelength Observations of Control Radio-Pulsars	106
7.1	Measured and Derived parameters for PSR J1732-3131	134
7.2	Archival data: Upper limits on flux densities of 16 gamma-ray pulsars at decameter wavelengths	140
7.3	Deep search: Upper limits on decameter wavelength flux densities of 10 gamma-ray pulsars	141

Chapter 1

Introduction

1.1 A brief introduction to pulsars

In 1967, Jocelyn Bell discovered a series of pulses repeating with a very stable period, at 81 MHz using the Mullard radio astronomy observatory. Re-detection at a fixed local sidereal time on several days confirmed the astronomical origin of the periodic signal, and it turned out to be the discovery of the first radio pulsar¹ B1919+21 (Hewish *et al.* , 1968). Considerations of small period, and the observed increase in period with time, excluded the possibility that the periodic signal could be due to the orbital period of binary stars. Models involving oscillations of white dwarfs and neutron stars were also rejected quickly, again due to considerations of small periods (< 1 s), and rotating neutron stars remained the only plausible explanation. Subsequent discoveries of Vela and Crab pulsars, in the then already known supernova remnants, led to unequivocal association of radio pulsars with the fast rotating neutron stars. Soon after its discovery at radio wavelengths, Crab pulsar was also detected in the archived X-ray and soft gamma-ray data (Fishman *et al.* , 1969a,b). To date, more than 2000 isolated and 213 binary radio pulsars² (Manchester *et al.* , 2005), 117 pulsars in gamma-rays³ and about 150 pulsars (isolated as well as binary) in X-rays have been detected.

The rotation periods (P) of known radio pulsars range between 1.4 milliseconds to 8.5 seconds. Pulsars lose their rotational energy in various forms, including the tiny loss due to radio emission, and their rate of rotation decreases with time. The period derivative (\dot{P}) is an impor-

¹The name ‘pulsar’ was coined as a portmanteau of ‘pulsating star’.

²<http://www.atnf.csiro.au/people/pulsar/psrcat/>

³The Second *Fermi*-LAT Catalog of Gamma-ray Pulsars (arXiv1305.4385).

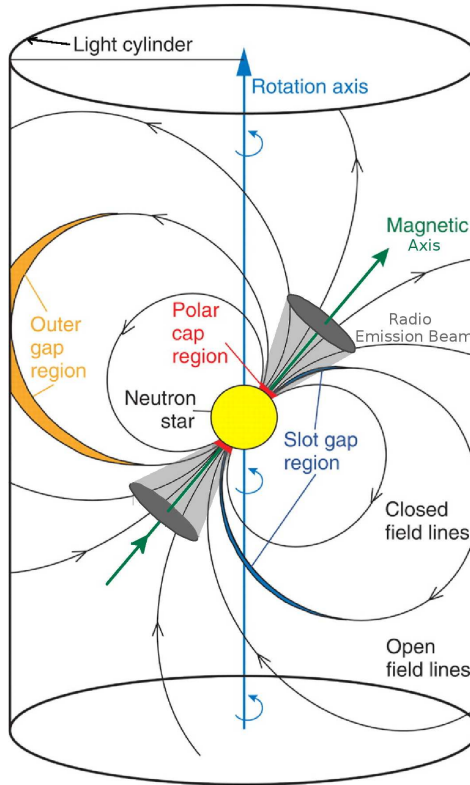


Figure 1.1: A toy model for pulsar and its magnetosphere (not drawn to scale): The radio emission is understood to be originated in narrow beams from each of the magnetic poles. The radio emission originating plasma in the narrow beams, defined by the open field line regions, are believed to be seeded from the polar caps (see section 1.3.2). The magnetic axis is mis-aligned with the rotation axis. Various models predict three different regions – “polar cap”, “outer gap” and “slot gap” regions – where gamma-rays could possibly be originated.

tant observational parameter. Assuming a model in which spin-down is due to magnetic dipole radiation alone, \dot{P} is used to estimate the surface magnetic field ($\propto \sqrt{P\dot{P}}$) and the characteristic age ($= P/2\dot{P}$) of pulsars. Generally, pulsars with $P \geq 20 \text{ ms}$ and $\dot{P} > 10^{-18} \text{ s/s}$ are considered as *normal pulsars*, and those with $P < 20 \text{ ms}$ and $\dot{P} \leq 10^{-18} \text{ s/s}$ are called *millisecond pulsars*. Pulsars are highly magnetized neutron stars. The strength of magnetic field at their surfaces ranges between 10^8 G for very old pulsars to above 10^{12} G for very young ones.

Radio pulsars emit narrow beams of electromagnetic radiation from each of the two magnetic poles (see a toy model of pulsar and its magnetosphere in Figure 1.1). The magnetosphere is filled with plasma that rotates with the star. The boundary where the velocity of plasma co-rotating with the star would equal to the velocity of light, is marked as light-cylinder. Co-rotation of plasma

breaks down somewhere before the light-cylinder boundary is reached, and the magnetic field lines which cross the light-cylinder are called open field lines. Radio emission is believed to originate in the open field line region. The magnetic axis is generally oriented at an angle to the rotation axis. If the emission beam, rotating with the star, sweeps across the observer's line of sight, a pulse of radio emission is produced. The brightness temperature estimated using the observed single/average pulse durations and intensities, is of the order of 10^{29} K. Such extremely high brightness temperature constrains the radio emission to be coherent. Pulsar radio emission is generally thought to originate from bunches of charged particles streaming along the open magnetic field lines above the star's magnetic poles. However, the actual details of the radio emission mechanism are still poorly understood.

A detailed introduction to all the properties of pulsars, and the diverse phenomena exhibited by them, is beyond the scope of this chapter⁴. In the following sections, we provide an introduction to the basic properties of pulsars, and only those phenomena that are relevant to the work presented in this thesis.

1.2 Average properties of pulsars

Averaging a sequence of single pulses, by folding over the pulsar rotation period, quickly leads to a stable profile shape. The time scale required to achieve a stable profile shape varies from a few hundred to a few thousand pulse periods.

1.2.1 Pulse shape and morphology

Although the shape and intensities of single pulses vary a lot, for a given pulsar, the integrated profile at a given radio frequency is usually stable from one observation to other. Variety of integrated profiles for a sample of 12 pulsars are shown in Figure 1.2. As exemplified by this figure⁵, the pulse shape varies considerably in complexity, from a single component profile to complex profiles with more than 5 components. Initially, millisecond pulsar profiles appeared to be more complex than those of the normal pulsars. However, later studies showed that the average number of components are comparable for the two classes (3 ± 1 components for normal pulsars, and 4 ± 1 for the millisecond pulsars, Kramer *et al.*, 1998). The pulsed emission of pulsars is generally confined within a small range of pulse longitudes, however, exceptions from this general trend have also been observed (e.g.,

⁴We refer the reader to Manchester & Taylor (1977) and Lorimer & Kramer (2004), for a detailed review of pulsar properties, theoretical background, pulsar observations and related instrumentation, and pulsar searches.

⁵Average pulse profiles for a large number of pulsars can be accessed from the European Pulsar Network pulse profile database: <http://www.jb.man.ac.uk/research/pulsar/Resources/ePN/>

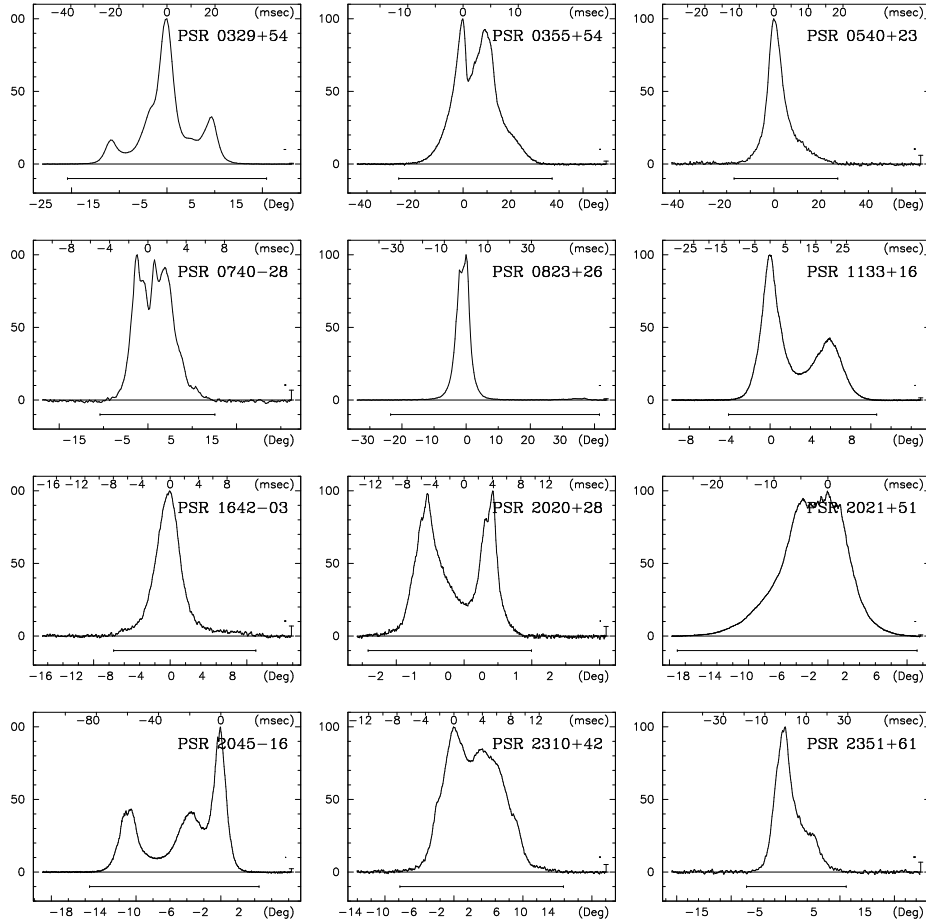


Figure 1.2: Average intensity profiles for a sample of 12 pulsars, observed at 1.41 GHz, are shown. For each of the profiles, the rotational phase (in degrees) and time (in milliseconds) are marked on the bottom and top horizontal axes, respectively [Figure taken from Seiradakis & Wielebinski (2004)].

emission from B0826-34 is seen at almost all the pulse longitudes). Emission from a broad range of pulse longitudes is observed generally for viewing geometries with small magnetic inclination angle, so that our line of sight samples the emission beam for a larger fraction of the rotation cycle. From a small fraction of the known radio pulsars, an additional component, *inter-pulse*, situated about half-way between the consecutive main pulses, has also been observed.

The average profiles exhibit important morphological differences. The hollow emission cone model (Komesaroff, 1970; Oster & Sieber, 1976) could explain the single and two-component profiles. When the observer's line of sight cuts the hollow cone, emission is seen from two edges of the cone resulting into a two-component profile. A single component profile is observed when the line of sight just grazes the emission cone. To explain further complex profiles, two additional

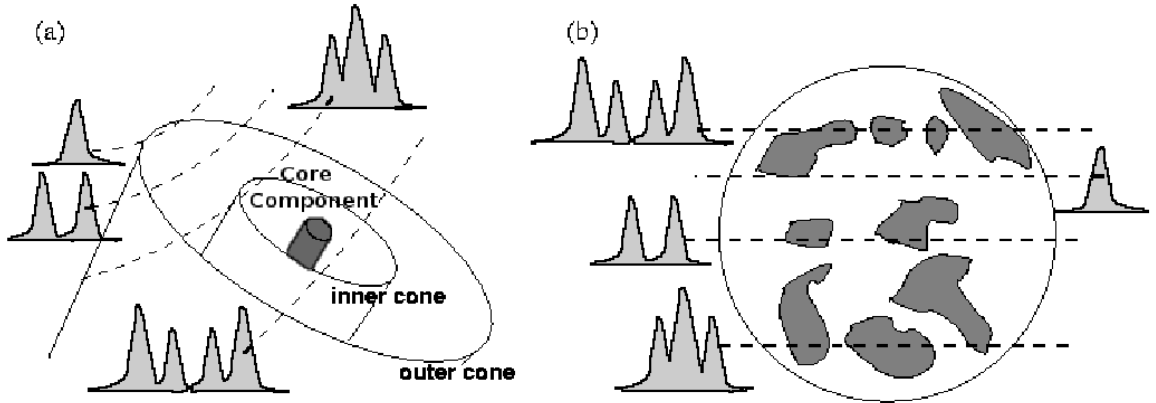


Figure 1.3: Origin of different number of pulse components in two competing beam models: (a) multiple hollow emission cones nested around the core-component (b) patchy emission beam. Figure is taken from “Handbook of Pulsar Astronomy” (Lorimer & Kramer, 2004), and appropriately modified to demonstrate the position of the core component as well.

modifications to the hollow cone model have been considered: (a) a pencil-beam, known as core component, exists along the magnetic axis (Backer, 1976), and (b) there could be multiple hollow emission cones nested around the central core beam (Oster & Sieber, 1976; Sieber & Oster, 1977; Rankin, 1993; Gil *et al.*, 1993). As demonstrated in Figure 1.3(a), different number of components can result from appropriate cuts of the observer’s line of sight. An alternative model suggesting the radio beam to be randomly filled up with discrete active emitting patches (Lyne & Manchester, 1988) could also explain the different number of observed pulse components (see Figure 1.3(b)). However, unlike the nested hollow cone model, this model is unable to predict the observed profile evolution with radio frequency (discussed in section 1.2.4).

Depending on the observed number of pulse components and the viewing geometry, Rankin (1983) categorized the average profiles in the following categories: [1] Conal-single (S_d) profiles consisting of a single pulse component originated due to line of sight grazing the emission cone; [2] Core-single (S_t) profiles that are completely dominated by the emission from the central beam in the form of a single component; [3] Double (D) profiles consisting of two prominent conal components bridged by broad, low-amplitude core emission; [4] Triple (T) profiles exhibit a discernible core component, flanked by two conal components; and, [5] Multiple (M) profiles consist of prototypically five components, involving a core component and four conal components.

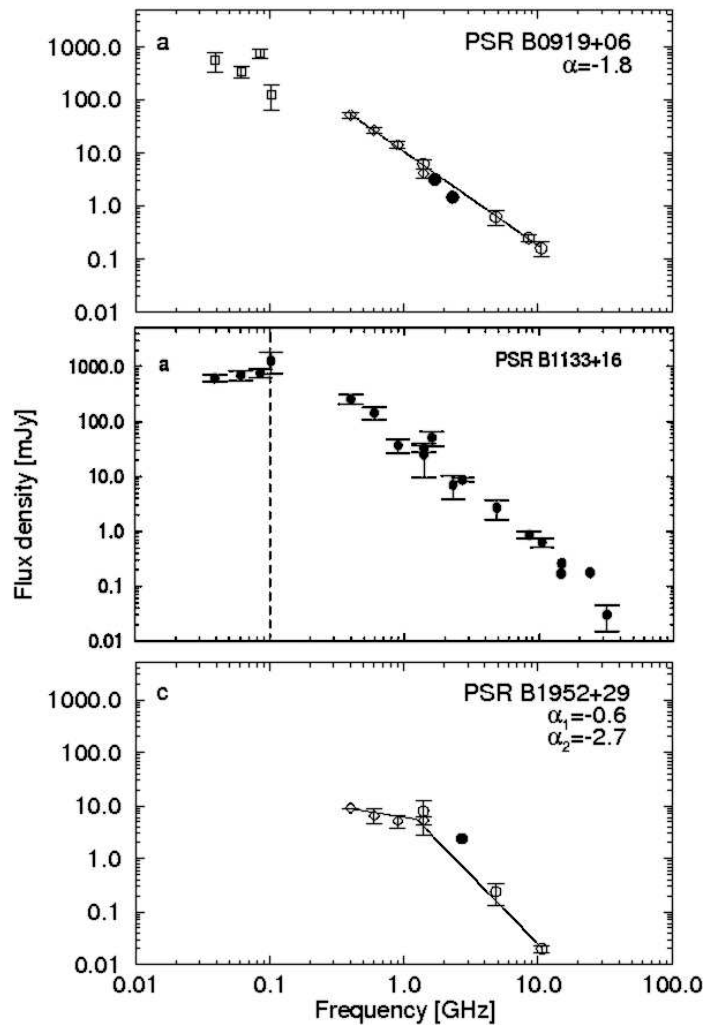


Figure 1.4: Examples of typical pulsar radio spectra. *Upper-panel:* A spectrum with $\alpha = -1.8$. *Middle-panel:* An example of low frequency turn-over in the spectrum. *Bottom-panel:* A two-power law spectrum with large difference in slopes. Figure reference: Maron *et al.* (2000)

1.2.2 Flux density spectra

Pulsars are generally weak radio sources. The mean flux density $S(\nu)$ of pulsars (measured as the integrated intensity of the pulse profile averaged over the pulse period) has a strong inverse dependence with the observing radio frequency. For most of the pulsars, this dependence can be approximated by a simple power law: $S(\nu) \propto \nu^\alpha$ for $\nu \gtrsim 100$ MHz. In a recent study of 281 pulsars (Maron *et al.*, 2000), spectra of the majority of pulsars could be described by the above simple power law with an average value of spectral index $\langle \alpha \rangle = -1.8 \pm 0.2$. However, the range

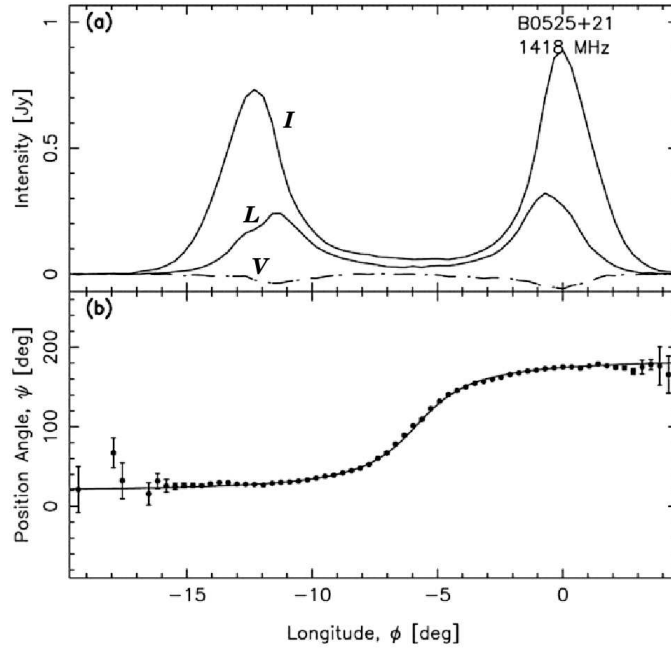


Figure 1.5: Full polarimetric average profile of the pulsar B0525+21. (a): The total and linearly polarized intensities are shown by the solid lines (marked by ‘ I ’ and ‘ L ’, respectively), while the circularly polarized flux density is marked by dashed-dotted line (‘ V ’). (b): The observed position angle of the linear polarization (dots with error bars as measurement uncertainties), and the fitted position angle as a function of pulse-longitude are shown together. Figure reference: Everett & Weisberg (2001).

of observed spectral indices is quite broad ($-4 \lesssim \alpha \lesssim 0$). About 10% of these pulsars show more complex behavior, and require two-component power law for a good spectral fit. Often, a spectral turn-over is also seen at lower frequencies (100–300 MHz). A few examples of typical spectra (taken from Maron *et al.*, 2000) are shown in Figure 1.4. Mean spectral index for millisecond pulsars has been found consistent with that for the normal pulsar population (Kramer *et al.*, 1998; Toscano *et al.*, 1998).

1.2.3 Polarization

Pulsars are among the highly polarized sources in the known radio universe. The average degree of linear polarization of pulsars is about 20%, while that of circular polarization is about 10% (estimated using a sample of 300 pulsars, studied at 600 and 1400 MHz; Gould & Lyne, 1998). However, profiles of many pulsars are much more polarized than the above estimated mean, and for several individual pulsars degree of polarization reaches as much as 100 percent. An example of a polarization profile is shown in Figure 1.5. Note that the position angle (PA) of the linearly

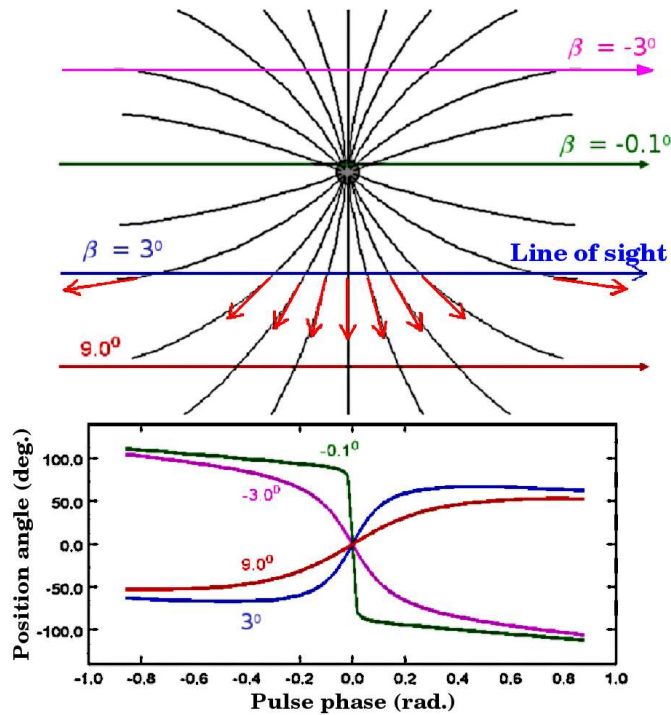


Figure 1.6: An illustration of the “Magnetic pole model” (Radhakrishnan & Cooke, 1969, generally called as “Rotating vector model”). Top: The black lines show the projection of the magnetic field lines as seen from a very small angle from the magnetic axis. Various horizontal lines (red, blue, green and pink) depict line of sight cuts across the emission beam for different values of the impact parameter β . For the line of sight corresponding to $\beta = 3^\circ$, the projected directions of the field lines are marked by red color arrows. Bottom: The expected curves of the polarization position angle as a function of pulse longitude, for various values of the impact angle, are shown in the corresponding colors. Note that the curves are shown only across about 100° of pulse longitude centered around the fiducial plane. Figure courtesy: Alice K. Harding, *Frontiers of Astronomy with the World’s Largest Radio Telescope* meeting, 2007 (www.naic.edu/~astro/frontiers/talks/AKH_pulsars.ppt).

polarized intensity, shown in the bottom panel, varies smoothly as a function of pulse longitude. This S-shaped sweep of the position angle was explained by Radhakrishnan & Cooke (1969) by assuming a rotating neutron star with the magnetic axis inclined at an angle to the rotational axis, and putting forward simple geometrical arguments. They argued that the plane of linearly polarized emission is parallel to the instantaneous direction of the magnetic field at the point of emission. The projected direction of the magnetic field rotates as the beam sweeps across the observer. Consequently, the PA varies rapidly at the profile center, and relatively slowly as we go away from the center (see Figure 1.6). This interpretation, known as “Rotating vector model” (RVM), predicts the position

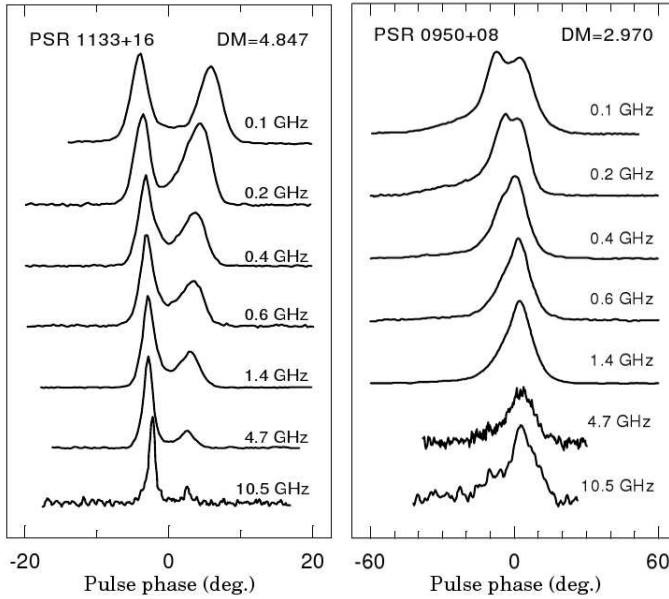


Figure 1.7: Pulse profiles for pulsars B1133+16 and B0950+08 aligned at various frequencies. As we go towards lower frequencies, the systematic increase in the separation between the two components of B1133+16, and the width of B0950+08, is clearly visible. The aligned profiles are taken from Kuzmin *et al.* (1998).

angle ψ as a function of the pulse longitude (ϕ) as follows (Komesaroff, 1970):

$$\tan(\psi - \psi_0) = \frac{\sin \alpha \sin(\phi - \phi_0)}{\sin(\alpha + \beta) \cos \alpha - \sin \alpha \cos(\alpha + \beta) \cos(\phi - \phi_0)} \quad (1.1)$$

where α is the magnetic inclination angle, β is the impact parameter (the closest approach of the line of sight to the magnetic axis), ϕ_0 is the longitude of the fiducial plane (i.e., the plane containing the magnetic and the rotation axis), and ψ_0 is the position angle at the fiducial point ϕ_0 . The steepest gradient of the PA happens to be at $\phi = \phi_0$, and is related to α and β by:

$$\left(\frac{d\psi}{d\phi}\right)_{\max} = \frac{\sin \alpha}{\sin \beta} \quad (1.2)$$

Many pulsars exhibit PA sweeps deviating from that predicted by the RVM. Particularly, millisecond pulsars show large deviations from the expected monotonic swings. Manchester *et al.* (1975), through their analysis of single pulses, observed that several sources exhibit rapid jumps in their PA curves, reaching nearly 90° . These jumps have been interpreted as due to interchange in dominance of two orthogonal polarization modes present in the radiation. Non-orthogonal jumps also have been observed for several pulsars. This phenomenon is generally referred to as *polarization mode changing*.

1.2.4 Profile evolution with frequency: radius-to-frequency mapping (RFM)

Profile shape for most of the pulsars shows significant evolution with frequency. The total pulse width and separation between profile components are seen to be systematically increasing for

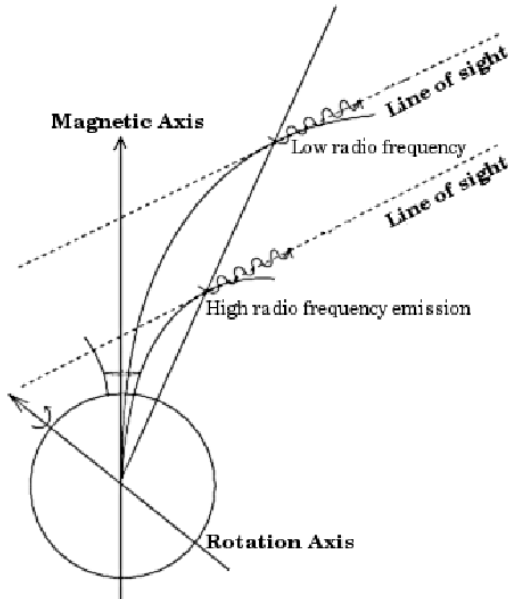


Figure 1.8: An illustration of radius-to-frequency mapping: Two field lines are shown from which radio waves at two different frequencies are originated for a given line-of-sight. Due to RFM, the high radio frequency (RF) waves originate from field lines closer to the star surface than those responsible for low RF waves. Note that the high RF waves are emitted closer to the magnetic axis than the low RF waves, and hence, the low RF profile is wider than its counterpart at high RF. This illustration also shows that the high RF waves originate from outer field lines, while the low RF waves from inner field lines. Figure reference: Smits *et al.* (2005).

most of the normal pulsars when observed at lower frequencies. Two examples of such evolution with frequency are shown in Figure 1.7. This effect has been interpreted as an indication that the emission at higher frequencies originates closer to the star's surface than that at lower frequencies (Komesaroff, 1970). This model is known as radius-to-frequency mapping (RFM; Cordes, 1978).

Note that there is a change in relative intensities of the two components of B1133+16, and the number of components appears to vary for B0950+08 (Figure 1.7) as a function of frequency. These are generally interpreted as different spectral indices of emitting regions and/or seeing different emitting regions due to geometrical factors.

Estimating emission heights

A model wherein the radio emission happens in the form of a narrow beam centered around the magnetic axis (Radhakrishnan & Cooke, 1969; Komesaroff, 1970), explains many of the observed average properties of pulsars, including RFM. In this model, the plasma moves along the open magnetic field lines and emit radio waves in the direction tangential to the magnetic field lines. RFM suggests that the profiles at different frequencies trace the open field line regions of the magnetosphere at different emission heights (see an illustration in Figure 1.8). The half-opening angle of the radiation beam (ρ) depends on the width of the open field line region, and increases with the emission height. For an observed pulse width W , ρ can be estimated if the viewing geometry (α and β) of the pulsar is known from polarization measurements. Since the profile width is defined by the

tangents to the last open field lines, the opening angle of the cone is given by (Gil & Kijak, 1993),

$$\rho \approx 1.24^\circ [r_6(\nu)]^{1/2} P^{-1/2} \quad (1.3)$$

where P is the rotation period in seconds and $r_6(\nu)$ is the emission altitude in units of 10^6 cm. We can use this expression to compute the emission heights from the derived opening angles. We emphasize here that the above geometrical expression provides us a lower limit on the emission height, since the emission might not extend up to the last open field lines.

In addition to the above geometrical approach, aberration and retardation effects are also utilized to compute the emission altitudes. These effects, if measurable, can provide reasonably accurate estimates of the emission altitudes if the sweep-back of magnetic field lines is taken in to account appropriately. For more details about the above two kinds of methods to estimate emission heights, we refer the reader to section 5.2.2 of this thesis, and Phillips (1992); Gil & Kijak (1993); Dyks & Harding (2004); Dyks *et al.* (2004).

1.3 Characteristics of single pulses

While integrated profiles are quite stable for pulsars, individual pulses show large variation in strength and exhibit a rich variety of structure on a range of time scales.

1.3.1 Giant pulses and micro-structures

Individual pulses varying in brightness by a factor of a few, as compared to the average profile, is not unusual for pulsars. However, a handful of pulsars occasionally emit giant pulses with an intensity up to 1000 times that of an average individual pulse. These giant bursts often have structures down to nanosecond time scales. The Crab pulsar was discovered through detection of its giant pulses. A recent discovery of nanosecond subpulses within the giant radio pulses from the Crab pulsar suggested that the plasma structures responsible for these emissions may be smaller than even one meter in size (Hankins *et al.*, 2003). Other than the Crab pulsar, a few more stars, e.g., B1937+21, B1821–24, B0540–69 etc., are also known to emit giant pulses.

Structures with duration of a few microseconds have been detected in the individual pulses of many pulsars. This phenomenon, known as ‘microstructure’ has been shown to be broadband, and sometimes quasi-periodic. Microstructure is exhibited by 30–70 percent of the individual pulses of many normal pulsars (Lange *et al.*, 1998).

1.3.2 Subpulse drifting

Individual pulses usually consist of one or more components called subpulses. The subpulses appear to be basic emission entities, and typically have a Gaussian shape. Components in the integrated profiles are formed when the strength and/or occurrence of subpulses is not uniform across the pulse longitudes. For many pulsars, subpulses in successive pulses have been observed to be drifting systematically across the profile. This phenomenon is known as *subpulse drifting* (first observed in B1919+21 and B2016+28 by Drake & Craft, 1968). Examples of this phenomenon seen in pulsars B0809+74 and B0818–13 are provided in Figure 1.9, wherein subpulses appear at the trailing edge of the profile, and drift towards the leading edge before disappearing several periods later. The spacing between the consecutive subpulses, generally visible within a given individual pulse, is generally denoted by P_2 (P_1 or P is used for the pulsar rotation period itself). The bands of drifting subpulses have been found to be periodic/quasi-periodic, and their period of recurrence is denoted by P_3 (these parameters are schematically illustrated in the *right panel* of Figure 1.9).

Following Backer (1973), a series of spectra computed separately for different longitudes throughout the profile, known as “longitude-resolved fluctuation spectra” (LRFS), is used for a quantitative determination of P_3 and further spectral studies of drifting subpulses. An example of LRFS, using the single pulse sequence of B0943+10, is presented in Figure 1.10. A strong feature at around 0.46 cycles/P is clearly evident throughout the profile. Note that the maximum frequency of a feature that can be seen in the LRFS without aliasing, is 0.5 cycles/P. With the “harmonic-resolved fluctuation spectrum” (HRFS) developed by Deshpande & Rankin (2001) and “2-dimensional fluctuation spectrum” (2DFS; Edwards & Stappers, 2002), the maximum unaliased detectable frequency reaches up to 1 cycle/P. The HRFS and 2DFS are also helpful in estimating the subpulse spacing P_2 .

The degree of modulation of pulse intensities is usually expressed by the modulation index m (see, e.g., “Pulsars” by Manchester & Taylor, 1977), given by

$$m = \frac{(\sigma_{\text{on}}^2 - \sigma_{\text{off}}^2)^{1/2}}{\langle I \rangle} \quad (1.4)$$

where $\langle I \rangle$ is the mean pulse intensity, and σ_{on} and σ_{off} are the root mean square (rms) variations of the pulse intensities and the off-pulse noise, respectively, about their corresponding mean values. Generally, the modulation indices are different at different pulse phases in a given pulsar.

Physical mechanism of subpulse drifting: the carousel model

Ruderman & Sutherland (1975, hereafter R&S) proposed a physical model for radio emission from pulsars that could explain the drifting subpulses. In their model, a polar magnetospheric gap, about 100 meters in height, is formed near the star surface spanning only the open field line

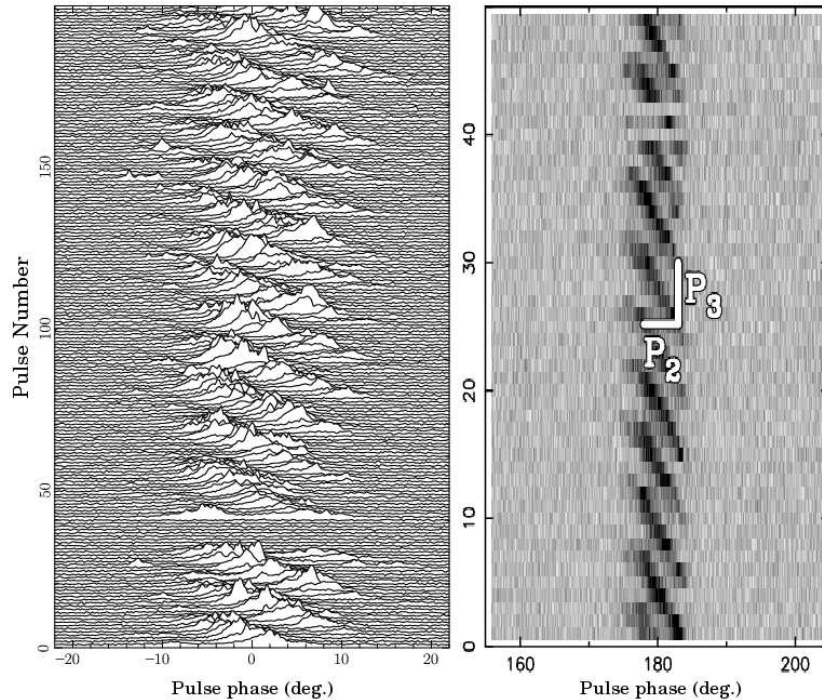


Figure 1.9: The *left* and *right* panels show stack of single pulses of the pulsars B0809+74 and B0818–13, respectively [The left and right Figures are taken from van Leeuwen *et al.* (2002) and Weltevrede *et al.* (2007), respectively]. The intensity variations in the right panel are coded in gray-scale (intensity changes from minimum to maximum as the color varies from white to black). Subpulses drifting from higher to smaller values of pulse phases are clearly apparent in both the panels. In the *left* panel, pulse-nulling can also be seen for the pulse number range of about 30 to 40.

region. The electric potential difference between the base and top of the gap is $\approx 10^{12}$ volts, and unlike everywhere else in the near magnetosphere, $\mathbf{E} \cdot \mathbf{B} \neq 0$ in the gap. The gap continuously breaks down due to forming of electron-positron pairs, called “sparking”. The gap electrons move towards the surface, while the positrons move out along the open magnetic field lines. R&S argue that, due to the extremely high electric potential and magnetic field in the gap, the curvature radiation from the “primary” particles can lead to a pair cascade, leading to a momentary discharge of the gap. The discharge causes $\mathbf{E} \cdot \mathbf{B}$ to fall rapidly at the location of the discharge, inhibiting formation of another simultaneous discharge within a distance $\sim h$ (the gap height) around it. Thus, the gap discharges through the formation of a group of discrete sparks. These sparks, assumed to be responsible for injecting the charged particles beyond the potential gap, form the basic emission entities in the open field line magnetosphere outside the gap, and cause the observed subpulse emission.

R&S further propose that the presence of potential gap alters the co-rotation velocity of

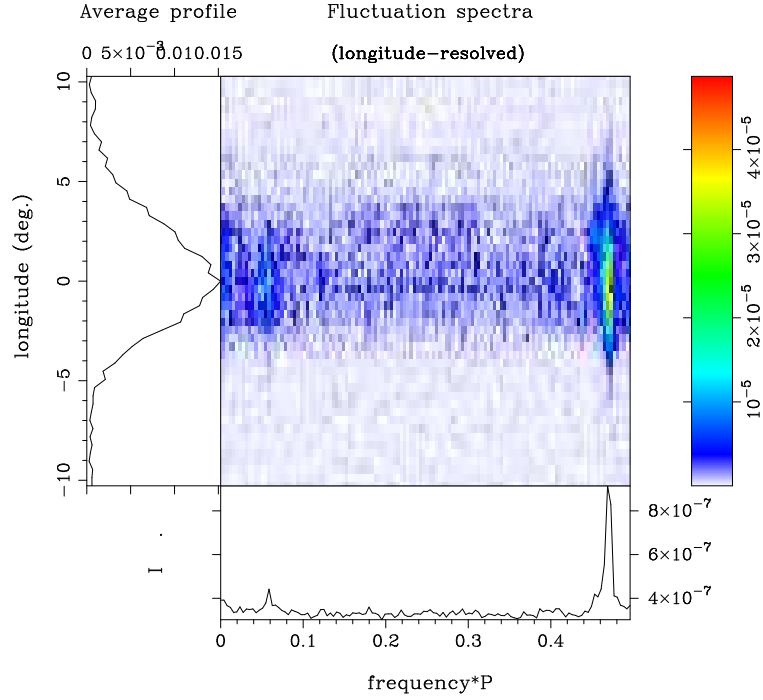


Figure 1.10: Example LRFS for pulsar B0943+10: The body of the figure shows the stacked fluctuation spectra computed separately for different longitudes throughout the profile shown in the *left panel*. The *bottom panel* shows the integral spectrum.

sparks, and the sparks drift around the magnetic pole due to the $\mathbf{E} \times \mathbf{B}$ drift. They derive the time for a spark to make a complete revolution about the magnetic pole (P_4) to be

$$\frac{P_4}{P} \approx 5.6 \frac{B_{12}}{P^2} \quad (1.5)$$

where B_{12} is the surface magnetic field in units of 10^{12} gauss, and the radius of the star and the potential difference across the gap are assumed to be 10 km and 10^{12} eV, respectively. Hence, R&S propose a carousel of sparks circulating around the magnetic axis. These sparks inject bunches of charged particles outside the gap which, then, move along the open magnetic field lines. Due to their curved trajectories along the field lines, these particles emit in radio wavelengths forming emission sub-beams (see an illustration in Figure 1.11). Whenever our line of sight crosses any of the sub-beams, a subpulse is observed. Since the sub-beams are seeded by the underlying carousel of rotating sparks, the emission sub-beams also circulate around the magnetic axis causing the drifting of subpulses across the profile width. If the carousel consists of N_{sparks} spark-discharges around the polar cap, then the carousel model strongly suggests that $P_3 = P_4/N_{\text{sparks}}$. The sub-pulse spacing P_2 is related with the sub-beam spacing, and can be found out if the viewing geometry, in addition

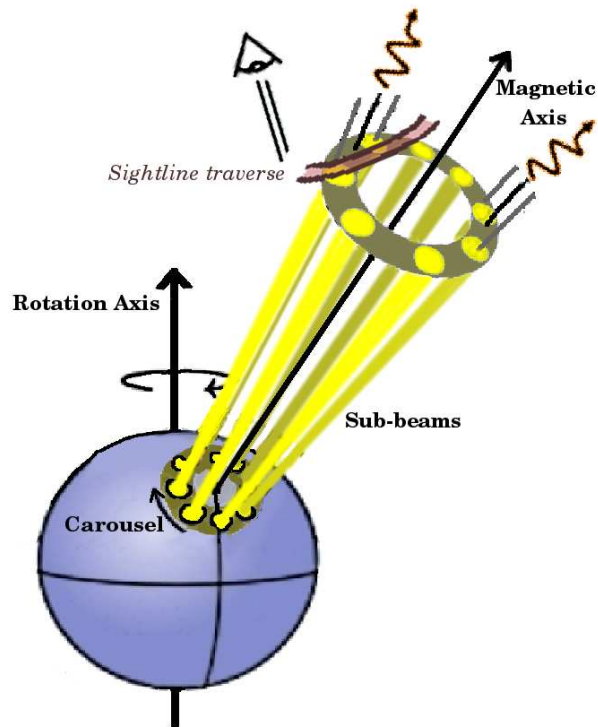


Figure 1.11: A schematic illustration of the carousel model (not drawn to scale): The blue sphere represents the neutron star, with mis-aligned rotation and magnetic axes. Eight sub-beams, seeded by a carousel consisting of same number of sparks circulating around the magnetic axis, are shown. Emission at a given frequency originates from a slice of these sub-beams at an altitude suggested by RFM. Constrained by the line of sight, only a tiny part of this slice is visible to the observer. An example sightline traverse is marked in the figure.

to the parameters P_3 and P_4 , is known.

Note that the carousel model naturally predicts the emission beam to be in the form of a hollow cone (consisting of sub-beams). As discussed in section 1.2.1, multiple components in integrated profiles suggest presence of nested hollow emission cones around the core component. To be consistent with the observations, corresponding modifications in the carousel model have been suggested (Gil & Sendyk, 2000). The modified carousel model consists of multiple carousels of sparks (as against a single carousel in the original model) with a central spark at the magnetic pole.

Mapping the carousel

As illustrated in Figure 1.11, observer can sample only a part of the slice of emission sub-beams, and effectively that of the polar cap. However, the carousel of sparks producing the sub-beams circulate around the magnetic axis, causing a different part of the polar cap to be sampled every time the observer's line of sight crosses the emission beam. If the carousel circulation period P_4 and the viewing geometry of the pulsar is known, the intensity fluctuations of the observed individual pulses in the observer's frame (i.e., in a system of pulse longitude ϕ , and geometrical parameters α and β) can be transformed to a frame centered at the magnetic pole and co-rotating with the pulsar (i.e., a system described by the magnetic colatitude and azimuth). Deshpande & Rankin (1999, 2001) developed such a *cartographic transform* to map the sub-beam configuration of the pulsar B0943+10. Following Deshpande & Rankin (2001), if the individual pulses are numbered by k from a reference pulse k_0 , and the pulse longitude ϕ is measured with respect to the fiducial longitude ϕ_0 , then the azimuth angle Θ is the sum of a rotation θ_{rot} and a transformation θ_{trans} as follows:

$$\Theta = A\theta_{\text{rot}} + B\theta_{\text{trans}} \quad (1.6)$$

where $A, B = \pm 1$, depending on the signs of the above two contributions. The rotation term accounts for the rotation of the carousel since the time of the fiducial longitude in the reference pulse k_0 , and is given by

$$\theta_{\text{rot}} = 2\pi[k - k_0 + (\phi - \phi_0)/2\pi]/P_4, \quad (1.7)$$

The transformation term, θ_{trans} , is essentially the magnetic azimuth as a function of pulse longitude

$$\theta_{\text{trans}} = \sin^{-1}[\sin(\alpha + \beta) \sin(\phi - \phi_0) / \sin R] \quad (1.8)$$

where R , the magnetic colatitude, is given by

$$R = 2 \sin^{-1}[\sin^2(\phi/2 - \phi_0/2) \sin \alpha \sin(\alpha + \beta) + \sin^2(\beta/2)] \quad (1.9)$$

After deducing the P_4 of the pulsar B0943+10, by a thorough analysis of single pulse sequences, Deshpande & Rankin (1999) used the cartographic transform defined by above equations to successfully reconstruct an image of the accessible emission zone. This reconstructed polar emission map is presented in Figure 1.12. Note that the presence of 20 discrete emission sub-beams is clearly evident in the polar emission map.

Subpulse modulation phase as a function of pulse longitude

Note that the azimuthal angle, Θ , in Equation (1.6) essentially represents the carousel rotation phase as a function of pulse longitude and pulse number. If the carousel consists of N_{sparks}

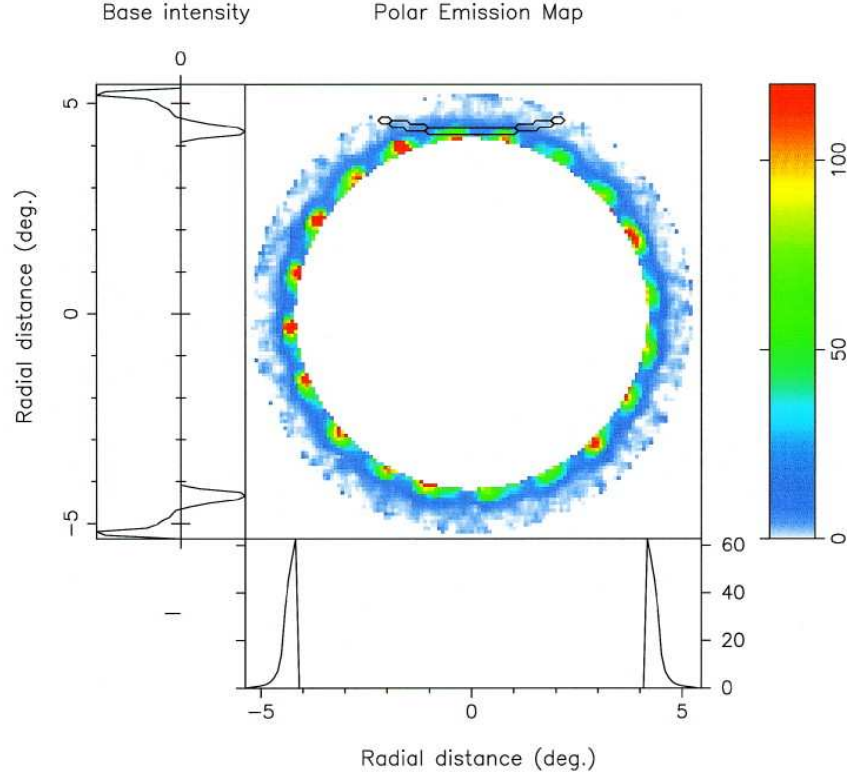


Figure 1.12: An image of the accessible emission region of B0943+10, reconstructed using the *cartographic transform* discussed in text [Figure taken from: Deshpande & Rankin (1999)]. The *main panel* shows the emission map projected on to the polar cap. The *bottom* and the *side* panels show the average and the minimum intensity profiles, respectively, as a function of the magnetic colatitude (i.e., the radial distance from magnetic axis). The sightline traverse is displayed as contours at the top of the polar emission map.

sparks, then the subpulse modulation phase as a function of pulse longitude is essentially $N_{\text{sparks}} \times \Theta$. Edwards & Stappers (2002) have provided an alternative form of the magnetic azimuth term θ_{trans} , using which they provide the expression for subpulse modulation phase as

$$\Theta_{\text{sub}}(\phi) = \Theta_0 + q N_{\text{sparks}} \tan^{-1} \left[\frac{\sin \zeta \sin(\phi - \phi_0)}{\sin \alpha \cos \zeta - \cos \alpha \sin \zeta \cos(\phi - \phi_0)} \right] \quad (1.10)$$

$$+(\phi - \phi_0) \left(n + \frac{P_1}{P_3^{\text{obs}}} \right)$$

where Θ_0 is the modulation phase at $\phi = \phi_0$, the factor q takes care of the sign of the modulation phase gradient, and $\zeta = \alpha + \beta$. Note that the observed subpulse modulation period P_3^{obs} , deduced

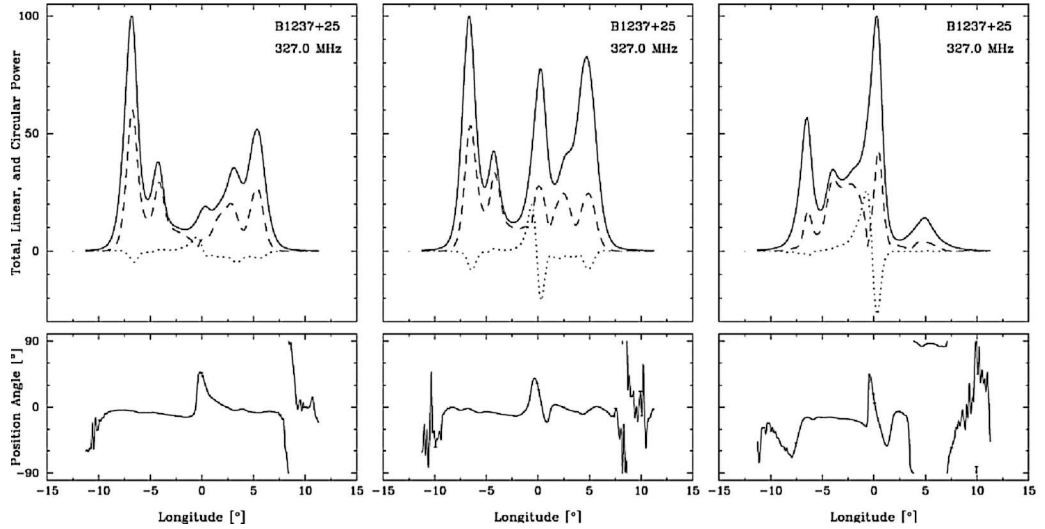


Figure 1.13: Average pulse profiles of the pulsar B1237+25 are shown in three different modes. The “quiet-normal-mode”, “flare-normal-mode”, and “abnormal-mode” profiles are shown in the *left*, *middle* and *right* panel respectively [Figures are taken from Srostlik & Rankin (2005)].

using the LRFS/HRFS, could be aliased. The actual modulation period P_3 could be expressed as

$$\frac{P_1}{P_3} = n + \frac{P_1}{P_3^{\text{obs}}} \quad (1.11)$$

where n is an integer, and for $n = 0$, $P_3^{\text{obs}} = P_3$ (i.e., no aliasing).

1.3.3 Pulse nulling

Emission from some pulsars suddenly disappears for a few pulse-periods. This behavior is called “pulse-nulling”. It is not clear whether the nulls really represent the complete absence of emission or the intensity is too low to detect. However, tight constraints have been put on emission by integrating only the null-pulses, and it is more likely that the emission switches off completely during the nulls. The null state duration varies from one to hundreds of pulse periods. This phenomenon is relatively common, and found in most of the normal pulsars (see an example of pulse nulling in Figure 1.9). In some pulsars, the nulls have been observed to occur periodically, which indicates that it probably may be a manifestation of the same processes which are responsible for sub-pulse drifting.

1.3.4 Profile mode changing

The integrated pulse profile for a pulsar remains remarkably stable. However, for some of the pulsars, the average profile has been observed to abruptly change from the so-called “Normal” (i.e., the relatively stable profile) to “Abnormal” mode, staying in that state for tens to thousands of pulse periods before switching back to the “Normal” mode. This behavior is called *profile mode-changing*⁶. Usually, mode-changing is seen to be broadband and happens in a very short time scale (takes less than one pulsar period). B1237+25 was the first pulsar noticed to have change in its average profile abruptly (Backer, 1970). Sometimes the number of profile modes are more than two as has been observed for the pulsars B2319+60 (Wright & Fowler, 1981) and B1237+25 (modal profiles are presented in Figure 1.13; see Srostlik & Rankin, 2005). It is not just the average pulse profile which is changed in a mode switch, but also the single pulse fluctuation behavior. The mode switch has also been reported to change the spectral index differently for different components in the pulse profile, resulting in a different frequency dependence of pulse profiles in abnormal mode. Despite the fact that many mode-changing pulsars have been studied in search of clues for the process responsible for this strange phenomenon, there is no elaborate theory which can explain mode-changing phenomenon successfully.

1.4 Pulsar searches

Detecting new pulsars essentially requires searching for periodic and dispersed⁷ signal. Some of the initial pulsar discoveries were made possible due to their strong individual pulses. However, most of the currently known pulsars are faint objects which require sensitive observations and folding the data over thousands of pulsar periods before a significant detection could be made.

1.4.1 Periodicity searches

Different search methods are preferred in different domains of observation and pulsar parameters. However, the most commonly used procedure is to find a series of periodic pulses of unknown dispersion measure (DM) and pulse period. The data are dedispersed⁸ to prepare time sequences corresponding to a number of trial DMs. Each of these time sequences are then subjected

⁶Note that profile mode changing is different from *polarization mode changing* (discussed earlier in section 1.2.3) across the longitude which is common even with a given profile mode.

⁷A pulsed signal is dispersed across the observation bandwidth due to frequency dependent refractive index of the interstellar medium. The amount of dispersion is characterized by a quantity called “dispersion measure” which represents the integrated column density of electrons between the observer and the source.

⁸For details on dedispersion, please refer to Chapter 6.

to a standard periodicity search procedure which includes Fourier transforming, followed by identification of significant spectral features. For long enough time sequences, the relative motion between the observatory and the source (due to rotation of Earth, and its motion around the Sun) becomes important, and should be corrected for before taking the Fourier transform. The standard approach is to transform the observed time series to solar system barycenter which is an inertial reference frame to a very good approximation.

To increase the sensitivity to narrow pulses, power contained in several harmonics in the spectral domain is combined using a technique called ‘incoherent harmonic summing’ (Taylor & Huguenin, 1969). For N harmonics of roughly equal power, this technique improves the sensitivity by a factor of the order of \sqrt{N} .

Once the candidate spectral features are selected above a chosen threshold signal-to-noise ratio (S/N) in the spectral domain, the raw data are dedispersed and folded at the candidate period and DM, and a variety of diagnostic plots are made to assess the significance and credibility of the signal. The diagnostic plots generally help to assess, among other things, the consistency of signal across the observation bandwidth and duration. Periodical signal from a pulsar would generally appear at many trial DMs, with the maximum S/N at the trial value closest to the actual DM.

Pulsars in binary systems

The effect of binary motion is to cause a change in the observed pulse period, due to Doppler shift, as a function of the orbital phase. This effect causes the spectral power to spread over a number of neighboring Fourier bins, reducing the sensitivity of the search significantly. One of the approaches to signal recovery is to transform the time sequence to the rest frame of an inertial observer with respect to the pulsar. Assuming a Keplerian model for the binary system, a blind search would require a 5-dimensional search of all the parameter space consisting of *DM*, *period*, *radial velocity of the pulsar along the line of sight*, *orbital eccentricity* and *longitude of periastron*. In practice, the last two parameters are dropped and a three dimensional search, known as ‘acceleration search’ is performed by assuming a constant orbital acceleration ‘ a ’ during the observation (i.e., the radial velocity $V(t) = at$). Different trial values of ‘ a ’ are used to cover a region of acceleration space. A number of frequency-domain techniques also have been proposed and successfully used to discover new pulsars in binary systems. Some of the frequently used frequency-domain techniques can be found in Ransom *et al.* (2002, 2001, 2003); Jouteux *et al.* (2002).

1.4.2 Single pulse searches

Although the periodic emission received from pulsars is generally faint, many pulsars emit bright individual pulses once in a while. Giant pulse emission is one of the forms of bright single

pulses. Also, strictly periodic emission is not detectable from some of the pulsars, e.g., that from the extreme nulling pulsars and rotating radio transients (RRATs). Such sources are generally detected through the analysis of their individual pulses. Searching for single bright pulses also consists of dedispersing the data at a number of trial DMs covering a suitable DM range, followed by an exercise in matched filtering to detect individual pulses of unknown shape and width above a chosen threshold S/N (see, for example, Cordes & McLaughlin, 2003). Once a candidate DM is found by detection of a strong pulse, deep periodicity search can be carried out. If a suitable number of individual pulses are detected at the same candidate DM (i.e., presumably from the same source), a simple analysis can be carried out to estimate the period.

Above, we have provided only a conceptual description of the some of the search procedures used to detect pulsars. A summary of many search techniques, with appropriate explanation, can be found in “Handbook of Pulsar Astronomy” (Lorimer & Kramer, 2004). Details of the single pulse search methodology are described in Chapter 6.

1.5 Structure of the thesis

The carousel model (Ruderman & Sutherland, 1975) has been quite successful in conceptually explaining the subpulse drifting phenomenon⁹. In the framework of this model, the emission sub-beams circulate around the magnetic axis, causing the observer to sample a different portion of the carousel every time the sightline traverses the emission beam¹⁰. Hence, over a sufficiently large observation period, different parts of the carousel would be uniformly sampled, and the emission patterns can be reconstructed. It is worth noting, however, that the life-time of the individual sparks need to be long enough to complete a few rounds around the magnetic pole, to determine the carousel rotation period and construct the emission maps. Determination of P_4 , and hence mapping of the sub-beam configuration, has been possible only for a handful of pulsars so far. In Part I of this thesis, we exploit the opportunity of mapping the complete sub-beam configurations provided by carousel rotation, to study the emission in multiple cones and any inter-relationship between them. Design and development of a unique multi-band receiver, presented in Part II, is motivated

⁹There have been difficulties with the quantitative predictions of this model. For example, in most of the pulsars, for which estimation of the carousel circulation period has been possible so far, the observed and predicted P_4 are not found to be consistent. However, the subpulse modulation analysis and results presented in this thesis assume only a carousel of sparks circulating around the magnetic axis, and do not depend on the quantitative details of the model. Wherever possible, the results drawn from the reconstructed polar emission maps are cross-confirmed using appropriate analysis of raw single pulse sequences.

¹⁰Obviously, we are assuming a general situation where the carousel circulation period is not an integer multiple of the pulsar rotation period.

by a possible three-dimensional (tomographic) study of the pulsar magnetosphere by simultaneously mapping the sub-beam configurations at various altitudes simultaneously.

Note that the parts of the polar cap inside a circular region of radius equal to the sightline impact angle, centered at the magnetic axis, remain inaccessible to the observer. For a sightline traversing through the magnetic axis, emission from the entire polar cap could be sampled and studied. B1237+25 offers us such a unique opportunity, wherein the line-of-sight crosses almost through the magnetic axis, presumably cutting across two emission cones and a core component. Chapter 2 presents our detailed analysis of a number of pulse sequences from this star and the reconstructed carousel emission patterns corresponding to the two emission cones and the core component. We have used these reconstructed conal emission patterns to study any inter-relationship between the two emission cones.

Radius-to-frequency mapping suggests that the high frequency radio emission originates close to the star, and regions of lower frequency emission progressively farther away. Hence, observations made over a narrow spectral range sample the details only in a slice of the emission cone. Simultaneous multi-frequency observations would essentially amount to sampling the polar magnetosphere at various altitudes. Using such observations, polar emission mapping at a number of emission-altitudes would allow “tomography” of the polar emission region, and might help in understanding the generation of sub-beam patterns and their evolution across the magnetosphere. In principle, simultaneous multi-frequency observations can be carried out by using several telescopes simultaneously. Chapter 3 discusses various practical difficulties we faced in such an effort, which motivated us to think of a superior alternative to carry out simultaneous multi-frequency observations. We designed a unique, self-contained receiver system – multi-band receiver (MBR) – that can facilitate observations simultaneously in 10 frequency bands sampling a large spectral range of 100–1500 MHz. Various details of the design, development and performance of the MBR are provided in Chapter 4. MBR was installed at the prime focus of the Robert C. Byrd Green Bank Telescope, and simultaneous multi-frequency observations of a number of bright pulsars were carried out. In Chapter 5, we present a few synoptic results from these observations to demonstrate the data quality obtained, and the kind of studies facilitated by the MBR.

Part III of this thesis, consisting of Chapters 6 and 7, presents search for radio emission from a different category of pulsars – “radio-quiet” gamma-ray pulsars. High sensitivity of the Large Area Telescope on the *Fermi*-satellite has helped in increasing the number of gamma-ray pulsars extraordinarily – from 7 to 117. Despite deep radio searches, counterparts of about one third of these gamma-ray pulsars could not be detected, suggesting these to be radio-quiet. However, all the radio searches for these pulsars had been made at radio frequencies ~ 300 MHz and above. The radio emission beams are expected to become wider at low radio frequencies, as suggested by RFM, increasing the probability of our line of sight passing through the beam. With a view of exploiting

this apparent advantage, we carried out deep searches for periodic as well as transient signal from many of the radio-quiet gamma-ray pulsars at decameter wavelengths. We used the archival data from a pulsar/transient survey, as well as carried out new extensive observations, at 34 MHz using the Gauribidanur telescope. Chapter 6 presents an introduction to the Gauribidanur telescope, details of our observations, and detection strategies and methodologies. Results of these searches are presented in Chapter 7.

Although the contents of three parts of this thesis are diverse in nature, and appear to be quite disjoint from each other, they all address different stages of detection and study of radio signals from pulsars. Regardless of their order, each of these three parts is believed to be complete with its own introduction and conclusions.

Part I

*Origin of Radio Emission in
Multiple Cones*

The multiple emission cones of the pulsar B1237+25

2.1 Introduction

The phenomenon of “sub-pulse drifting”, i.e., the systematic variation in position and intensity of sub-pulses, was noticed (Drake & Craft, 1968) soon after the discovery of the first few pulsars. Ruderman & Sutherland (1975; hereafter R&S) suggested this regular modulation to be a manifestation of a carousel of “spark” discharges circulating around the magnetic axis in the acceleration zone of the star because of the $E \times B$ drift. After almost two decades of the above proposition, Deshpande & Rankin (1999, 2001) developed a cartographic transform to map the systematic sub-pulse variations to a carousel of sub-beams projected on to the polar cap. They traced back the origin of the coherent modulation in pulse sequences of B0943+10 to a system of 20 sub-beams circulating around the magnetic axis. Their detailed study provided strong support to the carousel model proposed by R&S. The cartographically mapped emission pattern represent a slice of the emission cone at an altitude corresponding to the frequency of observation (as suggested by the radius-to-frequency mapping (RFM); Cordes, 1978). The deduced emission-map can provide valuable details of the radio emission (for example, spatial structure and distribution of sub-beams, their temporal and spectral evolution, etc.) in the sampled region of the polar magnetosphere.

In the above picture of a carousel of emission columns, the viewing geometry limits the accessible region of the slice in the polar magnetosphere which can be mapped. A tangential sight-line cut across the sub-beam ring(s) allows us to sample only the periphery of the carousel pattern,

Publications based on this chapter: Maan & Deshpande (2008) and Maan & Deshpande (2014).

and the circulation of sub-beams would manifest as the apparent sub-pulse “drifting” (i.e., primarily phase modulation within the pulse-profile). In case the sight-line traverse is near/through the magnetic pole (i.e., impact angle \ll cone radius), the modulation of sub-pulses will appear primarily as an amplitude modulation, and one would be able to sample the emission pattern, and hence the cone(s), more completely. The well-known bright pulsar B1237+25 offers one such unique example of viewing geometry. The multi-component average profile of this pulsar consists of two pairs of conal components and a core component (see, for example, average profiles in Figures 1.13 and 2.1). Such a profile is presumably produced by a sight-line which cuts two concentric emission cones and a central core beam almost through their common center. Using a sequence of pulses where the core-emission was almost absent, Srostlik & Rankin (2005, see their Figure 8; hereafter SR05) have shown a full “conal” position-angle traverse with an exceptionally steep sweep rate at the center ($-185^\circ \pm 5^\circ \text{ deg}^{-1}$, may be the largest ever observed), as expected from the magnetic pole model (Radhakrishnan & Cooke, 1969). Their estimate for the impact angle ($\beta \lesssim 0.25^\circ$) confirms that our sight-line indeed traverses very near (or probably through) the magnetic axis of this pulsar.

As expected from the viewing geometry of this pulsar, the prominent type of observed sub-pulse modulation is indeed the amplitude modulation of the pairs of conal-components. The core-component has been reported to be “incomplete” (SR05). Unlike many other pulsars, where the fluctuation spectrum of the core-component is generally featureless (Rankin, 1986), the core component of this pulsar shows presence of some features at very low fluctuation frequencies.

Like several other multi-component (“M”-category) pulsars, B1237+25 also exhibits emission components corresponding to both, the “inner” as well as the “outer”, cones. However, the co-existence of emission from both the cones in M-stars, and possible inter-relationship between them, if any, have remained poorly understood. An intriguing possibility that ‘the inner cone is emitted at a lower height along the same group of peripheral field lines that produce the outer cone’ had been suggested a long time ago by Rankin (1993). In the case of pulsar B0329+54, Gangadhara & Gupta (2001) show that the multiple cones appear to originate at different heights in the magnetosphere but along relatively nearby field lines. This supports the above possibility suggested by Rankin (1993), and has remained the only, but an indirect, evidence so far. The polar emission patterns corresponding to the two cones, if could be mapped, can help in finding out whether the emission in the two cones really share a common origin or not. These maps can also be useful in studying any other relationship between the emission in the inner and outer cones.

B1237+25, with a rich variety in pulse-to-pulse fluctuations and sight-line traverse very close to the magnetic axis, provides an important and challenging opportunity to study the characteristics of emission in the entire polar emission cone, and specially till close vicinity of the magnetic axis. With the specific aim of studying any inter-relationship between the sub-beam patterns responsible for emission in the two cones, we have analyzed four different pulse sequences (we denote them

as A, B, C and D, comprising 5209, 2340, 5094 and 4542 pulses, respectively) from this star observed at 327 MHz using the Arecibo telescope^{1,2}. In this Chapter, we present our analysis of these pulse-sequences, including the clarifying (polarization) mode-separated versions of sequence A, to map the sub-pulse fluctuations to the underlying patterns of circulating sub-beams. The sub-sequences used for constructing the emission maps primarily consist of “normal” mode sequences with minor contamination from “abnormal” mode, as detailed later. The reconstructed emission maps were then subjected to correlation analysis to study any interrelated properties of the emission patterns associated with the two conal rings and the central core-beam.

In section 2.2, we describe the analysis procedures we have followed to deduce and verify the sub-beam circulation period, and present polar emission maps for various pulse sequences. A possible inconsistency between various polar emission maps and the standard carousel model, in terms of the carousel rotation phase, is discussed in section 2.3. Details of the correlation analysis of the emission maps are provided in section 2.4, followed by a discussion on the results and their implications in section 2.5. Conclusions drawn from our study are presented in section 2.6.

2.2 The polar magnetosphere emission patterns

The pulse-to-pulse fluctuations in the above mentioned four single pulse sequences (A, B, C and D) were studied in detail, particularly to examine if a carousel of sub-beams can explain the rich modulations. Below we present our analysis procedure to examine the fluctuation properties at various time-scales to estimate and verify the carousel circulation period, followed by reconstructed emission maps using a number of selected sub-sequences.

2.2.1 Analysis procedure

To map the systematic sub-pulse fluctuations to a rotating carousel of sub-beams in the polar magnetosphere, we need to know the carousel circulation period (P_4 , i.e., the tertiary modulation period) and the viewing geometry of the pulsar (i.e., the magnetic inclination angle, α , and the sight-line impact angle, β). To find out the circulation period, we examine the fluctuation

¹These 327-MHz pulse sequences (A, B, C and D) were acquired using the Wideband Arecibo Pulsar Processor (WAPP2) on 2005 Jan 09, 2003 July 13, 14 and 21, respectively. Corrections for dispersion and interstellar Faraday rotation across the observation bandwidth were carried out, and various instrumental polarization effects were removed before producing the pulse sequences. Pulse sequence A has a resolution equivalent to $0^\circ.133$ in pulse longitude, while that in the other sequences is $0^\circ.352$. Further details on the observations of pulse sequence A, and sequences B,C and D can be found in Smith *et al.* (2013) and Srostlik & Rankin (2005), respectively.

²We are thankful to Joanna Rankin for making these pulse sequences and the polarization as well as emission mode separated versions of sequence A (Smith *et al.*, 2013) available to us.

power spectrum, as well as the auto/cross-correlation function, of the longitude-resolved intensity sequences. In the domain of fluctuation spectrum, the circulation period may reveal itself by the presence of one or both of the following features:

1. A low-frequency feature which directly corresponds to the circulation period,
2. A signature of amplitude modulation, due to the sub-beam intensity pattern in the presumed carousel, in the form of a pair of side-bands placed equidistant on the two sides of the secondary³ modulation feature (corresponding to P_3).

The information content in the auto/cross-correlation function is in principle the same as in the fluctuation power spectrum. However, signatures of any tertiary modulation may be more prominently seen in the correlation function when the secondary fluctuation features are of very low quality⁴ or if the circulation period itself is not constant. Particularly, a cross-correlation between fluctuations of the two pulse components which are expected to be associated with the same conal-ring (and hence sharing the same underlying modulation, but with a relative delay) can be very revealing. In any case, to establish the relevance of a spectral feature to the carousel circulation period, it is necessary to confirm the consistency of expected delay between the fluctuations of such pulse components with that apparent from either the cross-correlation function or from the phase-gradient in the corresponding cross-spectrum.

A typical example of the longitude-resolved fluctuation spectrum (LRFS) of this pulsar is shown in Figure 2.1. Presence of a broad feature at around 0.36 cycles/Period (hereafter c/P , with the rotation period $P \approx 1.382$ s) is clearly evident. The low Q -value of this secondary modulation feature makes it difficult to identify the presence of any side-bands associated with the tertiary modulation. The large width of this feature, along with the absence of any obvious low-frequency feature (corresponding to the carousel circulation), in the LRFS suggests that the underlying pattern of sub-beams is not stable over long durations ($\sim 1000 P$), i.e., on the time-scales over which the fluctuation properties are being examined. The irregularity may lie within the underlying emission pattern, i.e., in the inter-spacings and intensities of the sub-beams, as well as in the circulation period of the carousel.

To assess stability of the presumed carousel on shorter time-scales, we make use of the “sliding” fluctuation spectrum (SFS; introduced by Serylak *et al.*, 2009, and called S2DFS)⁵. SFS

³Various modulations in a typical intensity time-sequence are generally termed as follows: primary modulation refers to the modulation due to the pulsar rotation itself, the secondary modulation corresponds to the sub-pulse modulation (i.e., “drifting” or amplitude modulation), and tertiary modulation is that due to rotation of the carousel.

⁴Generally assessed by estimating the Q -factor of the corresponding spectral feature ($Q = \frac{f}{\Delta f}$).

⁵The only difference in SFS and S2DFS is in the procedure used to obtain the individual spectra in the stack. In S2DFS, 2-dimensional fluctuation spectrum is averaged to compute each of the spectra in the stack, while SFS make

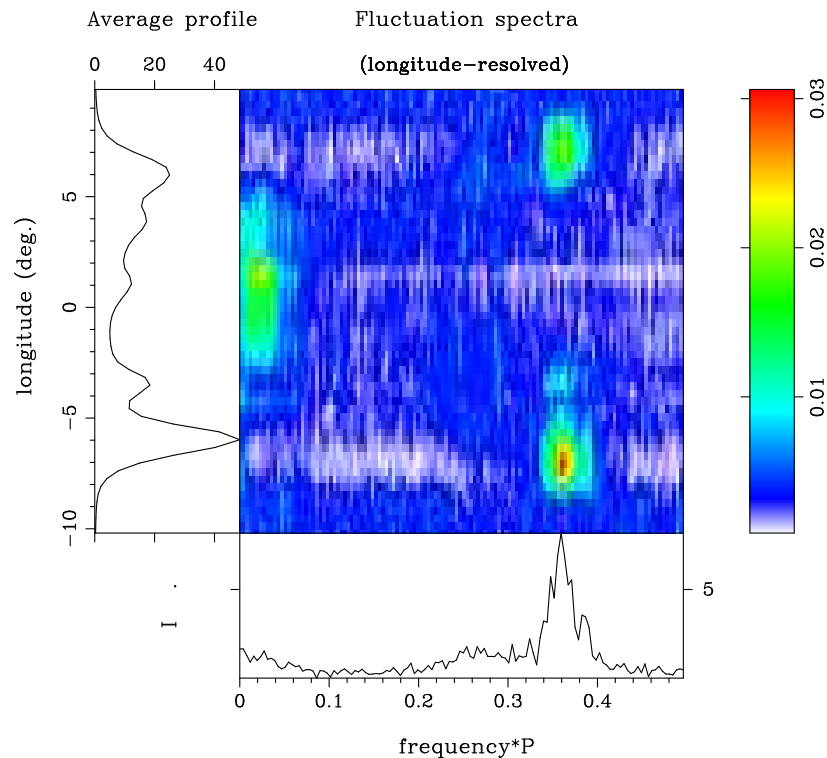


Figure 2.1: The central plot shows the longitude-resolved fluctuation spectrum for the pulsar B1237+25, at 327 MHz. Fluctuation spectrum was computed using a 256-point FFT averaged over the first 4096 pulses of the sequence C. The left panel shows the average profile (total intensity), and the integrated spectrum is shown in the bottom panel.

is a stack of fluctuation spectra computed using an n -period wide window which slides by a pre-decided number of pulses each time. Each of the fluctuation spectra in the stack is obtained by first computing the LRFS for the corresponding window, and then averaging over all the longitudes. Using the SFS, we can explore the stability and time-evolution of a modulation feature as well as detect spectral features corresponding to relatively short-interval tertiary modulations. Figure 2.2 shows an example of SFS computed for a sequence comprising of 750 pulses, with a 256-period wide window slided across the pulse sequence. Each time, the fluctuation spectrum integrated over all the longitudes was computed, and the window was slided forward by one pulse. Corresponding to each of the fluctuation spectra (rows in the main panel of Figure 2.2), the starting pulse number is marked as ‘Block Number’ in the left panel. The bottom panel shows the percentage number of times the spectral-power crosses a chosen threshold at each of the frequency bins. This panel is specifically

use of the LRFS for the same, as mentioned in the text.

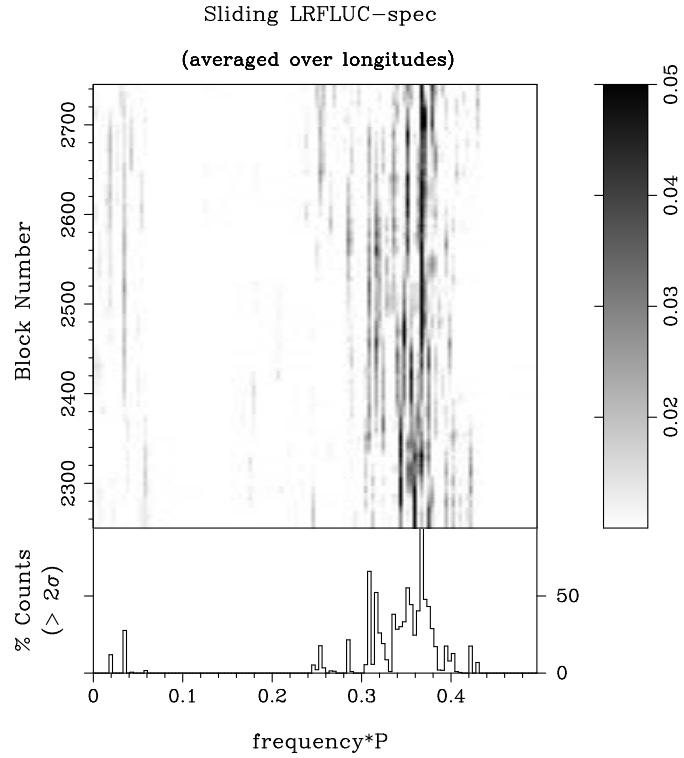


Figure 2.2: *Sliding Fluctuation Spectrum*: Each row in the main panel shows the fluctuation spectrum of a sub-sequence whose starting pulse number is marked as ‘Block Number’ in the left panel. The bottom panel shows the percentage number of times the spectral power in each of the frequency bins crossed a threshold of 2σ .

helpful in detecting a modulation feature associated with circulation of pattern(s) lacking stability over long durations, but appearing intermittently with an otherwise stable period. A low frequency feature ~ 0.035 c/P apparent in Figure 2.2, is seen to be prominent only in the Block Number range of about 2450–2600.

For each of the four pulse sequences, we examined two sets of SFS, computed using window widths of 256 and 512 periods. These sets were examined specifically for possible presence of a high-Q secondary modulation feature, any side-bands around it or any low frequency feature which may directly relate to the circulation period. Sub-sequences of appropriate lengths, corresponding to instances of significant spectral features in the SFS, were selected and investigated further for the credibility of the candidate circulation period suggested by the relevant features.

Table 2.1. Modulation parameter summary of various sub-sequences.

Sub-seq.	No. of Pulses	$P_4(P)^\dagger$	No. of sub-beams (N_{beam}^\ddagger)		Null Fraction(%)
			Outer Ring	Inner Ring	
A ₁	600	28.41 ± 0.16	18	18	05.0 ± 0.9
B ₁	256	18.27 ± 0.15	–	12	11.3 ± 2.1
C ₁	512	33.88 ± 0.27	–	12	04.7 ± 1.0
D ₁	512	23.23 ± 0.19	6–8	6–8	05.5 ± 1.0

Note. — For sub-sequences B₁ and C₁, the sub-beam spacing in the outer ring, and hence the corresponding number of sub-beams, could not be estimated unambiguously.

[†] P_4 values refined using the closure path, as described in the text, are presented here. The corresponding uncertainties are estimated using the fluctuation spectrum.

[‡]Note that when brightness of individual sub-beams is highly non-uniform (e.g., when only a few of them are bright), the number of sub-beams are prone to be underestimated. Also, varying sub-beam spacing, and incomplete sampling of the emission map (especially for a sub-sequence of small length, e.g., B₁, and towards the larger magnetic colatitudes) further limit the certainty with which the number of sub-beams can be estimated. Due to these reasons, the N_{beam} estimates are specifically less reliable for the last three sub-sequences, i.e., for B₁, C₁ and D₁.

2.2.2 The emission maps

After the above described analysis of the pulse sequences A, B, C & D, four sub-sequences (hereafter denoted by A₁, B₁, C₁ & D₁, each a subset of the pulse sequence suggested by its name) which showed one or more of the desired spectral signatures were chosen for further investigations. For each of these sub-sequences, to verify the candidate circulation period, the longitude-longitude correlation maps (Popov & Sieber, 1990) were examined to check if the fluctuations at pulse longitudes associated with the same emission cone (i.e., the same carousel) show the expected phase relationship (or lag). The auto/cross-correlation functions of intensity sequences corresponding to selected components were also examined for consistency of the observed phase relationship with the expected modulation. After such verification, the circulation period was further refined by using the ‘closure’ path provided by the inverse cartographic transform described in Deshpande & Rankin (2001). In this technique, best- P_4 is found out by searching in a small range around the candidate P_4 , and using cross-correlation (between the original pulse sequence and that synthesized from an emission map constructed using a given trial P_4 value) as figure of merit.

Figure 2.3 summarizes the fluctuation properties, and presents the evidences for the tertiary

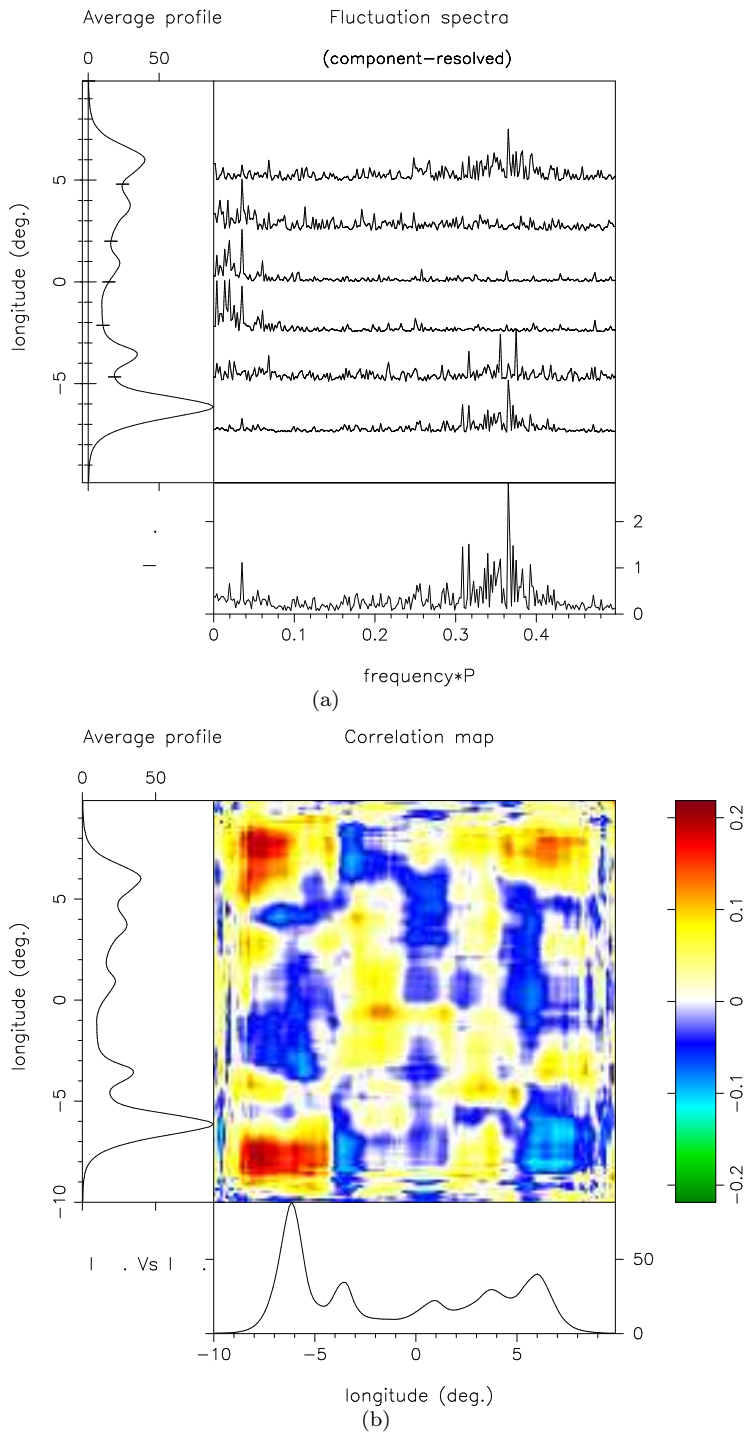


Figure 2.3: (a) *Component-Resolved Fluctuation Spectrum*: The body of the figure shows the average fluctuation spectrum for each of the sections marked in the average pulse-profile plotted in the left panel. The bottom panel shows the integrated spectrum. (b.) *Longitude-Longitude Correlation Map*: The central panel shows the cross-correlation of intensity fluctuations at different longitudes across the pulse window at a relative delay of 14 pulse periods, for the sub-sequence A_1 . The bottom and left panels show the average profiles corresponding to the original and delayed sub-sequence, respectively. A significant correlation between the first and last component is evident, consistent with a circulation period of about 28.5 P.

modulation in the sub-sequence A_1 (this sub-sequence consists of the largest number of pulses among the selected four sub-sequences). Figure 2.3(a) presents the fluctuation spectra averaged over longitude ranges identified with each of the components. The respective sections are as marked in the average pulse-profile plotted on the left hand side. Each of these spectra are normalized to their respective peak values. Merely to differentiate it from the conventional LRFS, we refer to it as component-resolved fluctuation spectrum (CRFS). A low-frequency feature at 0.0351 ± 0.0002 c/P is visible throughout the profile, suggesting the circulation period to be 28.5 ± 0.2 P . Further, as mentioned earlier, our line of sight cuts almost through the magnetic pole of the pulsar. Hence one would expect a phase difference of about 180° between the fluctuations in the pulse components corresponding to the same emission cone. This is consistent with the presence of significant correlation between the first and last components when correlated after a delay of $14 P$ (see Figure 2.3(b)). The correlation between the inner conal components is also visible, although it is not so prominent. These evidences support the view that the low frequency feature in the fluctuation spectrum is due to the circulation periodicity we are seeking for. A feature around 0.0196 ± 0.0004 c/P lies close to the first sub-harmonic of above feature, and has contribution primarily from the central region of the profile, i.e., from the core-component and region prior to it.

A map of the polar emission region constructed using a further refined value of the circulation period ($28.41 P$, by applying the ‘closure’ path mentioned earlier) and the geometrical parameters⁶ from Srostlik & Rankin (2005), is shown in Figure 2.4. Presence of 18 bright sub-beams in the outer emission cone is easily noticeable. Some of the sub-beams appear to be bifurcated or corrugated, however, that is expected from the discrete spread in the observed secondary feature. Interestingly, the secondary modulation period P_3 , calculated by dividing P_4 by the number of sub-beams, corresponds to the aliased value of the secondary modulation feature. This indicates that the observed feature around ~ 0.37 c/P might actually be a first order alias of its actual value around ~ 0.63 c/P .

A few percent ($\approx 5\%$) of the pulses in our sub-sequence A_1 show characteristics of the abnormal mode (as judged from mode-separated sequences). However, by analyzing this sub-sequence excluding the abnormal mode pulses, we have confirmed that the inclusion of these few percent pulses do not have any noticeable effect (neither qualitatively nor quantitatively) on the reconstructed emission map, as well as on the results of the subsequent correlation analysis presented in Section 2.4.

The candidate circulation periods for other sub-sequences were also successfully cross-validated by examining longitude-longitude correlation maps. Figure 2.5 shows the variety in polar emission maps constructed using these candidate P_4 values for the respective sub-sequences. Ta-

⁶ $\alpha = 53.0^\circ$, $\beta = 0.25^\circ$

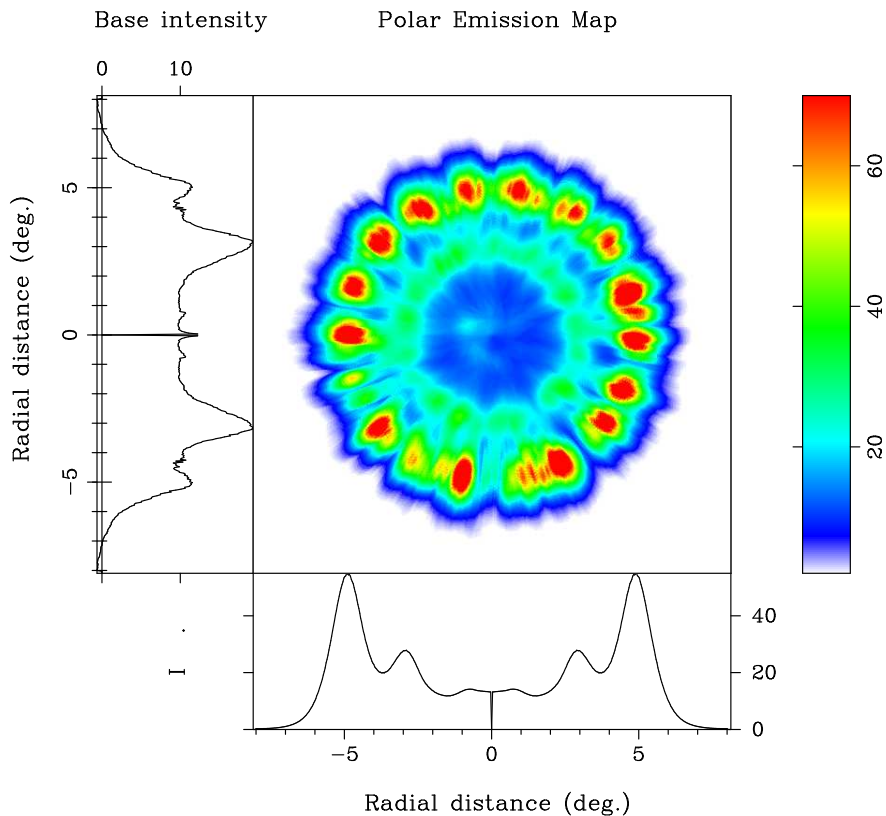


Figure 2.4: *Polar Emission Map*: An image of the accessible emission region of the pulsar B1237+25 at 327 MHz, constructed using the geometrical parameters and circulation period value mentioned in the text. The map of the emission region, shown in the main panel, is projected on to the polar cap. The bottom and the left-hand side panels show the average- and the base-intensity profiles, respectively, as functions of the angular distance from the magnetic axis. Note the easily distinguishable sub-beams in the outer and the inner conal-rings at radial distances of about 5 and 3 degrees, respectively.

ble 2.1 summarizes the relevant parameters for the different sets, namely, the number of pulses in each of the sub-sequences, the candidate P_4 along with the number of sub-beams in the mapped carousels corresponding to the two cones. Visual inspection of the emission maps, even after appropriate smoothing, could not help in estimating the number of sub-beams, except for the sub-sequence A_1 . In an attempt to determine the number of sub-beams in a more systematic way, azimuthal sequences averaged within ranges of radii corresponding to the outer and the inner carousels were computed by sampling the emission maps at uniform intervals of magnetic azimuth. These sequences were then Fourier transformed to estimate the periodic azimuthal spacing between the sub-beams, and hence the number of sub-beams in the carousel. Note that the above procedure is prone to under-estimate the number of sub-beams, when the intensities of individual sub-beams are highly

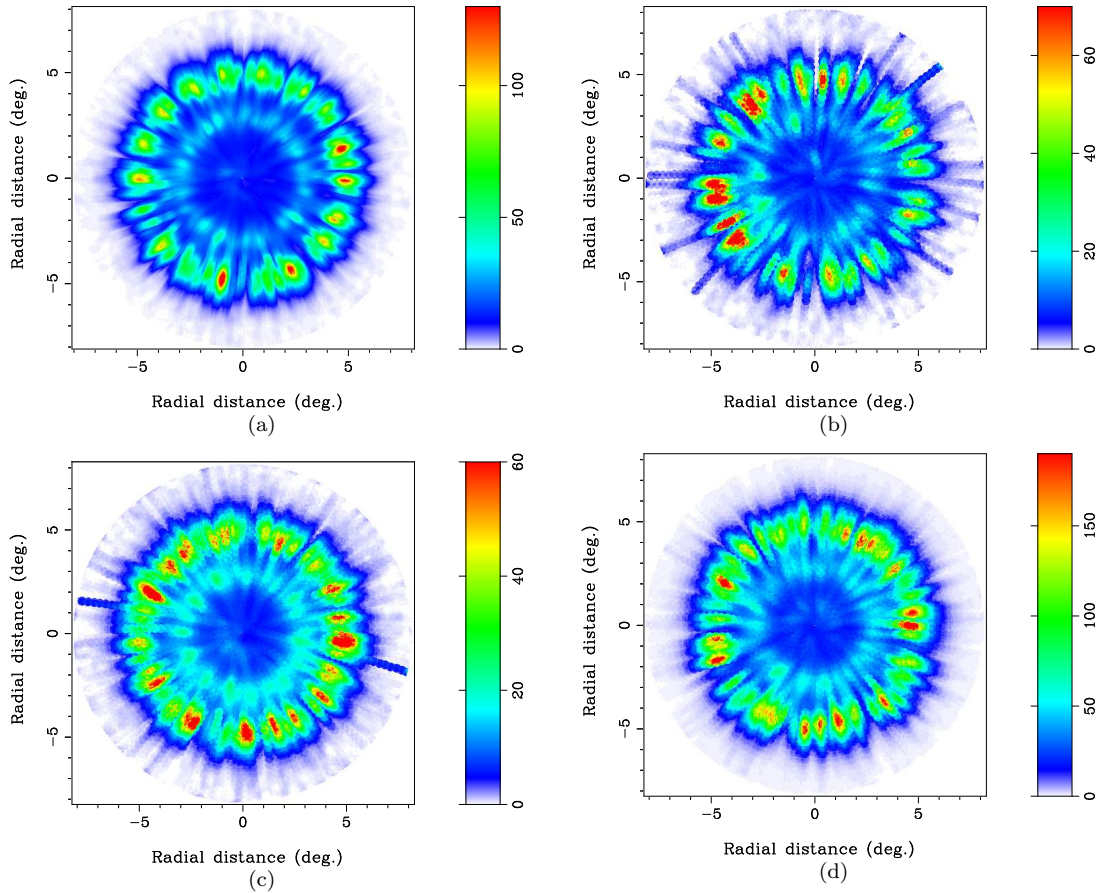


Figure 2.5: Polar emission maps constructed for various sub-sequences (A_1 : Top left; B_1 : Top right; C_1 : Bottom left; & D_1 : Bottom right) using the corresponding circulation periods mentioned in Table 2.1. These maps have been smoothed minimally, to show the details at small spatial scales.

non-uniform. Further, the sub-sequences of small lengths (e.g., B_1) are prone to under-sample the emission map (especially towards larger magnetic colatitudes), and hence might mislead to a wrong number of sub-beams. Due to these reasons, our estimates of the number of sub-beams are generally less reliable, and listed in Table 2.1 for the sake of completeness.

2.3 The modulation-phase and the carousel model

The sweep of the modulation phase across the pulse profile provides an important consistency check to assess if the observed fluctuation spectral feature is indeed a manifestation of the carousel rotation. Figure 2.6 presents the observed modulation phase profile corresponding to the low frequency feature observed, along with that expected from the carousel model, for each of the

four sub-sequences. A glaring mismatch between the observed and expected profiles is obvious. However, the above computation of the *expected phase profile* has implicitly assumed that:

1. The two carousels, corresponding to the two pairs of inner and outer conal components, rotate with the same circulation period,
2. There is no relative phase difference between the two (or more) carousels, and
3. The core component also originates from a compressed version of the conal emission pattern rotating with the same circulation period.

At least in the case of one pulsar (B0818-41; Bhattacharyya *et al.*, 2009), evidences have been found in support of the first assumption and against the second one. There has not been any study, to our knowledge, exploring the possibility considered in third assumption.

In view of the above, it is not unrealistic for the observed modulation phase profile to deviate from that expected from the carousel model. However, the deviation contributed by the relative phase offset(s) and/or any co-latitudinal overlap between the individual carousels, should be least prominent at the longitudes where the received flux density is expected to originate mostly from one of the cones, e.g., peaks of the leading and trailing components, and outskirts of the profile. Apparent lack of consistency between the observed and expected modulation phase profiles, even in such longitude regions, necessitates consideration of other possibilities.

Nulling may also contribute to deviations from the expected modulation phase profile. Pulsar B0809+74, due to its very stable drifting and frequent short nulls, is the only source for which the effect of nulls on the drift rate have been studied in details. A common picture which has slowly emerged from various studies of this aspect (e.g., Page, 1973; Unwin *et al.*, 1978; Lyne & Ashworth, 1983; van Leeuwen *et al.*, 2002) is that a perturbation at the onset of a null turns off the emission and abruptly alters the drift rate which, then recovers exponentially to its normal value. However, the actual behavior of the drift during the nulls remains still unclear. For example, a complete cessation of the drifting after a possible lag from the null onset, as well as a slowed-down drifting active throughout the null duration, is possible. For B0809+74, the speeding-up from slow/ceased drifting to normal starts on part way or at the end of the null duration, and the recovery time is proportional to the null-length (Lyne & Ashworth, 1983). Possible deviations from this picture, when we consider other pulsars, are not ruled out.

To explore if the apparent lack of stability in the presumed carousel patterns of B1237+25 is caused by the nulls, we have carried out a systematic search, for what otherwise may be a stable emission pattern, by modeling the effect of nulls in a number of different ways. We first identified all the pulses having energy below a chosen threshold as null-pulses. For this purpose, we examined the pulse-energy histograms of the four pulse sequences (as shown in Figure 2.7), and

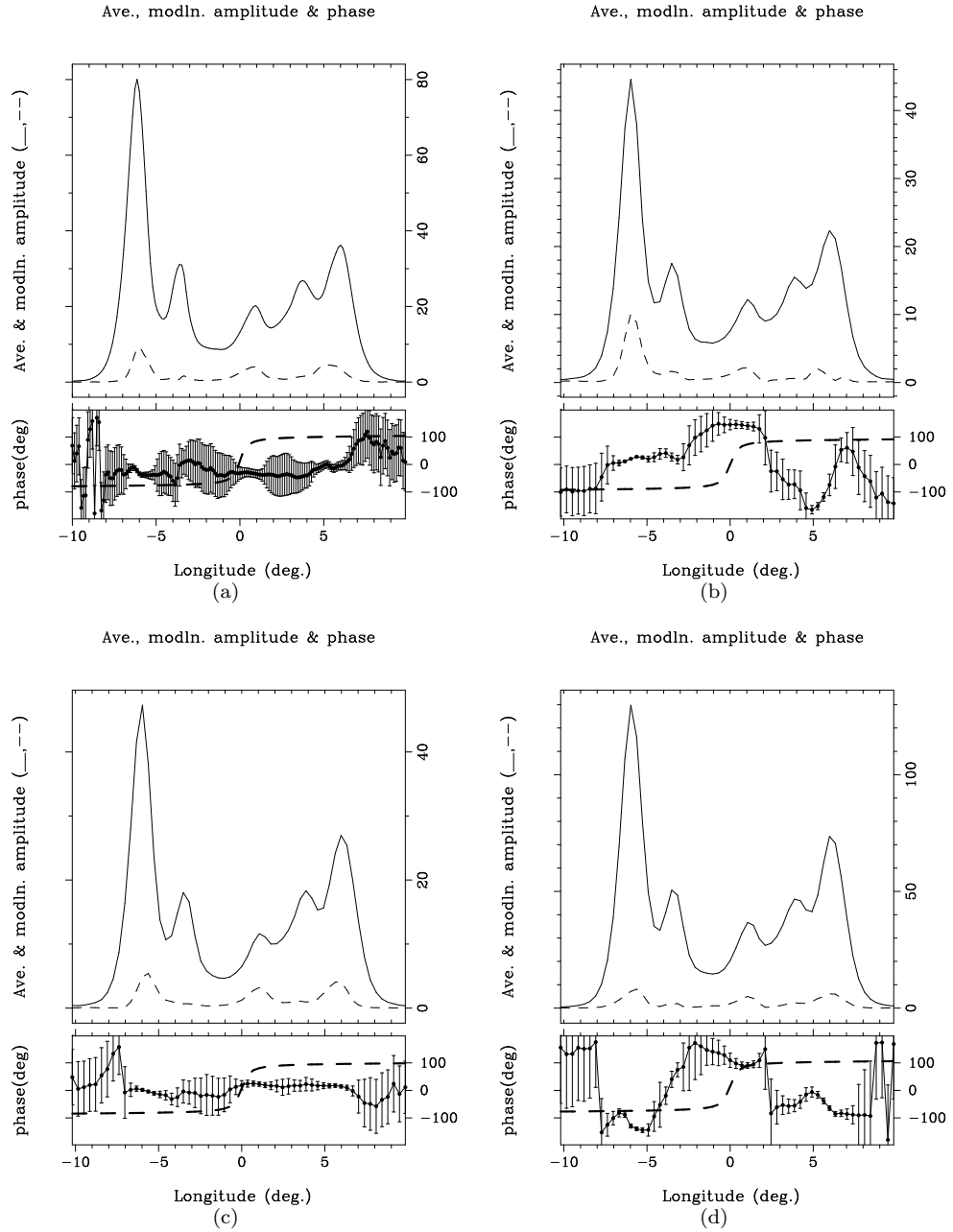


Figure 2.6: In each of the 4 sub-figures, the upper panel shows the stokes-I average profile (solid line), and the amplitude profile of the modulation presumed to be due to the carousel rotation (dashed line). The bottom panel shows the observed modulation phase profile with $\pm 1\sigma$ error-bars ($\pm 2\sigma$ for the last one) as a function of pulse-longitude, along with the modulation phase sweep expected from the carousel model (dashed line). The 4 sub-figures, (a), (b), (c) and (d), correspond to the sub-sequences A_1 , B_1 , C_1 and D_1 , respectively.

selected appropriate thresholds to include all the pulses under the narrow distributions centered at 0 as null-pulses. Note that the distributions of ‘normal’ and null-pulses partly overlap. However, number of pulses which could be mistaken as null-pulses, or the null-pulses which could be missed, because of this overlap, are estimated to be, on average, less than or about 0.5% of total number of pulses. Using the list of null-pulses, we modified the times of arrival of each pulse by a number of trial correction offsets (details of which are given below), and explored whether a stable carousel pattern could be obtained. We have assumed, in our following discussion, that the carousel of sparks recovers a common and stable rotation rate after every instance of perturbation caused by nulls, and the total time spent in the perturbation and recovery phase is dependent on the cumulative null-duration. Each affected section of the pulse-sequence (i.e., the section corresponding to irregular modulation) can be considered as starting from a given null and extending till the time when both, (a) the stable drift rate is attained, as well as, (b) the tertiary modulation phase is same as that before the null. If such sections are removed, the remnant sequence is expected to have coherent modulation due to carousel rotation. To effect such a correction, the time of arrival of n^{th} -pulse (T_n) is modified by the correction offset $\Delta T_{\text{offset},n}$, which depends on the cumulative time spent in all the irregular modulation phases till the n^{th} -pulse, in the following way: $T_{n,\text{modified}} = T_n + \Delta T_{\text{offset},n}$. We explored several forms of this correction offset, incorporating different possible dependences of the perturbation and recovery durations on the null-extent. These trial forms are detailed below, along with the model of the corresponding drift behavior. In each of the following forms of $\Delta T_{\text{offset},n}$, δT is the parameter to be varied in fine steps, and positive as well as negative values of δT are tried out:

1. $\Delta T_{\text{offset},n} = N_{\text{null-durations},n} \times \delta T$,

where $N_{\text{null-durations},n}$ is the total number of contiguous null-durations encountered from the beginning till the n^{th} pulse. The perturbation to the carousel (or to the carousel rotation) is instantaneous, recovery also starts instantaneously, and the recovery time is constant.

2. $\Delta T_{\text{offset},n} = N_{\text{nulls},n} \times \delta T$,

where $N_{\text{nulls},n}$ is the total number of null-pulses till the n^{th} pulse. The perturbation to the carousel is instantaneous, recovery also starts instantaneously, and the recovery time is proportional to the null-length.

3. $\Delta T_{\text{offset},n} = N_{\text{nulls},n} \times P + \delta T$

The perturbation to the carousel may or may not be instantaneous, but the perturbation time is less than the null-duration. The recovery starts only when the null-duration is over, and the recovery time is constant.

4. $\Delta T_{\text{offset},n} = N_{\text{nulls},n} \times (P + \delta T)$

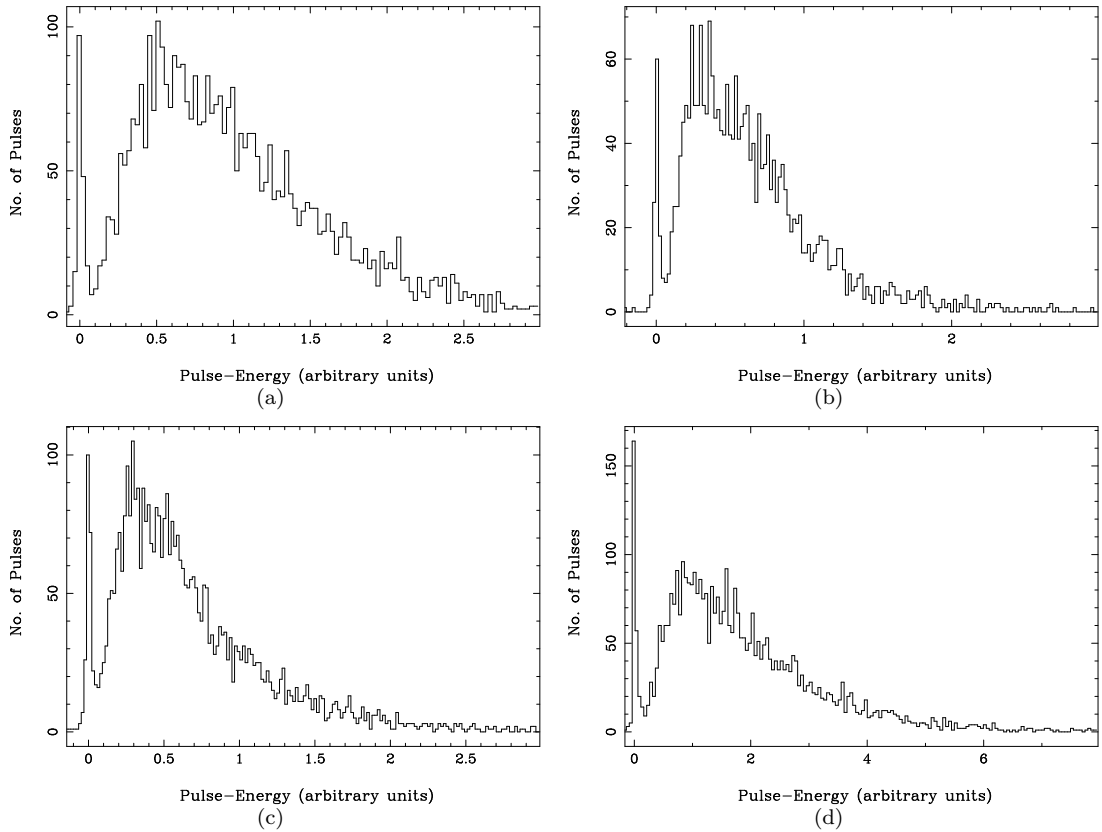


Figure 2.7: Relative pulse-energy histograms of the pulse sequences A, B, C and D are shown in the panels (a), (b), (c) and (d), respectively. For the pulse sequences A, C and D, the histograms have been obtained by using first 4096 pulses, while the histogram in panel (b) shows the pulse-energy distribution using all 2340 pulses of the sequence B.

The perturbation to the carousel may or may not be instantaneous, but the perturbation time is less than the null-duration. The recovery starts only when the null-duration is over, and the recovery time is proportional to the null-length.

Investigations of the fluctuation spectrum

Each of the above modeled correction offsets, with the variable parameter δT , was applied to the time sequences corresponding to the first and last components of the average profile. The parameter δT was varied in steps of one-tenth of the pulsar period. The resultant time sequences (which are now, in general, non-uniformly sampled) were Fourier transformed. The fluctuation spectra were examined for compact features. We note that the fluctuation spectrum, for a correctly modeled offset time, is expected to present a compact feature corresponding to the carousel rotation

time P_4 . Such a feature may also be accompanied by symmetric side-lobes due to uneven sampling. A compact secondary modulation feature was also sought for, although it may not be expected in general. Ideally, the feature corresponding to the carousel rotation should be present in the fluctuation spectra of both the components. Hence, this criterion was used to filter out the features not related to the carousel rotation. To explore the effects of null occurrences on the sub-pulse modulation in isolation, this analysis was also applied to sub-sequences free from profile mode changes (assessed via visual inspection), in addition to the full-length pulse sequences. None of the above modeled correction offsets resulted in a carousel rotation feature common in both the components.

It is possible that the perturbation and/or recovery time varies from one instance of nulling to other, and does not have any particular dependence on the time the pulsar spends in null-phase. Even in such a case, if the nulls are randomly distributed across the observed sequence, the observed P_4 may deviate from the actual value depending on the fractional time spent in nulls. As seen from Table 2.1, P_4 might appear to have an inverse dependence on the null-fraction, however, given our limited statistics, it will be too premature to infer any details based on this apparent dependence. In the absence of any particular guidance forthcoming from the above mentioned modeling of effects of null-occurrences in identifying a stable carousel rotation period, and hence in disentangling the corresponding effects in the modulation phase profile, we proceed with the presumed association between the observed low-frequency features and the carousel rotation for various sub-sequences.

2.4 The emission in the two cones

The emission patterns presented in section 2.2.2 clearly show presence of two carousels corresponding to the two pairs of conal components and a diffuse pattern corresponding to the core region. To explore more about the origin of multiple emission cones, and particularly, any inter-relationship between them, below we present a correlation analysis of these emission patterns and estimate the altitudes of emission corresponding to the two cones.

2.4.1 The correlation properties

To estimate possible correlation between the patterns associated with the conal and core components, the radial profiles from the emission maps were obtained at uniform intervals (1°) of magnetic azimuth, and then this whole azimuth sequence of radial profiles was subjected to correlation analysis over the full span of azimuthal shifts. The maximum correlation for each pair of radii (i.e., magnetic colatitude) and the corresponding azimuthal shift was found out, and plotted in two maps: “The Polar Correlation map” and “The Polar Azimuthal-Shift map”, respectively. Figure 2.8

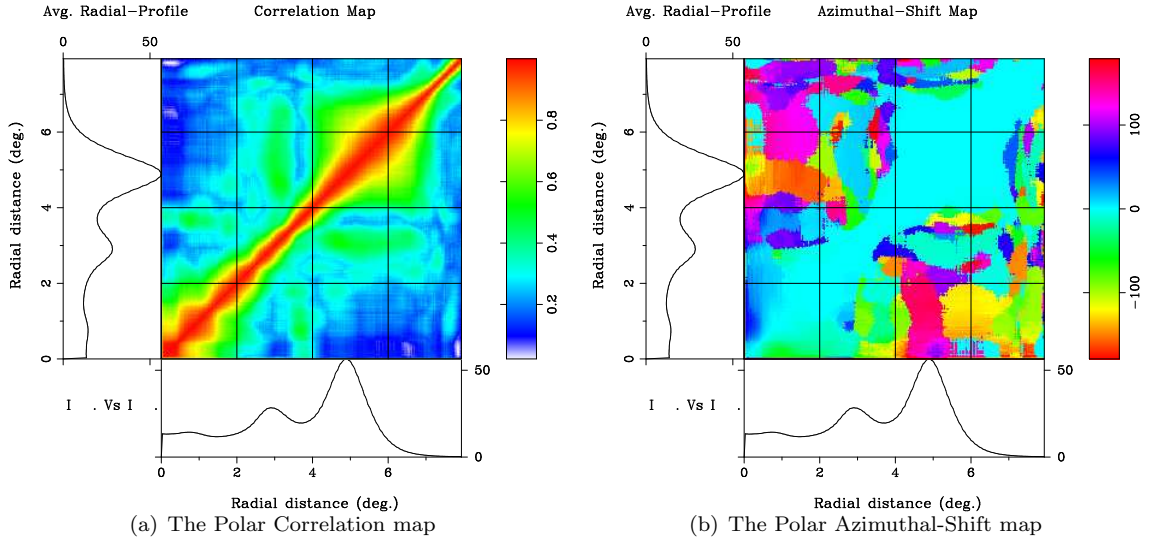


Figure 2.8: (a) The central panel shows the map of maximum correlation coefficient (normalized) values computed for fluctuations at each pair of the magnetic colatitude. The bottom and left-hand side panels show the average radial (i.e., magnetic co-latitudinal) profiles. (b) The central panel shows the map of magnetic-azimuthal shifts (in deg.) corresponding to the maximum correlation coefficient values plotted in (a). The bottom and left-hand panels show the average radial profiles.

shows these maps computed for the emission map presented in Figure 2.4 (i.e., for the sub-sequence A_1)⁷. In these maps, the $1\text{-}\sigma$ uncertainty in the (normalized) correlation coefficients is estimated to be about 0.1. A number of points to be noted from these correlation maps are as follows.

- 1.) Significant correlation (maximum is nearly 60%) is seen between the two conal rings at non-zero azimuthal shift. Also, there is significant correlation (maximum reaches about 50%) between the diffuse pattern corresponding to the “core”-emission and the region between the two conal rings.
- 2.) The “boxy” patterns symmetric about the autocorrelation track corresponding to the peaks of the outer cone and the core-emission are due to the finite radial width of the corresponding patterns (for the outer cone, it is centered slightly towards the outer edge of the cone). It is quite surprising that there is no apparent “boxy” pattern corresponding to the inner cone.
- 3.) In the “box” corresponding to the core-emission, the azimuthal-shift corresponding to the maximum correlation increases smoothly if we go perpendicular to the diagonal line corresponding to the auto-correlation. This trend continues along the outward radial direction till we reach the inner cone’s peak. For the outer-conal region, this trend is not so prominent and visible only towards

⁷The diagonal line in the correlation map, from top right to the bottom left, corresponds to the “zero”-azimuthal shift autocorrelation, and by definition, a normalized correlation coefficient of unity.

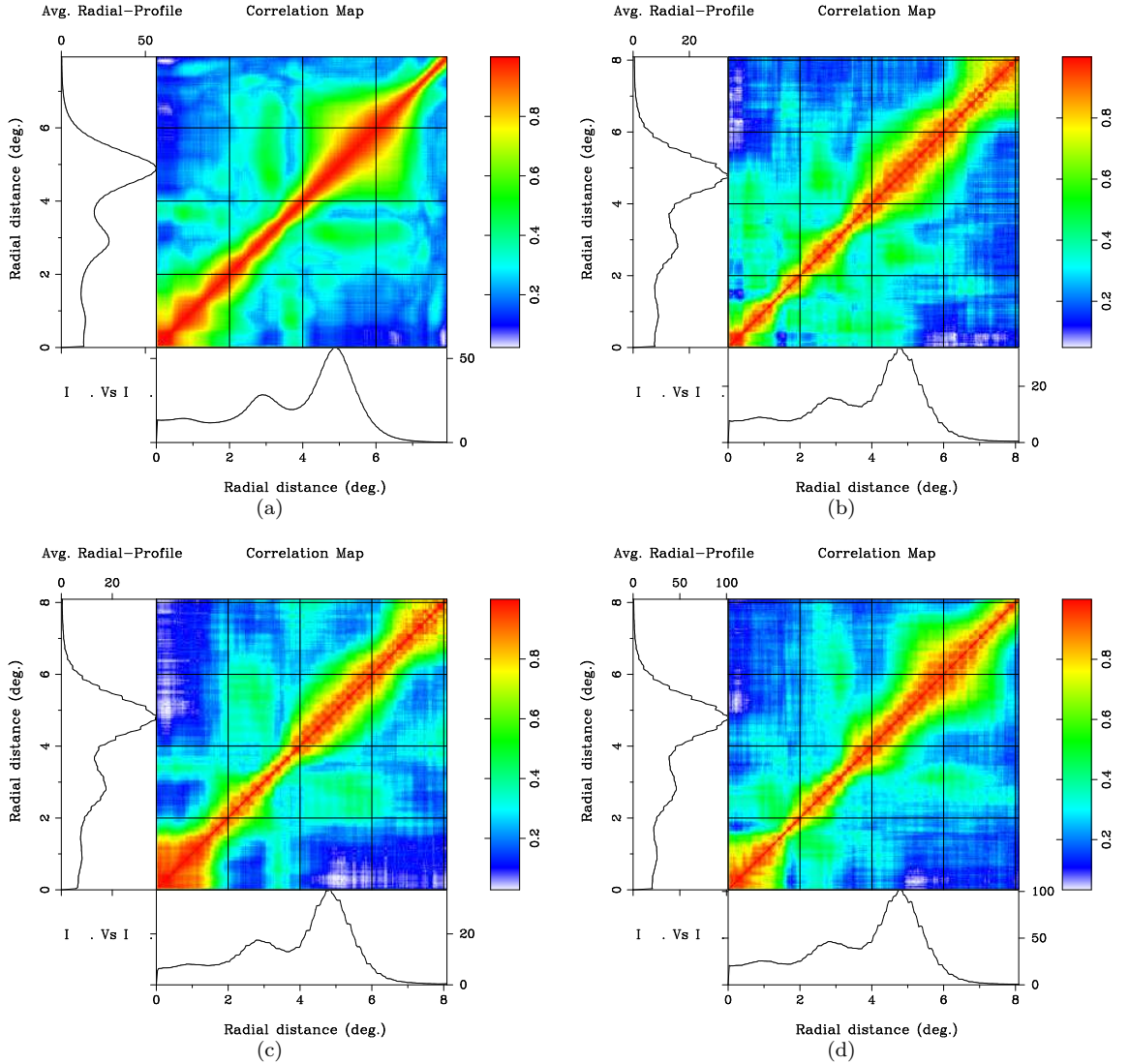


Figure 2.9: The Polar Correlation maps for all the sub-sequences.

the edges. These systematic variation in azimuthal-shift might be indicating a small azimuthal twist of the pattern as we go away from the magnetic axis, prominently seen only at low magnetic co-latitudes.

Similar correlation patterns, specifically showing the correlation between the two conal patterns as well as between the core and inter-conal region, were observed in the maps constructed for other sub-sequences discussed above. For ready comparison, the polar correlation maps and the azimuthal-shift maps for all the four sub-sequences are shown in Figures 2.9 and 2.10, respectively. A

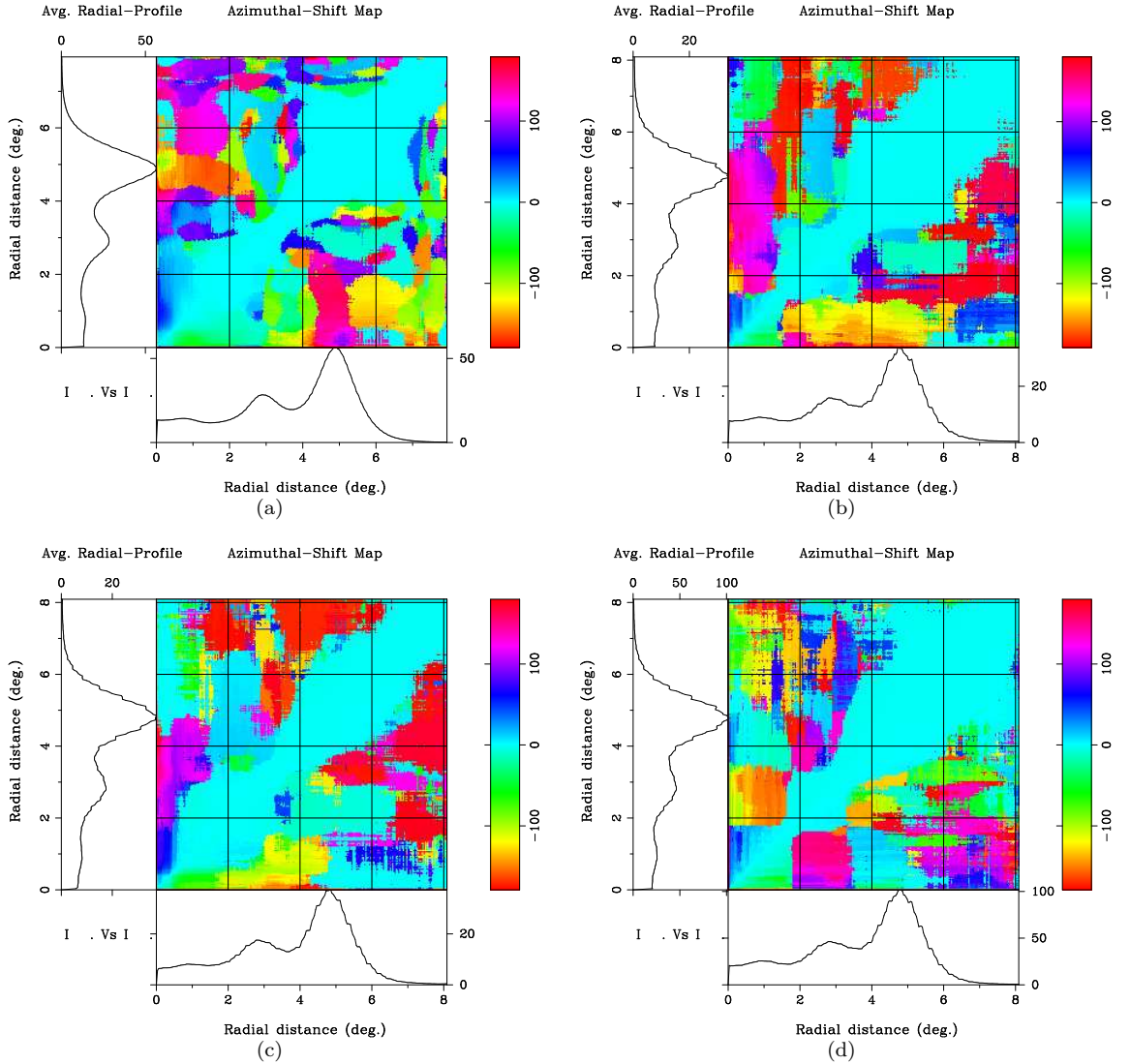


Figure 2.10: The Polar Azimuthal-Shift maps for all the sub-sequences.

noticeable difference between various correlation maps is that the locations of enhanced correlation with the core-region vary across the radial direction, in some cases even extending up to the regions corresponding to the two conal patterns.

To present a quantified measure of the correlation parameters, azimuthal sequences averaged over narrow radial sections, each about half a degree to one degree wide in colatitude, centered at the plateau corresponding to significant correlation between the two conal rings, were correlated. To measure the shifts between the correlated pair of patterns more precisely, the cross-spectrum was

Table 2.2. Correlation between the *outer* and *inner* conal emission patterns: Summary of parameters.

Sub-seq.	Correlation Parameters		
	$\rho_{\max}(\%)$	$\Delta\phi_{\text{az}}(^{\circ})$	$\Delta\tau(\text{P})$
A ₁	47	-30.3 ± 0.3	-2.39 ± 0.03
B ₁	46	$+13.3 \pm 0.4$	$+0.67 \pm 0.02$
C ₁	47	$+10.0 \pm 0.3$	$+0.94 \pm 0.03$
D ₁	31	$+09.9 \pm 0.3$	$+0.64 \pm 0.02$

Note. — The maximum percentage correlation is denoted by ρ_{\max} , and the corresponding magnetic azimuthal shift, $\Delta\phi_{\text{az}}$ (in degrees), is the amount by which the pattern corresponding to the outer cone lags behind that corresponding to the inner cone. The uncertainty in $\Delta\phi_{\text{az}}$ corresponds to 68% confidence interval around the χ^2 -minimum. $\Delta\tau$ is the absolute time-delay equivalent to the above shift in units of pulsar rotation periods.

examined to select spectral features with amplitudes above a chosen threshold, and the corresponding phase profile was fitted with a linear gradient. The azimuthal shifts corresponding to the best-fit phase-gradients (determined by minimizing χ^2), along with the maximum correlation between the above pair of averaged azimuthal sequences, are presented in Table 2.2. We will discuss more about these correlation parameters in the next section.

We have also seen the emission pattern of the core-region to be correlated with that of the “inter-conal” region. However, the significance and the radial location of the enhanced correlation is not consistent across various sub-sequences. While trying to quantify the correlation parameters for this pair of patterns, the phase-gradients were found to be poorly fitted. Hence, we have limited our further discussion only to the correlation between inner and outer cone emission patterns.

Polarization modal emission maps and their correlation properties

Based on a study of average polarization (or rather depolarization) properties of a few conal single and double profile pulsars, Rankin & Ramachandran (2003) proposed that the primary polarized mode (PPM) and the secondary polarized mode (SPM) emission elements of the circulating sub-beams are offset from each other in magnetic azimuth as well as colatitude. The already observed magnetic azimuth offset between the PPM and SPM beamlets of B0943+10 (Deshpande & Rankin, 2001) corroborated well with this proposition, although no offset in magnetic colatitude was found for this pulsar. Smith *et al.* (2013) and Rankin & Ramachandran (2003) have argued that the

Table 2.3. Emission-altitude estimates.

Cone	Location Parameters			Emission-Height (RPS method)		Emission-Height (MRPS method)	
	$\phi_l(^{\circ})$	$\phi_t(^{\circ})$	$\Delta\phi_{\text{obs}}(^{\circ})$	$h_{\text{em}}(\text{km})$	$[\%R_{\text{lc}}]$	$h_{\text{em}}(\text{km})$	$[\%R_{\text{lc}}]$
Outer	-6.65	5.45	0.60	345	[0.52]	694-740	[1.05-1.12]
Inner	-4.16	3.16	0.50	288	[0.44]	617-662	[0.93-1.00]

Note. — ϕ_l & ϕ_t are the locations of the leading and trailing emission components that constitute the cone, and $\Delta\phi_{\text{obs}}$ is the amount by which the cone-center precedes the fiducial point. R_{lc} (~ 66000 km) is the radius of light cylinder.

sub-beams corresponding to the orthogonal polarization modes (hereafter OPM) of B1237+25 are offset in magnetic azimuth (although their argument is based on the phase analysis of the secondary modulation unlike the complete carousel mapping analysis for B0943+10). Hence, it is important to assess whether the observed azimuthal offset between the inner and outer conal emission patterns has its possible origin in our usage of mixed-mode pulse sequences.

In Figure 2.11, we have plotted the polar emission map reconstructed using only the PPM power from the sub-sequence A_1 as a color image, and that using only the SPM power as contours⁸. The geometrical parameters and the circulation period assumed are same as mentioned earlier for this sub-sequence. Note that the inner conal components exhibit hardly any modulation in the (already very weak) SPM emission, leading to structures only in the outer ring in the corresponding contour map. The SPM emission in the outer ring, on average, follows the PPM power sub-beams very closely. No apparent azimuth offset between the OPM sub-beams, and the PPM and total power resulting in virtually the same emission maps (compare the image-maps in Figures 2.11 and 2.4) already confirm that mixing of the OPMs have not induced the observed offset between the two conal patterns. A formal correlation analysis, as described above, using the PPM emission map provides the same results as those with the total power map, further confirming our conclusion above that the observed azimuthal offset between the two conal emission patterns does not have its origin in complexity of the OPMs.

⁸Other properties of the 2-way OPM-separated sequences that are used for constructing these maps, can be found in Smith *et al.* (2013).

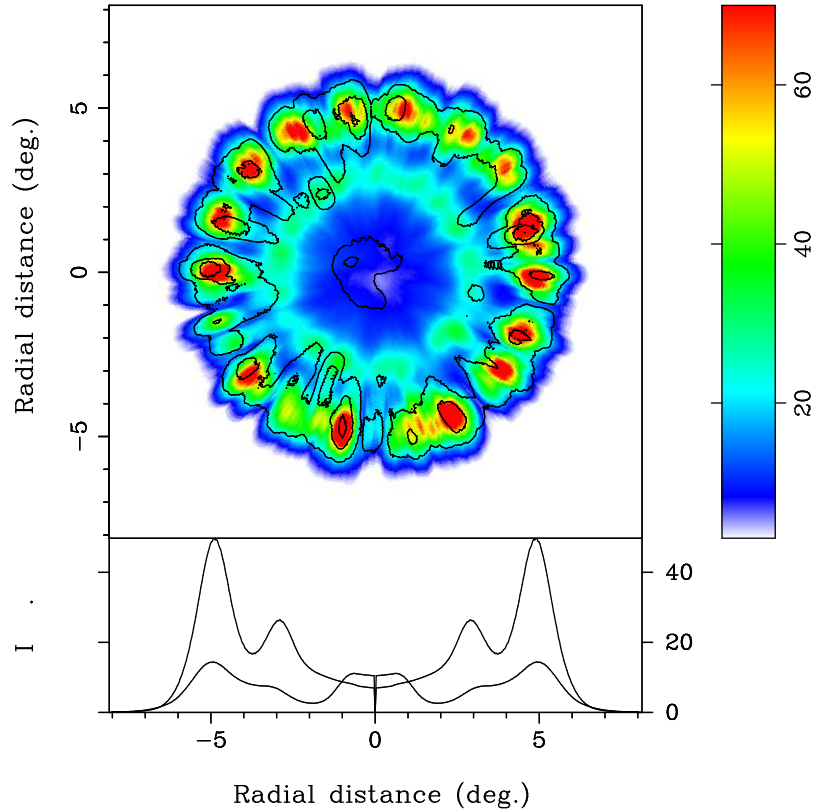


Figure 2.11: *Polar maps of the emission corresponding to the two OPMs*: The color-image shows the polar emission map constructed using only the PPM power from the sub-sequence A_1 , and using the geometrical parameters and circulation period value mentioned in the text. The overlaid contours show the emission map constructed using only the SPM power from this sub-sequence. We see that, on average, SPM emission follows the PPM beams very well, without any offset in magnetic azimuth. The bottom panel shows the average-intensity profiles for the two modes (PPM: higher intensity profile; SPM: lower intensity profile), as functions of the angular distance from the magnetic axis. Note that the conal SPM power (contour-map) is much weaker compared to its PPM counterpart — it is only about 25–30% (on average) of PPM power, as indicated by profiles in the bottom panel.

2.4.2 The emission altitudes

To estimate the emission altitudes of the two cones, we apply the relativistic phase shift (RPS) method discussed by Dyks *et al.* (2004) and Dyks (2008). Since the core component is expected to be emitted at very low altitudes, we do not expect any shift in the position angle (PA) inflexion point with respect to the fiducial point. Further, the PA inflexion point was estimated from a sub-sequence consisting of significant flux density in the core-component, and used as the fiducial point. The positions of various component peaks were estimated by fitting the average profile with

a series of Gaussian functions (6 components were required to achieve a reasonable fit), which in turn were used to estimate the center of the two cones. The emission altitude estimates obtained using the RPS method are shown in the Table 2.3.

When compared with the altitude estimates based on geometrical analysis, which is supposed to provide a lower limit on emission altitudes, above values seem to be under-estimated by a factor of 2 or so. These estimates are smaller than even those reported at 1.41 GHz by Kijak & Gil (1997). Their empirical relationship predicts an altitude of ≈ 570 km at 327 MHz. Dyks & Harding (2004) have shown that the phase shift due to the rotational sweep-back of magnetic field lines becomes comparable to those due to the aberration and propagation delays at emission altitudes $\lesssim 1\%$ of the light cylinder radius, and neglecting these would result in under-estimation of the emission heights. Shown in the second half of the Table 2.3 are the constraints on the emission altitudes obtained by following the procedure described in Dyks & Harding (2004) which includes the rotational sweep-back effects (for convenience, we shall refer to this method as “modified relativistic phase shift”(MRPS) method). These estimates are now consistent with the lower limits derived using geometrical considerations.

2.5 Discussion

We have presented the underlying configurations of emission sub-beams of the pulsar B1237+25, reconstructed using a number of candidate P_4 values inferred by analyzing the rich sub-pulse modulations in a number of single pulse sequences from this M-category star. The sub-beam configurations vary across different sub-sequences, and no firm (harmonic) relationship is apparent between various inferred P_4 values, suggesting that the underlying sub-beam configurations are not stable over long durations. The short scale variations in the emission maps, along with very low-Q feature corresponding to the secondary modulation, indicate that the configurations are not quite stable even within the interval of short subsequences considered here.

Nulling can cause perturbation in the carousel rotation, and hence in the sub-beam drift rate, resulting in the observed irregular patterns in the rotating frame. The large range of the sub-beam circulation periods, inferred from various sub-sequences, also made us wonder if it has any relationship with the fraction of time the pulsar remains in null-mode. There is indeed a hint of an inverse relationship between P_4 and null-fraction. However, the apparent dependence is not statistically significant enough to draw any inference. We tried to model the effects of nulls as perturbation in the carousel rotation followed by recovery to a stable rotation rate, and searched for a stable carousel of sub-beams. Results from our modeling of the time spent in the perturbed and recovery phases in 4 different ways suggested that the recovery time does not depend linearly on the preceding null-duration, and is possibly random or has a non-linear dependence. Even for suitably

long null-free sub-sequences, we did not see an indication of a stable emission pattern through our spectral and correlation analysis. The observed profile of modulation phase across the pulse-window deviates significantly from that predicted by the carousel model. The deviations appear to be random across various sub-sequences, and further suggest lack of stability in the emission patterns, unless the mismatch is actually pointing to failure of the standard carousel model.

The major question we have been trying to address is: do the “inner” and “outer” cones share the same seed bunch of particles for their excitation? This question had been raised first by Rankin (1993), followed by ‘indirect’ evidences by Gangadhara & Gupta (2001) which, in case of pulsar B0329+54, seem to support the view that the emission in multiple cones is associated with the same set of magnetic field lines but at different altitudes. The polar emission maps of the pulsar B1237+25 have provided us a comprehensive way to study any relationship between the sub-beam patterns responsible for the emission in the inner and outer cone. As evident from the polar correlation map for the sub-sequence A_1 discussed in previous section, the patterns associated with the two cones are significantly correlated with each other, and consistently so, for the other sub-sequences discussed above (see Table 2.2). This correlation between the two patterns, in our view, provides a ‘direct’ evidence that the same seed pattern of “sparks” is responsible for the emission in the two cones. It is worth noting here that the actual correlation between the two patterns would probably be even higher, since (a) the possible lack of stability of the sub-beam configurations, and (b) the possible overlap between the radial extents of the carousels, combined with the fact that there is a relative azimuthal shift between them, would have smeared the mapped patterns.

Further, noting the emission altitude estimates in Table 2.3, along with the above evidence, it seems an obvious and plausible interpretation that the same underlying pattern is responsible for the same frequency emission at two distinct altitudes. In this “multi-altitude emission” picture, the inner cone emission comes from a lower altitude than the emission in the outer cone, along the same bunches of magnetic field lines. However, as noted by Rankin (1993) and Mitra & Rankin (2002), the profile shape evolution with frequency reflecting the flaring of the magnetic field lines (as suggested by the RFM) is consistent only in the outer conal components. The inner cone shows no or negligible RFM. Hence to explain the lack of profile shape evolution with frequency, additional considerations, which may be intrinsic or extrinsic to the emission, would be required.

The sub-beam patterns in the two conal rings are offset (relative to each other) by apparently different magnetic azimuthal shifts for different circulation period values. However, for the sub-sequences B_1 , C_1 , and D_1 , the azimuthal shifts seem to be more compatible with each other, and all of them confine around $+10^\circ$ (see Table 2.1). The azimuthal shift for the first sub-sequence (i.e., for A_1) seems to be inconsistent with that for the other three. However, we should note that the phase gradients we fit over *limited* parts of the cross-spectrum, and hence our estimates of the azimuthal shifts, are subject to possible aliasing due to the secondary modulation. Note that the

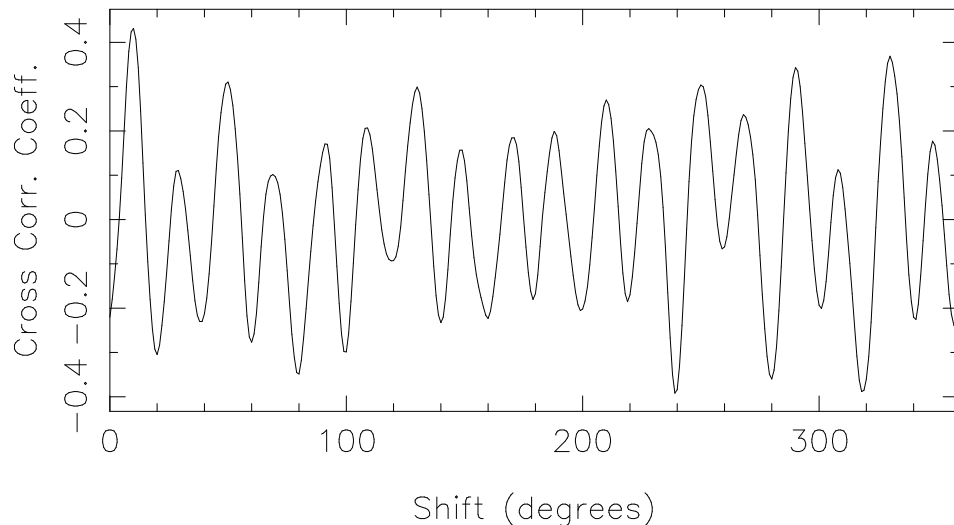


Figure 2.12: Cross-correlation between the outer and inner conal emission patterns as a function of azimuthal shift between the two, computed for the sub-sequence A_1 .

sub-beam spacing for this sub-sequence is about 20° , and hence, a shift of $+10^\circ$ could be seen aliased at -30° . Our assertion about the aliasing is well supported by the cross correlation between the inner and outer patterns, as shown in Figure 2.12. A shift of about $+10^\circ$ actually corresponds to the maximum in the correlation function⁹. Hence, all the sub-sequences consistently show an offset of about $+10^\circ$ between the patterns corresponding to the emission in the outer and inner cone. This large offset indicates a twist in the emission columns between the two different emission altitudes. A similar scenario was proposed by Rankin *et al.* (2003) to explain the mode-switching phenomenon in B0943+10, wherein the emission columns (coupled with the magnetic field) are twisted progressively by the rotating star as they move up in the relatively weaker magnetic field regions.

The other important question of our primary concern is the origin of the core-component. Although the core-component does not show any signature of corresponding secondary modulation feature seen in the conal-components (~ 0.37 c/P), the tertiary modulation feature is present throughout the profile (Figure 2.3) and prominently so in the “core-region” (i.e., the region covering the core-component and the region prior to it). This observation is true for all the sub-sequences explored above. Gupta & Gangadhara (2003) have proposed two additional components, just leading and trailing the core component, constituting a third emission cone. However, Srostlik & Rankin (2005) could confirm presence of only one of these two components — the one situated just before the core component.

⁹The correlation at about -30° is within 3σ uncertainty limits of the maximum at about $+10^\circ$. Correlation functions for the other three subsequences show the most likely shifts consistent with those in Table 2.2.

Presence of the sixth component, along with the above evidence that the core-region shares the same circulation as the two conal sub-beam patterns, might suggest that at least some of the core emission also originates from a compact and ‘further in’ sub-beam pattern. The diffuse nature of the pattern, i.e. the absence of discrete sub-beam like structures, would then explain the lack of secondary modulation feature in the fluctuation spectrum as it would be attenuated by smoothing due to the finite sub-beam width. The “white” fluctuation spectrum for the core-emission seen in many cases (specifically for core single profile stars; Rankin, 1986) may be explained if the diffuse nature of the pattern approaches uniformity. Having the above picture, one may speculate that both the core and conal emission stem from the same seed pattern at different heights in the magnetosphere, which in its unresolved form constitutes the core component and at suitable higher distance gets resolved out (longitudinally as well as latitudinally) into a system of sub-beams that we see in the conal-emission. It should be emphasized here that this picture would require further considerations similar to what we need to explain absence of RFM in the “inner” cone.

The emission in the core-region appears to be correlated with that in the inter-conal region (Figure 2.8). However, the inconsistency in localization and significance of this correlation across various sub-sequences limits our confidence in inferring any further detail based on this correlation. None of our earlier inferences are however affected by this limitation.

2.6 Conclusions

With the specific aim to find out whether the emission in the outer and inner cones of the pulsar B1237+25 share a common origin or not, we have mapped and studied the underlying emission patterns for a number of pulse sequences from this star. We summarize the conclusions from our study in the following points:

1. The underlying carousel(s) of sparks for this pulsar lack stability over long durations, even when the pulsar remains in the same emission mode. The sweep of the modulation phase across the pulse longitudes deviates from that predicted by the carousel model. These deviations pose a serious challenge to the widely accepted standard carousel model, unless their origin is caused by irregularities/perturbations on time-scales much lesser than the lengths of our individual sub-sequences.
2. The emission patterns corresponding to the outer and inner cones are significantly correlated with each other, implying that the emission in the two cones share a common seed pattern of sparks. The emission in the two cones is probably due to multi-altitude emission by the same bunches of particles, and along the same sets of magnetic field lines.
3. The emission patterns corresponding to the outer and inner cones are offset from each other,

consistently across various sub-sequences, by about 10° in azimuth. We have confirmed that the observed offset does not have its origin in complexity of the orthogonal polarization modes. This large offset indicates certainly a twist in the emission columns, and most likely in the magnetic field geometry, between the two different emission altitudes.

4. Presence of a compact, diffuse and ‘further-in’ carousel of sub-beams is consistent with the observed modulation in the core component of the pulsar B1237+25. The featureless spectrum observed for many core-single pulsars can be explained if the diffuse pattern approaches uniformity.
-

Part II

Tomography of the Pulsar Magnetosphere: Development of a Multi-band Receiver

Multi-band receiver: Motivation

Even after several decades of pulsar studies, we remain far from being able to relate the puzzling rich details exhibited by pulsars to the physical processes responsible for the observed radio emission. While the average pulse profile with polarization information reveals the viewing geometry (Radhakrishnan & Cooke, 1969) and gives some clues about the possible emission mechanisms (e.g., see Rankin, 1983, and other papers in the same series), the fluctuations from pulse to pulse seem to be more crucial and promising in probing the underlying physical processes (see, for example, Drake & Craft, 1968; Backer, 1973; Deshpande & Rankin, 1999). Over the past decade, studies of such fluctuations in pulsar signals suggest that plasma processes responsible for pulsar emission may be organized into a system of columns seeded by a carousel of “spark” discharges in the acceleration region with steady circulation around the magnetic axis.

Estimation of the carousel circulation time, and hence “cartographic” mapping of the observed emission to a system of emission columns has been possible so far only for a limited number of pulsars, and the important factors determining such configurations and the pattern circulation are yet to be fully understood. Further, any possible connection between the profile/polarization mode changes, as well as nulling, observed in several pulsars and the circulating patterns also needs careful investigations. To enable these investigations, ideally, we need full polarimetric single-pulse data on how the emission columns and their configuration evolves with emission height and time. This demands simultaneous single-pulse observations across a wide frequency range implied by the so called radius-to-frequency mapping (RFM); with the high frequency emission originating close to the star surface, and regions of lower frequency emission progressively farther away. As suggested by the RFM, observations made over a narrow spectral range sample the details only in a transverse slice of the emission cone. Multi-frequency observations, made simultaneously, would essentially amount to sampling the polar magnetosphere at various altitudes. With such observations, polar emission

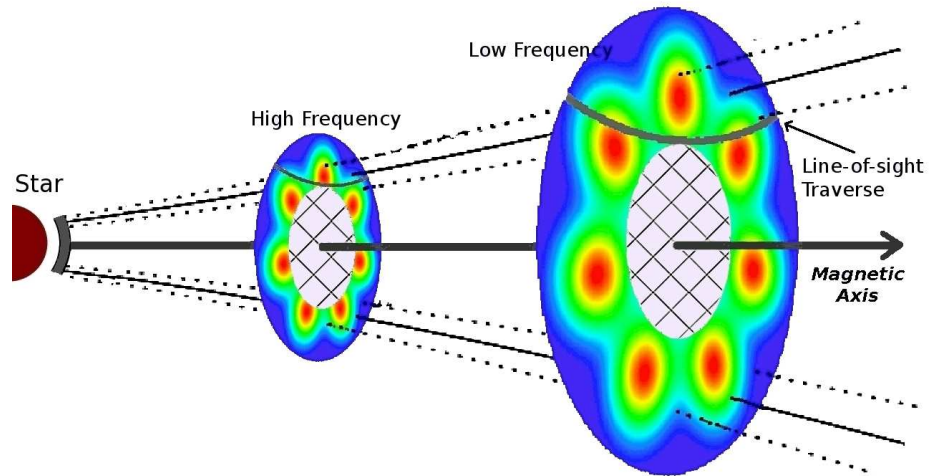


Figure 3.1: A cartoon to illustrate tomography of the polar emission region, wherein two of the many possible slices of the emission cone are shown consistent with the radius-to-frequency mapping. The gray arcs indicate the line-of-sight traverse. Given the single pulse time sequences, 2-D pictures similar to those shown in the example slices, can in principle be mapped using a cartographic transform (as described in Chapter 1). The size of the inner inaccessible region (cross-hatched) is determined by how close our sight-line gets to the magnetic axis.

mapping at a number of emission-altitudes would not only allow “tomography” of the polar emission region (see an illustration in Figure 3.1), but also might provide much needed clues about generation of sub-beam patterns, associated polarization and more importantly, their evolution across the magnetosphere.

To carry out simultaneous multi-frequency observations, we first took the natural approach of making use of several existing telescopes simultaneously. Below we discuss briefly our effort of coordinating several telescopes which had several shortcomings in providing desirable quality data across various frequency bands, and prompted us to seek a superior alternative. Below, we first describe our attempt to use the existing facilities, and then the better alternative we attempted.

3.1 An approach using many telescopes simultaneously

We proposed and carried out multi-frequency observations of a number of bright pulsars simultaneously at 5 frequencies using four different telescopes. The Giant Metrewave Radio Telescope (GMRT) was used to observe at 236 MHz and 622 MHz simultaneously, while the observations at

other three frequencies were carried out using the Gauribidanur Low-frequency Array¹ at 35 MHz, the National Mesosphere–Stratosphere–Troposphere (MST) Radar facility² (located at Gadanki, near Tirupati, India) operating at 53 MHz and the Ooty Radio Telescope (ORT) at 327 MHz. The Gauribidanur Array and the MST radar facility can observe the sources for short time spans (~ 40 and 15 minutes respectively) only around their meridian transits. Hence the sources with nearby transit-times were constrained to be observed on different days. Also, as the radio frequency interference (RFI) challenges increase at low frequencies (35 & 53 MHz), we requested to schedule the observations such that the respective source transits happened to be in the nights. Due to the above constraints, the observations were carried out in 5 different observing sessions distributed over about nine months.

Although we were successful in coordinating and using several telescopes for carrying out the simultaneous multi-frequency observations, desired simultaneity and data quality across various bands could not be obtained, primarily because of the following:

1. *Synchronization:* The accuracy of the time-stamp marking the start-time of the observations was not adequate enough, specially at the Gauribidanur Array, MST radar and ORT, to synchronize the observed single pulse sequences in the off-line processing.
2. *Sensitivity:* Sensitivities of the telescopes operating at very low frequencies, like the Gauribidanur Array and MST radar, are affected by many other factors like ionospheric conditions, RFI situation, hour-angle coverage etc., in addition to the telescope/observation parameters, viz. the collecting area, frequency bandwidth and the observation duration. The bright sky background and inherent weak emission from pulsars at these frequencies, in addition to constrained observation durations, also proves to be limiting. In our simultaneous multi-frequency observations, only 3 out of the 11 observed pulsars could be detected at 53 MHz, while none could be detected at 35 MHz. Even for those 3 pulsars which could be detected, the duration of the observation was limited and only about 600 periods long pulse sequences could be observed. These results at low frequencies left us with observations effectively in 3 higher frequency bands which, as mentioned above, lacked the desired simultaneity. The poor signal-to-noise ratio (S/N) of observations at highest frequency (622 MHz, see Figure 3.2) also limited our investigations at single pulse level.
3. *Polarization:* The Gauribidanur Array and the ORT have single linear polarization receptors. Although the MST radar consists of crossed Yagi antennas, signal only from a single polariza-

¹For more details, see Chapter 6 of this thesis and http://www.rri.res.in/aa_ep.html#1

²This national facility is situated at Gadanki, India. For more details, see <http://www.vigyanprasar.gov.in/comcom/develop73.htm>

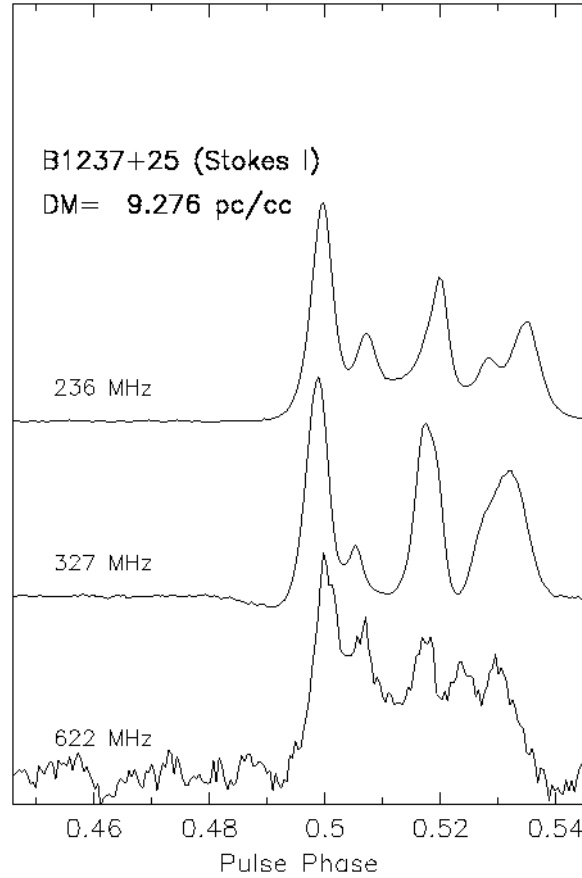


Figure 3.2: Average profiles of the bright pulsar B1237+25 obtained from observations using the GMRT and the ORT. The profiles are manually aligned with each other. About 1600, 1300 and 2300 periods long pulse sequences, at 622, 327 and 236 MHz, respectively, have been used to obtain these average profiles.

tion could be recorded. The linear polarization information, in such cases, can be derived for the average profiles based on the expected Faraday modulation across the observing bandwidth (Ramkumar & Deshpande, 1999). The polarization mode changes observed in many pulsars necessitate availability of polarization information for each of the single pulses. However, this information is difficult to recover at single pulse level unless each of the single pulses is detected with significant S/N. Depending on the number of Faraday modulation cycles across the observing bandwidth, and the profile-shapes corresponding to the two polarization modes, the total intensity average profile and the single pulse modulation properties obtained from observations using single linear polarization receptors can turn out to be quite different from the actual ones. One such example can be seen in Figure 3.2, wherein the last two components of the average profile at 327 MHz appear completely merged into each other, while these

components seem to be resolved in the average profiles at lower and higher frequencies.

3.2 Towards a superior alternative

In the previous section, we demonstrated some of the practical difficulties in carrying out simultaneous multi-frequency observations using many telescopes simultaneously. Apart from inherent complexities in coordinating/scheduling several telescopes at different geographical locations, their available setups generally have undesirable differences in, say, hour angle coverage, aperture shape and filling factor, polarization response, ionospheric contributions, synchronization (time-stamp) accuracy, calibration schemes, sensitivity, RFI-free bands and data formats.

A superior alternative which provides the desired simultaneous multi-frequency observations, avoiding all the above complexities, is to have a “self-contained” multi-band system for use with a single large aperture. Such a system would include a suitable feed, broadband front-end, parallel analog and digital receiver pipelines, along with appropriate monitoring, synchronization and data recording systems. In next chapters, we describe our design of such a multi-band system which was successfully built and tested at the Raman Research Institute, and present synoptic results from observations of a number of bright pulsars, carried out simultaneously at 10 frequency bands sampling the spectrum from 100 MHz to 1.4 GHz, using this receiver system with the Green Bank Telescope.

Chapter 4

Multi-band receiver : Design and development

In this chapter, we present detailed design of a self-contained multi-band receiver (MBR) system elaborating on our design study of multi-band feed – the first element in the signal path – followed by a brief account of the actual development of the setup carried out at the Raman Research Institute (RRI). The MBR system, intended for use with a single large aperture, facilitates sensitive and high time-resolution observations simultaneously in 10 discrete frequency bands sampling a wide spectral span (100–1500 MHz) in a nearly log-periodic fashion. The development of this system was primarily motivated by the need for tomographic studies of pulsar polar emission regions. Although the system design is optimized for the primary goal, it is also suited for several other interesting astronomical investigations. The system consists of a dual-polarization multi-band feed (with discrete responses corresponding to the 10 bands pre-selected as relatively RFI-free), a common wide-band radio frequency (RF) front-end, and independent back-end receiver chains for the 10 individual sub-bands. The raw voltage time sequences corresponding to each of the two linear polarization channels for each of the 10 spectral bands, are recorded, sampling 16 MHz bandwidth at the Nyquist rate, simultaneously. The MBR system was successfully built and tested at RRI, and used with the Robert C. Byrd Green Bank Telescope (GBT) of the National Radio Astronomy Observatory¹ for carrying out simultaneous multi-frequency observations of a number of pulsars.

Publications based on this chapter: Maan *et al.* (2013) and Maan *et al.* (2009).

¹The National Radio Astronomy Observatory is a facility of the National Science Foundation operated under cooperative agreement by Associated Universities, Inc.

4.1 The MBR system design: An overview

The design in the form of a block-diagram along with the signal route is shown in Figure 4.1. The basic requirement of such a receiver system is to have a prime-focus feed element, which has good response in the desired parts of the radio spectrum. While there are many practical difficulties in designing and fabricating the basic feed antenna having uniform response over the entire broad-band of interest (about 1:15 range; 100 MHz to 1.5 GHz), and then in processing (digitization, recording etc.) the signal with that large bandwidth (if achieved), it is much simpler, feasible and realizable to use an antenna which is designed to have gain/response only in certain spectral windows of interest, and then sample and record the signal only in these bands. In the next section, we present a design study of such an antenna, more specifically called as “*multi-band feed*”.

In the “*front-end*”, the signal from the feed is amplified, and the unwanted signal outside the wide-band of interest is filtered out. The first amplifier in the signal route — the low noise amplifier (LNA) — is desired to be as close to the feed as possible, to minimize any possible signal loss in, and noise contribution from, the intermediate signal path (cables, connectors etc.). The filtered wide-band signal is then transferred to the “*back-end*” (which is generally situated in receiver/control-room, far away from the feed) over the optical fiber. Here the signal is power-divided into eight sub-bands of interest². Each of these eight parts go through separate, but similar, receiver/processing chains before the data gets recorded in the respective storage devices. The similarity in various chains would help to keep the flexibility of sub-band selections (in number and their center frequencies) as well as provides ease in debugging the system whenever required. All the receiver chains share a common frequency reference and GPS based synchronization. These receiver chains are controlled and monitored by M&C PC via their respective computers (using Ethernet) in the “*monitoring & control unit*”.

4.2 Multi-band feed: A design study

A wide-band feed (about 1:15 range in frequency) along with appropriate back-end can be used to realize multi-frequency observations by utilizing the collecting area offered by large aperture telescopes. But, one is likely to suffer from the severe RFI (typically 40-80 dB above the level expected from astronomical signals) in several bands over such a wide frequency range. Various RFI mitigation techniques used in the off-line processing are of little use if the hardware receiver pipeline itself is driven to its non-linear response due to these strong RFI. With a view of selectively rejecting the RFI-contaminated bands at the feed itself, we explored the possibilities of having a

²The system was originally proposed to provide operation with 8 sub-bands. However, 2 additional back-end chains, built as spares, were also made part of the system providing operation with a total of 10 sub-bands.

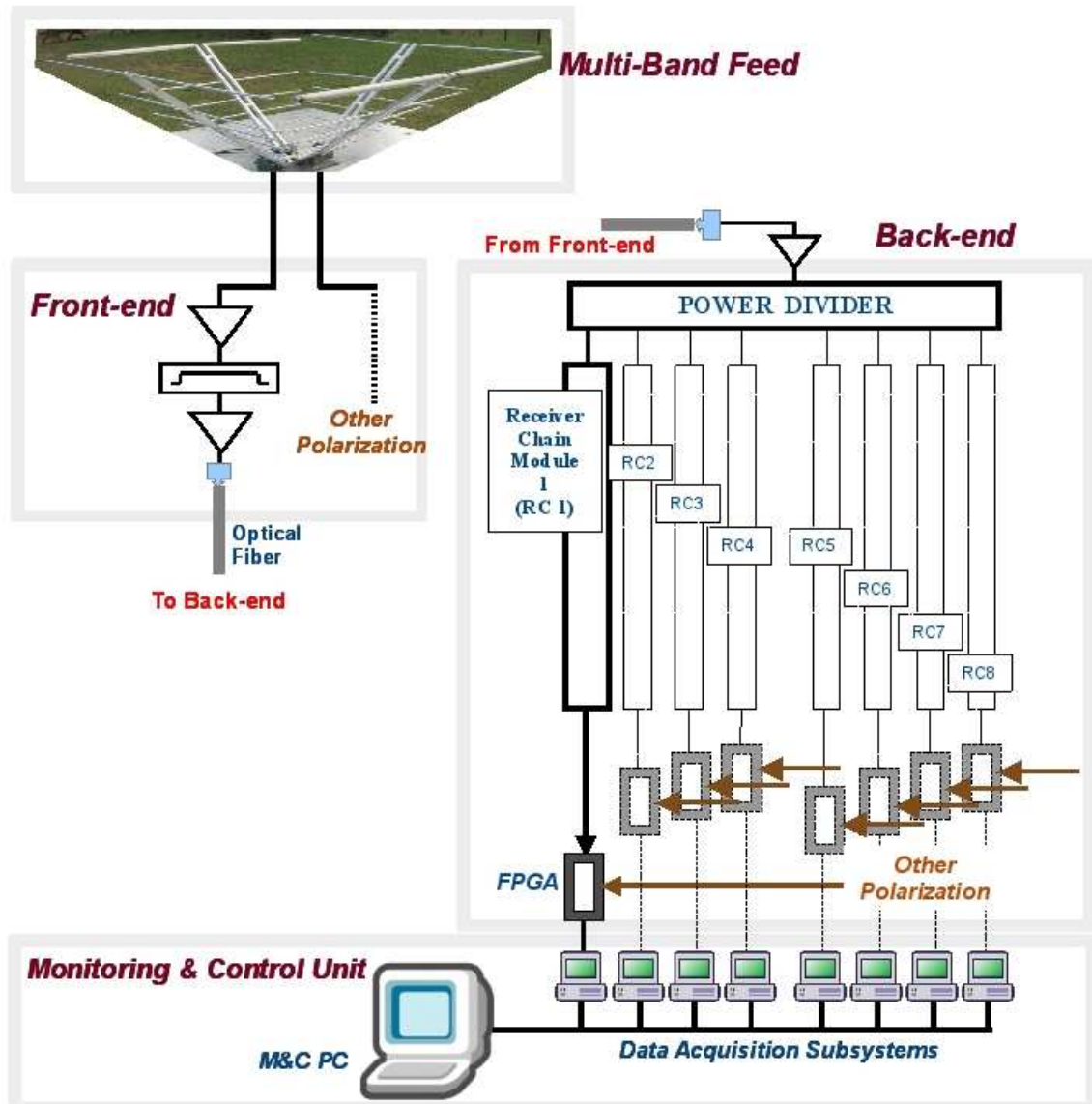


Figure 4.1: The basic design of the multi-band receiver.

multi-band feed antenna spanning a wide frequency range, but which would have good response only in a number of pre-selected RFI-free windows³. Below we present a comparative study of the two designs investigated by us, along with detailed characterization of radiation pattern of one of these designs.

³An RFI survey at the observing site (i.e., at the GBT) was performed primarily around the desired bands, and the nearest available relatively RFI-free regions were selected.

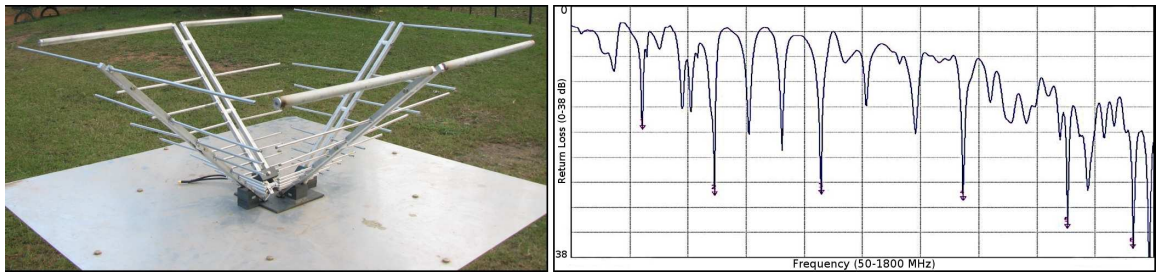


Figure 4.2: *Left:* A photograph of the mechanical model of the first design. *Right:* Return-loss measurements for one of the polarizations in the frequency range 50-1800 MHz.

4.2.1 New multi-band feed designs: An overview

The designs we have investigated use the basic configuration of multiple pairs of dipoles as in the “Eleven Feed” (Olsson *et al.*, 2006). The Eleven feed is a dual-polarization wide-band feed with a decade plus bandwidth and a nearly constant beam-width throughout the band. Its basic configuration consists of a set of parallel folded dipole-pairs separated by half a wavelength. All the dimensions of the dipoles (like length, separation, height above the ground plane) are scaled with frequency so as to provide the log-periodic shape. The major advantages of this feed are (a) constancy of phase center location with frequency (which comes from the symmetrical placement of dipoles), and (b) good matching E & H beams, making it suitable for illuminating the reflector antennas over wide bands. More details about the physical dimensions, structure and performance parameters of the Eleven Feed (0.15–1.5 GHz) can be found in Olsson *et al.* (2006). This feed has been claimed to be scalable in any frequency range and a number of models in different frequency ranges have been successfully tried out (e.g., Olsson *et al.*, 2004, 2005, 2006).

Given the good performance of the Eleven Feed over a wide band (about 1:10 range in frequency) and its suitability for use with parabolic reflectors, we conducted simulations using the (freely available) Numerical Electromagnetics Code⁴ (NEC2) exploring the possibilities of rejecting some particular parts of the spectrum by sparsely packing the folded dipoles⁵. Although the results did show discrete responses, the response locations and the number of responses could not be associated clearly with the dipole lengths and number of dipoles, respectively. Aiming for 9 to 10 discrete bands, at pre-decided center-frequencies with fractional bandwidths of about 10% to 15%, we tried the following two designs with the same basic configuration as that of the Eleven Feed, but using simple half-wave dipoles instead of the folded dipoles in the latter.

⁴See <http://www.nec2.org>

⁵A mechanical prototype of the Eleven Feed, scaled to the frequency range of 300-1000 MHz, was used to successfully establish the correspondence between the simulation results and those obtained in practice.

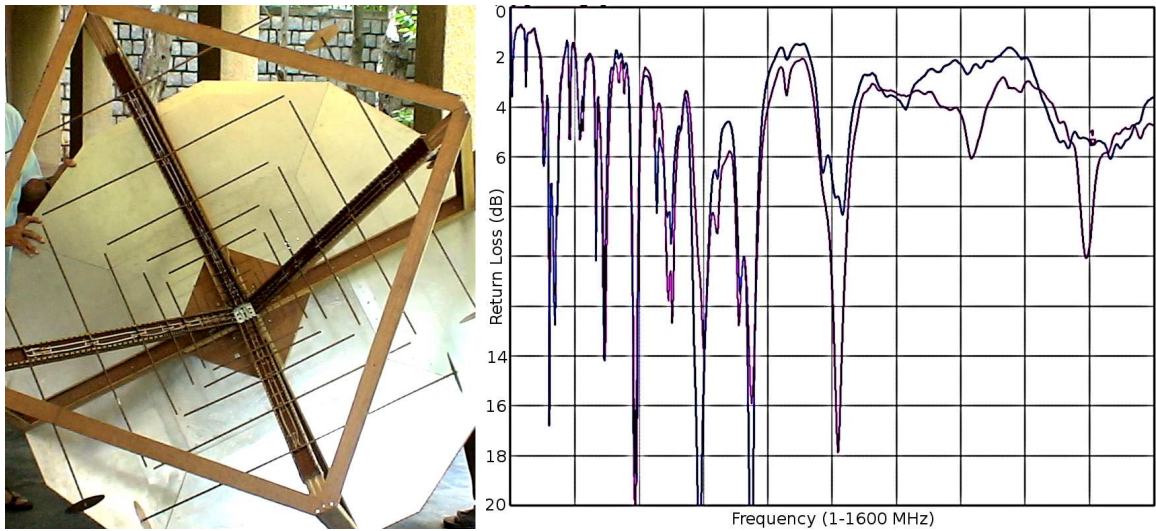


Figure 4.3: *Left:* A photograph of the designed feed with feed-lines constructed using the co-axial cables. *Right:* The return-loss measurements for the two linear polarizations overlaid on each other.

Design 1: Eleven Feed with simple half-wave dipoles

This design consists of nine half-wave dipoles (as against folded dipoles in the Eleven Feed) using aluminium tubes. The dipoles are arranged in a similar log-periodic conical arrangement as in the case of the Eleven Feed. The maximum dimensions of the feed are decided by the lowest resonant frequency of interest (width: $0.5 \lambda_{max}$, height: $0.25 \lambda_{max}$). Figure 4.2 shows a picture of the mechanical prototype fabricated at RRI based on this design, along with the return-loss measurements for one of the polarizations. A balun (without any impedance transformation) was used at the feed point for these measurements. The return-loss includes the losses and mismatch, if any, due to the balun itself. While this design showed promising responses at some of the desired frequencies, a proper correspondence could not be established for the extra (i.e., unwanted) responses. Furthermore, the radiation beam pattern simulated using NEC2 showed that significant power is distributed in the side-lobes, particularly at the higher frequencies, thereby making it unsuitable for use in parabolic reflector antennas. Further detailed probe revealed that the metallic feed-lines are not behaving merely as transmission lines, but are themselves radiating, thus modifying the overall feed response in a way that is difficult to disentangle.

Design 2: Eleven Feed with simple half-wave dipoles and co-axial feed-lines

Since any radiation from the feed-lines in the above design has to be shielded, our second design incorporated feed-lines constructed using co-axial cables connecting the half-wave dipoles (similar to those in Design 1). Here, the outer conductors of these co-axial cables are connected to

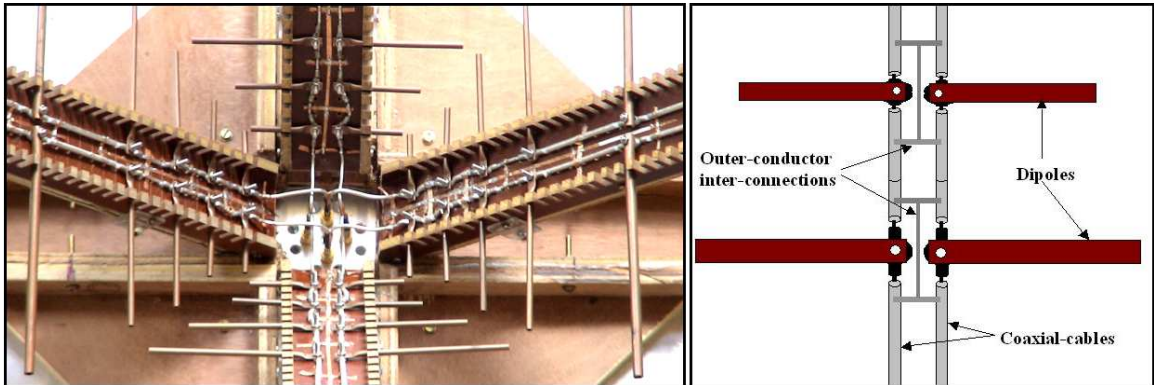


Figure 4.4: *Left:* A zoomed-in view of the central part of the feed in Figure 4.3 (Design 2), showing the co-axial feed-line connections at the feed-point. *Right:* A schematic demonstrating the connections between the dipoles and the feed-lines, and the inter-connections between the outer conductors of the co-axial cables.

the common ground (same as for the reflector), and act as a useful shield. A mechanical prototype⁶ of this design was realized at RRI and tested (see Figure 4.3 for a photograph of the designed feed and return-loss measurements for the two polarizations; the connection details are shown in Figure 4.4). We were successful in achieving return-loss better than 12 dB at six of the nine aimed frequency bands, with about 10 dB rejection in the unwanted parts of the spectrum. Preliminary radiation pattern measurements also showed satisfactory response for the discrete bands. To decrease the mechanical dimensions, the longest dipole was made shorter and end-loaded with a copper-disk (providing equivalently larger electrical length) such that the resonance still occurs at the frequency of interest.

4.2.2 Further characterization of the second design

After the encouraging results from the preliminary tests conducted at Gauribidanur using the second design, elaborate tests were carried out using astronomical sources with the aim of characterizing the radiation pattern of this feed. The collecting area offered by a single GMRT dish ensured the needed sensitivity for these measurements⁷. To assess how well the feed illuminates the dish across the wide spectral span, raster-scans across Cas-A were taken using a new grid-pointing scheme. Since the beam-widths are expected to be proportional to the wavelength, this scheme

⁶A wood-like material was used to fabricate a generic template providing a base for the feed-lines and the dipoles. The multiple number of grooves on the sides of the template provided the flexibility of replacing a particular dipole with another of different length and/or changing the position of a dipole with respect to the ground plane, thus providing us a convenient way of tuning the center frequencies of the selected bands.

⁷The multi-band receiver, which was in the “testing-at-site” stage at that time, was used as the back-end.

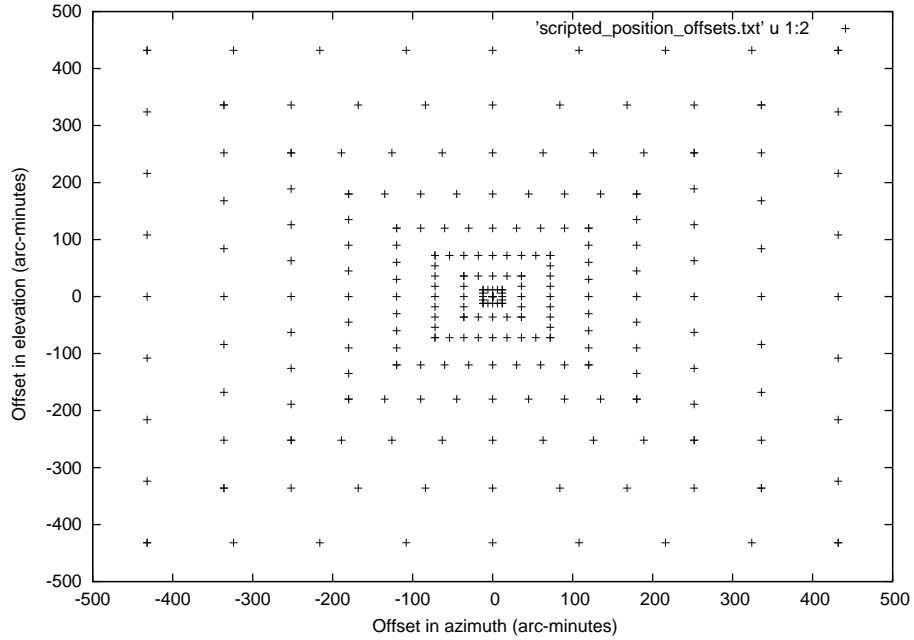


Figure 4.5: An optimum grid pointing scheme to appropriately sample the beams across wide frequency range by taking raster-scans across a strong source (e.g., Cas-A).

was designed to have finer sampling at the center and coarser as we go away from the source, so that appropriate angular sampling of beam patterns can be achieved at all the frequencies (see Figure 4.5).

Since the phase information is not available in the grid-scan measurements, we Bessel-interpolated the beams using the Fourier relationship between the focal and aperture plane field distributions, and noting the constraint on the aperture diameter. Using this method iteratively (which is equivalent of “clean”, a technique commonly used in imaging; and also a phase-retrieval method when sufficient number of constraints can be put), we obtained the 2-D aperture illumination patterns in each of the individual frequency bands. For six of the bands where we had observations with adequate signal-to-noise ratio, the corresponding azimuthally averaged voltage illumination functions⁸ (corresponding to 22.5 meter radius of the GMRT dish) are shown in Figure 4.6. These were then fitted with Gaussian functions, to estimate the beam-widths and tapers at the dish-edge. Table 4.1 summarizes these estimates along with the corresponding G/T-values⁹ estimated using the measurements from drift-scan across the sun.

⁸By “voltage illumination function”, we shall be referring to “modulus-of-complex-voltage illumination function”.

⁹G/T is the ratio of the antenna gain (G) and the system noise temperature (T), and serves as a figure of merit to quantify a receiver system’s performance.

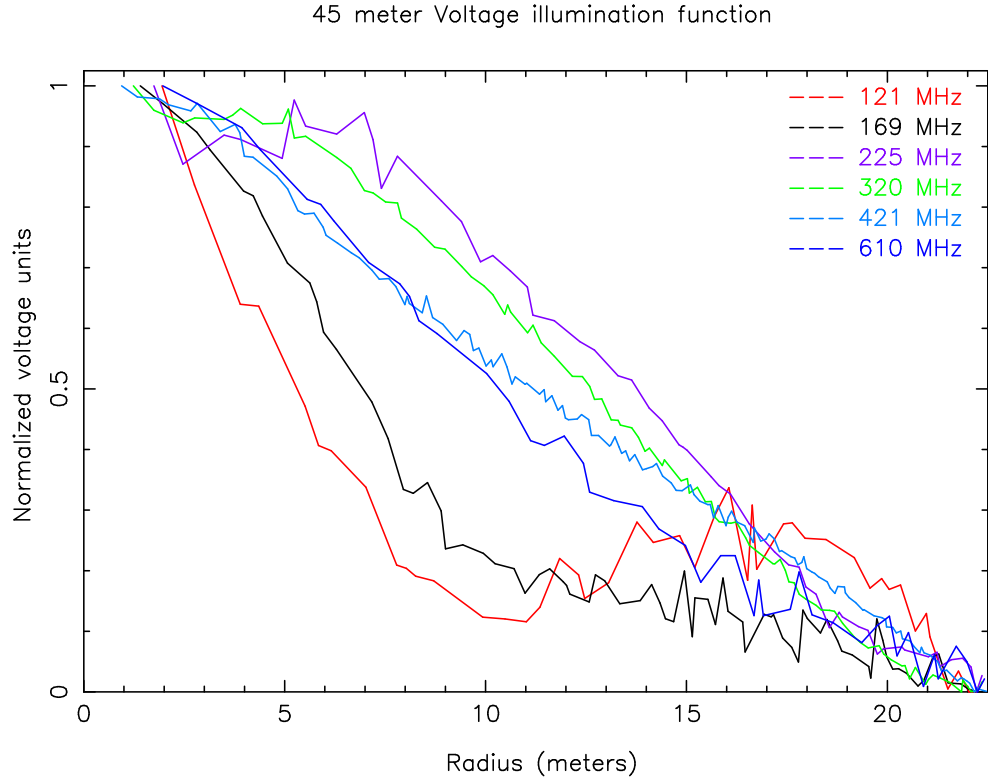


Figure 4.6: The azimuthally-averaged radial illumination function.

Table 4.1: Summary of the edge-tapers and G/T for 9 bands

Frequency (MHz)	Edge-Taper (dB)	G/T (dB)	Frequency (MHz)	Edge-Taper (dB)	G/T (dB)
121	30.5	—	610	11.9	9.23
169	22.8	—	815	—	7.75
225	6.9	-0.75	1197	—	7.35
320	8.7	0.45	1420	—	6.31
421	8.7	5.38			

Notes: (a.) For last three bands (815, 1197 & 1420 MHz), illumination functions, and hence the edge-tapers, could not be estimated because of not having adequate S/N;

(b.) First two bands (121 & 169 MHz) were heavily contaminated by RFI, so the edge-tapers indicated here for these bands may not reflect actual value (for the same reason, G/T also has not been estimated for these bands).

4.2.3 The bottom line

The original design of the Eleven Feed cannot reject the bands selectively, and the first feed-design, in its present form, does not give us controllability over the discrete frequency responses. The second feed-design does provide us control over the response locations and fairly good rejection in the unwanted parts of the spectrum. Also, it shows moderate values of edge-tapers and G/T for most of the bands, although modifications are required to further improve the response, specifically to have appropriate taper at the edge of the shaped reflector so that most of the offered collecting area can be utilized. The dissimilarity between the return-loss values for the two polarizations towards the high frequencies (1197 and 1420 MHz; Figure 4.3), and generally low sensitivity at higher frequencies is probably caused by phase-mismatch between the corresponding pairs of dipoles. Overall, the tests conducted with the second feed-design indicate that it is a potential candidate for a multi-band feed.

In the present forms of the two designs we have investigated, the second design is closer to the desired multi-band feed with controllable spectral responses. Appropriate improvements and optimization of the parameters using software and field-experiments would make it evenly sensitive in all the desired bands. However, given the large number of electrical connections inherent to this design, further mechanical design considerations would be needed to make it more sturdy and further suitable to use at the focus of a large aperture. The first design, although mechanically sturdy, would require more basic improvement in its electrical design before it becomes usable as a multi-band feed.

4.3 Description of the MBR system in its present form¹⁰

The overall block diagram of the MBR system, in its present form, is shown in Figure 4.7. The signal path begins with a dual linear polarization multi-band feed sensitive to 10 discrete bands within a spectral span of 100–1600 MHz, followed by appropriate pre-amplification, filtering, up-conversion, transmission over the optical fiber, down-conversion, splitting in to bands of interest, superheterodyning to intermediate frequency (IF), digitization and recording. Below we briefly describe various parts of the MBR system along this signal path.

¹⁰The present form of the MBR system is due to significant efforts from a large number of people. Author's contribution lies in designing the system, a design-study of the multi-band feeds (discussed in previous section), participation in various tests of the system carried out in the lab, at the Gauribidanur field station and those using one of the GMRT dishes, and analysis of data obtained from the observations using the GBT (presented in the next Chapter).

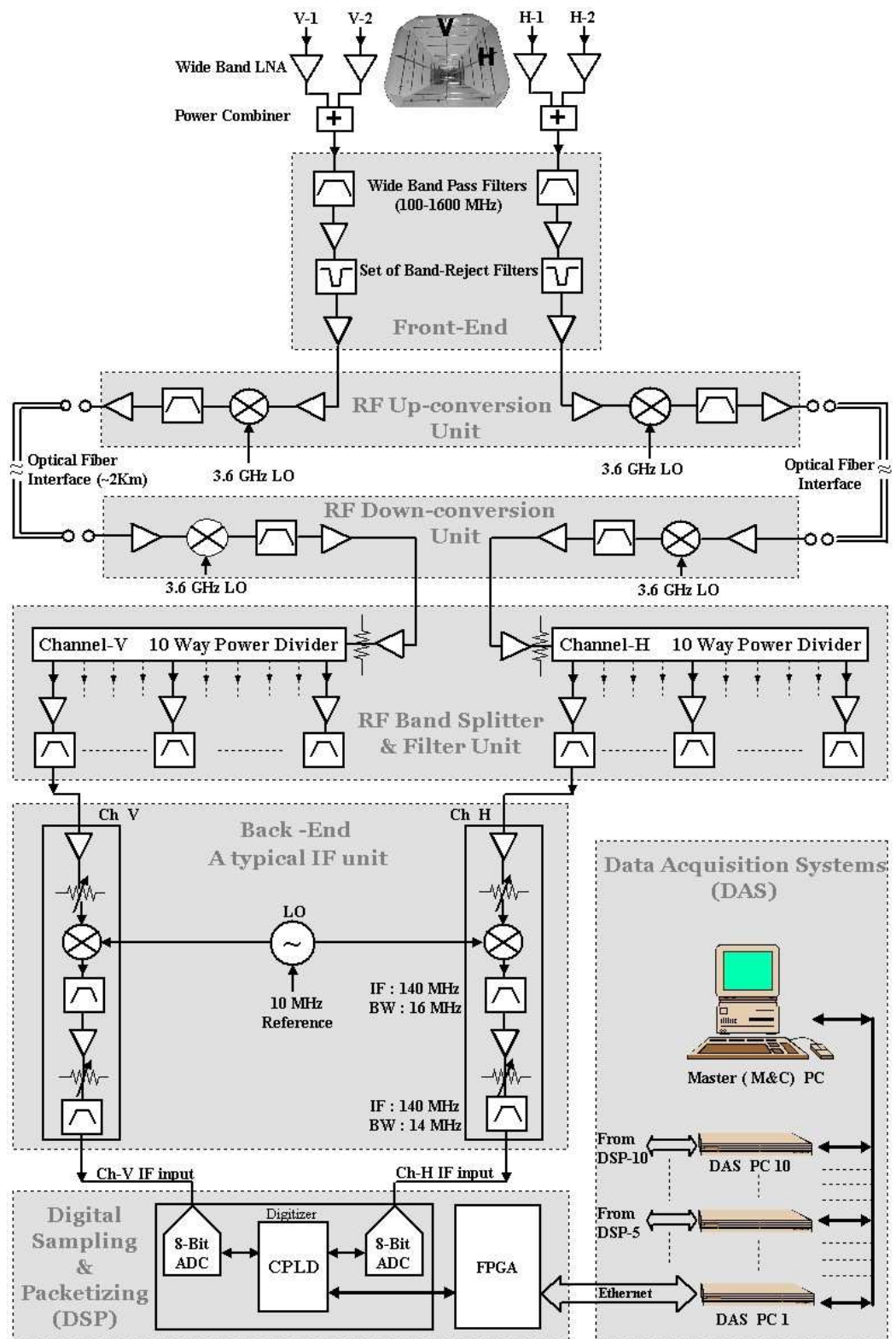


Figure 4.7: Overall block diagram of the MBR.

4.3.1 Multi-band feed

The final design of the multi-band feed consists of log periodic dipole-arrays arranged in pairs at 45° about the symmetry axis for each one of the two linear polarizations, similar to that in the first design described in the previous section. However, to avoid any radiation from the feed-line itself, the pair of aluminium square rods forming the feed-line are arranged in a plane perpendicular to the plane of dipoles, and the feed-line past the longest wavelength dipole is terminated with a stub of optimum length. Also, the dipole arrays in this design consists of an extra shorter dipole past the highest frequency resonant dipole. The basic conical arrangement of the elements, carried forward from the Eleven Feed, ensures that the phase center remains at the apex of the cone in the reflector plane independent of frequency. Also, as mentioned earlier, the in-phase combination of the two dipole arrays, at angles $\pm 45^\circ$ about the feed axis and corresponding to a given linear polarization, provides a good match between the E and H plane beams, necessary to illuminate circular apertures uniformly. The edge taper inferred from the beam-width measurements is in the range -15 dB to -20 dB. The feed cross-polarization is found to be at the level of -20 dB.

4.3.2 RF front-end

Each of two dipole-array outputs corresponding to a linear polarization is first amplified separately and then the two are combined in phase. A wide-band (≤ 2 GHz) LNA with a typical gain of around 20 dB and noise-figure less than 1.3 dB over the band of interest is used to amplify the signals. The pre-amplified signals, after the respective pairs are combined, provide dual orthogonal polarization outputs that are passed through a band limiting filter (100–1600 MHz). After further nominal amplification, the bands associated with known strong RFI signals (e.g., FM radio signals, TV transmission & mobile communication and those particular to the geographical location of the system; presently GBT) within our primary band are rejected using a cascade of home-made band-reject filters. At this point, since the primary contaminants are removed, a larger amplification is possible and is indeed needed to compensate (in anticipation) for the transmission loss in the cables carrying the signals from feed location to the receiver room. The modules in the receiver room prepare the signal for subsequent transmission to the equipment room via the existing optical fiber system at GBT. These modules upconvert the RF band of 100–1600 MHz to 2000–3500 MHz, using a local oscillator (LO) of 3.6 GHz. Noting that the band is flipped in this translation, appropriate length RF cable is introduced in the path (in order to use its frequency dependent attenuation characteristics) to at least partly compensate for the effect of gain-slopes introduced in the earlier stages. In the equipment room, the received band is downconverted back to the original RF band of 100–1600 MHz, using an LO again of 3.6 GHz.

Table 4.2: RF Filter Specifications

S.No.	Center Frequency (MHz)	Band-width (MHz)
1	119	20
2	172	21
3	232	37
4	330	38
5	425	46
6	629	59
7	730	62
8	825	82
9	1200	112
10	1450	104

4.3.3 Sub-band receiver chains

The wide-band RF signal, for each polarization channel, received in the equipment room is split into 10 fixed sub-bands after adequate amplification in anticipation of the power-divider losses. The bandwidths of the filters separating the different bands vary typically between 20 to 120 MHz, decided based on the RFI situation. The details of the central radio frequency values and the corresponding bandwidths of the 10 RF sub-bands are given in Table 4.2. The chosen bands provide nearly log-periodic sampling within the wide-band.

The 10 pairs of signals, thus obtained, are processed through very similar high gain chains, each consisting of an amplifier-attenuator combination for RF, a mixer followed by a filter, an amplifier-attenuator combination and another band-defining filter for IF, in that sequence. The LO frequency can be selected in steps of 1 MHz, within a range large enough to tune in to any region of the respective RF sub-bands. Care is taken in choice of the IF frequency to ensure that the IF as well as any image band falls outside the respective RF sub-band. Thus, the IF center frequency for most of the chains is 140 MHz, while it is 70 MHz for the two lowest RF bands (below 200 MHz). The IF-filters, each of 16 MHz bandwidth, provide a sharp roll-off characteristic and good rejection outside the IF band. The second of the IF-filters is necessary to suppress the out-of-band noise-floor contributed by the electronics following the first of the IF-filters. The independent attenuators in the RF and IF sections, which are computer controlled and provide attenuation within 0 to 31 dB in steps of 0.5 dB, are used to adjust the signal level to ensure operation in the linear regime of the chain. The net amplification in the signal path is arranged to be typically in excess of 100 dB so as to provide a suitable level of IF input to the analog-to-digital converter (ADC).

The IF signals for the two polarizations corresponding to a given sub-band are digitized directly using harmonic sampling. The sampling clock frequency used for digitization is 33 (31.25) MHz for IF bands at 140 (70) MHz. At the start of each acquisition, the clocks are synchronized

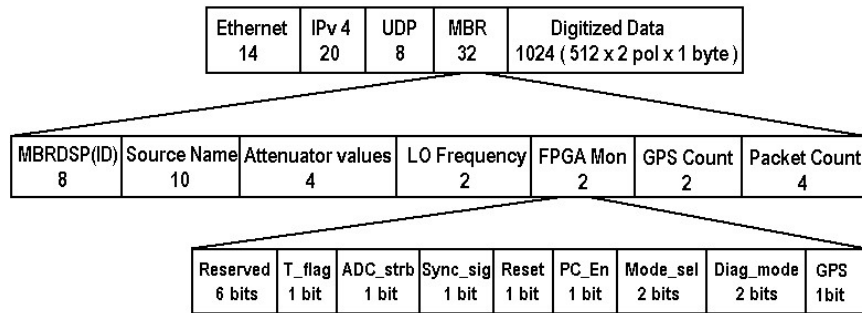


Figure 4.8: Ethernet data packet structure (the numbers shown in the first two rows are in terms of bytes, as opposed to bits in the third row).

with respect to 1 PPS signal generated from GPS-disciplined rubidium standard. The dual channel 8-bit samples along with strobe are time multiplexed and passed to the following module.

The digital back-end is realized using a Xilinx-ML506 evaluation board consisting of a Virtex-5 FPGA (Field Programmable Gate Array), and a rack-mountable PC. The designed functionality in the FPGA includes generation of both the sampling clock (66/62.5 MHz, used by ADC) and a 100 MHz clock used for reading the ADC data buffered through a FIFO (First In First Out). These programmable clocks are generated from an input (common) reference clock at 10 MHz. A GPS-disciplined rubidium-based 1 PPS input to the FPGA is used for both, synchronization at the start of the acquisition as well as for its time-stamping. Several pieces of information relevant to receiver settings and acquisition details (sent from the control software on the PC) are decoded, using a separate section of the firmware, before their inclusion in the packet header. The FPGA logic is designed to transmit the data and header information in packet form, using the user datagram protocol (UDP). Each data packet consists of 42 bytes of protocol header (Ethernet, IP and UDP headers), 32 bytes of MBR header (which contains the identity of the receiver, status information like mode of operation, GPS counter, and packet counter), and 1024 bytes of digitized data (dual-polarization, interleaved), as shown in Figure 4.8. Any change made in the system settings is reflected instantaneously in the headers associated with the acquired data (i.e., in the data-packet immediately following the change).

4.3.4 Monitoring and control software

The monitoring and control of the MBR as well as data acquisition are handled by a specially developed software suite. The 10 rack-mountable PCs, referred to as data acquisition subsystems (DAS), interconnected through a GbE-switch and coordinated by a master monitoring-and-control (M&C) PC, together form a part of the digital back-end, and provide a platform on which the relevant codes are executed.

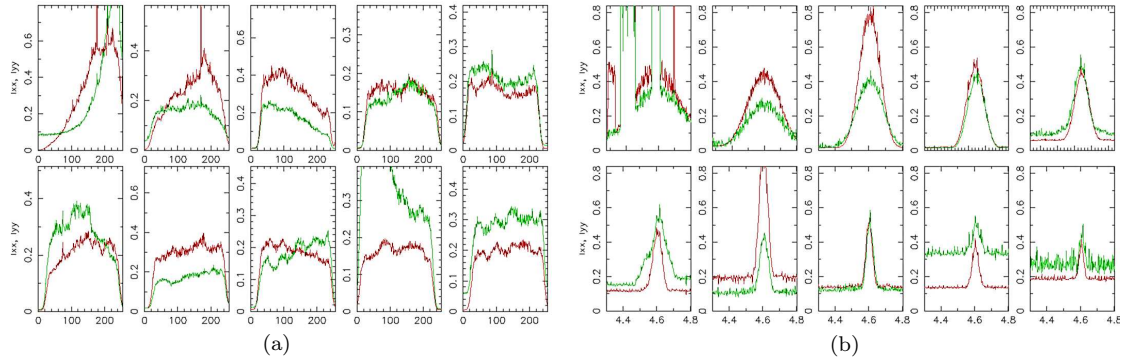


Figure 4.9: A snapshot of spectra as well as total power time-sequences being monitored in quasi-real-time, simultaneously in the 10 frequency bands, is shown here. Panel (b) shows total power scan-data of slewing across the bright source Cas-A, while panel (a) shows the spectra corresponding to the last averaged samples of the time-sequences shown in panel (b). The two curves in each of the sub-panels correspond to the two orthogonal polarizations. Each one of the spectra consists of 256 channels across 16 MHz of bandwidth, and the total extent of the horizontal axes shown in panel (b) corresponds to about half a minute.

The command-based control facilitates (a) setting of RF/IF attenuation and LO frequency relevant to the analog section, and (b) GPS synchronization, specifying bit-length/sample, duration and mode of acquisition, etc. for the digital back-end, along with initiation and termination of data acquisition. When triggered, instances of the data-acquisition program run on the DAS machines, each recording packeted data (received through a GbE link from the digital back-end) to the local disk at full rate, as well as sending ‘sniff-mode’ data at a much reduced rate (typically, 1 out of every 1000 packets) to the M&C machine for monitoring and recording for subsequent processing.

Checking for the expected pattern in the packet counter values, available in the headers of packets received on the M&C machine, serves as a quick diagnostic of acquisition on the respective DAS machines. Processing of these sniffed data is performed by a separate software and quasi-real-time spectra (in full Stokes), as well as total power time-sequences, can be monitored (see an example in Figure 4.9). This software also facilitates estimation and automatic adjustment of the gains of individual receiver chains to equalize the output power levels, a tool often used before the start of acquisition. Spectral scans can also be performed, by stepping through LO settings, to assess system gain and RFI occupancy across the accessible spectral span, for all chains simultaneously (see an example spectral scan in Figure 4.10).

For completeness, detailed block diagrams of various key sections of the hardware, and details of the software architecture, along with the usage of available commands, are provided in Appendix B.

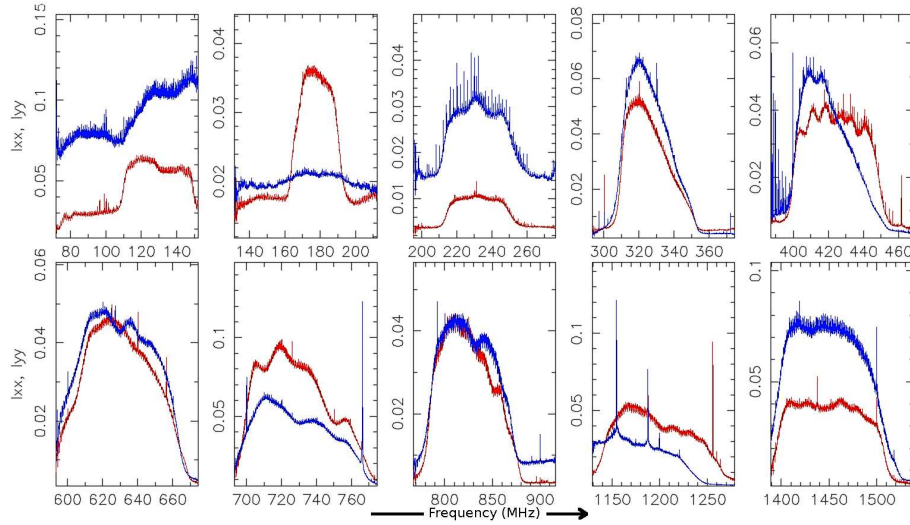


Figure 4.10: An example test scan performed through the accessible spectral span, simultaneously for all the chains, to check performance of the respective filters. The malfunctioning of two filters (in the top left panels, for one of the polarizations) is evident.

4.3.5 Tests and performance

After successful intensive laboratory tests, performance of the MBR system was assessed through preliminary observations, wherein the broad beam of the multi-band feed was slewed across bright astronomical sources. These tests were conducted at the RRI field station — Gauribidanur observatory — which provided a relatively RFI free environment. To test the system including its use with a shaped reflector, the earlier-version of the feed was installed at the prime focus of one of the GMRT dishes. We discussed some of these tests and their results in Section 4.2. These tests provided valuable feedback which prompted improvements in the feed design and in the filtering strategy in the front-end.

After appropriate revisions, the system was moved to Green Bank in May, 2009. After the system was fully installed, test observations were conducted on a few bright continuum sources. These resulted in measurements of the beam patterns as well as helped in deciding the optimum location of the feed based on a focus scan. Attenuation/gain adjustments necessary to operate within linear regime of the optical fiber system at GBT were incorporated, and using spectral scans, regions of better sensitivity were identified for each of the bands. Slew-scans across the bright radio source Cas-A (as shown in Figure 4.9(b), obtained simultaneously in all the 10 bands) were used to estimate the beam-widths (full widths at half power) corresponding to the two polarizations. These estimates are shown as a function of wavelength in Figure 4.11. As desired, the illumination of the GBT dish by the multi-band feed appears uniform across frequency (reflected by the goodness of the

linear fit). If interpreted assuming Gaussian illumination, the illumination efficiency is about 75%. Given possible differences in the E and H plane beams, and the different diameters of the GBT dish in the orthogonal directions (i.e., 100 and 110 meters), the implied edge-taper would be in the range -15 dB to -20 dB.

We have used the slew-scans across Cas-A also to estimate the cross-polarization of the system (which includes the feed as well as the receiver system). We use the quantity $M_{CP} \equiv \sqrt{(U^2 + V^2)}/I - \sqrt{2/(bw \times \tau)}$, at the time when the source is positioned at the telescope beam center, as a measure of the cross-talk between the two orthogonal polarizations. Note that I, Q, U and V are Stokes parameters, and the second term corrects for the statistical bias that is expected to be acquired by the first term. Here we have made two reasonable assumptions: (1) the system temperature is nearly equal to the source temperature (Cas-A is a bright source), and (2) Cas-A is an unpolarized source. The above measure suggests the cross-polarization for the first 8 (lower frequency) bands to be in the range -15 to -20 dB. For the 1200 and 1450 MHz bands, the corresponding measures are -10 dB and -8 dB, respectively. Note that the above estimates are made by first computing M_{CP} for each of the frequency channels and then averaging over the individual frequency bands. Computing M_{CP} directly from band-averaged Stokes parameters generally underestimates the cross-talk due to presence of linear/non-linear phase gradients (across the band) of instrumental origin¹¹.

Focus scans taken on strong continuum sources during the commissioning tests indicate the feed phase center to be independent of frequency. Although the feed performance is as desired in these aspects, we find significant loss of sensitivity at the higher frequency bands in general, and at the 1200 and 1450 MHz bands in particular (this also reflects in the slew-scans presented in Figure 4.9(b)).

Implicit in our feed design is the requirement that the two dipole arrays corresponding to a given linear polarization are phased correctly, particularly at the frequencies of interest. This requires matching of spectral responses between the two arrays, and any mismatch in them would cause improper phasing (since phase may vary rapidly about the respective resonant frequencies), and consequently significant de-phasing across the primary reflector that the feed illuminates. In practice, the desired match is difficult to ensure at higher frequencies where small differences in the mechanical structure and feed-point connections can cause noticeable mismatch. Such a mismatch, if it exists, would manifest in distortion of the resultant beam shape. Except in one of the bands (i.e., at 630 MHz, and in one of the polarizations, as seen in second row's first subpanel of Figure 4.9(b)), such distortion is not apparent, indicating reasonable match within the array pair in all other bands,

¹¹In our case, the cross-polarization estimated using band-averaged Stokes parameters turns out to be in -30 to -40 dB range. We find mostly non-linear gradients in the phase ($\tan^{-1}(V/U)$) that result in this under estimation of the cross-talk.

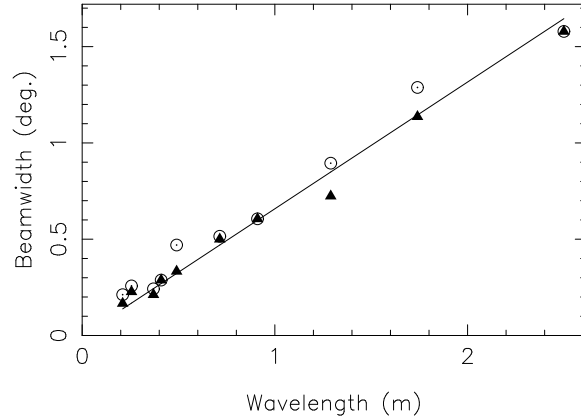


Figure 4.11: Estimated beam-widths from Cas-A scans are examined for linear dependence on wavelength (corresponding to the center frequencies listed in Table 4.2). The circles and triangles correspond to the estimates for the beams associated with the orthogonal linear polarizations. The solid line indicates the best-fit linear trend modeling the wavelength dependence of the observed beam-widths.

including those at higher frequencies.

A closer look at the beamwidth estimates reveals that they deviate significantly from the mean trend at the two shortest wavelengths (Figure 4.11), possibly implying the illuminated area to be effectively smaller by a factor of about two at these wavelengths. Another potential cause for the loss in sensitivity is related to S/N in different bands viewed at the stage of optical fiber transmission. Spectral dependence of the amplifier gains and cable losses together causes significant gradient in the signal level across our wide band, although we have tried to reduce it as much as possible. Due to constraints on the total RF power level to be input to the fiber transmission unit (after allowing for due headroom for RFI), the contrast in spectral density of our signal to that of the transmitter noise gets seriously compromised in bands where signal level is relatively low (resulting from gain slopes). Improvement in sensitivity at the higher bands would necessarily require addressing both these issues, with suitable modifications in the feed design as well as employing multiple fibers to carry different sections (2 to 3) of the wide band separately to avoid degradation of S/N. While these are being pursued, efforts are also going on to miniaturize the whole receiver, significantly reducing its physical size for ease of portability.

For completeness, we also mention infrequent but noticeable occurrences of data-slips, caused by occasional slowness in capturing of the high-rate stream of packets to the disk, in the present data. This issue has now been resolved by using a software tool Gulp (Satten, 2008) which provides a significantly larger buffer between packet-capturing from the ethernet and disk-writing, enabling lossless capture of packets at high rates.

4.4 Summary

In this chapter, we have presented the design and development of a novel self-contained multi-band receiver which opens up a new powerful mode of simultaneous multi-frequency observations in 10 bands when used with a sufficiently large aperture. The raw voltage recording enables full flexibility in dynamic spectral resolutions, and also enables coherent dedispersion when needed. Although the development of the MBR is primarily motivated by the tomographic studies of pulsar polar emission regions and would aid probe of several aspects of pulsar emission at single-pulse resolution, the potential of simultaneous multi-frequency observations facilitated by such a system can not be overstated. In particular, while looking for fast transients, simultaneous view in multiple bands is of tremendous advantage in decisively discriminating the signals of astronomical origin from those due to RFI. While the enhancement in the formal sensitivity due to the increase in available bandwidth can be quantified trivially, the added advantage of being able to verify the consistency of a dispersed signature of any candidate event across such a wide band, though crucial, is not easily quantifiable. Apart from this, in many other multi-frequency single-dish studies where simultaneity of observations may not be crucial, usage of the MBR can help save telescope time, and the implicit compatibility in data spans, types and formats, etc., in multiple frequency bands would offer a desired ease in off-line data processing and comparisons. This capability would benefit in studying spectral evolution of the *average* properties of pulsars (e.g., pulse intensity and shapes in full Stokes), and propagation effects (including interstellar scattering/scintillation), as well as in several single-dish continuum studies (including polarization), in general. The MBR also offers a significant tunability in the center frequencies of each of the 16-MHz wide sub-bands separately, a feature advantageous particularly for surveys/studies of recombination lines. The design details of several components could be of relevance to on-going and future developments in radio astronomy instrumentation, for example, those related to the Square Kilometre Array (SKA) and Five hundred meter Aperture Spherical Telescope (FAST). The design and structure of the MBR is generic enough to enable its use at any suitably large single-aperture telescope.

Pulsar observations using the MBR:

Synoptic results

After successful laboratory tests as well as the field tests (including sensitive tests using large shaped reflector), about 20 hours of observations were carried out with the Green Bank Telescope using the MBR. These observations, each typically a few kilo-periods long, were carried out on a number of bright pulsars, along with short duration pointings at (or slews across) the bright continuum sources Cassiopeia-A (hereafter Cas-A), Cygnus-A and Crab as flux calibrators. In this chapter we present illustrative examples of type of data, as well as a few synoptic results, using the simultaneous multi-frequency GBT observations of the well known bright pulsars B0329+54 and B0809+74, obtained with this MBR system.

5.1 Synchronization and data quality

As described in the previous chapter, instances of data-acquisition program can be run simultaneously on each of the DAS machines by sending appropriate command from the M&C PC. However, before recording of the packeted data to the respective local disks starts, the time on each of the DASs is synchronized with that on the M&C PC. This preliminary synchronization avoids large offsets in the time-sequences recorded in different bands. The GPS counter value noted in the MBR header of each of the recorded packets is used to achieve finer synchronization. This counter denotes the number of seconds since the local mid-night, and is incremented in sync with the 1 PPS input (from GPS) to the FPGA. The packet containing increment to a common GPS counter value in each of the recorded time-sequences is located and used for synchronizing. The synchronization accuracy achieved using this method is nominally limited by the sampling time ($\sim 16 \mu s$), but

adequate for many studies, including the proposed tomographic study of the pulsar magnetosphere. It is to be emphasized here that further accuracy in synchronization, if required, can be achieved by using the full time-sequences of GPS counter values (instead of using just the first increment to a common value).

To illustrate the quality of data obtained, raw Stokes-I dynamic spectra for nine frequency bands¹, across a span of 2 seconds, are shown in Figure 5.1. These dynamic spectra, observed in the direction of the bright pulsar B0329+54, have been time-synchronized using the method explained above. Further, the data across various bands have been shifted, removing the relative dispersion delays between the respective bands (referenced to respective center frequencies). The faint slanted and curved streaks within the bands highlight the single dispersed pulses. As expected, the slope of the streaks becomes shallow as we go to lower frequency bands with steep increase in the dispersion delays across the respective bands. The first band (centered at 117 MHz) is severely contaminated by strong wide-band (e.g., white patch between ~ 24.9 and 25 s) as well as narrow-band RFI. The RFI contamination in this band was generally found to be severe.

5.2 Spectral evolution of average properties of the bright pulsar B0329+54

In studying spectral evolution of the average properties of pulsars, e.g., pulse intensity and shapes in full Stokes, simultaneity of observations is not crucial. However, usage of the MBR can help save telescope time, and the implicit compatibility in data spans, types, and formats, in multiple frequency bands offers a desired ease in off-line data processing and comparisons. In this section, we illustrate these using our B0329+54 observation, and present synoptic results demonstrating the spectral evolution of its average total intensity properties.

5.2.1 Analysis procedure

The raw voltage time sequence corresponding to each of the 9 frequency bands and 2 linear polarization channels (hereafter X and Y channels), was Fourier transformed in blocks of 512 samples², translating to complex dynamic spectrum with 256 spectral channels. The dynamic spectra corresponding to the X and Y channels were auto- and cross-correlated to produce dynamic spectra

¹The 10th band data were unavailable due to an unfortunate computer crash.

²Each packet of data consists of 512 samples from each of the two polarization channels. Thus, processing in blocks of 512 samples proved to be convenient in Fourier transforming as well as in taking care of data slips. Also, the choice of 256 channels ensured that the dispersion smearing within the channel width, even at the lowest frequency band, is smaller than our final temporal resolution.

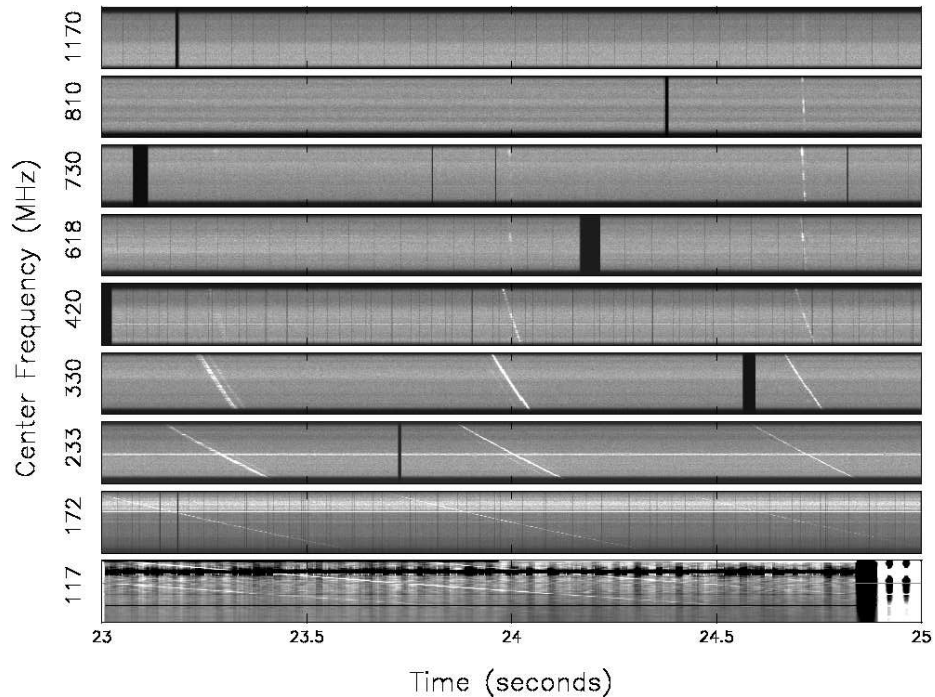


Figure 5.1: Dynamic spectra for each of the nine bands (stacked together) from B0329+54 observation, across a 2 seconds span, are shown here. In these gray-scale coded images, lighter colors correspond to higher intensity values. The randomly distributed dark vertical lines across various bands are due to data slips mentioned in the previous chapter.

for each of the four parameters: intensities³ I_X , I_Y , Stokes-U and Stokes-V. Further, appropriate number of such successive raw spectra were averaged to achieve a final temporal resolution of ~ 0.5 ms.

The filter-bank format data obtained as above, for each of the four parameters, were dedispersed and folded over the pulsar period to produce dedispersed folded dynamic spectra. The dispersion delays across various bands were corrected with respect to a common reference frequency (100 MHz). Note that the exact value of the dispersion measure (DM), used to dedisperse the data, determines the dispersion delays to be corrected between observations at different frequencies. Hence, the alignment of average profiles, specially at low frequencies, depends critically on the accuracy with which the DM is known. For a given bandwidth, sampling time and signal-to-noise ratio (S/N), the accuracy with which DM can be estimated is inversely proportional to cube of the center

³Stokes-I = $I_X + I_Y$, and Stokes-Q = $I_X - I_Y$

frequency. Hence, we used the folded dynamic spectra at the 172 MHz band⁴ to estimate the DM to be 26.754 ± 0.004 pc/cc. The uncertainty in the above estimated DM implies a corresponding uncertainty in the alignment of average profiles, at the lowest and highest frequency bands, to be about 1.2 milliseconds.

Since the present study is concentrated on the spectral evolution of only Stokes-I, we only flux calibrate the data using the scans across the bright continuum source Cas-A (see Figure 4.9(b) in the previous chapter). For each of the 10 bands and two polarization channels, the slew scan across Cas-A was fitted with a Gaussian function to estimate the peak deflection, its position, and the off-source contribution. The observed intensities were averaged (to increase the S/N), within ± 1 standard deviation around the peak, and the associated average spectra were used to estimate the system gain in each of the X and Y channels as a function of frequency. A polyharmonic function — a combination of a polynomial and an harmonic function — was fitted to this deduced gain pattern. Generally, a 3rd order polynomial in combination with 2 orders in harmonic function provided reasonable fits. Since the S/N towards the edges of the band decreases because of the filter roll-off, 10% of the spectral channels on either side of the band were excluded while fitting these functions. For the nine bands, for which pulsar data are available, the deduced gain patterns, along with the fitted smooth functions, are shown in Figure 5.2.

The dedispersed and period-folded dynamic-spectra were gain (and flux) calibrated using the above fitted smooth gain patterns. In addition to 10% of the spectral channels on both sides of the band, the channels identified as contaminated by RFI were also rejected while preparing the gain-calibrated band-averaged profiles for each of the bands. Figure 5.3 presents the gain calibrated average profiles of total intensity, linearly polarized intensity, circularly polarized intensity and position angle at various frequency bands. Since the profiles are not polarization/leakage calibrated, the profile shapes in the last three sets may deviate significantly from the true profiles. The total intensity profiles have been normalized with the respective peak-values, to clearly show the spectral evolution of the weaker conal components. In the following subsections, we study the spectral evolution of the total intensity average pulse profile in detail.

5.2.2 Spectral evolution of the emission altitude

To estimate the altitude of the region producing the emission at a given observing frequency, generally one of the two different approaches are followed: the “geometric” and the “relativistic” method. The geometric method takes into account the viewing geometry, and the emission altitudes

⁴The data at the lowest frequency band, i.e., at 117 MHz, could have provided better accuracy, but the severe RFI contamination made this band unsuitable for DM estimation. The alignment of flux calibrated average profiles across various frequency bands was found to be consistent with the DM estimated using the 172 MHz band.

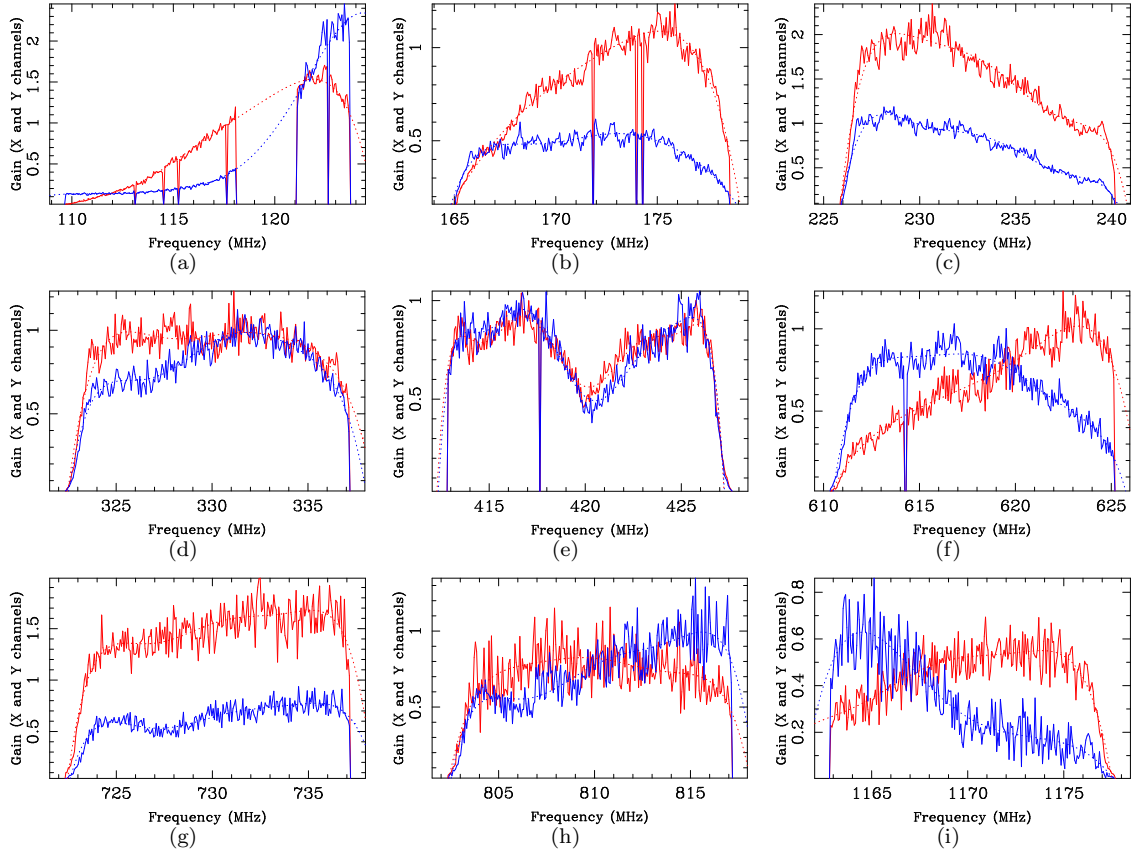


Figure 5.2: The system gain for each of the two polarization channels, X and Y (red and blue colors), and nine frequency bands (center frequency increases from left to right, and then top to bottom) are shown here. The smooth dotted line curves represent the best fitted polyharmonic functions to the deduced gain patterns (solid line curves). The sharp dips in some of the deduced patterns correspond to the RFI contaminated frequency channels which were rejected in this processing. A broad dip at the center of the 420 MHz band is probably due to feed response.

are generally estimated using the profile width (Cordes, 1978; Phillips, 1992; Gil & Kijak, 1993), assuming that the radiation beam extends till the last open field lines which, in turn, correspond to the polar cap boundary. Since the observed emission may be confined well within the polar cap (due to intrinsic emission characteristics), the geometric method generally provides a lower limit on the emission altitudes. The relativistic method considers the effects of aberration and retardation on the average profile(s) of intensity and/or the position angle (PA). The shift of the average intensity or PA profile with respect to a fiducial point, or the relative shift between the two profiles is then used to estimate the emission altitudes (see, for example, Gangadhara & Gupta, 2001; Dyks *et al.*,

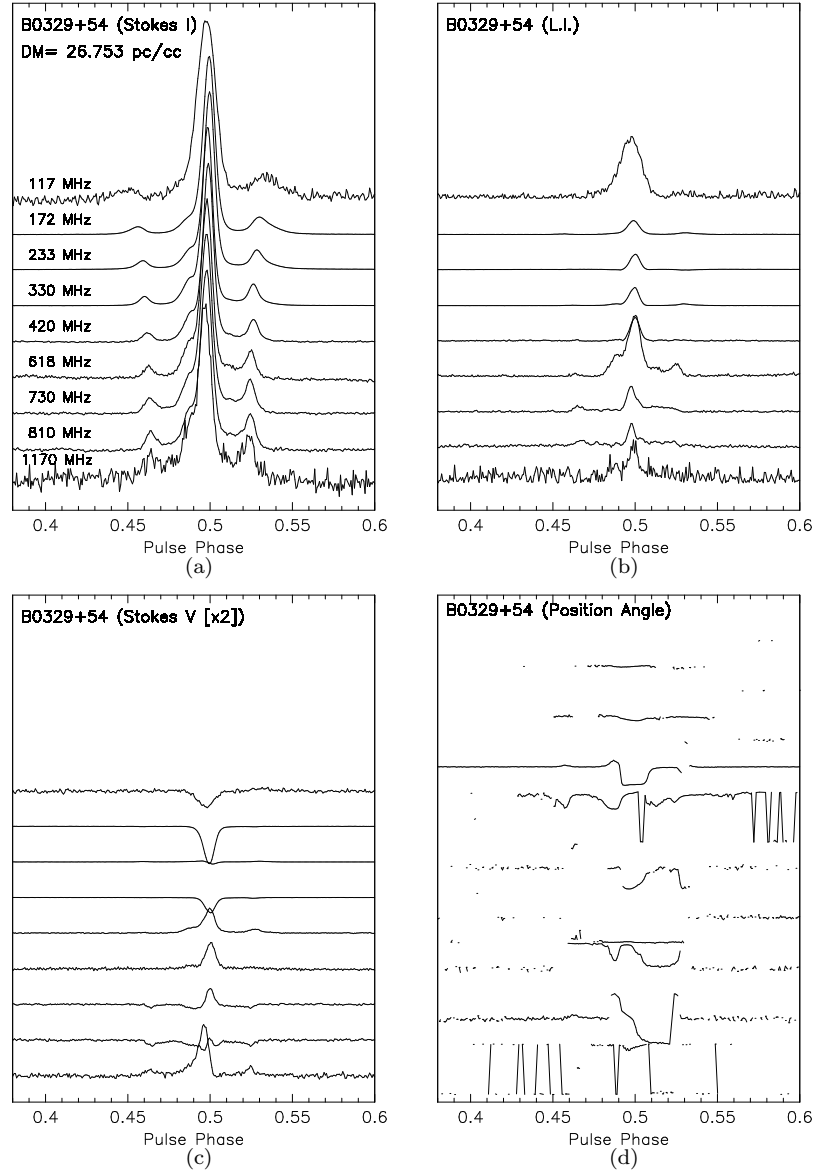


Figure 5.3: As marked in the panels, the average total intensity (Stokes-I), linearly polarized intensity (L.I.), circularly polarized intensity (Stokes-V), and position angle (PA) profiles of the bright pulsar B0329+54 obtained from simultaneous observations in the nine bands, after appropriate dedispersion and gain-calibration, are shown across various frequency bands in four different panels. For each of the bands, the three intensity profiles (Stokes-I, L.I. and Stokes-V profiles) are normalized by the respective peak of the Stokes-I profile, and the PA profile variations are shown in the range -90° to $+90^\circ$. Further, the actual Stokes-V amplitudes are half of what are shown here, and the position angles are displayed only for those longitudes where L.I. is $\geq 1\sigma$ above the off-pulse mean.

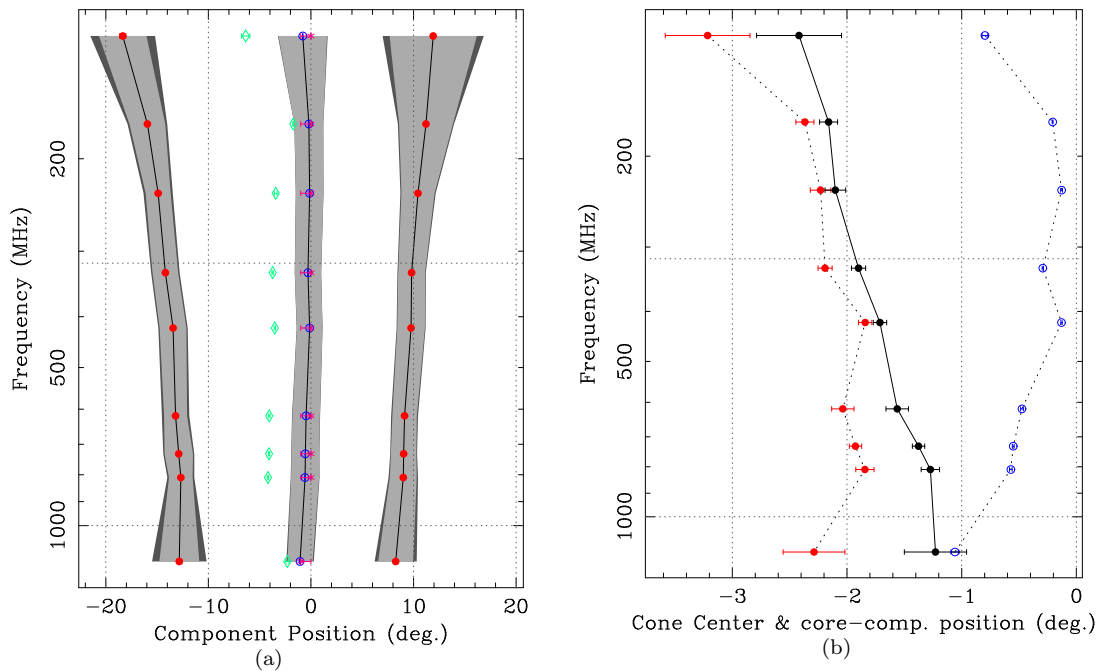


Figure 5.4: *Left*: A summary of the fitted parameters (component positions and widths) of the bright pulsar B0329+54 as a function of observation frequency is shown. The fitted positions of the components are marked by different symbols along with the associated fit-uncertainty (error-bars). For the two conal (the leading and trailing components, red filled circles) and the core component (blue open circles), the fitted component-widths are shown by the light-gray shades, while the dark-gray shades on the two sides represent the uncertainty in the fitted widths. Center positions of the fourth component, the one just before the core component, are marked by green diamonds. For the fifth component (a broad, low-amplitude component, magenta stars), the error-bars represent the restricted range instead of the associated uncertainty in the fitted position. *Right*: The cone-center, i.e., the center of the two outer conal components, and the core component position as a function of frequency are shown in red and blue symbols respectively. The black filled circles show the shift in the cone-center with respect to the core-component.

2004; Dyks, 2008).

To obtain the parameters necessary for estimating the emission heights using the above two methods, we characterize the separate emission components by modeling the average profiles as a sum of several individual Gaussian components. The apparent number of pulse components in the profile was used as the initial guess of the number of individual Gaussian components required to best fit the pulse profile. Although the average profiles seem to be consisting of 4 components, an additional broad, low peak-amplitude component was required at almost all the bands to achieve a

reasonably good fit⁵. A fit was considered acceptable when the fractional deviations, corresponding to the minimum reduced χ^2 , were less than or of the order of 10% – 20%, where the average profile has $S/N \gtrsim 5$. For most of the bands, the minimum reduced χ^2 values obtained are near unity. The observed and the fitted profiles, along with the fit residuals, are presented in Figure B.12. The separate emission components, modeled as individual Gaussian components, are also shown along with the observed average profiles in Figure B.11.

Figure 5.4(a) presents a summary of the fitted component positions and widths for the average profiles at nine frequency bands. Flaring of the conal radiation beam expected from the dipolar field (depicted by the separation between the two conal components) is apparent, especially towards the lower frequencies. Similar significant evolution of the component width is also apparent across frequency. However, for the present discussion we concentrate only on the quantities required for estimating the emission altitudes. Assuming the dipolar geometry, and following Phillips (1992), the emission altitude r_G is related to the the profile-width, w , at frequency ν by the equation:

$$r_G = \frac{4}{9} \kappa r_{LC} \theta_{\text{beam}}^2; \quad \sin^2 \left(\frac{\theta_{\text{beam}}}{2} \right) = \sin^2 \left(\frac{w}{4} \right) \sin \alpha \sin(\alpha + \beta) + \sin^2 \left(\frac{\beta}{2} \right) \quad (5.1)$$

where θ_{beam} is the half opening angle of the radiation beam, α is the magnetic inclination angle and β is the line-of-sight impact angle with the magnetic axis. Here, r_{LC} is the light cylinder radius, and the parameter κ accounts for the possibility that corotation of the magnetic field and plasma breaks down within a fraction of the light cylinder distance. Hence, κr_{LC} is the maximum corotation radius.

The profile width is generally estimated as the full width between 10% intensity levels in the pulse profile. However, such an estimation is more prone to be affected by sensitivity of the observations and possible differences in the component intensities. To minimize this effect, we use the fitted widths and positions of the two outer conal components to estimate the pulse longitudes at the outer edges of the average profile where the expected intensities would be 10% of the respective conal component peak values, and define the difference between these two longitudes as the profile width.

The emission altitudes, r_G , can be computed from Equation (5.1) using the above estimated profile widths, and the viewing geometry parameters ($\alpha = 32^\circ.1 \pm 3^\circ.0$, $\beta = -3^\circ.4 \pm 1^\circ.0$; Mitra & Rankin, 2002). However, these estimates would be uncertain by the multiplicative factor κ ($0 < \kappa \leq 1$). In Table 5.1, we have shown computed values of the quantity r_G/κ , i.e., the emission altitudes scaled by the unknown multiplicative factor, for each of the frequency bands. Note that the

⁵Gangadhara & Gupta (2001) have claimed to detect, by using their “window-threshold technique”, as much as 9 emission components for this pulsar. For the synoptic results being presented here, we would be concentrating only on the two strong outer conal components and the core component. Fitting the average profiles only with 5 components, including one of the inner conal component and a broad component, appears to be suitable for this purpose.

formal uncertainty, obtained by propagating the errors in various quantities, is primarily contributed by the large uncertainties in α and β estimates⁶.

The effects of aberration and propagation time delays, if measurable, provide an independent way (relativistic method) of estimating the emission altitude without requiring information about the viewing geometry. If the core component originates from an altitude very near to the star surface (as against the conal components which most likely originate from an higher altitude following the RFM), and if the cone emission is axially symmetric around the core emission in the reference frame corotating with the star, then the phase shift of the midpoint between the conal component maxima with respect to the core component is estimated to be:

$$\Delta\phi \approx \frac{2r_{\text{R}}}{R_{\text{lc}}} \quad (5.2)$$

where r_{R} is the conal emission altitude (estimated using the relativistic method; Dyks *et al.*, 2004). The estimated phase shift at each of the bands is presented in Figure 5.4(b), along with the cone centers and core component peak position as a function of frequency. The emission altitudes, r_{R} , estimated using these phase shifts and the above relationship, are also listed in Table 5.1.

The emission altitudes obtained by the geometric method, when compared to those computed using the relativistic method, seem to be underestimated⁷. As indicated earlier, the geometrical method assumes that the radio emission region fills the extent bounded by the last open field lines. However, a partially active polar cap would result in partial filling of the beam, and hence result in underestimation of the emission altitudes by a factor $\approx (W/w)^2$, where W is the true opening angle of the last open field lines. Inverse of this factor would provide an estimate of the fraction of the total polar cap region responsible for the observed emission. Last column of Table 5.1, denoted by δ_{PC} , presents these estimates, using the emission altitudes r_{G} and r_{R} , and assuming κ to be 1. A weighted mean value of δ_{PC} , by assuming inverse-square of the associated uncertainties as the respective weights, comes out to be 0.58 ± 0.04 . Hence, only about 60% of the polar cap region appears to be active, implying the field lines associated with the radio emission to be located up to about 0.75 of the polar cap radius, and not till the edge. These quick findings are consistent with the earlier inferences that the field lines *associated with the peaks* of the outer emission cone are located at about 0.6–0.7 of the distance to the edge of the polar cap (Dyks *et al.*, 2004; Gangadhara & Gupta, 2001).

Our estimates of the emission altitudes above are based on the assumption that the core

⁶The contributions of uncertainties in the α and β estimates to that in r_{G}/κ , are proportional to $\sin^2(w/4)$, causing the uncertainty in r_{G}/κ to increase with w , i.e., towards the lower frequencies.

⁷Note that the factor κ can have values between 1 and 0, and can not compensate for the apparent underestimation of r_{G} .

Table 5.1. Summary of estimated component positions and emission altitudes.

Frequency (MHz)	ϕ_l ($^\circ$)	ϕ_t ($^\circ$)	ϕ_c ($^\circ$)	w ($^\circ$)	r_G/κ (km)	$\Delta\phi$ ($^\circ$)	r_R (km)	δ_{PC}
116.69	-18.35 ± 0.30	11.92 ± 0.22	-0.80 ± 0.03	42.25 ± 1.18	576 ± 150	-2.42 ± 0.37	721 ± 110	0.80 ± 0.24
171.69	-15.95 ± 0.07	11.21 ± 0.04	-0.21 ± 0.00	35.13 ± 0.38	415 ± 73	-2.16 ± 0.08	644 ± 23	0.65 ± 0.12
232.75	-14.90 ± 0.08	10.44 ± 0.04	-0.13 ± 0.01	30.50 ± 0.38	327 ± 57	-2.10 ± 0.09	626 ± 27	0.52 ± 0.09
329.75	-14.20 ± 0.06	9.81 ± 0.03	-0.29 ± 0.01	28.67 ± 0.30	295 ± 48	-1.90 ± 0.06	566 ± 18	0.52 ± 0.09
420.25	-13.45 ± 0.05	9.76 ± 0.02	-0.13 ± 0.01	28.05 ± 0.27	285 ± 46	-1.71 ± 0.06	510 ± 17	0.56 ± 0.09
617.75	-13.20 ± 0.09	9.13 ± 0.04	-0.47 ± 0.01	26.54 ± 0.39	261 ± 45	-1.56 ± 0.10	465 ± 29	0.56 ± 0.10
729.75	-12.89 ± 0.05	9.04 ± 0.02	-0.55 ± 0.01	26.72 ± 0.28	263 ± 42	-1.38 ± 0.05	410 ± 16	0.64 ± 0.11
809.75	-12.69 ± 0.07	9.00 ± 0.04	-0.57 ± 0.01	26.17 ± 0.38	255 ± 44	-1.27 ± 0.08	379 ± 24	0.67 ± 0.12
1170.25	-12.84 ± 0.24	8.26 ± 0.11	-1.06 ± 0.04	27.74 ± 0.93	280 ± 73	-1.23 ± 0.27	366 ± 81	0.76 ± 0.26

Note. — ϕ_l , ϕ_t and ϕ_c are the estimated center/peak positions of the leading and trailing conal components, and the core component respectively. The profile width, w , is estimated following the procedure mentioned in text, and is equal to $(\phi_t - \phi_l) + 0.911 \times (w_t + w_l)$, where w_t and w_l are estimated widths of the trailing and leading conal components, respectively. $\Delta\phi$ is the shift of the center of the conal components $([\phi_l + \phi_t]/2)$ with respect to the core component position. δ_{PC} provides an estimate of the fraction of the total polar cap region responsible for the observed emission.

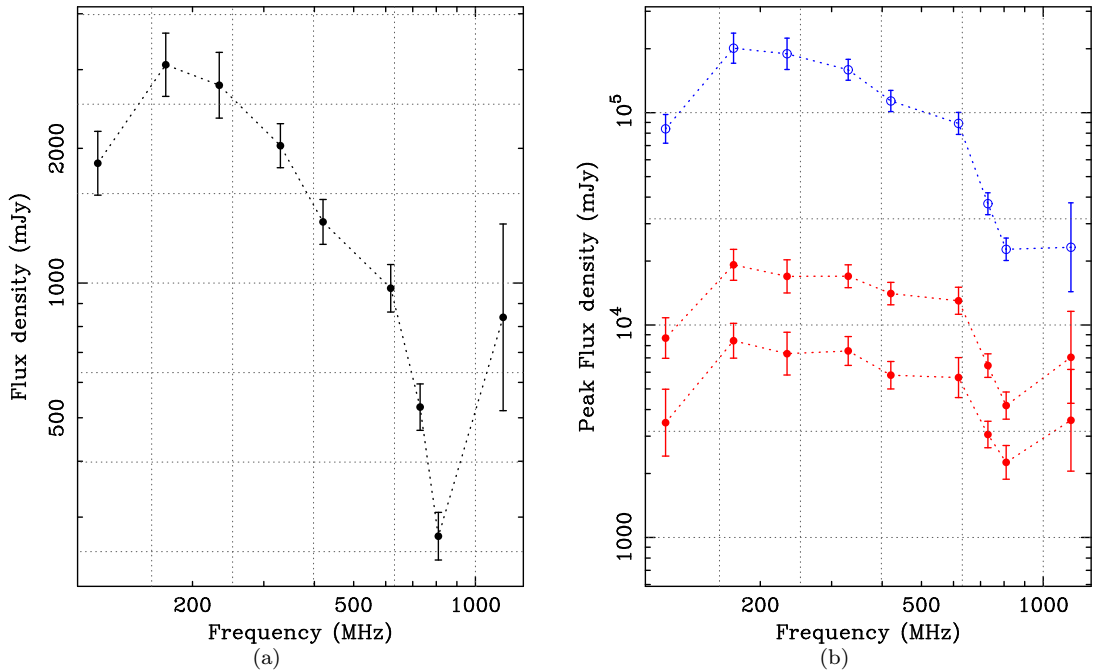


Figure 5.5: **Left:** Spectrum of the mean radio flux density from the pulsar B0329+54, using the measurements at 9 frequency bands of the MBR in the range 100–1200 MHz, is shown. A spectral turn-over at around 200 MHz is clearly visible. **Right:** Spectra of the conal (*red curves*) and core (*blue curve*) component peak radio flux density are displayed for the same frequency range.

emission originates very near to the star surface⁸. More realistic estimates could be obtained by measuring the shift of the center of conal component maxima with respect to the point-of-inflexion in the polarization position angle curve. The shift with respect to this new fiducial point, then, can be related to the emission altitude (Dyks, 2008, Relativistic Phase Shift method) by:

$$\Delta\phi (\equiv \phi_{\text{PA}} - \phi_{\text{profile}}) \approx \frac{4r_{\text{R}}}{R_{\text{lc}}} \quad (5.3)$$

Since this pulsar exhibits a fairly comparable strength of two orthogonal polarization modes, position angle density plots would need to be appealed to estimate the position angle inflexion-point, after the data are polarization calibrated, etc.

⁸Any possible misalignment in profiles across the wide band (e.g., due to usage of slightly incorrect DM) is irrelevant in computation of the emission altitudes, since the required parameter (w and $\Delta\phi$) measurements are band-specific.

5.2.3 The radio emission spectrum

Since the average profile data are already flux calibrated in units of the flux density of the bright continuum source Cas-A, the emission spectrum can be quickly estimated. It is now well known that the radio flux density of Cas-A has been decreasing. Vinyaikin (2007) estimated the frequency dependence of the secular rate of change in the flux density of Cas-A as

$$d_\nu(\% \text{ year}^{-1}) = (0.66 \pm 0.06) - (0.066 \pm 0.056) \log \nu[\text{GHz}] \quad (5.4)$$

The above frequency dependence was derived for the time interval 1980–2004. It seems fair to assume that the above secular rate of change in flux has not changed in a few years following the above interval, and we can use the same estimate for our Cas-A observation in 2009. Further, the absolute flux density of Cas-A as a function of frequency, following Baars *et al.* (1977), is given by the following spectral fit:

$$\log S_\nu^{\text{Cas-A}}[\text{Jy}] = a + b \log \nu[\text{MHz}] + c \log^2 \nu[\text{MHz}], \quad (5.5)$$

where the coefficients a , b and c are estimated to be slightly different for the frequencies below and above 300 MHz. Baars *et al.* (1977) provide the estimate for these coefficients in the higher frequency range for epoch 1980.0, and the complete spectrum for epoch 1965.0. Their estimates of the three coefficients for $\nu < 300$ MHz (epoch 1965.0), are 5.625 ± 0.021 , -0.634 ± 0.015 and -0.023 ± 0.001 , respectively. For the frequencies above 300 MHz (epoch 1980.0), only the coefficients a and b were required for a good fit to the observed spectrum, which were estimated to be 5.745 ± 0.025 and -0.770 ± 0.007 , respectively. Using these two sets of coefficients in Equation (5.5), and the frequency dependent rate of change in flux from Equation (5.4), we estimate the Cas-A flux densities at the center frequencies of all the bands, for our observation epoch. The Cas-A spectrum thus obtained is used to compute the mean flux density (averaged over the period) spectrum of the pulsar B0329+54 (see Figure 5.5(a)). A spectral turn-over at around 200 MHz is clearly seen, consistent with the turn-over frequency reported in literature (240 ± 15 MHz; Malofeev & Malov, 1980). For a quick comparison between the spectral behaviors of the core and conal emission, the spectra of the conal and the core component peak flux densities are also presented in Figure 5.5(b). Within the measurement uncertainties, the spectral behaviors of the two conal components are same, while the spectrum of the core emission appears to be steeper than that of the conal emission. However, before spectrum could be used for comparing the spectral behaviors of various components, or for other sensitive purposes, e.g., fitting the spectrum to estimate the turn-over frequency and the spectral indices on the two sides of this frequency, etc., we wish to note the following aspects relevant to the reliability of the estimated spectrum.

1. The possible impact of interstellar scintillation over the broad spectral range of our observations need to be assessed and corrected for. For the pulsar B0329+54, the decorrelation

bandwidth over this spectral range is expected to vary from about a few kHz to tens of MHz, and the modulation timescale from about a minute to tens of minutes (Kramer *et al.*, 2003). Given that the profile is computed by averaging over the observation duration (~ 1 hour), flux density variations due to diffractive scintillations are expected to average out, resulting estimates reflecting the intrinsic flux density values at lower frequencies. However, given the large decorrelation bandwidth and time-scales of scintillation, the estimates in the high frequency bands could still be affected by scintillation.

2. The apparent overestimation of the flux density in the 1170 MHz band is possibly caused by poor S/N observation of the corresponding Cas-A slew scan in this band, specially in one of the polarization channels, and hence a poor fit of the scan by a Gaussian function. This low sensitivity is reflected, to some extent, in the associated uncertainty.

Keeping these sources of uncertainty in mind, we estimate the spectral index in the range 230–620 MHz to be -1.1 ± 0.1 for the mean flux density, and -0.4 ± 0.2 , -0.3 ± 0.1 and -0.8 ± 0.1 for the two conal and the core components, respectively.

5.3 Tomography of the pulsar magnetosphere

From several pulsars observed to study drifting subpulses, we use our B0809+74 observation to illustrate construction of an emission region tomograph. This pulsar exhibits remarkably stable pattern of drifting subpulses across the pulse window (Vitkevich & Shitov, 1970; Page, 1973). As described in the earlier part of this thesis, given the viewing geometry and the emission pattern circulation period (P_4), such fluctuations in the single pulse sequence can be transformed to reconstruct the underlying carousel pattern of sub-beams in its rotating frame (Deshpande & Rankin, 1999, 2001). For the illustration below, we use data in the lowest 4 frequency bands, since the pulsar could not be detected in the other higher frequency bands (in our observations). We would like to emphasize that these lowest 4 frequency bands sample significant portion ($\gtrsim 50\%$) of the emission height range accessible with the MBR spectral coverage.

5.3.1 Subpulse modulation properties and the emission maps

As examples illustrating the raw data quality and subpulse drifting, small sections of the time-synchronized single pulse sequences of B0809+74 observed at the first four MBR frequency bands are shown in Figure 5.6. The data at the lowest frequency band, i.e., at the 117 MHz band, were severely contaminated by RFI. Apart from the several small time sections of data which were rejected due to the RFI, a significant fraction of the observed bandwidth was also found unusable, and had to be excluded while computing the average intensity time sequence. Nevertheless, the subpulse

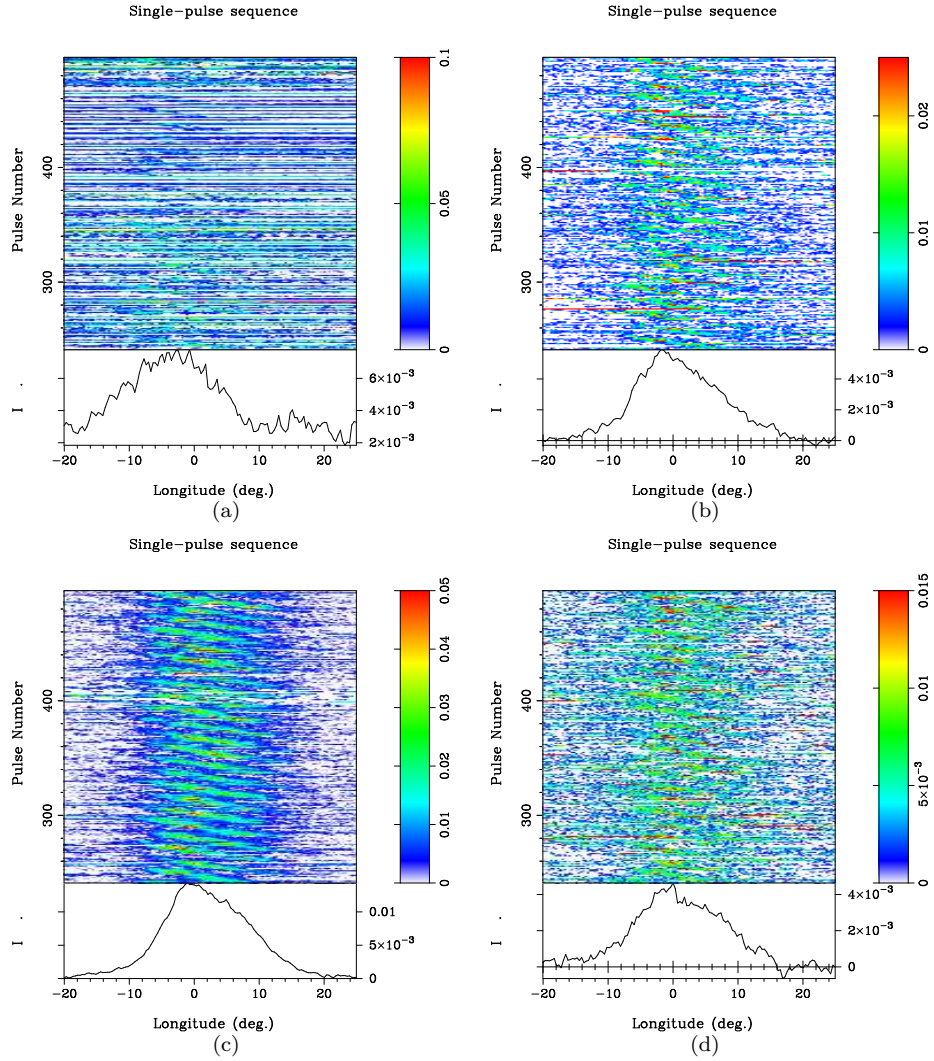


Figure 5.6: The 4 panels show small sections of the raw single pulse sequences (period-stacked and selected longitude range) of B0809+74 observed at the first 4 MBR frequency bands (117, 172, 233, and 330 MHz, for panels from left to right, top to bottom, respectively). For all the bands, the sequences are time-synchronized.

drifting bands are clearly visible in the next three spectral bands. For the following analysis, we use 2048-period long pulse sequences, time-synchronized across the bands.

Estimation of the circulation period might be possible directly, if an associated spectral signature (such as a low frequency fluctuation feature or as side-bands of a primary modulation feature) is detectable in the fluctuation spectrum. Alternatively, the time-period between passages of the consecutive sub-beams (i.e., interval between the subpulse drift bands; P_3) combined with

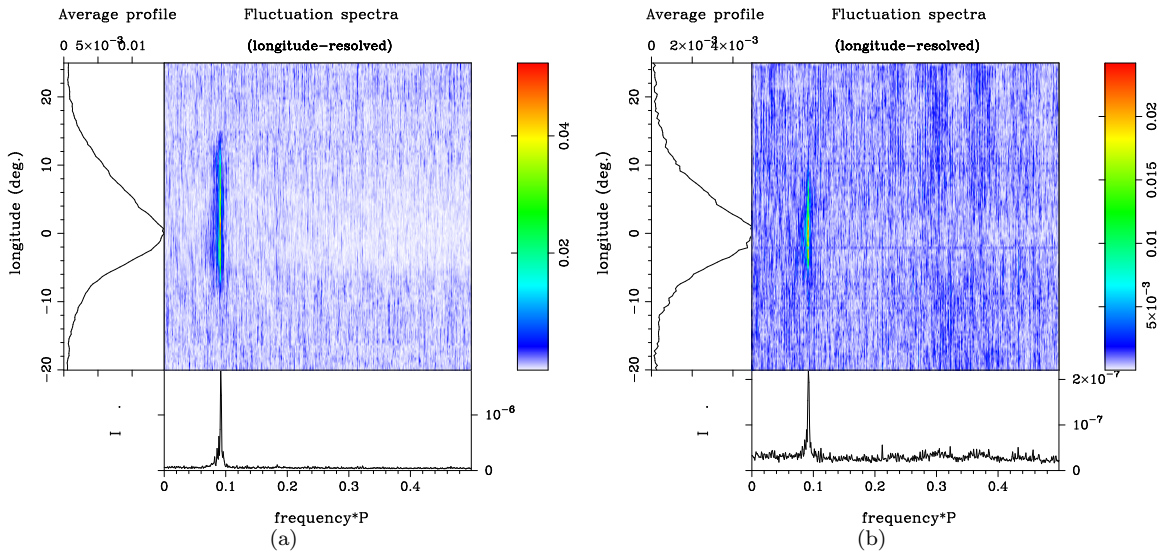


Figure 5.7: The central images in the *left* and *right* panels show the longitude resolved fluctuation spectra of B0809+74 at 233 and 330 MHz, respectively. The corresponding average profiles are shown in the side sub-panels, while the bottom sub-panels display the integral spectra.

their total number (N) could also be used to estimate P_4 ($= N.P_3$). In the present case, our fluctuation spectral analysis revealed a single high- Q feature in an otherwise featureless spectrum (see the bright feature in the longitude resolved fluctuation spectra at 233 and 330 MHz, shown in Figure 5.7). Position of this feature, at around 0.09 cycles/Period, was found to be consistent within the associated measurement uncertainties at the 172, 233 and 330 MHz bands. A similar estimate at the lowest frequency band could not be made due to inadequate S/N, caused by severe RFI contamination mentioned earlier. Our spectral analysis of the data at 233 MHz – the band with best S/N data among the four bands – provides an estimate of P_3 to be 10.8529 ± 0.0007 spin periods. Although, no direct signature of the circulation period is apparent in the fluctuation spectrum, the narrowness of the feature associated with P_3 argues strongly in favor of its integral relationship with P_4 , and also that the coherence in this drift sequence appears to be largely unaffected by ‘nulling’, if any. For this pulsar, Rankin *et al.* (2006b) suggest the number of sub-beams to be in the range 9–11. Using the geometrical parameters⁹ from Rankin *et al.* (2006a), and assuming a total of 9 sub-beams, the pulse sequences are cartographically transformed to map the emission pattern for each of the four sub-bands. These emission pattern maps are presented in Figure 5.8.

⁹Magnetic inclination angle $\alpha = 8.8^\circ$, and sight-line impact angle $\beta = 4.7^\circ$.

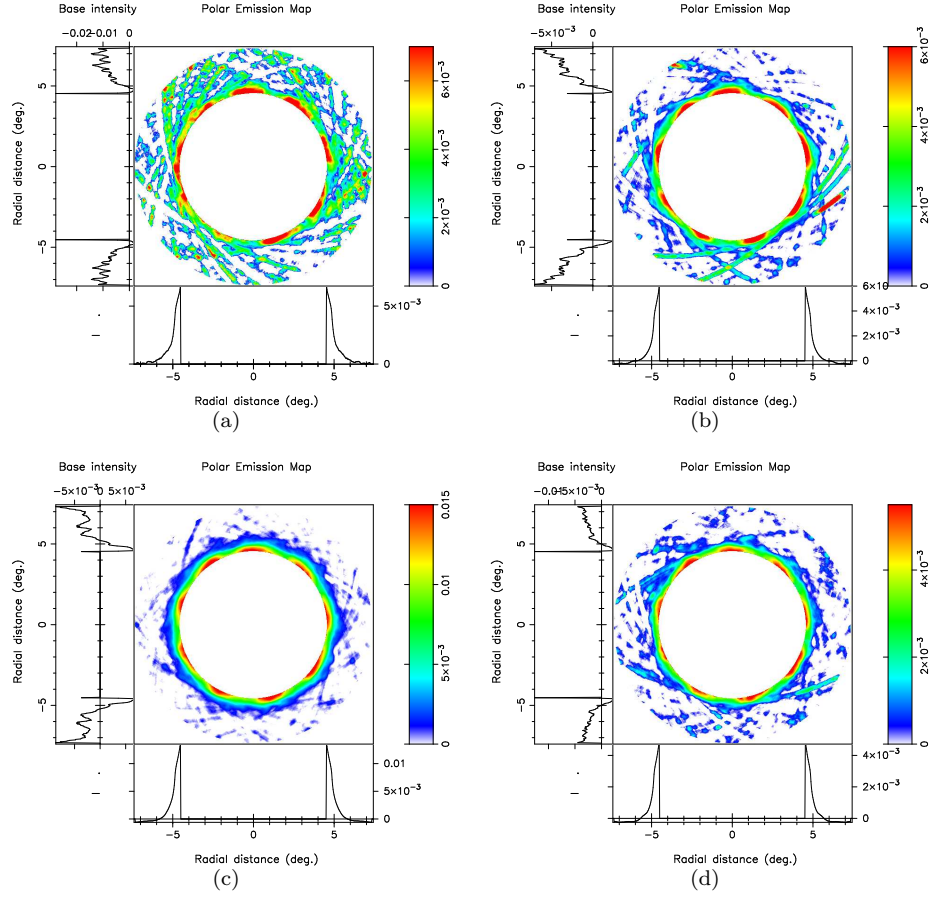


Figure 5.8: Cartographically mapped emission patterns of B0809+74 using the pulse sequences at the bands 117 MHz, 172 MHz, 233 MHz and 330 MHz are shown in (a), (b), (c), and (d) respectively. In each of the panels, the bottom sub-panel shows the average radial intensity, while the left sub-panel shows the minimum radial intensity.

5.3.2 A preliminary tomograph

While further details of analysis on this pulsar and the assumed carousel circulation period would be discussed elsewhere, here we present a preliminary tomograph of the polar emission region of this pulsar in Figure 5.9, by vertically stacking the underlying emission patterns mapped at the 4 lowest frequency bands. The relative locations and sizes of these patterns, although chosen conveniently, are nonetheless consistent with the essential qualitative trends of radius-to-frequency mapping and geometry of the emission cone. The overall similarity of the patterns across frequency, in terms of the number of sub-beams (the high intensity regions corresponding to the red color)

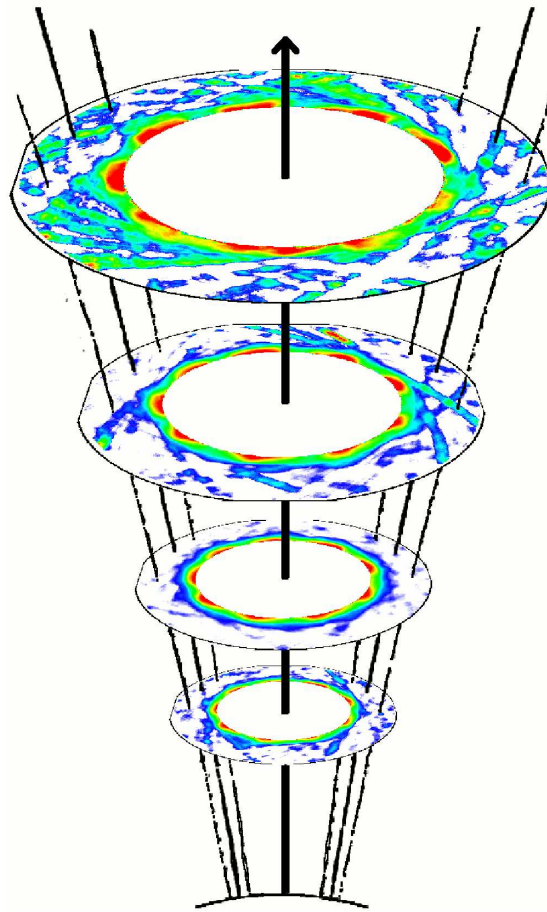


Figure 5.9: A preliminary tomograph of the polar emission region of B0809+74.

and their relative locations, is clearly evident. The partial sampling of the radial extent of the sub-beam is seen to improve systematically towards lower frequencies, corresponding to the expected broadening of the polar emission cone.

5.4 A multi-band search for fast transients

Explorations of the transient sky at radio wavelengths on a routine basis have started very recently. Transient events are generally classified into two categories: fast and slow. This primary distinction between the two types is driven by considerations of detection techniques as well as the underlying emission physics. The fast transients have timescales generally less than a few seconds (say 5 s), implying coherent emission processes. The slow transients are primarily outflows or explosive events (often incoherent synchrotron emission, occasionally thermal) with timescales

generally more than a few seconds.

The propagation effects in the interstellar medium (e.g., dispersion, temporal broadening due to scatter, etc.) are crucial to be considered in the fast transient detection techniques. The dispersion across the observed bandwidth is a primary factor in detecting the fast transients (see, for example, Cordes & McLaughlin, 2003). However, many classes of terrestrial signals, e.g., swept-frequency RFI¹⁰, perytons (Burke-Spolaor *et al.*, 2011a) etc., may also mimic the dispersive nature of the astronomically originated signals. Moreover, excluding pulsars and RRATs (Rotating Radio Transients), most of the transient events are generally one-time events. Hence, it is necessary to have observational and detection techniques which can distinguish between these local and the astrophysically originated signals. A detection made simultaneously in several small bands, such as those facilitated by the MBR, in a broad spectral range (1 : 10–15 range) can help in decisively discriminating between the above two types of signals. Although there would also be an enhancement in the sensitivity (due to increase in available bandwidth), the crucial advantage of such an approach is the confidence in detection of any astrophysical signal acquired by checking the consistency of a dispersed signature across such a wide band¹¹. As an example, we show the single pulses from the bright pulsar B0329+54 in Figure 5.10, corresponding to the dynamic spectra presented in Figure 5.1, after the data are dedispersed within individual bands and time-aligned¹² across the wide-band. The simultaneous detection in various bands, with the expected dispersive delays across the wide band, illustrates the astrophysical origin of the single pulses.

As mentioned above, since the transient events are mostly one-time events, detection of a transient simultaneously in multiple bands would also be crucial in providing an excellent opportunity to investigate its spectral behavior across a significant part of the radio spectrum, and to study the underlying physical processes responsible for the emission.

5.5 Summary

In this chapter, we have presented samples of the different types of data obtained from our simultaneous multi-frequency observations with the GBT using the MBR, and given a flavor of selected studies using these observations. We used our observation of the bright pulsar B0329+54

¹⁰See an illustrative example in the next part of this thesis.

¹¹An ideal approach would be to search simultaneously at two or more well separated geographical locations as well.

¹²The stacked single-pulses in this Figure may suffer from tiny misalignment in absolute observation time and/or slightly incorrect value of dispersion measure used to dedisperse and align the data across the wide band. These are presented only to demonstrate the simultaneous detection and study of transient pulses across a wide spectral range.

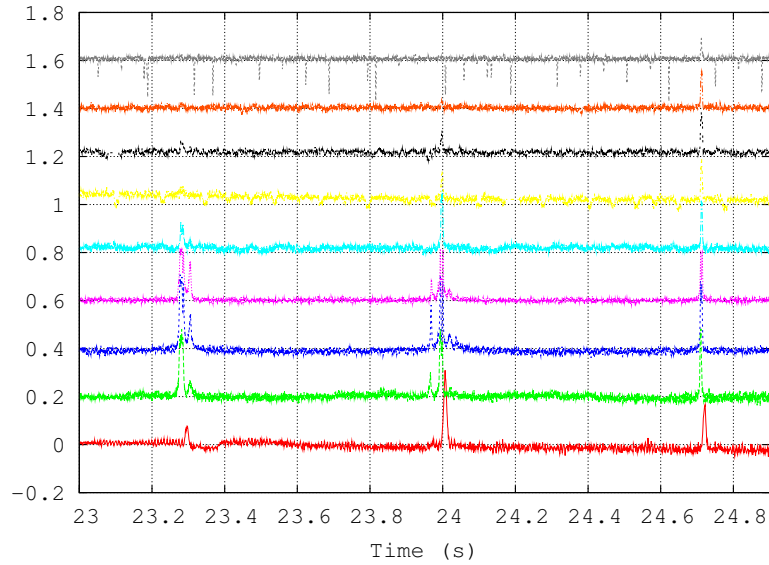


Figure 5.10: Corresponding to the dynamic spectra (in the direction of B0329+54) shown in Figure 5.1, the dedispersed single pulses for each of the nine bands (stacked together) across a ~ 1.9 seconds span are shown here. These sequences are presented only as an example of single pulse detection and study across a broad range of the radio spectrum, and the effects of data-slips, RFI contaminations etc., have not been taken care of appropriately.

to study average properties of the radio emission (profile-shape, emission altitude and the radio spectrum), and presented some synoptic results. We have also presented a preliminary tomograph of the polar magnetosphere of the pulsar B0809+74, using our simultaneous observations in four frequency bands in the range 117–330 MHz. We also discussed very briefly how crucial such a multi-band receiver can be in searching for fast transients and decisively discriminating them from the terrestrial signals which may otherwise mimic the properties of astrophysically originated signals across narrower bands. To aid this discussion, we also demonstrated detection of single pulses simultaneously in multiple bands using our observation of the bright pulsar B0329+54.

Part III

*Searches for
Decameter-wavelength
Counterparts of Radio-quiet
Gamma-ray Pulsars*

Search for radio counterparts of gamma-ray pulsars: Motivation, observations, and detection methods

6.1 Introduction

The Fermi Large Area Telescope (LAT) with its large effective area of $\sim 9500 \text{ cm}^2$, large field of view ($\sim 2 \text{ sr}$), narrow point spread function $\sim 0.6^\circ$ at 1 GeV (normal incidence) and broad energy range (20 MeV – 300 GeV), is a highly sensitive instrument for γ -ray observations. Because of this vast improvement in sensitivity compared to past γ -ray missions, an extraordinary increase has been seen in the number of pulsars detected in gamma rays. Apart from the detection of gamma-rays from a large number of known radio pulsars, it was for the first time possible to perform blind searches for pulsars in γ -rays. These blind searches have so far discovered 36 γ -ray pulsars from the data recorded by the Fermi-LAT (Abdo *et al.*, 2009; Saz Parkinson *et al.*, 2010; Pletsch *et al.*, 2012). There are mainly two kinds of competing theoretical models for the high energy emission from pulsars, viz. the Polar cap models and the Outer gap models. The ratio of radio-quiet to radio-loud γ -ray pulsars is an important discriminator between these two types of models. The LAT-pulsars discovered in blind searches need not necessarily be radio-quiet, and hence need to be searched for radio pulsations. Despite deep radio follow-up searches, so far only four of these LAT-discovered pulsars could be detected (J1741–2054, J2032+4127, J1907+0602 & J0106+4855; Camilo *et al.*, 2009; Abdo *et al.*, 2010; Pletsch *et al.*, 2012), suggesting that the radio-quiet pulsar population might actually be quite large. However, all the deep follow-up searches were carried out at high

radio frequencies (around 1 GHz and above, except a few at 300 MHz ; Ray *et al.* , 2011; Pletsch *et al.* , 2012), and the lower frequency domain still remains relatively unexplored.

At low radio frequencies, pulsar emission beams become wider (suggesting the so called radius-to-frequency mapping of pulsar radio beams), increasing the probability of our line-of-sight passing through the emission beam. A classic example is B0943+10, which is detected only below ~ 1 GHz because our line-of-sight misses the relatively narrow emission beam at higher frequencies almost completely (see, for example, Weisberg *et al.* , 1999; Deshpande & Rankin, 2001). Also, a recent study (Ravi *et al.* , 2010) suggests that, for high- \dot{E} (i.e., young) and millisecond pulsars, radio emission beam widths are comparable to those of γ -ray beams. Therefore such pulsars, if already detected in gamma-rays, can be expected to be beaming towards us. Given the widening of radio beams at low frequencies even for normal pulsars, follow-up searches of these γ -ray pulsars at very low frequencies (< 100 MHz) could also be revealing. Any detection would open an otherwise rare possibility of studying these objects at such low radio frequencies. On the other hand, a non-detection might provide stringent upper limits on the radio flux from these sources. Thus a search for radio emission from LAT-discovered pulsars at low frequencies is essential for completeness before discriminating between the polar cap and outer gap models.

Many of the pulsars discovered by the *Fermi*-LAT happen to be within the area of the sky surveyed using the Gauribidanur telescope at 34.5 MHz in the years 2002 to 2006. Therefore, we searched through the archival data from this survey, for any periodic or transient pulsed signal along the direction of 17 of these radio-quiet gamma-ray pulsars.

Subsequently, motivated by an intriguing detection resulting from the above search, we embarked on an observing program of deep searches for the radio counterparts, using the Gauribidanur radio telescope at 34 MHz. In the first round of this program, observations were made in the direction of 10 of the so-called radio-quiet gamma-ray pulsars¹. More than 20 observing sessions were carried out towards each of the target sources. Data from these multiple sessions were time-aligned², co-added and searched for a dispersed signal at the periodicity of the target pulsar.

In the following sections, we present (a) a brief description of the radio telescope and the receiver setup used for the archival as well as the new observations, (b) a discussion on reactivation of the telescope required to carry out the deep search observations, and (c) a detailed description of our search strategies and methods, along with a few illustrations.

¹We shall use the phrases “new observations” and “deep search observations” interchangeably to refer to the observations carried out under this program.

²We shall use the phrases “time-aligned” and “phase-aligned” interchangeably.

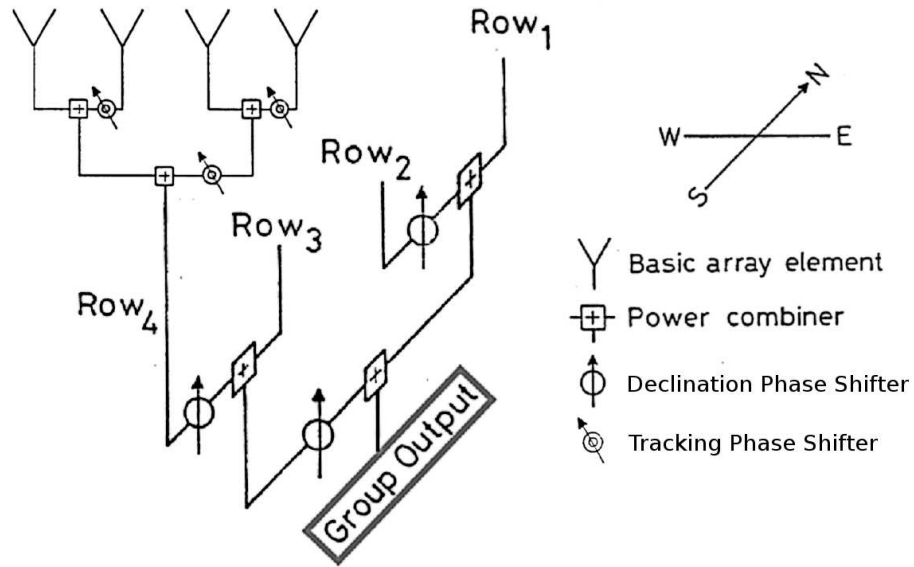


Figure 6.1: Configuration within each of the 10 EW array groups (See Deshpande *et al.* (1989), Figure 2a).

6.2 A brief introduction to the Gauribidanur radio telescope

The Gauribidanur Radio Telescope — built and operated by the Raman Research Institute and the Indian Institute of Astrophysics in a joint collaborative program — is a large radio telescope operating at decameter-wavelengths (Deshpande *et al.*, 1989). Originally the telescope consisted of 1000 broad band, single polarization (east-west orientation) fat dipoles arranged to form a 1.38 km long EW array along the East-West (E-W) direction, and a 0.45 km long South array extending southwards from the center of the EW array. The two arrays, hence, formed the shape of the letter “T”. The EW array consists of four rows of dipoles, each consisting of 160 dipoles. The South array, which was dismantled a few years ago, consisted of 360 dipoles. The archival as well as the new observations were carried out using only the EW array (consisting of 640 dipoles).

Four rows in the EW array are separated by 5 meters from each other in the North-South (N-S) direction. Within each row, output of four consecutive dipoles along the E-W direction are combined in a Christmas-tree fashion using balanced (open-wire) impedance transmission line (open wire), transformers and a BALUN³. This combination of 4 dipoles is referred to as “basic array element” or “basic element”. Further, the EW array is divided into 10 groups, each group consisting of 16 basic elements arranged in the form of a 4×4 matrix. Within each group, the outputs of the 16 elements are combined together as shown in Figure 6.1. For each of the East and West arm

³A balun is an electrical device that converts a balanced signal to an unbalanced signal.

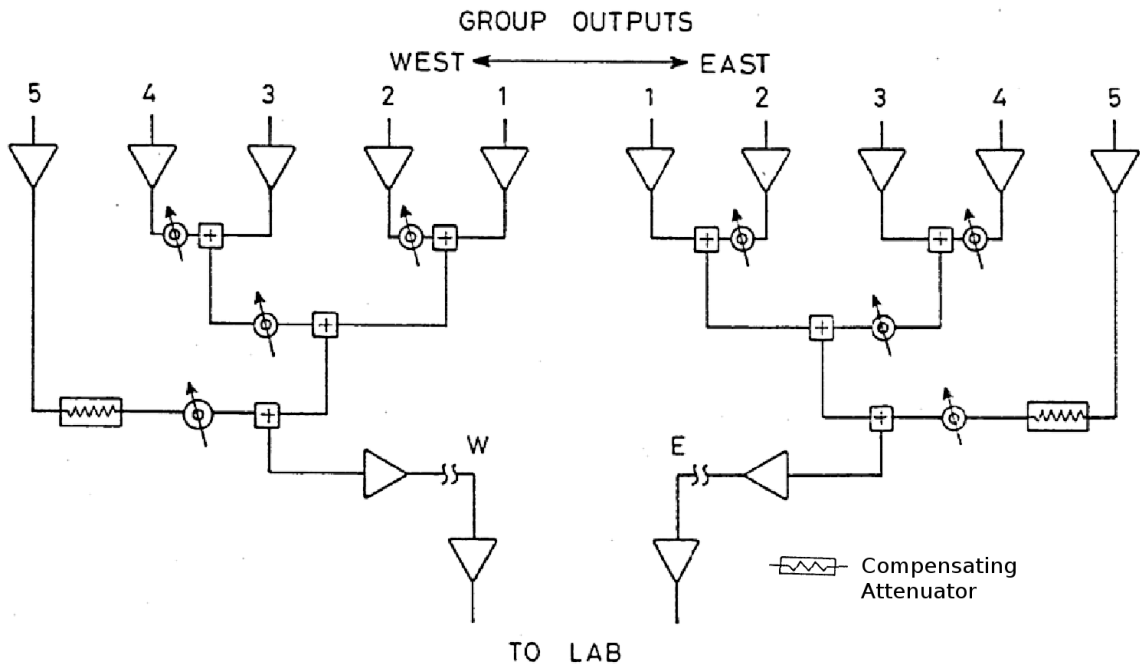


Figure 6.2: Separate combinations of the five group outputs, available from each of the East and West arm of the EW array, in the form of a Christmas-tree (See Deshpande *et al.* (1989), Figure 2b).

of the EW array, five group outputs are combined separately with equal delay and amplitude in a Christmas-tree fashion (see Figure 6.2). The two arm outputs, thus formed, are further amplified and brought to the lab where these are added after a small delay correction.

The electronic steering of the array beam is achieved by introducing phase gradients⁴ across the aperture. The declination phase-shifters between various rows, as marked in Figure 6.1, provide the capability of pointing at any declination between -45° and $+75^\circ$. The tracking phase-shifters introduced at various stages (as shown in Figures 6.1 and 6.2), along with the control system, are used for tracking the source for a limited duration near its meridian transit-time. Tracking is realized by introducing 63 sequential phase-gradients along the E-W direction, which correspond to tilting the hour-angle beam at 63 different positions (31 positions on either side of the zenith). This limited tracking facility allows a source to be tracked over a total span of $10^\circ.5$ centered around the meridian. Equivalently, a source at declination δ can be tracked for about $42 \times \sec(\delta)$ minutes⁵. For more details of the antenna system, design considerations, and the control and tracking system, we

⁴Usage of phase gradients, instead of delay gradients, limits the usable bandwidth somewhat.

⁵Observing time in each of the 63 beam positions is $40 \times \sec(\delta)$ sidereal seconds.

refer the reader to Deshpande *et al.* (1989).

The observations were made using the EW array in total power mode. The effective collecting area offered by this array, at the instrumental zenith of $14^\circ.1$ declination, is about 12000 m^2 . The beam-widths (full width at half-power) of this array are $21'$ and $25^\circ \times \sec(Z)$ in right ascension and declination respectively, where Z is the zenith-angle.

6.3 Reactivation of the telescope

After the pulsar/transient survey observations were carried out using the E-W array during the years 2002–2006, the telescope had been inoperative, and hence not maintained, for about 6 years (2006 to 2012). During this period, the electronic components in the field (phase-shifters, amplifiers and pre-amplifiers, transformers and BALUNs), dipoles, and the wooden poles supporting the dipoles, were adversely affected due to routine exposure to the severe environmental conditions (primarily rainfall and strong lightening). As a result, a significant amount of mechanical and electronic reconstruction, as well as testing of the array was required before we could start the deep search observing program in 2012. A significant, non-contiguous part of the array had to be mechanically reconstructed (degraded/broken dipoles and wooden poles were replaced). Most of the electronic components were brought to the lab, and tested to identify and replace the malfunctioning modules.

6.3.1 Phasing of the dipole-array

The array of dipoles can be realized as a single dish looking at zenith with equivalent collecting area, if the signal received at the dipoles can be added with equal delay and amplitude. This criterion of “in-phase” addition has to be satisfied at all the ‘signal combination stages’ shown in Figure 6.1 and 6.2. We will refer to this process of equalizing the delay and amplitude at all the combination stages as “phasing”.

Once the reconstruction was complete, the dipole array had to be re-phased. Primary phasing of the array is achieved by ensuring that the total cable lengths from each of the basic elements to the lab are equal. However, the physical path-length from a basic element to the lab consists of many segments of cables, and possible small errors in these segments may accumulate to a significant fraction of wavelength, i.e., large enough to possibly cause out-of-phase addition of signal at various combination stages. Since many of the cable segments were replaced, re-phasing of the array was necessary.

Ideally, the electric path length of the signal, from each of the basic elements to the lab or center of the EW array, should be measured and equalized. However, such an approach would require

a test setup with cables of lengths of the order of at least half of the EW array's length. Hence, a 'relative segmented phasing' scheme was followed. In this approach, the electric path lengths from the individual dipoles to the group outputs were equalized between the central two groups, i.e., the first groups of the East and West arms. Then the 2nd and 3rd groups in both the arms were phased with respect to the respective first groups. Subsequently, 4th and 5th groups were phased with respect to the 3rd groups. This relative phasing ensured the equalization of the electric path lengths from individual dipoles to the group output levels for all the 10 groups. The electric path lengths from the group outputs to the center of the EW array were equalized in a similar fashion (which understandably required much smaller number of measurements). Any possible phase difference between the East and West arm signals, caused by the path lengths from center of the array to the lab, could then be measured and corrected easily.

Once the above relative segmented phasing was over, confirmatory measurements for relative path lengths from the individual dipoles to the center of the EW array were carried out. These measurements were performed only for 16 dipoles per group, i.e., say for one basic element from each of the rows within the group. The above segmented phasing scheme was also extremely helpful in identifying any remaining problematic areas, which could have been difficult to locate otherwise. After one round of segmented phasing was over, subsequent phasing, whenever required, was carried out in a non-segmented fashion (i.e., like the above confirmatory measurements).

During the above process of phasing, the beam had been kept pointed at zenith, i.e., the phase-shifters did not contribute any additional path lengths. Additional tests were carried out by steering the beam to a different location than zenith. Depending on the hour-angle and declination of the selected location, the tracking and declination phase-shifters would contribute additional path lengths. Phase measurements relative to those when the beam was pointed at zenith, showed expected changes.

6.3.2 The acquisition setup

The phased array output signal is down-converted, digitized and recorded using the Portable Pulsar Receiver⁶ (PPR; Deshpande, Ramkumar, Chandrasekaran & Vinutha, in preparation) and an acquisition PC with LINUX based platform. PPR has been designed as a generic back-end unit which can be used at any observatory to sample and record signals down converted to an appropriately low frequency (preferably ≤ 50 MHz), and with a bandwidth < 2 MHz. Independent units of PPR have been successfully used at the Gauribidanur radio telescope, the Mauritius radio telescope (see, for example, Issur, 2002), MST radar facility, and the Pushchino radio astronomy observatory⁷.

⁶http://www.rrri.res.in/dsp_ral/ppr/ppr_main.html

⁷<http://www.prao.ru/English/radiotelescopes/telescopes.html>

The analog section of the PPR mixes the radio frequency signal with a local oscillator signal of appropriate frequency to generate the IF (intermediate frequency) of 10 MHz. PPR incorporates a fast data acquisition system (DAS), consisting of three main parts: digitizer, sampler and bit-packing logic unit, and the interface to the PC. The raw voltage sequence is digitized using a 3-level comparator, and sampled at the Nyquist rate (2-bit, 4-level quantization). A bit packing logic packs 8 consecutive samples (2 bits each) into a 16 bits (i.e., 2 Bytes) word, which is then passed to the PC through a serial communication port and recorded on to the hard disk. After every 4096 words of actual data, a ‘marker word’ is also passed to the PC and recorded. The marker word consists of a 16 bit pattern, wherein the 8 most significant bits are always zero and the 8 least significant bits act as a counter (modulo 256) of how many 4096 word blocks of data have been transferred. In the off-line data processing, the above marker pattern, along with the expected sequential increment in the marker values are looked for to locate and deal with possible slips in the data acquisition.

PPR has been successfully used at the Gauribidanur radio telescope for more than a decade now. An old PPR unit, sampling the signal with a bandwidth of about 1 MHz, was used for the survey observations. For the deep search observations, a relatively new PPR unit was used. This new unit facilitated a bandwidth of about 1.5 MHz. More details of the observations are discussed in the next section.

Accuracy of the time-stamp

Before sampling of the data starts, the timing logic waits for the DAS to provide an “Enable Transmission” signal at the trailing edge of the 1 pulse per second (PPS) from a global positioning system (GPS) interface. This synchronization is necessary if, (1) observations at different sites are to be carried out simultaneously, and/or (2) observations at different epochs are to be combined later in the off-line processing. As we will see later, our deep search strategy is based on time-aligning and combining the observations carried out at different epochs.

The time-stamp, consisting of start date and time of acquisition, is produced by reading the PC clock at the time of acquisition program execution, and the time string is written in the format *HH:MM:SS.ss*. Since the actual acquisition starts at the trailing edge of the 1 PPS, and the leading edge of the pulse arrives at the start of next second, the seconds part of the actual acquisition start time string would be:

$$T_{\text{seconds-part}} = \text{int}(SS.ss) + 1.0 + W_{PPS} \quad (6.1)$$

where W_{PPS} is the width of the 1 PPS used, and equals 200 *ms* in our case. After this correction to the acquisition start time, the pulsar data observed at different epochs can be phase-aligned.

The accuracy required in the time-stamp, to phase-align the pulsar data observed at differ-

ent epochs, is at least of the order of $1/100^{\text{th}}$ of the pulsar period⁸. For the above synchronization with the 1 PPS from GPS, and a PC with an adequately stable hardware clock, it generally suffices if the PC time is periodically synchronized with an official time reference like UTC (Coordinated Universal Time). However, for an old PC such as our data acquisition PC, the computer's clock is prone to drift. Even an error of only 0.001% in the PC clock frequency would make it off by almost one second per day. For our data acquisition PC, the clock drift seemed to be worse, resulting in offsets of as much as about 10 seconds per day. Updating the computer's clock too often, to keep the offset from UTC within acceptable range, is not a practical approach. Hence, to keep the system time synchronized with the UTC, we have used an operating system daemon "ntpd" that synchronizes the system clock to remote Network Time Protocol⁹ (NTP) public time servers. The "ntpd" program operates continuously while adjusting the system time as well as the clock frequency. We have used open access "stratum 0" level (the highest level in a hierarchical, semi-layered system of levels of clock sources) NTP time servers, implying that the network time is obtained either directly from, or from a computer connected directly to, the devices like atomic clocks, GPS clocks or other radio clocks. Multiple number of such time servers were used to have enough redundancy in case one or more of the servers happen to be unavailable.

NTP usually maintains the time accurate within tens of milliseconds, and can achieve 1 millisecond accuracy in ideal conditions. Further, the acquisition program was modified such that the execution always starts around 500^{th} millisecond of a second. Since the actual data acquisition start time is synchronized with 1 PPS from GPS which arrives only at the beginning of a second, we can afford any inaccuracy with magnitude < 500 milliseconds (in practice, the number is more like 400 ms) in our system clock. Hence, the system time synchronization achieved using the NTP is more than adequate¹⁰.

⁸For a search-optimum temporal resolution of a few milliseconds, we will be dealing with about 100 to 200 number of bins across the periods of most of the pulsars of our interest. Hence, an accuracy of about $1/100^{\text{th}}$ to $1/200^{\text{th}}$ of the pulsar period would suffice for combining the multi-epoch pulsar data in phase, assuming a pulse duty-cycle of at least a few percent. The actually obtained accuracy, due to the 1 PPS from GPS, is much better than the above requirements and is adequate enough for longer period/smaller duty cycle pulsars as well.

⁹For more details on NTP, please refer to the online information at <http://www.ntp.org/> .

¹⁰Scheduled "leap seconds" modifies the UTC by one second to synchronize the timescale to the rotation of earth. Since NTP delivers UTC, and it has no mechanism for remembering the history of leap seconds, entire NTP timescale is shifted by 1 second for every instance of leap second insertion. The total shift, till the date of observations, is taken care of in the off-line processing.

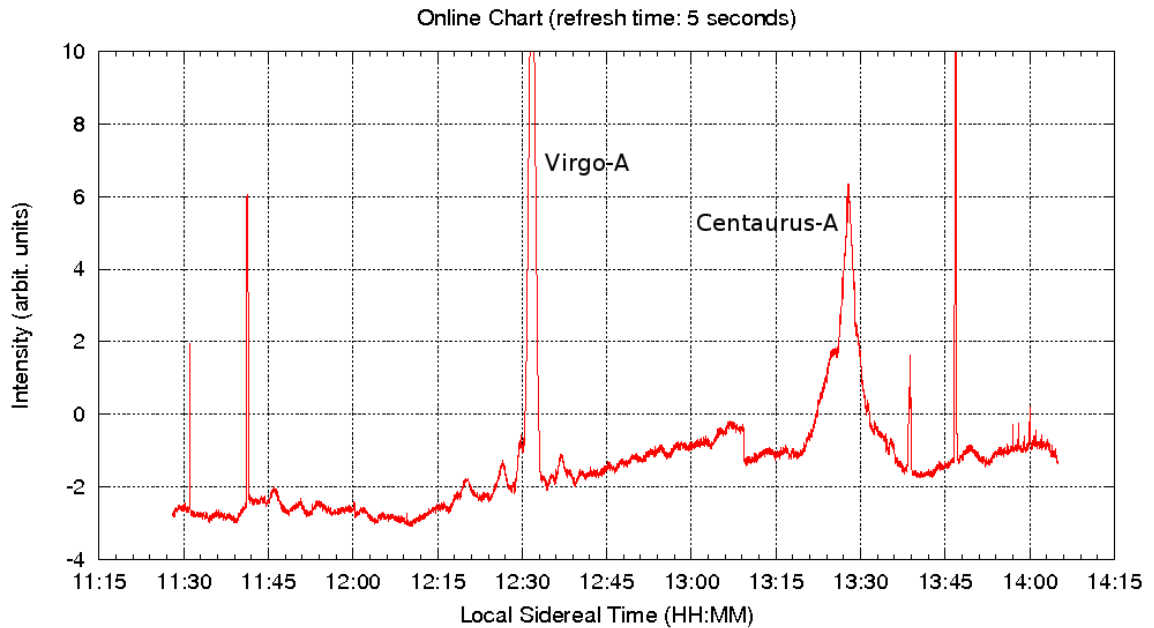


Figure 6.3: A snapshot of quasi-real time monitoring of total power sequence.

6.3.3 The monitoring setup

It is very useful to monitor the spectral and temporal variations of the signal output from the telescope in real-time/quasi-real-time, to keep an eye on the system health in general, and for quick feedback, particularly while debugging the system.

We first tried out a monitoring setup (in software) on the acquisition PC, by sniffing 1 sample out of every 100 samples received. However, we soon learned that the processing and hard-disk writing speed offered by the (~ 10 years) old acquisition PC are not adequate enough for the (quasi-)real time computation and plotting of the spectrum and time-series, without substantially affecting the rest of the computer processing. Specifically, the number of occurrences and sizes of data-slips increased substantially when data were acquired in parallel with the above temporal and spectral monitoring. Subsequently, we utilized a separate single channel (of 30 kHz bandwidth) correlation receiver¹¹ in total power mode to monitor the temporal variations of the output signal, sampled at 1 second intervals. The recorded time sequence, updated every 5 seconds with the latest 5 samples, is displayed using the gnuplot graphing utility in this quasi-real-time (i.e., updated every 5 seconds) monitoring setup. The center frequency of the single channel receiver is normally 34.5 MHz, but can be changed to several other frequencies in the range 34–35 MHz. Figure 6.3 shows

¹¹See *section 2.2.2* of Deshpande (1987) for more details of this receiver.

a snapshot of total power sequence being monitored as a function of local sidereal time (LST), presented as an online “chart” record. A small jump near the LST of $\sim 13:10$ corresponds to a small change in the system gain because of steering away of the declination beam from zenith ($14^\circ.0$) to declination of the bright radio source Centaurus-A ($-43^\circ.0$). The right ascension (RA) beam had been kept pointed towards zenith. Transits of the sources Virgo-A and Centaurus-A, indicating the expected beam shapes in RA at the respective declinations, are marked in the figure. These particular transit observations were carried out early morning, i.e., during RFI-quiet part of the day. A couple of strong RFI occurrences, at the start as well as towards the end, are still visible. For spectral monitoring with desired flexibility, we used a commercial spectrum analyzer.

6.4 Observations and pre-search data processing

Observing setup and the pre-search data reduction process for the archival and the new observations are essentially same, except for change in values of a few parameters, as would become apparent from the details below.

6.4.1 The archival data

The pulsar/transient survey was carried out in the years 2002 to 2006 using the EW array of the Gauribidanur telescope at 34.5 MHz. Since the declination beam width of the EW array is $25^\circ \times \sec(Z)$, the full accessible declination range (-45° to $+75^\circ$) could be covered with 5 discrete pointings in declination: -30° , -05° , $+14^\circ$, $+35^\circ$ and $+55^\circ$. Appropriate pointings in RA were made to cover the full range of 0–24 Hrs.

Seventeen of the radio-quiet gamma-ray pulsars are in the sky area observed as a part of the above survey. We have used the archival data along these 17 directions to search for any pulsed emission (transient or at the periodicity of these pulsars). A total of about 14 hours of archival observations are available along these 17 directions. Details of these observations can be found in Table 6.1.

6.4.2 Deep search observations

In the year 2012, we carried out multiple observing sessions (> 20 sessions per source) for 10 of the radio-quiet gamma-ray pulsars under the deep search observing program. During these observations, two groups (at the two ends) of the EW array were not available, and the observations could utilize only 80% of the potential effective collecting area of the EW array. A slightly larger bandwidth and longer session durations of these observations, as compared to those of the archival observations, together provided a little more sensitivity, despite the 20% loss in

Table 6.1. Decameter Wavelength Observations of Radio-quiet Gamma-ray Pulsars

Target PSR	R.A. (J2000.0)	Dec. (J2000.0)	Period (s)	Archival Data		New Observations
				Pointing	t_{obs} (s)	t_{obs} (s)
				Dec.($^{\circ}$)	$[N_{sessions} \times t_{session}]$	$[N_{sessions} \times t_{session}]$
J0357+3205	03:57:52	+32:05:25	0.4441	+35	2×1200	24×1800
J0633+0632 [†]	06:33:44	+06:32:35	0.2974	+14	1×1200	46×1800
J0633+1746 [†]	06:33:54	+17:46:13	0.2371	+14	1×1200	46×1800
J1732–3131	17:32:33	–31:31:23	0.1965	–30	10×1200	125×1800
J1741–2054*	17:41:57	–20:53:57	0.4137	–30	1×1200	—
J1809–2332	18:09:50	–23:33:35	0.1468	–30	3×1200	21×1800
J1813–1246	18:13:24	–12:45:59	0.0481	–05	4×1200	—
J1826–1256	18:26:09	–12:56:33	0.1102	–05	3×1200	—
J1836+5925	18:36:14	+59:25:30	0.1733	—	—	33×1800
J1846+0919	18:46:26	+09:19:46	0.2256	+14	1×1200	—
J1907+0602*	19:07:55	+06:02:16	0.1066	+14	1×1200	—
J1954+2836	19:54:19	+28:36:06	0.0927	+35	2×1200	—
J1957+5033	19:57:39	+50:33:18	0.3748	+55	1×1200	—
J1958+2846	19:58:40	+28:45:54	0.2904	+35	2×1200	—
J2021+4026	20:21:30	+40:26:45	0.2653	+35	4×1200	24×1800
J2032+4127*	20:32:13	+41:27:25	0.1432	+35	2×1200	—
J2055+2539	20:55:49	+25:40:02	0.3196	+35/+14	2×1200	22×1800
J2139+4716	21:39:56	+47:16:13	0.2828	—	—	23×1800
J2238+5903	22:38:28	+59:03:41	0.1627	+55	1×1200	22×1800
Total Observation Duration:					13.67 Hours (41 Sessions)	170 Hours [†] (340 Sessions)

[†]The position coordinates of the pulsars J0633+0632 and J0633+1746 ([RA,Dec]=[06:34:26, 6.5] and [06:34:38, 17.8] respectively, precessed to the epoch of observations) lie close to each other. We observed both of these pulsars simultaneously by pointing towards the direction [06:34:26, 10 $^{\circ}$.0] (since both the pulsars fall in the same beam, and well above the half power points). While computing the total number of sessions (or the total observation duration), the observing sessions of these pulsars are *not* counted separately.

*Radio counterpart of J1907+0602 was reported while our searches were going on (Abdo *et al.* , 2010), while those of J1741–2054 and J2032+4127 were already known (Camilo *et al.* , 2009).

collecting area. Further relevant details of these observations can be found in Table 6.1. Two radio pulsars, B0834+06 and B1919+21, were also observed regularly (almost every day) as “control pulsars”, given their persistent and relatively brighter pulsed emission at these frequencies. Details

Table 6.2. Decameter Wavelength Observations of Control Radio-Pulsars

Control PSR	R.A. (J2000.0)	Dec. (J2000.0)	Period (s)	t_{obs} (s) [$N_{sessions} \times t_{session}$]
B0834+06	08:37:06	+06:10:15	1.2738	139×1800
B1919+21	19:21:45	+21:53:02	1.3373	134×1800
Total Observation Duration:				136.5 Hours (273 Sessions)

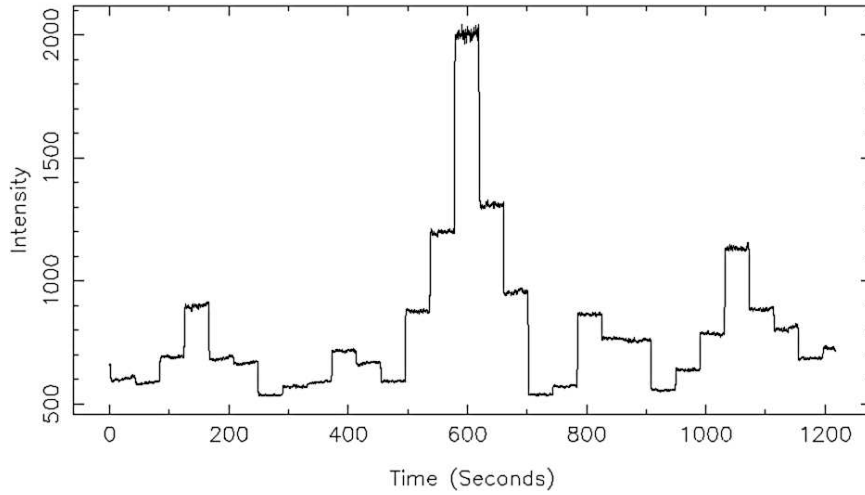


Figure 6.4: Typical system gain variations, while tracking the source, are shown (the intensity units are arbitrary). For details please refer to the text.

of observations of these pulsars are provided¹² in Table 6.2.

¹²Although the observational details of the target and control PSRs are listed only till the epoch MJD=56299.0, a few of the radio-quiet pulsars, along with the two “control pulsars” are still being followed up. A number of pulsars from rest of the radio-quiet population are also planned to be observed under the same deep search observing program. These subsequent observations, and analysis thereof, are beyond the scope of this thesis, and will be reported elsewhere.

6.4.3 Pre-search data processing

In each observing session, raw signal voltage sequence is directly recorded at the Nyquist rate (with 2-bit, 4-level quantization) using the PPR for the observing session duration, while tracking the source. For the archival data, the voltage time sequence from each of the observing sessions is, in the off-line processing, Fourier transformed in blocks of 512 samples, resulting in dynamic spectrum with 256 spectral channels across 1.05 MHz bandwidth centered around 34.5 MHz, and temporal resolution of ~ 1.95 ms (after averaging 8 successive raw power-spectra). While for the new observations, appropriate parameters are chosen to finally achieve 1024 channels across 1.53 MHz bandwidth centered around 34 MHz, and a temporal resolution of ~ 2 ms.

Optimum sampling time

For a given spectral channel width $\Delta\nu$, the best achievable time resolution is limited by the receiver filter response time ($\Delta t_{\Delta\nu} \approx [\Delta\nu]^{-1}$). However, the pulsed signals of astrophysical origin also get smeared due to the interstellar dispersion. The dispersion effects are characterized by the dispersion measure (DM) of the source¹³. While the relative dispersive delays between the time series corresponding to different frequency channels can be corrected for (see section 6.5.1), the dispersion smearing across the individual channel widths (Δt_{DM}) remains uncorrected (unless a ‘‘coherent’’ dedispersion is carried out). Hence, the effective time resolution for a pulse is approximately a quadratic sum of $\Delta t_{\Delta\nu}$ and Δt_{DM} , i.e.,

$$\Delta t = (\Delta t_{\Delta\nu}^2 + \Delta t_{DM}^2)^{1/2} \quad (6.2)$$

In the above formulation, we have assumed that the DM is exactly known, i.e., there is no error in DM. Note that the broadening due to interstellar scattering also contributes significantly to Δt , especially at our low frequency of observations. This broadening is highly dependent on distance and direction of the source, and is estimated as a statistical function of DM (Cordes & Lazio, 2002). Since such an estimation generally comes with large uncertainties and may cause non-optimum estimation of Δt , we have excluded this in our present discussion.

The optimum sampling time, for a given DM, is equal to the minimum possible Δt which we find out using the Equation (6.2) as:

$$t_{\text{samp}} \text{ (ms)} = 128.8 \times \left(\frac{DM}{\nu_c^3} \right)^{1/2} \quad (6.3)$$

where ν_c is the center frequency of observation (in MHz). To obtain the above expression, we have substituted for Δt_{DM} using the information in section 6.5.1. Note that the corresponding optimum

¹³DM is the column density of electrons, along the line of sight, between the source and the observer. For more details, please refer to *section 6.5.1*.

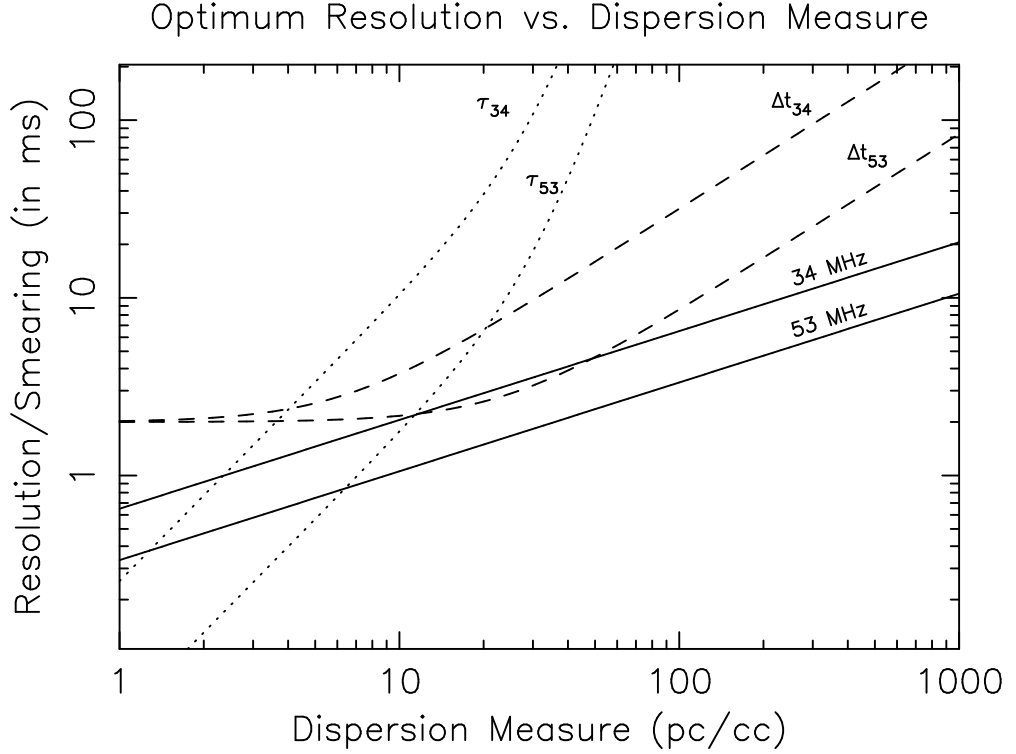


Figure 6.5: The solid line curves represent the optimum time resolution as a function of DM, for center frequencies 34 and 53 MHz, as marked on the curves. The dashed and dotted lines present the actual resolution achieved and the scattering time scales estimated at these frequencies, as a function of DM.

channel width is given by:

$$\Delta\nu \text{ (MHz)} = 0.1098 \times 10^{-4} \times \left(\frac{\nu_c^3}{DM} \right)^{1/2} \quad (6.4)$$

which corresponds to the condition that the receiver filter response time is equal to the dispersion smearing across the channel width. Number of channels and the sampling time (~ 2 ms) we have used, are optimum for a DM of about 10 pc/cc. The optimum time resolution, and the actual achievable time resolution for our chosen parameters (i.e., a quadrature sum of our chosen sampling time of ~ 2 ms and dispersion smearing across the channel width) at center frequencies of 34 and 53 MHz, are shown in Figure 6.5.

System gain variations due to tracking

As described in section 6.2, tracking of a source is realized by stepping the beam in hour angle every $40 \times \sec(\delta)$ sidereal seconds. The phase-shifter configurations, including their insertion

losses, change for each of these pointings in hour angle, making the system gain vary sharply at the transition from one beam pointing to another. These discrete beam transitions are identified in the off-line processing, and the data for each of the beams are normalized with the corresponding system gain. An example presenting these sharp gain variations is shown in Figure 6.4. The beam position with the maximum system gain (at around 600 s) corresponds to the meridian-transit (i.e., all the phase-shifters are by-passed). For any two beams equidistant from the meridian-beam, the phase gradient introduced across the EW array is of the same amplitude but opposite in sign. Hence, the amount of loss introduced by the phase-shifters for such beam positions would be equal, making the gain pattern to be roughly symmetric around the meridian-beam (since the array has a symmetric grading).

Any sensitivity change due to gain changes at beam transitions, is rather smaller, since the system temperature still remains dominated by the sky background. However, unlike the system gain, the sensitivity reduces monotonically as the beam is tilted away from the meridian, following the gain pattern of the primary beam of the basic array element (which has a FWHM width of about 15°). Since the tracking is confined within about $\pm 5^\circ$ of the meridian, the last beams (i.e., $\pm 31^{\text{st}}$ beams) are expected to have a sensitivity of about 75% of that at the meridian. Note that, in our typically 30-minute long observations centered around the meridian, even for the sources with declinations near to the instrumental zenith, the beam pointings in hour angle are required only till $\pm 23^{\text{rd}}$ beams (on the two sides of meridian) which have sensitivity of about 0.85 of that at the meridian. For declinations away from the instrumental zenith, this factor improves rapidly (since further smaller number of pointings in hour angle would be needed), and on the average, 95% of the sensitivity at meridian is easily achieved throughout the observation duration.

Any significant RFI that is narrow in bandwidth and/or time is identified using appropriate statistical analysis, and the affected data are excluded in all further processing. Further, we normalize the total power at each sample of the dynamic spectrum to suppress all signals that are broadband and are of non-dispersive nature.

The resultant data in filter-bank format, from individual observing sessions, are subjected to two types of searches — single pulse search and the search for periodic signal. Since the rotation ephemerides of our target pulsars are known from their timing models based on the LAT γ -ray data, searching for dispersed signals from these pulsars at the relevant periods is straight forward. However, as we will see below, searching for any transient signal (in the form of single bright pulses) from these pulsars is also important, especially at our low frequency of observations. Also, since we have adequate accuracy in the recorded time-stamp, combining the multiple session/epoch data using the gamma-ray timing solutions enables deeper search for any dispersed signal at the periodicity of these pulsars. These three kinds of searches are described in more detail in the following sections.

6.5 Single pulse search: motivation, methodology, and challenges at low frequencies

Periodic signals from pulsars at such low frequencies are generally very weak, and detectable only from a very small fraction of the total pulsar population. However, it is not uncommon to find the intrinsic strength of a single pulse, or a part of the pulse, increase many fold from its average (e.g., in the form of explicit excursion as in giant pulses/radiation spikes, or as a part of general sub-pulse level intensity fluctuations). How well such signals can be differentiated from mere noise fluctuations, or those due to radio frequency interference (RFI), depends not only on their relative strength, but also on the correspondence between the observed and the expected pulse arrival times, and whether any clear manifestation of their propagation through the intervening medium, as for distant astronomical sources, is evident.

Further, at low frequencies, searches for periodic pulsed signals are severely affected by the interstellar scattering. At decameter wavelengths, the pulse broadening due to the interstellar scattering is expected to be significantly large (note the dotted curves in Figure 6.5). As the broadened pulse-width becomes comparable to, and subsequently larger than, the pulsar-period, the periodic pulsed fraction drops sharply, making its detection less likely. In such cases, search for single bright pulses may still be possible depending on their intensities, and the characteristics of the smearing due to interstellar scattering would need to be incorporated in optimally searching across the pulse-width as well.

6.5.1 Methodology

Search for single bright pulses of astrophysical origin looks for the dispersive signature across the observing band at a number of trial DMs, and reports its significance, in case of detection above a given threshold (see, for example, Cordes & McLaughlin, 2003). Our single pulse search methodology is detailed in the following steps.

1. Dedispersion

The time of arrival of a pulsed signal varies across the frequency because of the interstellar dispersion, a characteristic that serves as a primary identifier for signals from distant astronomical sources. The relative delay at a frequency ν with respect to a reference frequency ν_0 is given by:

$$\Delta t \text{ (ms)} = 4.15 \times 10^6 \times \text{DM} \times (\nu^{-2} - \nu_0^{-2}) \quad (6.5)$$

where ν and ν_0 are in MHz, and DM (Dispersion Measure in units of pc/cc) is the column density of electrons along the line of sight, between the observer and the source. We carry out “incoherent”

or “post-detection” dedispersion¹⁴ of the filter-bank data, wherein the time sequence corresponding to each of the frequency channels is shifted to compensate for the delay suggested by Equation (6.5) for a given DM, and then the data are averaged over the bandwidth to produce an average time sequence, usually retaining the original temporal sampling.

Since the DM is not known a priori, data are dedispersed for a number of trial DMs. The spacing between the trial DM values is determined by the maximum dispersive smearing across the bandwidth that can be tolerated in the final dedispersed time series, in comparison with the sampling interval in time. Hence, the optimum spacing between the trial DMs can be estimated as:

$$\Delta DM \text{ (pc/cc)} = 1.205 \times 10^{-7} \times (\nu_c^3 / BW) \times t_{\text{samp}} \quad (6.6)$$

where the total bandwidth BW , and the center frequency ν_c are in MHz, and t_{samp} is the sampling time in milliseconds.

Let us recall that the pulse broadening due to interstellar scattering is estimated as a statistical function of DM (Cordes & Lazio, 2002). Since, such an estimation generally comes with large uncertainties, we had excluded the scattering effects in our estimation of the optimum sampling time in Equation (6.3). This exclusion may cause an increase in computation time since Δt would be underestimated. However, inclusion of a scatter broadening estimate, with large uncertainty, may result in overestimation of Δt , and hence in a reduced sensitivity of the search. In practice, a large range of DM is searched, and a temporal/spectral resolution that is optimum throughout the range can not be achieved. The sampling time and the number of channels in our filter-bank data are optimum for a DM of about 10 pc/cc. Further, note that as the DM increases, the optimum t_{samp} also increases, making the optimal DM spacing larger at higher DMs (see Figure 6.5, and Equations 6.3 & 6.6). Hence, for a given range of DMs to be searched, computational resources can be used efficiently without compromising additionally on the search sensitivity if the DM spacing is decided as a function of the trial DM. A typical mapping from DM to trial DM-step number, using the observational parameters for archival observations, keeping the step-size optimum throughout the DM range, is shown in Figure 6.6.

2. Matched Filtering

The process of dedispersion, and subsequent identification of bright pulses, in itself is an exercise in matched filtering, with the highest signal-to-noise ratio (S/N) achieved when the data are dedispersed for the correct DM. After dedispersion, time series corresponding to each of the trial DMs, are individually subjected to a common detection criterion.

¹⁴ “Coherent” or “pre-detection” dedispersion needs to be carried out on the raw voltage sequence (which contains the phase information), and requires more computational resources.

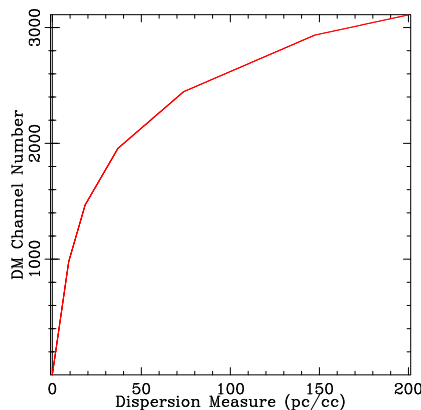


Figure 6.6: A typical mapping of trial DM-step (or DM-channel) number to DM, reflecting the optimum spacing between the consecutive trial DMs, is shown.

Following usual practice, we have chosen pulse amplitudes crossing an appropriate S/N threshold as a detection criterion. We note that the S/N of a pulse peaks when the effective smoothing (and in our case, also the sampling time) matches the detected width of the pulse. Since the intrinsic widths of the signals are unknown, a boxcar function of varying width is generally used to smooth the time-series, and then examine the peak S/N as a function of the boxcar-width. For pulse-shapes symmetric around the pulse-peak, highest S/N is achieved when the boxcar-width is approximately equal to the pulse width. In such cases, or in the absence of any knowledge about the pulse broadening function, the above smoothing approach provides an efficient approximation to optimal detection. However, at decameter wavelengths, it is necessary to consider the effects of scattering in the intervening medium. Even at moderate DMs, the apparent pulse shape at such low frequencies is expected to be dominantly affected by the interstellar scattering. The resultant effect is usually modeled as a convolution of intrinsic pulse profile with a truncated (one-sided) exponential function. Thus, for optimum detection, a given dedispersed time-sequence is smoothed (match-filtered) with a truncated exponential template, before subjecting to detection criterion. We use templates of different widths, in systematic trials, to effectively carry out a search also in the apparent pulse-width (or scatter broadening).

3. Thresholding

The detection threshold is chosen based on how many “false alarms” can be tolerated in the final candidate list. “False alarms” are threshold crossings caused solely by the random noise. To determine a reasonable threshold, we assume the statistics of the observed time series amplitudes to be Gaussian in nature. If N_{tot} is the total number of points in a time series corresponding to a

trial DM, then the expected number of “false-alarms” N_f crossing a threshold of η (in units of the rms noise) solely due to noise, are given by the following expression:

$$\text{erf}(\eta/1.414) = 1 - 2 \times N_f/N_{tot} \quad (6.7)$$

where $\text{erf}()$ is the *error function*. Hence, for a chosen “false alarm” rate, corresponding threshold can be determined. In practice, the observed signals generally deviate from Gaussian statistics due to presence of RFI. Depending on how much the data are affected by RFI, the actually used threshold is often slightly higher than that expected from Equation (6.7).

For a given time series, it is possible that the computed mean and rms are biased by a few very strong pulses. To get an unbiased (or robust) estimate, mean and rms are recalculated by using the previous estimates to detect and exclude the strong pulses above a given S/N threshold. This process is continued iteratively till the computed mean and rms no more differ from their respective values in the previous iteration.

4. Diagnostics

Results of the single pulse search, displayed in a set of diagnostic plots, summarizing the statistics and quality of data, help in first-level assessment of the candidate detections for their astrophysical origin. An example of such diagnostic plots is presented in Figure 6.7, which shows histograms of S/N and of DM, a scatter plot of S/N vs. DM, and a plot displaying the distribution of “events” in time and for all the trial DMs, above a threshold of 5σ . The S/N histogram clearly deviates from the Gaussian curve at high S/Ns. The DM histogram and the scatter plot show detection of a number of bright single pulses from the pulsar B0834+06 at the expected DM, i.e., the DM of the pulsar (~ 12.88 pc/cc). The DM histogram and the scatter plot are complementary to each other. A single bright pulse may not appear in the DM histogram but will be detected in the scatter plot. On the other hand, a number of weak pulses at the same DM would be clearly seen in the DM histogram but may not show themselves (depending on their strength) in the scatter plot.

5. Candidate event analysis

Once a (candidate) pulse above an appropriate threshold is detected, further investigations are necessary to find out whether the source of the pulse is astronomical or not. Although sometimes not sufficient, the critical assessment of the candidates involves at least the following steps.

(a) *Examination of the spectrum:* Most of the transient signals of astrophysical origin are expected to be broadband, at least in comparison to our observation bandwidth. Hence, it is important to verify if the candidate pulse contribution exists across the whole bandwidth. If the signal is linearly polarized, the apparent signal strength may vary significantly across the bandwidth due to

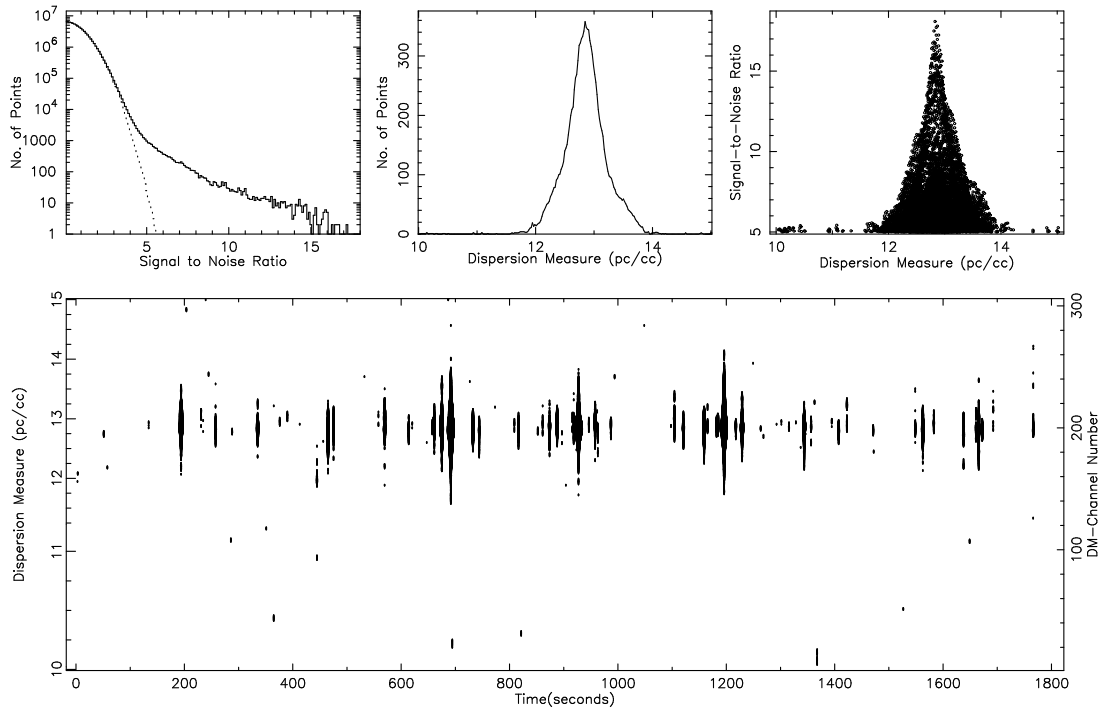


Figure 6.7: Results of search for single bright pulses from the pulsar B0834+06 at 34 MHz, observed using the Gauribidanur telescope. Results are shown for search across a narrow range of DM (10–15 pc/cc). **Top left:** The solid curve presents the S/N histogram of all the data points above the mean (i.e., for $S/N > 0$). The dotted (inner) curve shows the expected histogram for pure noise with Gaussian statistics. **Top middle:** Number of data points above a threshold of 5σ are shown as a function of DM. A broad peak centered around the DM of the pulsar B0834+06 is clearly evident. **Top right:** Scatter plot of DM and S/N is shown. Detection of significantly bright pulses at the DM of the pulsar is obvious. **Bottom:** All the data points above the chosen threshold have been plotted vs. DM and time. The size of the data points (plotted as circles, not readily apparent in this particular plot) is directly proportional to the S/N of the data point.

the Faraday modulation, since our telescope is sensitive only to single linear polarization. However, existence of such a modulation itself would support the astronomical origin of the signal. Even if the detected signal has bandwidth narrower than the observation bandwidth, the relative delays in pulse arrival times within the signal bandwidth, expected due to the interstellar dispersion, should be evident. Generally, an inspection of the dynamic spectra at and around the candidate pulse suffices for largely determining whether or not the signal is of astronomical origin. A relevant example is discussed later in the subsection 6.5.2.

(b) *A scrutiny for “swept-frequency” RFI:* Our pre-search processing looks for and excises any significant RFI that is narrow in bandwidth and/or in time. And, our procedure of normalizing the

total power at each time sample of the dynamic spectrum, suppresses all signals that are broadband *and* are of non-dispersive nature. Only those RFI which carry a dispersive signature, necessarily broadband, can escape this scrutiny. The “swept-frequency” RFI can indeed sometimes mimic the dispersive signature, normally identified with astronomical origin. However, the times of arrival of these “swept-frequency” RFI are generally linearly proportional to the frequency (as against the inverse-square dependence in case of astronomically originating signals). Hence, we select dynamic spectra in a small time range around a candidate event, and dedisperse the data with linear delay gradients ($\Delta t \propto \nu$) spanning similar delay ranges, and compare the results with those using ν^{-2} law. For astronomical signals, the significance of detection is expected to be lower for the linear chirp.

Once a candidate pulse passes the above two kinds of tests, we proceed to find out its possible association with a known source, etc. If a large number of pulses are detected at a common DM, then a few stronger of these are used to assess and confirm their astronomical origin before using all the detected pulses for further studies, e.g., to search for a periodicity.

6.5.2 Challenges at low frequencies

Search for bright single pulses at low frequencies (≤ 100 MHz) is more challenging than that at higher frequencies, primarily due to:

Interstellar scattering

Broadening of pulsed signals by multi-path scattering does significant damage to the S/N. The scatter broadening is approximately proportional to $\nu^{-4} \times DM^2$, implying that the apparent pulse shape at low frequencies is expected to be dominantly affected by the interstellar scattering. Some effects of scattering cannot be really removed using any software or hardware processing. However, our approximation of the pulse broadening function as a one-sided exponential function does help in detecting any scattered pulse through matched filtering. Figure 6.8 illustrates the optimal detection of single pulses from the pulsar B1919+21, observed at 53 MHz using the MST radar, when the truncated exponential template width becomes comparable to the detected pulse width. The number of pulses detected (not shown separately, but apparent in Figure 6.8) also becomes maximum at the optimum template width.

Radio Frequency Interference

RFI contamination is generally more severe at low frequencies. While the RFI that are narrow in spectral and/or temporal domain can be detected and excised relatively easily, typical broadband non-dispersive RFI are suppressed by our normalizing process.

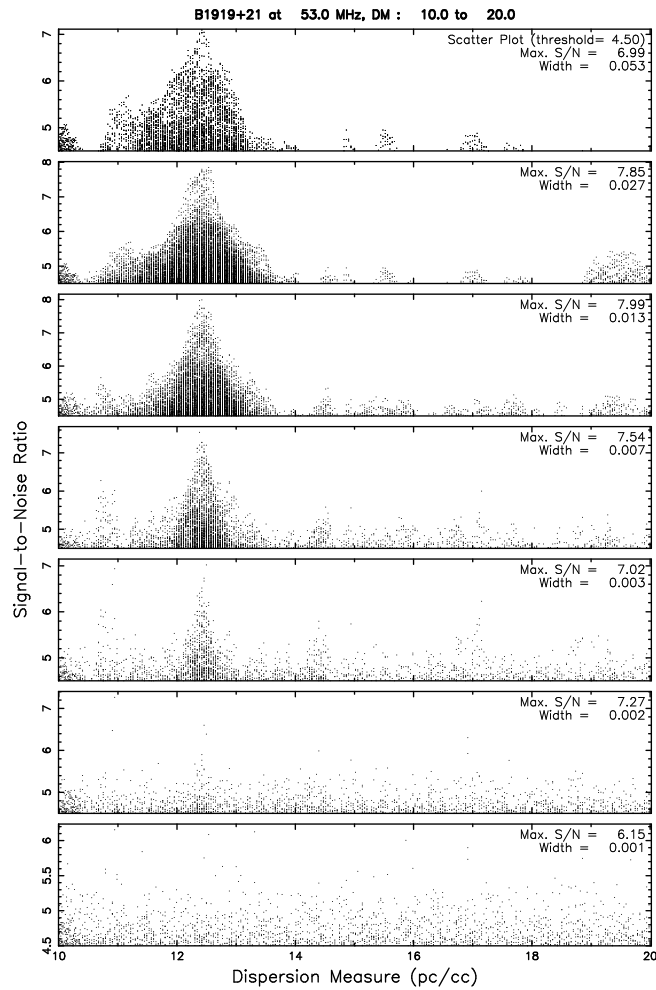


Figure 6.8: Results of single pulse search for the pulsar B1919+21 at 53 MHz, after the time sequences are match filtered with a truncated exponential template of varying width. Each of the subplots shows the scatter plot of S/N vs. DM obtained when the time sequence is smoothed with a template of width (in ms) marked on the top right corner of the subplot. The marked widths are rounded off to the nearest millisecond, and the lower most subplot shows the results without any smoothing.

It is very unlikely for an RFI to mimic the distinct dispersion characteristics at such low frequencies through out the bandwidth (dispersion delay per unit DM, across a bandwidth of 1 MHz centered at 34 MHz, is > 200 ms). However, a strong RFI sweeping across even a little portion of the band can result in a misleading/spurious detection of dispersed signature. One such example of a spurious detection is presented in Figure 6.9. Note that there is no particular indication in the diagnostic plots that the detection could be a spurious one. It is revealed only when we examine

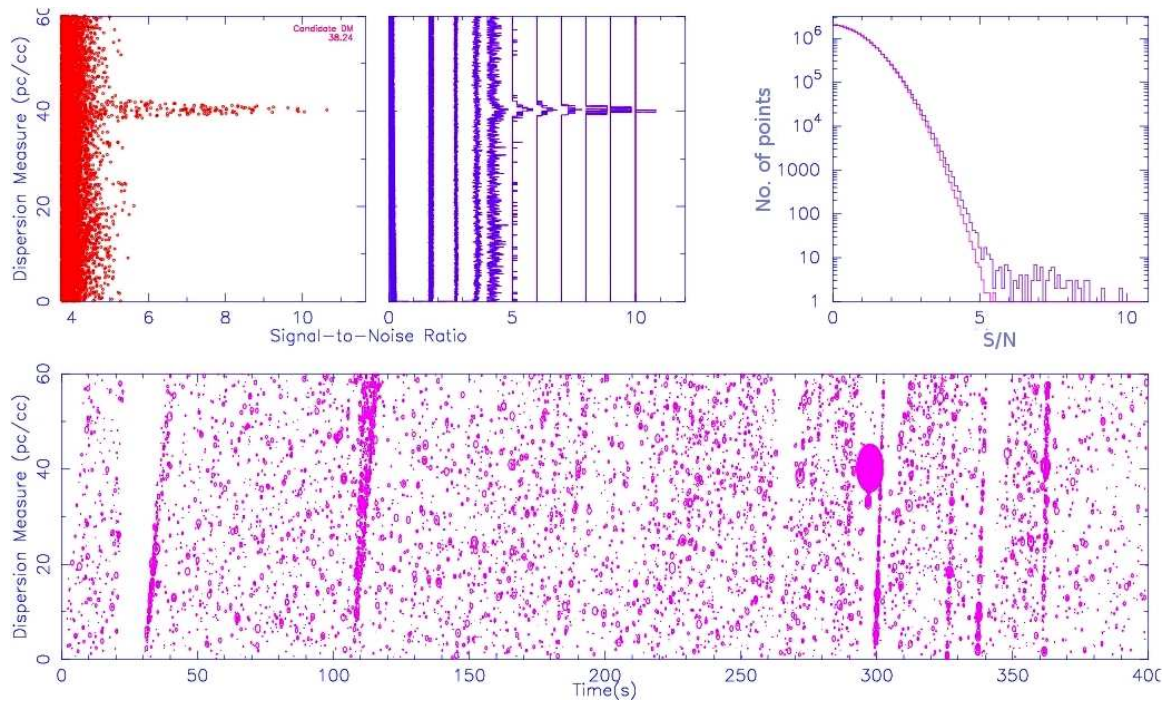


Figure 6.9: Search diagnostics plots, show a spurious detection of a dispersed pulse at time ~ 300 s, and at a DM of about 38 pc/cc. The top-middle subplot shows the number of points above a threshold that is equal to the ordinate, vs. DM. Tilted streaks across the full DM range at around 110 seconds and at a few more occasions are due to unidentified RFI. For this particular data set, the dispersion delays were corrected with respect to the lowest frequency, hence the tilt.

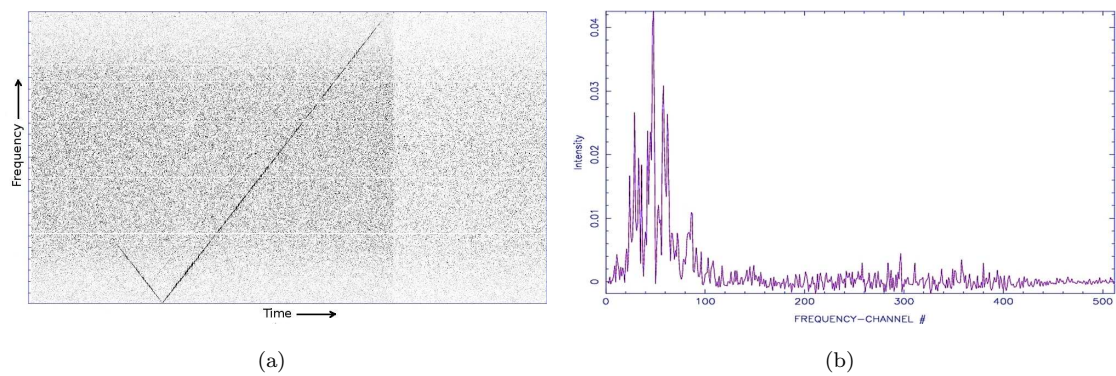


Figure 6.10: The dynamic spectra in a time range selected around, but not centered at, the spurious detection in Figure 6.9, and the spectrum at the peak of the detected pulse are shown in the left and right panels respectively.

the spectrum of the detected pulse. Figure 6.10 shows the dynamic spectrum in time range around the detected pulse, and the spectrum at the peak of the pulse. It is clear that a small aliased part of a “negatively” swept-frequency RFI in the lower portion of the band has resulted in the spurious detection. The spectrum at the peak of the detected pulse shows that most of the contribution is indeed from the lower part of the bandwidth, as apparent in the dynamic spectra.

Other than the swept-frequency RFI, a variety of other broadband RFI have been encountered during our search. Most of these are weak and un-dispersed but have varying power across the band as well as across their small temporal widths. Because of these variations in power, the normalization process can not suppress their effects completely. However, inspecting the spectrum of a candidate event suffices in most cases to determine whether the detection is spurious or genuine.

Lastly, we highlight the advantage the single pulse search has, with an illustrative example. Periodicity search needs a number of pulses to be present in the data to be searched for, and the sensitivity of such a search, specially at low frequencies, is limited by the scatter broadening (reducing the pulsed fraction). On the other hand search for transient signals is sensitive to even a “single” bright pulse, even if partially buried in RFI. Further, pulsed signals originated from sources at different DMs can be detected simultaneously. This particular aspect makes this search more effective if more than one source happen to be in the same beam, a likely situation specially for a broad beam like our telescope has. We present an illustrative example of this in Figure 6.11, wherein single pulses are detected from the pulsars B0943+10 and B0950+08, simultaneously, at their respective DMs of about 15.4 pc/cc and 2.97 pc/cc. For this particular data set, observed using the MST radar at 53 MHz, the beam was initially pointed towards the pulsar B0943+10. As the sky drifted, signal from B0950+08 could also be seen. Note that the pulsar B0943+10 is detected only due to one strong pulse at around $t=45$ s, demonstrating the sensitivity of single pulse search.

6.6 Search for periodic signal

Since the rotation ephemerides for the radio-quiet pulsars are known (Ray *et al.*, 2011, and the timing models provided by the LAT team¹⁵), folding the time sequence over the respective rotation period¹⁶ (after corrections for the barycentric motion of the Earth) was performed for

¹⁵<https://confluence.slac.stanford.edu/display/GLAMCOG/LAT+Gamma-ray+Pulsar+Timing+Models>

¹⁶It is important to estimate, and correct for, any drift in the sampling clock. For the archival data, we analyzed a number of observing sessions towards known pulsars, and concluded that there was no clock drift. However, for the new observations using the new PPR unit, we noticed a significant drift in the sampling clock. The drift rate was estimated using the B0834+06 observations at 49 different epochs (see Appendix C). For time sequences from each of the observing sessions, the sampling interval was corrected using this estimate before carrying out the search for any periodic signal.

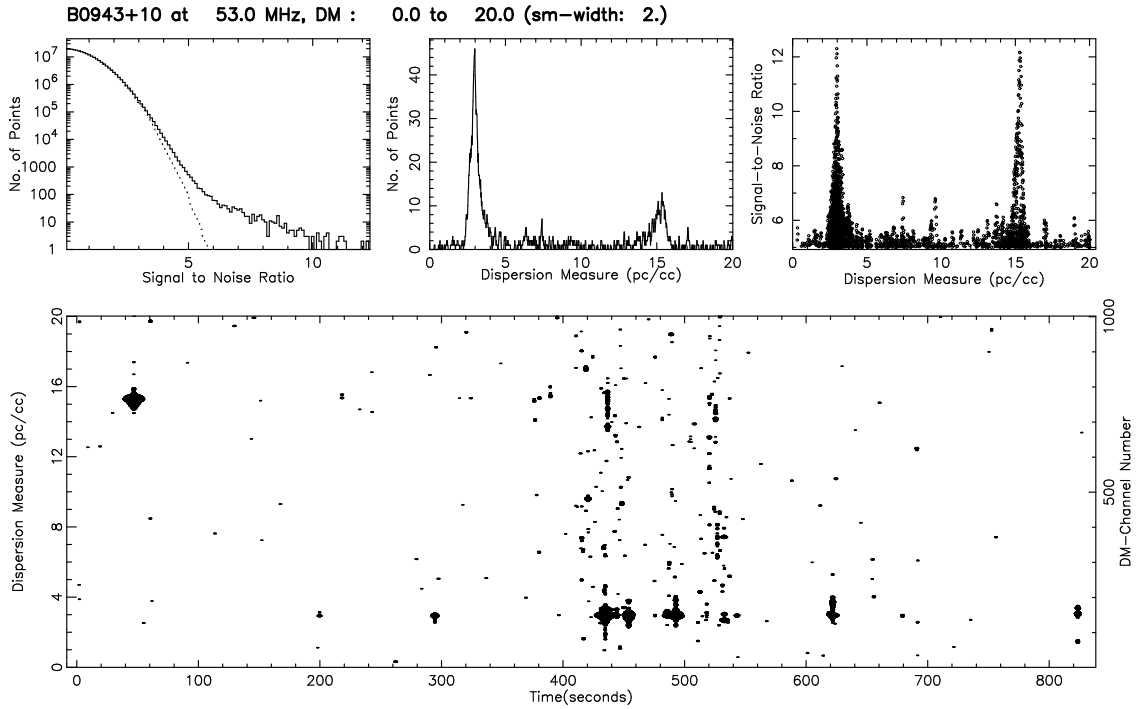


Figure 6.11: Simultaneous detection of bright pulses from the pulsars B0943+10 and B0950+08 is demonstrated. For explanation of individual plots, please refer to Figure 6.7.

each of the frequency channels to enhance the S/N. Then, this “folded” dynamic spectrum was used to search for any significant dispersed pulse-profile. Peak S/N above a threshold was used as the criterion for detecting the candidates. However, highest S/N is expected when effective time resolution becomes equal to the pulse-width, so that the total pulse energy is contrasted with the smoothed noise. This becomes particularly important for a candidate having a large pulse-width (a number of reasons contribute to the apparent width; e.g., prominent effect of interstellar scattering at low frequencies, intrinsic pulse-width etc.). An optimum search across trial pulse-widths was thus carried out in each of the dedispersed-folded profiles. For completeness, we also extend the search across the period domain (although over a narrow range of period offsets). In Figure 6.12(a), we present a two-dimensional cut (as a function of DM and pulse-width) of the results of 3-D search procedure mentioned above, when applied to data from one of the observing sessions of the survey towards the pulsar B0834+06. Clearly, a narrow pulse of width $\sim 15^\circ$ is detected at the expected DM of about 12.88 pc/cc.

We note however that the S/N of the peak in the average profile as a figure of merit can lead to large errors in estimating the true DM when the individual frequency channel profiles have

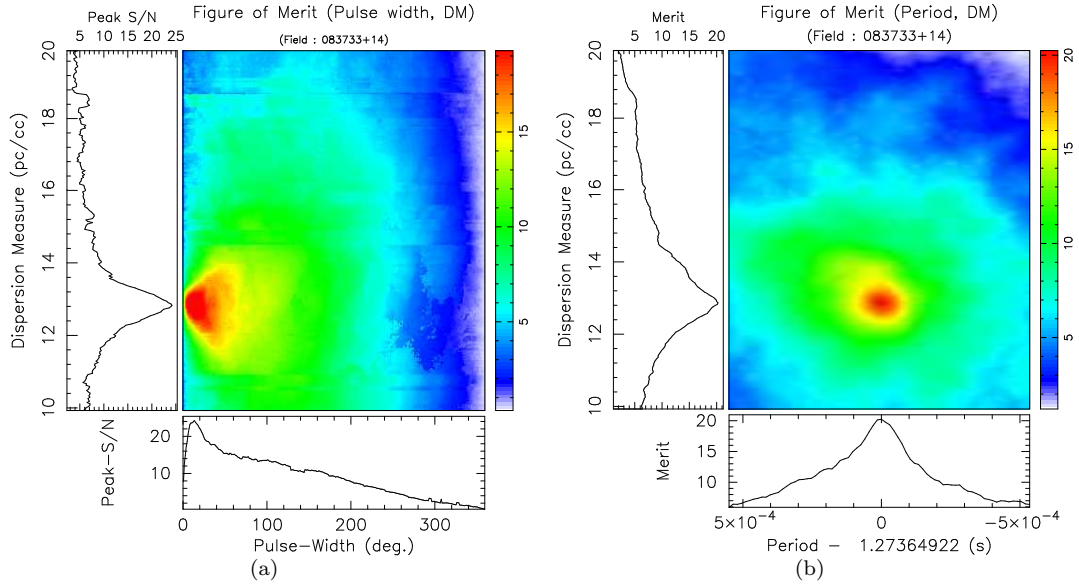


Figure 6.12: *Left*: The main panel shows peak S/N in the folded profiles corresponding to each combination of the trial values of smoothing width and DM. The isolated peak defining the preferred combinations is apparent near DM ~ 12.88 pc/cc and pulse-width $\sim 15^\circ$. For ease of viewing the typical variations, the side and bottom panels provide vertical and horizontal cuts at the position of maximum peak-S/N in the main panel. *Right*: The main panel shows the significance of the folded profile as a function of DM and period. A narrow range of period values around the actual period has been chosen. For the best-fitting period, the figure of merit variations as a function of DM are shown in the side panel. Corresponding to the best-fitting DM, the bottom panel shows the variations of the figure of merit as a function of the period offset.

poor S/N. There is also a related bias towards compactness of the average profile while searching for best-fit DM. We therefore use sum-of-squares (SSQ) of average intensities across the profile as a figure of merit¹⁷. Significance of the average profile assessed in this manner and as a function of DM and period-offset, is shown in figure 6.12(b). For weak signals, use of SSQ as a figure of merit allows a less biased estimate of DM.

¹⁷See Appendix C for more discussion on figure of merit.

6.7 Deep search for periodic signals by combining multi-epoch observations

In the above search for periodic signal from the radio-quiet gamma-ray pulsars, the sensitivity was limited by, among other factors, the duration of observations in each session. Since we have observed our target pulsars in multiple observing sessions¹⁸, our sensitivity for detecting a periodic signal could be enhanced, if the data from all the observing sessions could be time-aligned and combined. Nominally, the sensitivity would increase by square-root of the number of observing sessions, given that the observation duration was same for all the session.

While the enhancement in sensitivity is important, the deep search program was motivated by two more crucial aspects:

1. Even for the handful of pulsars which are detectable at such low frequencies, the received periodic signals are very weak. Specially at these low frequencies, level of RFI contamination and the ionospheric scintillations, in addition to the interstellar scintillations, can hinder detectability of such weak signals. Hence, a weak source, even if intrinsically persistent, may not be detected in all the observing sessions. In addition, the source may also be intrinsically variable. Hence, it is important to observe the same field a multiple number of times.
2. Assuming Gaussian statistics for noise, a detection even at 5σ might appear quite significant (chance probability of such a detection is less than 0.6×10^{-6}). However, the measured statistics generally deviate from the expected Gaussian nature due to RFI contamination, and the possibility that a 5σ detection is due to some weak RFI can not be ruled out. Hence, the detection threshold is generally kept a little higher, typically from 8σ to 10σ . However, detection of even a relatively weak periodic signal, but in more than one observing sessions on different days, consistent in pulse-shape and at the same phase of the period, cannot be ruled out as a manifestation of a chance occurrence or some RFI. Such consistency across observing sessions, is therefore crucial to raise the level of confidence in establishing the astrophysical origin of an otherwise weak signal.

With the above motivations, deep search was carried out for periodic signal from 10 of the radio-quiet pulsars. Below we describe the methodology we have followed to time-align and combine the multi-epoch observations, and present some illustrative examples of the performance of this setup.

¹⁸It was ensured to carry out more than 20 observing sessions for each of the target pulsars.

6.7.1 Methodology

We use the pulsar timing software “Tempo” to predict the ephemeris of pulse phase (expressed in the form of a polynomial)¹⁹. The input timing models for the gamma-ray pulsars, estimated directly from the LAT gamma-ray data, are provided by the LAT team²⁰, while those for the radio pulsars are obtained through the ATNF pulsar database²¹. The rotation period and the pulse phase at the start of an acquisition are calculated using the polynomial coefficients obtained from Tempo, and the sampling interval is corrected for the estimated clock drift-rate.

Time-aligning and co-adding²²

For each of the frequency channels in the filter-bank data, the time sequence is folded over the above extrapolated rotation period of the pulsar, to prepare period-folded dynamic-spectrum, which we shall refer to as “folded-dyn-spectrum” here onwards. While folding the data, the above calculated pulse-phase is assigned to the first sample in the time series, and the time ranges identified as RFI-contaminated in the pre-search processing are not included. For each of the observing sessions, the folded-dyn-spectrum is written out to an appropriate disk-file.

Since we have used the initial pulse-phase predicted by Tempo, the folded-dyn-spectra are naturally phase-aligned and can be co-added directly²³. While co-adding, the average band-shape modulation is removed, and the frequency channels identified as RFI contaminated for individual observing sessions are excluded. Also, the “effective integration time (t_{eff})” (i.e., the total observation duration – RFI contaminated duration) may vary from one observing session to other, resulting in different rms noise in the folded data from different sessions. To account for these differences, a suitably weighted sum of the folded-dyn-spectra is computed. Figure 6.13(a) presents an example of co-added folded-dyn-spectrum for our control radio pulsar B0834+06, using data from a number of observing sessions. The otherwise weak signal in the individual observing sessions, has become clearly evident after phase-aligning and combining multi-epoch data.

¹⁹For more information about Tempo, please refer to the website: <http://www.atnf.csiro.au/research/pulsar/tempo/> .

²⁰<https://confluence.slac.stanford.edu/display/GLAMCOG/LAT+Gamma-ray+Pulsar+Timing+Models>

²¹<http://www.atnf.csiro.au/people/pulsar/psrcat/>

²²In the following discussion, we shall refer “adding in phase, and taking average over the number of observing sessions” as co-adding.

²³Direct co-addition is possible because the other relevant observation parameters, i.e., the bandwidth, number of frequency channels, have been kept same.

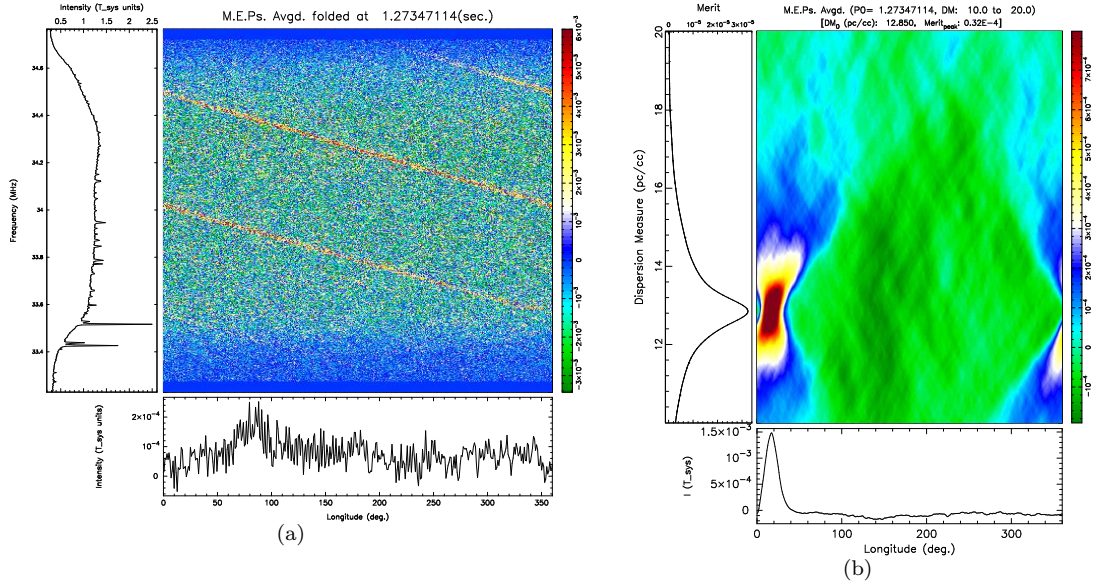


Figure 6.13: *Left*: The main panel shows the folded-dyn-spectrum for the control radio pulsar B0834+06, co-added over a number of observing sessions. The side and the bottom panels show the averages on the respective sides. *Right*: Each row in the main panel shows the dedispersed average profile corresponding to the DM marked on the vertical axis of the side panel. The side panel shows the significance of the average profiles, in terms of the figure-of-merit, as a function of DM. The bottom panel shows the dedispersed average profile corresponding to the best-fitting DM.

Searching for a dispersed signal

Searching for a dispersed signal in the co-added folded-dyn-spectrum is straight forward. The dynamic spectrum is dedispersed for a number of trial DMs and the significance of the resultant average profiles is assessed. To enhance the S/N, the profiles are smoothed to a resolution of about 20° to 30° in pulse-longitudes, and SSQ or χ^2 is used as the figure of merit to assess the profile significance. Results of this procedure when applied to the dynamic spectrum shown in Figure 6.13(a), are presented in Figure 6.13(b). A strong detection at the expected DM of the pulsar is obvious. The high S/N profile in the bottom panel corresponds to the best-fit DM. As described in the previous section, an optimum search across trial pulse-widths is also carried out in each of the dedispersed-folded profiles.

Consistency check: examining the average profiles

Once a candidate detection of dispersed pulse is made at the periodicity of the pulsar, consistency between the shape and phase of the average profiles across the individual observing

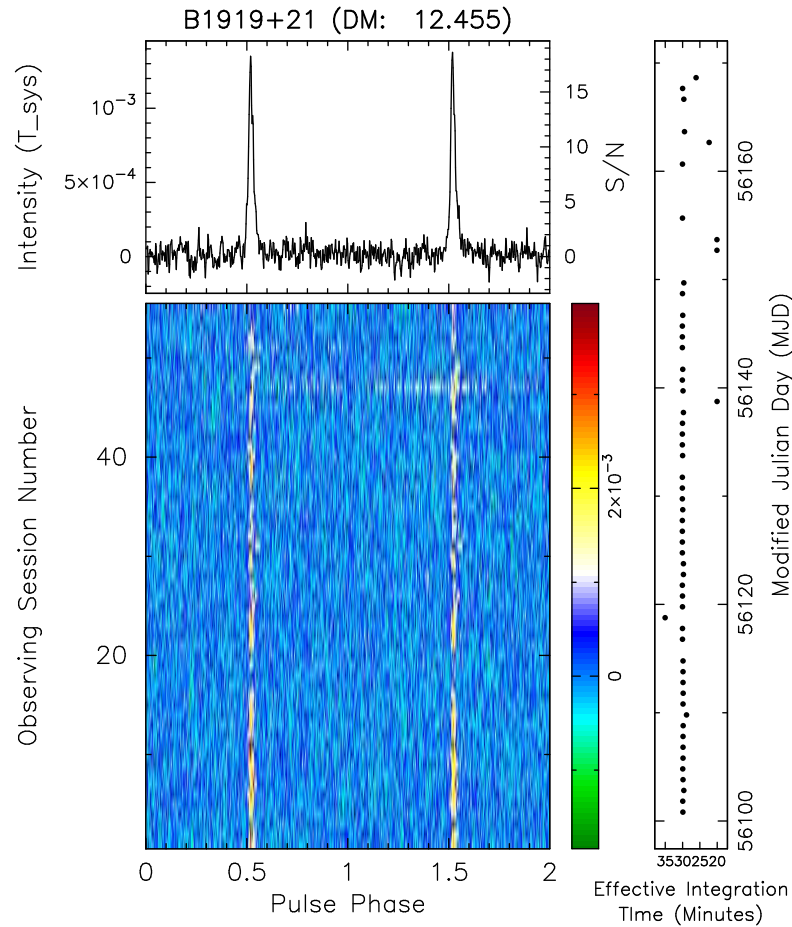


Figure 6.14: The main panel shows the time-aligned average profiles of the control pulsar B1919+21, observed at different epochs. The observing session numbers are arranged in ascending order of their date of observation, i.e., the last session corresponds to the latest observations. Data are folded at twice the pulsar period, to confirm the periodicity. Top panel shows the co-added average profile. For each of the observing sessions, corresponding to each row in the main panel (i.e., image plot), a dot is marked in the right hand side panel indicating the modified julian day (MJD) of the observation, and the effective integration time.

sessions and those of the co-added average profile is assessed. Following a process similar to preparing the folded-dyn-spectra, data are dedispersed and folded at twice the pulsar period for each of the observing sessions. These 2P-folded profiles are then plotted, stacked above each other, along with the co-added profile to assess the above mentioned consistency. Such a stack using about 55 days of observations towards our control pulsar B1919+21, is shown in Figure 6.14.

We end this section with a sample detection illustrating the enhancement in sensitivity achieved by combining the multi-epoch observations in phase. Before the deep search observing

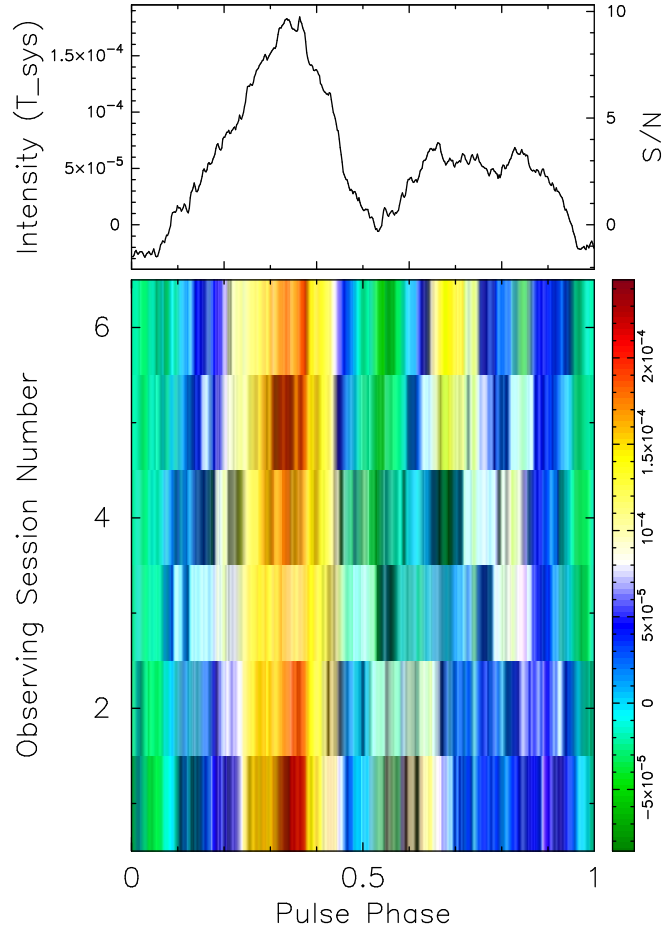


Figure 6.15: The image plot shows the time-aligned average profiles of the high DM pulsar B0525+21 observed at different epochs. Top panel shows the co-added profile.

program, the highest DM at which a pulsar had been detected at decameter wavelengths, using the Gauribidanur telescope, was 34.4 pc/cc (Pulsar B0628–28; Deshpande, 1987; Deshpande & Radhakrishnan, 1992). By time-aligning and co-adding the observations carried out at a number of different epochs, we are able to detect an appreciably high DM pulsar, B0525+21 at a DM of about 50.94 pc/cc. For each of the ~ 40 -minute observing sessions in the direction of this pulsar, we computed dedispersed average profiles. None of these average profiles have S/N more than 4 to 5σ , and on many days the pulse strength was well below 3σ . Hence, a detection could not have been made using only the individual observing sessions. However, the consistency in the rotation phase at which the weak pulse appears across various observing sessions, confirmed the detection of the periodic signal from this pulsar. Also, it allowed us to obtain a relatively higher S/N average profile

by phase-aligning and co-adding the folded profiles observed on different days. In Figure 6.15, we have chosen data from 6 epochs (out of 13 sessions) when the pulse strength was more than 3.5σ , and time-aligned the average profiles from these sessions. A co-added profile with S/N of about 10σ , and consistency of the arrival phase of the main pulse component (at around normalized pulse phase of 0.45 in the above figure) at various epochs is clearly visible. The profiles, co-added as well as those from individual sessions, have been smoothed with a 45° (i.e., 0.125 of the normalized pulse phase) wide window, to enhance the S/N. The second pulse component, at around normalized pulse phase of 0.75, is weak and not visible at all the epochs. Note that the widths of both the components are quite large, probably due to scattering, and the periodic signal could still be detected because of the large rotation period of the pulsar.

6.8 Summary

A large population of gamma-ray pulsars has been emerging since the launch of the *Fermi*-satellite. A significant fraction of these pulsars have been found to be radio-quiet in the follow-up searches at high radio frequencies so far. In this chapter, we have presented our motivation to search for counterparts of these so far “radio-quiet” gamma-ray pulsars at decameter wavelengths. We have described in detail the telescope and the observing setup used to carry out the observations at these low frequencies. Further, we have discussed the relative importance of different kinds of searches at these frequencies, and have presented in detail the methodologies of these search techniques. We have also presented a few examples of pulsars at 34 MHz and 53 MHz, demonstrating the potential scope of these searches at such low frequencies. In the next chapter, we will present results of our searches for decameter wavelength counterparts of several of the radio-quiet gamma-ray pulsars.

Chapter 7

Search for radio counterparts of gamma-ray pulsars: A possible detection and other results

Various search strategies described in the previous chapter were applied to the archival data as well as to the data obtained from the deep search observations. The archival data of the pulsar/transient survey, available in the direction of 17 of the radio-quiet gamma-ray pulsars¹, were searched for periodic as well as any transient pulsed signal. All except one of our target pulsars remained undetected in both kind of searches. Our possible detection of periodic radio pulses along the direction of the LAT-pulsar J1732–3131, corresponds to a period of 0.19652 ± 0.00003 seconds and dispersion measure of 15.44 ± 0.32 pc/cc. We discuss the details of this candidate detection in section 7.1, followed by results of our deep follow-up observations of this star in section 7.2. None of our target gamma-ray pulsars could be detected above a threshold of 8σ , in our deep search for pulsed signal at the expected periodicities. In section 7.3, we present the upper limits on decameter wavelength flux density from our target sources. Intriguingly, a few strong dispersed pulses were discovered in a couple of observing sessions. These detections are briefly described in section 7.4, followed by a summary of our search results in the last section.

Publications based on this chapter: Maan *et al.* (2012) and Maan & Aswathappa (2014).

¹Three of these gamma-ray pulsars (J1741–2054, J1907+0602 and J2032+4127) are no more radio-quiet now, see Table 6.1.

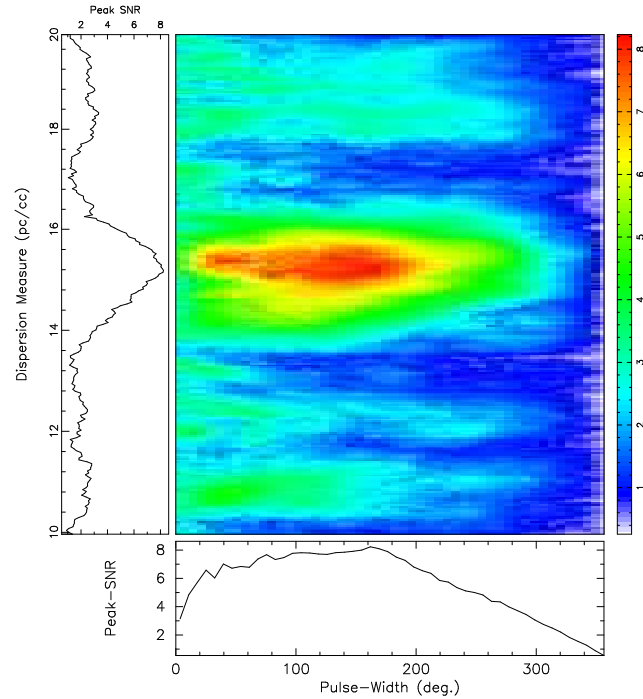


Figure 7.1: The body of the figure shows the S/N of the peak in the folded profiles corresponding to each combination of the trial values of smoothing-width and DM. The plateau defining the preferred combinations is apparent in the range ~ 80 - 180 degrees in smoothing-width, and ~ 14.8 - 15.6 pc/cc in DM. For ease of viewing the typical variations, the left and bottom panels provide vertical and horizontal cuts at smoothing-width= 160° and DM= 15.19 pc/cc through the data plotted in the central panel.

7.1 A candidate detection of radio emission from J1732–3131 in archival data

The candidate detection of periodic radio pulses from this pulsar has been possible in only one of the many sessions of observations made with the Gauribidanur radio telescope, when the otherwise radio weak pulsar may have apparently brightened many folds. The details of the results of our periodic and single-pulse search, and their implications relevant to both, the pulsar and the intervening medium, are presented below.

7.1.1 Search for periodic pulsed signal

We carried out a search in the 3-D space of DM , $pulse-width$, and $period$, following the procedure described in section 6.6. A two-dimensional cut in the DM , $pulse-width$ space, of the

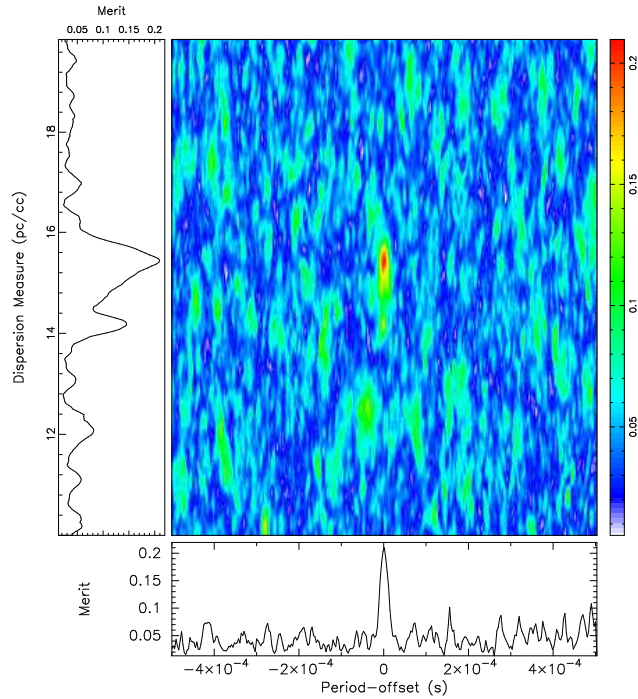


Figure 7.2: The main panel shows the significance of the folded profile as a function of DM and period. A narrow range of period-values around the actual period has been chosen. For the best-fit period, the figure-of-merit variations as a function of DM are shown in the left subplot. Corresponding to the best-fit DM (15.44 pc/cc), the bottom subplot shows the variations of figure-of-merit as a function of the period-offset.

results of our 3-D search procedure applied to data from one of the observing sessions in 2002, is shown in Figure 7.1. Clearly, a broad pulse is detected at DM of 15.2 ± 0.4 pc/cc; see the S/N profile in the bottom panel, where a broad S/N peak is seen in the range ~ 80 -180 degrees, indicating structures within the pulse on these scales. We note however that the S/N of the peak in the average profile as a figure of merit can lead to large errors in estimating the true DM when the individual frequency channel profiles have poor S/N, as is the case presently. There is also a related bias towards compactness of the average profile while searching for best-fit DM. We therefore use the sum-of-squares (SSQ) of average intensities across the profile, as discussed in the previous chapter, as a figure of merit. The significance of the average profile assessed in this manner and as a function of DM and period-offset is shown in Figure 7.2. The isolated peak in figure of merit map is striking and allows a less biased estimate of DM (15.44 ± 0.32 pc/cc), which we adopt in further discussion. Also, the period of 0.19652(3) s, suggested by this isolated peak, is consistent with that extrapolated from the available ephemeris (Ray *et al.*, 2011) to the epoch of our observation [0.19652125(2) s].

In Figure 7.3, the average profiles corresponding to the above mentioned two figures-of-

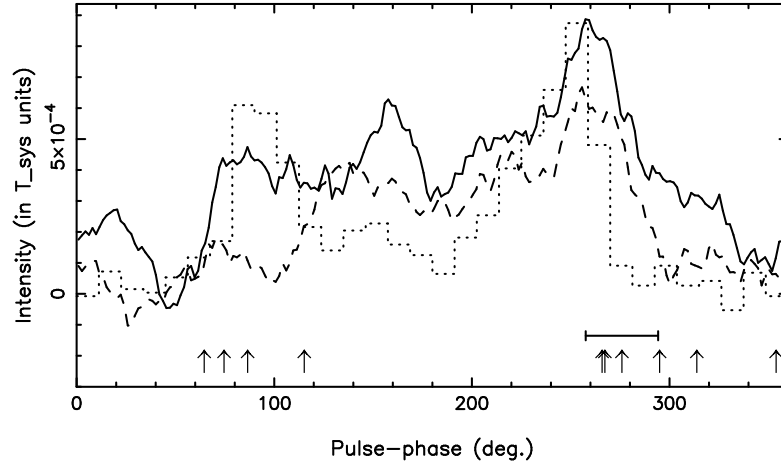


Figure 7.3: Average pulse-profiles at 34.5 MHz (solid and dashed; corresponding to $DM = 15.44$ pc/cc and 15.2 pc/cc respectively), a scaled version of the gamma-ray pulse-profile (dotted) and the positions of peaks of 10 bright pulses (arrow-marks) are shown together for ready comparison. The radio profiles were smoothed by a 25 degree wide window, and manually aligned with the gamma-ray profile. The horizontal bar denotes the average width of the bright pulses, which, on average, are about 200 times brighter than the peak intensity in the average profile.

merit are shown (peak S/N based: dashed-line; SSQ based: solid-line) for ready comparison. Both the profiles have been smoothed by only 25 degrees wide window, to retain the primary details in the profile, although the S/N would be less than optimum. We would like to emphasize here that although folding of random noise can also produce impressive profiles (as exemplified in Ramachandran *et al.*, 1998), peak amplitude in such profiles would still be constrained within the noise limits (i.e., full swing within 3σ to 4σ of the noise). In the present case, the peak-S/N in the average profile (Figure 7.3; solid-line) is estimated to be about 7. Here, the used value of noise standard deviation (in units of T_{sys}) is deduced directly from the time-bandwidth product, assuming only 75% of the total bandwidth. If we were to use a more optimistic estimate, using the rms-deviation computed from the dedispersed time sequence, the peak-S/N would exceed 9. It is clear that even the conservative estimate of the peak-S/N (i.e., 7) is well outside the above mentioned threshold, and hence the claimed signal in the average profile can not be dismissed as mere manifestation of random noise. Consistency of the periodic signal across the duration of our observation is shown in Figure 7.4.

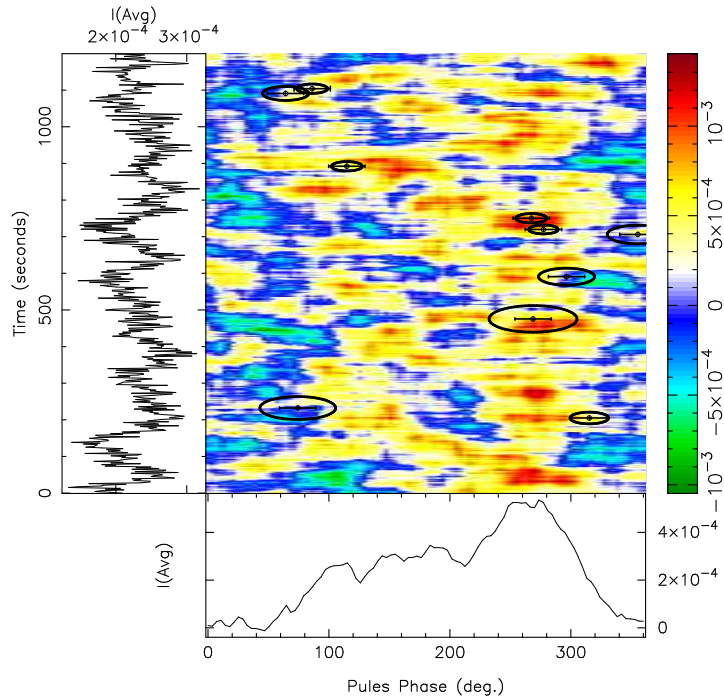


Figure 7.4: A stack of partially averaged profiles is shown in the body of the figure. Each of the profiles is smoothed by 60° in longitude to increase the S/N. The centers of the overlaid ellipses show the positions of 10 single pulses. The size of the ellipse is linearly proportional to the peak-S/N of the pulse, while the horizontal bars represent the pulse-width. The bottom sub-plot shows the net average profile. The average intensity in each of the sub-folds is shown in the left sub-plot.

7.1.2 Search for single bright pulses

In our search for single bright pulses, with different trial DMs and smoothing widths, we found the highest number of pulses (10) exceeding our detection threshold of 4.5σ at a trial DM of 15.55 pc/cc, and a smoothing width of 8 time samples, in contrast with the expectation of less than one pulse from noise excursions (specifically, 0.27 for the sequence of 77950 independent samples). These single pulses vary in their strengths from 4.5σ to 5.2σ , and were found to be distributed more or less uniformly throughout the total duration of the observation (see Figure 7.4). When these 10 individual pulses (belonging to the DM-bin of width 0.29 pc/cc) were aligned and averaged together, the signal-to-noise ratio (S/N) improved as expected, providing a refined estimate of DM (15.55 ± 0.04 pc/cc). Figure 7.5 shows this average, where the dispersive nature of the resultant pulse in the dynamic spectrum is apparent. But, we need to remind ourselves that however appealing the appearance of such an average dispersed pulse may be, it is to be viewed with caution. A relevant illustration, though in a different context, can be found in Goldsmith *et al.* (2008), where

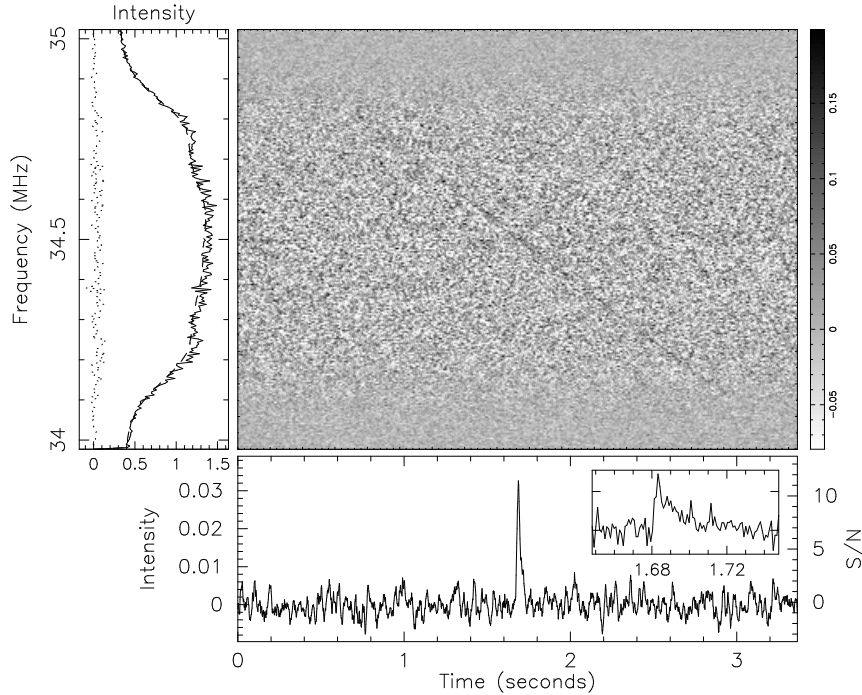


Figure 7.5: Dynamic spectrum of the 10 single pulses aligned and averaged together (to enhance S/N) is shown in the main panel. The data are smoothed by a rectangular window of width about 16 ms. The bottom sub-plot shows the pulse obtained after correcting for the delays corresponding to $DM = 15.55$ pc/cc. The left panel shows the average spectrum (dashed), the spectrum corresponding to the pulse-peak (solid) and the residuals (dotted) on the same scale. The inset in the bottom subplot shows average dedispersed pulse without any smoothing.

constructive alignments and co-additions are shown to result in spurious peaks which are entirely due to random noise. The present situation is potentially no different from the above example, except that now we might have noise manifestations that are pre-selected on the criteria of better match with certain dispersive characteristics. When many such realizations are combined, as in our average of 10 pulses, naturally the result will show the same dispersive pattern even more clearly. The only parameter which will distinguish between possible spurious pattern and the real signal, if any, is the S/N of the resultant pattern. Hence, to assess the real significance of the resultant average pulse, the above procedure was repeated a number of times, in each using 10 strongest pulses at an arbitrarily chosen DM (understandably, this required us to reduce the threshold). The corresponding average dedispersed pulse was found to be consistently weaker than that in Figure 7.5. However, the difference was not very significant (S/N lowered only by 1 or 2). This is not very surprising considering the fact that S/N of 4 out of the 10 pulses (at the candidate DM of 15.55 pc/cc) are only

marginally above our detection threshold (a higher detection threshold of 5σ would have left with us only 2 excursions which are too few to seek a refined DM). Given this poor distinction between the average of ten pulses at the candidate DM and those at other DMs, the confidence with which inferences can be drawn about their possible association with the pulsar (assessed through their apparent longitudes), their average width and a refined DM they may imply, is rather limited, and these results are to be viewed with due caution².

7.1.3 Confirmatory Checks

To further assess the credibility of the above detection, the folded profiles prepared using the two halves of the frequency band separately, and those using alternate frequency channels were examined for the dispersion signature correspondingly. In another sanity check, a two-dimensional search in DM and pulse-width was carried out on the folded profiles made using only odd and even period-numbers separately. Both independently showed peak around $DM \sim 15.4$ pc/cc. We also carried out these searches on two fields observed on the same day just 20 minutes (in right ascension) prior to and after the field containing the candidate. No sign of dispersed signal around this period was found in either of the fields. This makes it unlikely that the above detection of a periodic signal could have been a result of some man-made or system originated signal.

Intriguingly, for rest of the 9 observing sessions, neither of the two kinds of searches showed any significant detection. In the following section, we discuss various possibilities which may have caused these non-detections, along with the implications of parameters determined from our data (see Table 7.1).

In any case, the confirmatory checks described above are of relevance and importance in any search of periodic signals, and are recommended for weeding out spurious manifestations of noise and RFI.

7.1.4 Discussion

In Figure 7.3, the average profile of the LAT-pulsar J1732-3131 at 34.5 MHz (solid-line) is compared with the pulse-profile as seen in gamma-rays (dotted-line; Ray *et al.*, 2011, see their Figure 25). The radio profiles have been aligned with gamma-ray profile manually, since the accuracy in the

²Our detection threshold is admittedly and deliberately kept low (4.5σ) compared to those commonly used, to minimize the probability of ‘miss’, which of course increases the false-alarm rate. Hence, there is a finite probability that some or most of these excursions may not correspond to the sky signal we are looking for. We note, however, that these observations were conducted at late night hours, when possible RFI is at its minimum, if not absent. The fact that the excursions span such a narrow range above our particularly low detection threshold, suggests to us absence of contamination from RFI, narrowing the causes to random noise or real signal. These single pulses also passed our “swept-frequency” scrutiny described in section 6.5.1.

Table 7.1. Measured and Derived parameters for PSR J1732-3131

Known Parameters (from Ray <i>et al.</i> , 2011)		Measured and Derived Parameters	
Right Ascension (J2000.0)	17:32:33.54	Dispersion Measure (pc/cc)	15.44 ± 0.32
Declination (J2000.0)	-31:31:23.0	Best-fit Period (s)	0.19652 ± 0.00003
Pulse Frequency (s^{-1})	5.08794112	Epoch of period (MJD)	52384.9209
Frequency first derivative (s^{-2})	-7.2609×10^{-13}	Distance, d_{PSR} (pc)	600 ± 150
Epoch of frequency (MJD)	54933.00	Pulse Width (degrees)	< 200

estimated DM value is not adequate enough for absolute phase-alignment. The apparent similarity between the profiles at these two extreme ends of the spectrum is striking, although there are possible differences. At radio frequencies, the significant pulsed emission is confined to about 70% of the period, with possibly bridging emission between the two gamma-ray components (i.e., between 120° to 220°).

Origin of single pulses in the direction of J1732–3131 ?

The distribution of single bright pulses (Figure 7.3; see the “arrow-marks”) in longitude is bimodal rather than uniform, visiting regions near the leading and trailing components of the main broad pulse in the radio-profile. Given that (1) no obvious association of these single pulses with any of the known pulsars in the field-of-view is apparent (based on DM), (2) the dispersion measure suggested by these bright pulses ($DM=15.55 \pm 0.04$ pc/cc) falls within the uncertainty limits of that associated with the periodic signal (15.44 ± 0.32 pc/cc), (3) the profile shapes at these two DM values are indistinguishable (not shown in figure 7.3, but assessed separately), and (4) the positions of these pulses are correlated with the outer regions of the pulse-window; it is difficult to rule out the possibility that these single pulses share their origin with the periodic signal. At the same time, the statistics of only 10 pulses is too poor to conclusively rule out chance segregation in longitude. Giant pulses/radiation spikes are usually seen to confine themselves within the average pulse window (Lundgren *et al.* , 1995; Ables *et al.* , 1997). However, in the case of J0218+4232 (Knight *et al.* , 2006), the giant pulses concentrate just outside the rising and trailing edges of the broad radio pulse, and interestingly, those regions match with the locations of the peaks in the high energy (X-ray) profile. If our single pulses are real, then their apparent distribution is reminiscent of the situation in J0218+4232, and the peaks in the gamma-ray profile could correspond to the single pulse locations if the gamma-ray profile were to be shifted by about 180° compared to what is shown in Figure 7.3 (gamma-ray profile presented in Figure 7.3 was shifted by an unknown amount for easy comparison with the radio data). Given this, and the apparent relative brightness of our

single pulses, the possibility of their being “giant” pulses can not be ruled out.

Flux density estimate

The half-power beam-width at this declination is almost 35° (in declination). Therefore, we take the sky temperature estimates at various points across the beam from the higher resolution synthesis sky-map at 34.5 MHz (Dwarakanath & Udaya Shankar, 1990), and a weighted average of these using a theoretical beam-gain pattern provides us an estimate for the system temperature. For the present case, it is estimated to be 57000°K (receiver temperature contribution is negligible). Using this calibration, and assuming an effective collecting area of 8700 m^2 (in the direction of the pulsar) we estimate the average flux density (pulse-energy/period) of this pulsar at 34.5 MHz to be about 4 Jy. The average peak flux density of the 10 bright pulses would be about 800 Jy.

Non-detection at other frequencies and in other observing sessions

The mean flux density at 34.5 MHz, combined with the upper limit on the flux density at 1.4 GHz (0.2 mJy; Camilo *et al.*, 2009), suggests a spectral index $\alpha \lesssim -2.7$ assuming no turn-over in the spectrum (a tighter upper limit given by Ray *et al.* 2011 from their deeper search suggests further steeper spectral index). Although such a steep spectrum could explain the non-detection of the pulsar at higher frequencies, its detection in only one out of ten observing sessions at 34.5 MHz necessitates consideration of following possibilities.

1. *Extrinsic to the source:* This pulsar may actually be emitting below our detection limit, and favorable refractive scintillation conditions possibly raised the flux above our detection limit during one of our observing sessions.
2. *Intrinsic to the source:* The source may be an intermittent pulsar or a radio-faint pulsar which comes in “radio-bright” mode once in a while.

In either of the above possibilities, the spectral steepness mentioned above would be an overestimate.

Distance estimates

For $\text{DM}=15.4\text{ pc/cc}$ and the direction of the pulsar ($\text{RA}=17:32:33.54$, $\text{Dec}=-31:31:23.00$), the Cordes & Lazio (2002, here onwards C&L) electron density model yields³ a pulsar distance (d_{PSR}) of $600 \pm 150\text{ pc}$. This agrees well with the d_{PSR} estimates of $0.77^{+0.41}_{-0.35}\text{ kpc}$ and $0.86^{+0.49}_{-0.30}\text{ kpc}$ by Wang (2011), using the correlation between the gamma-ray emission efficiency and a few pulsar parameters (generation-order parameter and B_{LC}). Alternatively, these distance estimates

³The typical uncertainty in distance estimated using the C&L model, as quoted above, is believed to be 25%, however in some cases the estimates can be uncertain even by a factor of 2.

combined with the model electron density along the pulsar direction, give consistent DM value. However, the pulse broadening because of the interstellar scattering as predicted from C&L model (87_{-35}^{+50} ms), appears to be over-estimated by a large factor, given the narrow widths of bright pulses (about 20 ms or narrower) and the width of pulse components in the average pulse-profile.

Follow-up observations at higher frequencies (100 to 300 MHz) and with better sensitivity would be useful for confirming the most likely association of the bright pulses with the pulsar, and might help in improving the DM estimate. If confirmed, the comparison between the pulse profiles in the two extreme parts of the electromagnetic spectrum, and the location of radio bright single pulses would provide further insight into emission in the form of giant pulses (e.g., Hankins *et al.* , 2003; Knight *et al.* , 2006) or radiation spikes (e.g., Ables *et al.* , 1997).

7.2 Deep follow-up observations of J1732–3131

Motivated by the above detection, we have carried out deep follow-up observations of J1732–3131 and several other gamma-ray pulsars, using the observing setup described in the previous chapter. In the direction of J1732–3131, we carried out 125 observing sessions, each 30-minutes long, amounting to a total of 62.5 hours. Data from each of the observing sessions were subjected to search for bright single pulses as well as periodic signal. No significant detection was made in either of the searches. In our single pulse search, all the candidates above 5σ were examined, while a threshold of 8σ was used for a confident detection in the search for period signal. We also combined the data from all the observing sessions using the known ephemeris of this pulsar (Ray *et al.* , 2011), however no dispersed periodic signal above our threshold of 8σ was found. The upper limits on pulsed emission from this pulsar, at our detection thresholds, are provided later in this chapter along with those for the other target sources.

Although, we did not have any significant detection in our above mentioned searches, possibility of a signal weaker than our detection threshold can not be ruled out. Since we have an estimate of the dispersion measure from our candidate detection of this pulsar, we can look for possible presence of a weak periodic signal at that DM and which is consistent across our observing sessions. Further, allowing for the possibility that the periodic signal might be very weak, if at all present, we carefully chose the observing sessions that are virtually free from RFI contamination (assessed by visual inspection of dynamic spectrum), and where the dedispersed folded profiles have amplitude range more than 4σ . Such average profiles, corresponding to 21 observing sessions, are time-aligned and presented in Figure 7.6. For comparison, we have overlaid the average profile from the original detection (dotted line) on the net average profile of all the 21 sessions (solid line) in the upper panel. The two profiles are manually aligned, since the time-stamp accuracy of the archival observation is not adequate enough. The two profiles, observed 10 years apart, are strikingly similar,

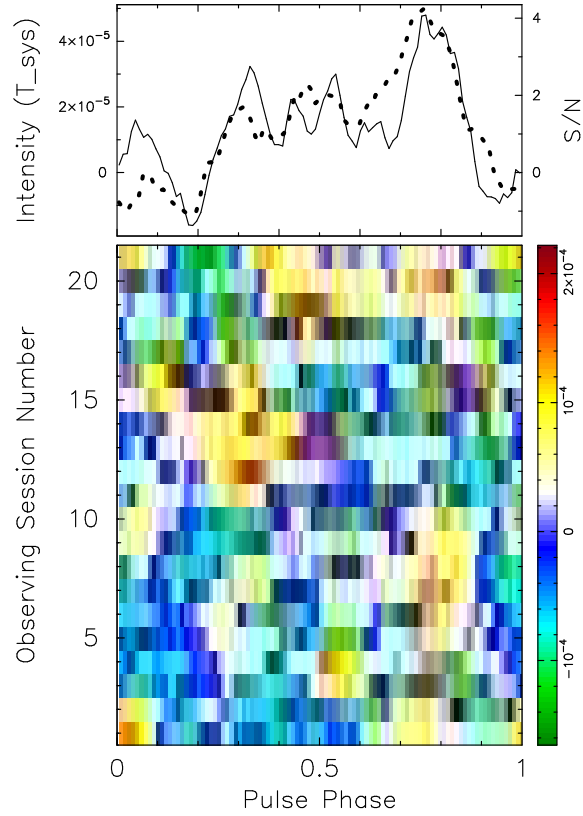


Figure 7.6: Various rows in the color image show time-aligned average profiles of J1732–3131 observed at different epochs. The upper panel shows the net average profile (solid line) and the average profile from our candidate detection in archival data (in dotted line; see Figure 7.3), for ready comparison. Intensity range of the latter profile is normalized to that of the former. All the individual profiles in the color image as well as the two profiles in the upper panel are smoothed by a 45° wide window.

and consistent with each other within the noise uncertainties.

Note that the peak-to-peak S/N of the average profile is barely reaching about 5σ . However, the observed consistency between the average profile shape obtained by combining data from multiple epochs (21 sessions) and that from the original detection 10 years ago, compels us to infer that (a) our candidate detection was not a mere manifestation of noise or RFI, and (b) the LAT-pulsar J1732–3131 is not radio-quiet. If true, the dispersion measure to this pulsar is 15.44 ± 0.32 pc/cc.

7.3 Upper limits on pulsed radio emission

Single pulse search sensitivity

In our single-pulse searches, the peak flux density $S_{\text{peak}}^{\text{SP}}$ of a temporally resolved pulse (Cordes & McLaughlin, 2003), is given by the radiometer equation:

$$S_{\text{peak}}^{\text{SP}} = (S/N)_{\text{peak}} \times \frac{2k_B T_{\text{sys}}}{A_e(z) \sqrt{n_p} W \Delta\nu} \quad (7.1)$$

where, T_{sys} is the system temperature⁴, $A_e(z)$ is the effective collecting area as a function of zenith-angle (z), $\Delta\nu$ is the observation bandwidth, n_p is the number of polarizations, and $(S/N)_{\text{peak}}$ is peak signal-to-noise ratio of the pulse corresponding to a smoothing optimum for its observed width of W . For Gauribidanur telescope, n_p is equal to 1.

A pulse with intrinsic pulse width, w_i , may get significantly broadened due to various pulse-broadening effects (e.g., interstellar scattering, receiver filter response time, etc.). Hence, the observed pulse width, W , can be expressed in terms of w_i and various pulse-broadening effects (see, e.g., Lorimer & Kramer, 2004) as

$$W = \sqrt{w_i^2 + \Delta t_{\text{samp}}^2 + \Delta t_{\Delta\nu}^2 + \tau_{\text{sc}}^2} \quad (7.2)$$

where, t_{samp} is the chosen sampling time, $\Delta t_{\Delta\nu}$ is the receiver filter response time, and τ_{sc} is the pulse broadening due to interstellar scattering. Note that we have not considered the residual dispersion smearing across widths of the individual frequency channels, since the trial DM range was sampled in appropriately fine steps.

Further, assuming that the pulse energy is conserved, we have $S_{\text{intrinsic}}^{\text{SP}} \times w_i = S_{\text{peak}}^{\text{SP}} \times W$; where $S_{\text{intrinsic}}^{\text{SP}}$ is the intrinsic peak flux density of the pulse. Hence, the minimum detectable intrinsic flux density, i.e., above a threshold of $(S/N)_{\text{min}}$, of a single pulse of intrinsic width w_i , can be expressed (see, e.g., Burke-Spolaor *et al.*, 2011b) as

$$S_{\text{intrinsic, min}}^{\text{SP}} = \frac{W}{w_i} \times (S/N)_{\text{min}} \times \frac{2k_B T_{\text{sys}}}{A_e(z) \sqrt{n_p} W \Delta\nu} \quad (7.3)$$

For a T_{sys} of 10000 °K, Figure 7.7 shows the minimum detectable pulse energy (i.e., $S_{\text{intrinsic, min}}^{\text{SP}} \times w_i$ for $(S/N)_{\text{min}}$ of 5) for intrinsic pulse widths of 1, 10 and 50 ms, as a function of DM. The solid and dotted curves correspond to the parameters of our new observations and the archival data, respectively⁵. To estimate τ_{sc} , we have followed the scatter broadening dependence

⁴ T_{sys} is equal to the sky temperature, T_{sky} , since the receiver temperature is negligible compared to T_{sky} at these frequencies.

⁵We have used the collecting area corresponding to a pointing declination at or near to the instrumental zenith of 14°.1. For a declination away from zenith, $S_{\text{min}}^{\text{SP}}$ will increase by a factor of $\sec(z)$.

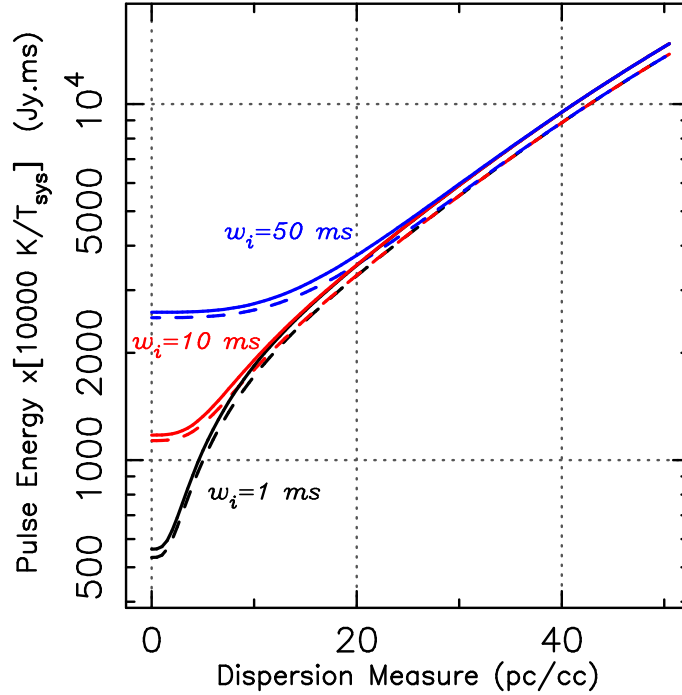


Figure 7.7: The curves of minimum detectable pulse energies, normalized by T_{sys} in units of 10000 °K, for intrinsic pulse widths of 1, 10 and 50 ms, are shown as a function of DM. The solid and dotted curves correspond to the new observations and the archival data, respectively.

on DM as modelled⁶ by Ramachandran *et al.* (1997). Note that the scatter broadening dominates over other pulse-broadening effects at sufficiently high DMs (above 10 and 25 pc/cc for w_i of 10 and 50 ms, respectively), beyond which sensitivity of our single pulse search, in terms of pulse energy, becomes independent of the intrinsic pulse width. For pulses with smaller intrinsic widths (< 1 ms), the observed pulse width is limited by our sampling time (~ 2 ms), and the corresponding sensitivity curves will follow that for $w_i = 1$ ms.

For a nominal observed pulse width of 100 ms, 5σ upper limits on peak flux densities detectable in our single pulse searches towards each of the target pulsars using the archival data and those from new observations are presented in Table 7.2 and 7.3, respectively. For the archival observations, our target sources were generally offset from the center of the beam. Assuming a theoretical beam-gain pattern, we calculated the factor F by which the beam-gain reduces at the

⁶The functional form of the scattering delays, as modelled by these authors, is: $\tau_{sc}(\text{ms}) = 4.2 \times 10^{-5} DM^{1.6} \times (1 + 3.1 \times 10^{-5} DM^3) \lambda^{4.4}$, where λ is the wavelength of observations in meters.

Table 7.2. Archival data: Upper limits on flux densities of 16 gamma-ray pulsars at decameter wavelengths

Target PSR	Pointing offset ($^{\circ}$)	T_{sky} ($^{\circ}\text{K}$)	$S_{\text{min}}^{\text{SP}}$ (Jy)	$S_{\text{min}}^{\text{P0}}$ (mJy)
J0357+3205	3	18100	71	217
J0633+0632	7	19900	87	265
J0633+1746	4	19900	76	230
J1741–2054	9	62600	371	1127
J1809–2332	6	62400	334	1017
J1813–1246	8	76000	366	1114
J1826–1256	8	80100	386	1174
J1846+0919	5	62900	248	755
J1907+0602	8	71700	335	1020
J1954+2836	6	45000	196	595
J1957+5033	4	35300	172	523
J1958+2846	6	47100	205	623
J2021+4026	5	43200	180	548
J2032+4127	6	38200	166	505
J2055+2539	9	35900	185	564
J2238+5903	4	28100	137	416

Note. — 1. “Pointing offset” is the difference between the pointing direction and the true direction of the target pulsar in declination. Note that the declination beam-width is $\sim 25^{\circ} \times \sec(\text{zenith-angle})$. The flux density limits computed at the beam center are corrected for targets offset from the pointing direction by assuming a theoretical beam-gain pattern, and the corrected limits are presented as $S_{\text{min}}^{\text{SP}}$ and $S_{\text{min}}^{\text{P0}}$.

2. The upper limits for both kind of searches are computed for a detection threshold of 5σ .

3. The sensitivity limits for the single pulse search are computed for a nominal pulse width of 100 ms, while those for the periodicity search are computed for a duty cycle of 10% and observation-duration of a single observing session, i.e., 1200 s.

target source position, relative to the beam-center⁷. The flux density limits estimated at the beam center were then scaled-up by the above correction factors computed for respective source position offsets. These corrected limits are presented in Table 7.2.

⁷Note that $F = 1.0$ at the beam-center, i.e., no pointing-offset, and $F > 1.0$ for non-zero offsets.

Table 7.3. Deep search: Upper limits on decameter wavelength flux densities of 10 gamma-ray pulsars

Target PSR	T_{sky} (°K)	$S_{\text{min}}^{\text{SP}}$ (Jy)	$S_{\text{min}}^{\text{P0}}$ (mJy)	Comparison with previous searches [†]			
				S_{previous} (mJy)	ν_{obs} (MHz)	$S_{\text{previous}}^{\text{Scaled}}$ (μJy)	$S_{\text{min}}^{\text{P0,Scaled}}$ (μJy)
J0357+3205	17200	67	34	0.043 ^c	327	2	20
J0633+0632	19900	76	28	0.075 ^c	327	4	17
J0633+1746	19900	96	36	150.0 ^a	35	94	21
J1732–3131	51400	271	73	0.059 ^c	1374	57	43
J1809–2332	74900	348	193	0.026 ^c	1352	24	114
J1836+5925	24700	128	55	0.070 ^c	350	4	32
J2021+4026	44100	181	92	0.051 ^c	820	17	54
J2055+2539	30400	114	60	0.085 ^b	327	5	35
J2139+4716	32500	143	74	0.171 ^d	350	11	44
J2238+5903	29700	154	82	0.027 ^c	820	9	48

Note. — The total effective integration time, used in computation of $S_{\text{min}}^{\text{P0}}$, excludes the time-intervals rejected as RFI contaminated. Time-intervals cumulating to about one observing session duration were rejected for J0633+0632, J0633+1746 and J1809–2332. For J1732–3131, only 85 sessions worth effective integration time could be used out of a total of 125 observing sessions.

[†] S_{previous} are the flux limits taken from literature at frequency ν_{obs} . Wherever needed, these limits were scaled to 5σ -level, before compiling into the table. For comparison, our limits at decameter wavelengths and those from literature are scaled to 1.4 GHz using a spectral index of -2.0 , and presented as $S_{\text{min}}^{\text{P0,Scaled}}$ ($= S_{\text{min}}^{\text{P0}} \times [\frac{1400}{34}]^{-2}$) and $S_{\text{previous}}^{\text{Scaled}}$ ($= S_{\text{previous}} \times [\frac{1400}{\nu_{\text{obs}}}]^{-2}$), respectively.

References — ^a Ramachandran *et al.* (1998); ^b Saz Parkinson *et al.* (2010); ^c Ray *et al.* (2011); ^d Pletsch *et al.* (2012).

Periodic signal search sensitivity

For periodicity searches, the minimum detectable flux density $S_{\text{min}}^{\text{P0}}$, i.e., at the threshold signal-to-noise ratio $(S/N)_{\text{min}}$, is given by (Vivekanand *et al.*, 1982):

$$S_{\text{min}}^{\text{P0}} = (S/N)_{\text{min}} \times \frac{2k_B T_{\text{sys}}}{A_e(z) \sqrt{n_p t_{\text{obs}} \Delta\nu}} \sqrt{\frac{W}{P - W}} \quad (7.4)$$

where, W is the pulse width, P is the pulse period and t_{obs} is the total integration time. For archival data, t_{obs} is equal to the total observation duration of a single session, i.e., about 1200 s. For new observations, t_{obs} equals the cumulative observation duration of all the sessions⁸.

⁸Since we have time-aligned and integrated data from all the observing sessions.

Although we insist on a minimum S/N of 8σ for a confident detection of periodic signal, we have examined and assessed all the candidates above 5σ . Table 7.2 and 7.3 present the average flux densities (S_{\min}^{P0}) which would have been detected 5σ -level in our search for signal at the expected periodicity of various target pulsars. For uniformity, we have assumed W to be 10% of the pulse period. For archival data, the flux density limits have been corrected for any source offset from the pointing-center, following the procedure explained earlier in the context of single pulse search sensitivity.

To compare our flux limits with those from the previous deep searches at higher frequencies, we have scaled the upper limits at decameter wavelengths and those at higher frequencies (from the literature) to 1.4 GHz. These scaled values are listed in the last two columns of Table 7.3. We have assumed a spectral index of -2.0 which lies on the steeper side of the average spectral index range for pulsars (-1.6 to -2.0 ; Maron *et al.*, 2000), and no turn-over in the spectrum till the frequency of our observations, i.e., 34 MHz. Despite the large background sky-temperature at our observing frequency, for a couple of stars our flux density limits are better than those from deep searches at higher frequencies, and in other cases they are only within a factor of few of the limits from shorter wavelength searches. If the lack of radio emission from the LAT-discovered pulsars is indeed due to unfavorable viewing geometries, then the stars which could possibly be detected at decameter wavelengths⁹ can be expected to have steep spectrum. If we assume a moderately steep spectrum with an index of -2.5 (for comparison, spectral index of B0943+10 is -3.7 ± 0.36 ; Maron *et al.*, 2000), most of our flux limits become better than or comparable to those reported at higher frequencies.

7.4 Giant radio pulses/flares from unknown source(s)

In a couple of observing sessions, when the telescope beam was pointed towards our target sources J0633+0632/J0633+1746, a few ultra-strong, dispersed pulses were detected in our single pulse search. The search results for one of these sessions are presented in Figure 7.8, wherein detection of a couple of strong pulses (peak $S/N > 40\sigma$, see the top-right and bottom panels) is clearly evident. Note that the histogram of ‘No.of points’ vs. DM is adversely affected by strong RFI occurrences at around 725, 745 and 878 seconds (apparent as vertical streaks in the bottom panel), but the strong pulses show themselves clearly in the S/N vs. DM plot (top-right panel) at a DM of about 2 pc/cc. A few relatively weaker pulses, but well above our threshold, were detected in another observing session, at a different DM of about 3.3 pc/cc.

⁹Because the probability of our sight-line passing through the emission beam increases at lower frequencies due to RFI.

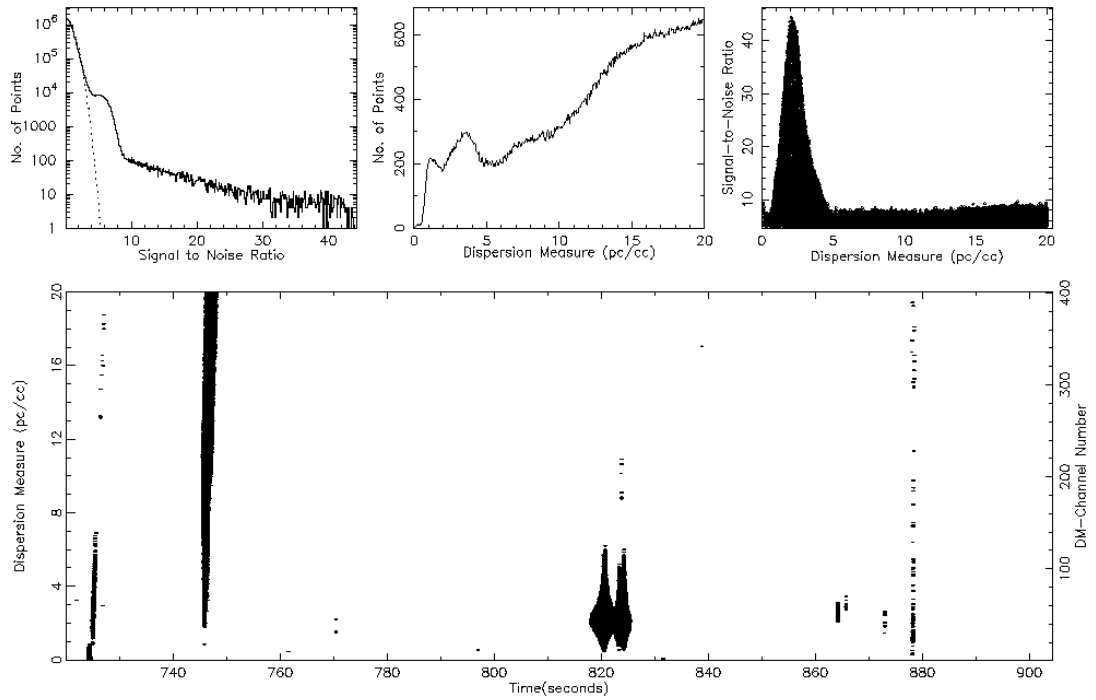


Figure 7.8: Single pulse search results presenting detection of bright dispersed pulses in one of the observing sessions discussed in section 7.4. For details of individual sub-plot contents, please refer to Figure 6.7.

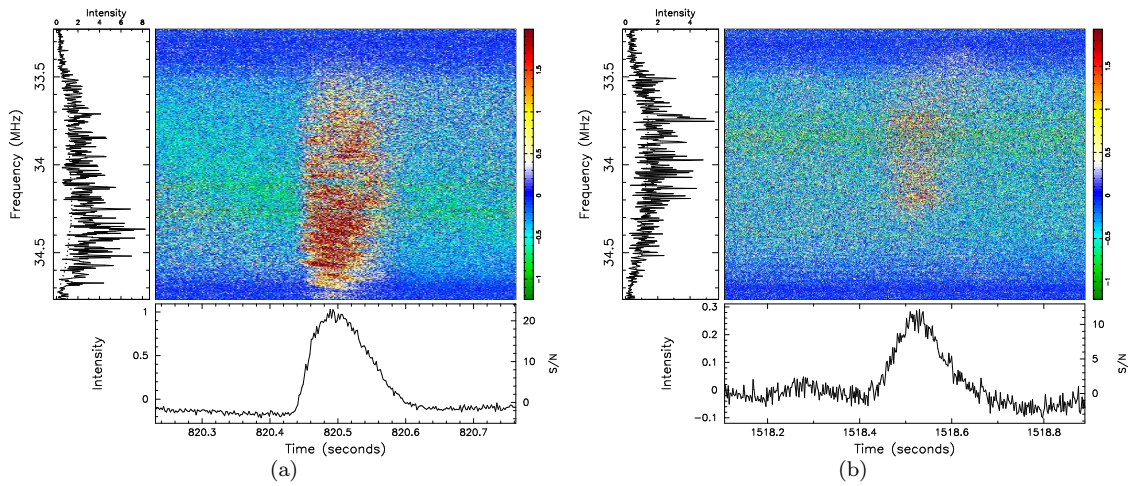


Figure 7.9: The dedispersed dynamic spectra of two bright pulses, one from each of the two observing sessions discussed in section 7.4, are shown in the central panels of (a) and (b). The bottom sub-panels show the average dedispersed profiles. The sub-panels on the left side show the spectral powers corresponding to the peak in the average profiles (solid line) and the average off-pulse spectrum (dashed line).

The dynamic spectra of the brightest pulses from each of the two sessions, after dedispersion using the respective most likely DMs, are shown in Figure 7.9. Note that the pulse in Figure 7.9(a) seems to have significant power throughout our observed bandwidth, while that in 7.9(b) has noticeable power only in about one third of the band near its center. Additionally, the first pulse also seem to have systematic modulation in its spectral power, indicating a possibility of its being highly linearly polarized. Further, assuming the sources to be at the respective beam-centers, the peak flux densities of these two pulses would be about 3300 and 1500 Jy, respectively. Note that the energies of these strongest pulses in the two sessions, about 330000 and 187500 Jy ms respectively¹⁰, are comparable to typical energies of giant pulses from the Crab pulsar at decameter wavelengths (Popov *et al.*, 2006). Hence, these detections may be revealing giant pulse emission from known/unknown pulsar like objects in our large field of view. Given the large difference¹¹ in two candidate DMs, it seems unlikely that the transient pulses detected in the two sessions originated from the same source.

The entire data for the two observing sessions were dedispersed using the respective candidate DMs. No significant signal at the expected periodicities of our target pulsars J0633+0632 and J0633+1746 was detected in the resultant time sequences. However, a possible association between these strong pulses and our target sources still can not be ruled out, and such a possibility is being explored further.

7.5 Summary

In this chapter, we have presented results of our single pulse and periodicity searches at decameter wavelengths, towards the direction of a total of 19 gamma-ray pulsars. Searches using the archival data from the pulsar/transient survey, as well as deep searches using new observations were carried out. We have presented a possible detection of J1732–3131, seen in the archival data, and discussed its implications relevant to the pulsar and the intervening medium. In our deep follow-up observations of this pulsar, no significant detection of pulsed emission (single-pulses or periodic signal) could be made. However, a low-S/N grand average profile (obtained from time-aligned, co-added data from several observing sessions) appears completely consistent with that from the original detection. This consistency in profile shape, at observing epochs 10 years apart, can be viewed as a compelling evidence that the pulsar J1732–3131 is not radio-quiet. Decametric signals from none of our other target gamma-ray pulsars exceeded our 8σ detection threshold. However, the non-detections provide useful upper limits on decameter wavelength flux density of these pulsars, as

¹⁰The widths of the two pulses are estimated to be about 100 and 125 ms.

¹¹The uncertainty associated with the candidate DMs is less than or of the order of 0.1 pc/cc.

listed in Table 7.2 and 7.3. Despite the large background sky-temperature, our flux density limits are comparable to or better than those from deep searches of these pulsars at high radio frequencies. Two of our target pulsars have shown intriguing indications of pulsed radio emission, although at a very low significance ($S/N \lesssim 5\sigma$). We are carrying out follow-up observations to enable deeper searches of pulsed radio emission from these candidates. Lack of radio detection from most of our target sources indicate that a large fraction of our sample may indeed be radio-quiet. Consequently, the high fraction of gamma-ray pulsars being radio-quiet is consistent with the predictions of “narrow polar-cap” models for radio beams and “fan-beam outer magnetosphere” models for gamma-ray emission.

Conclusions and future perspectives

Although there is a general consensus that the radio emission from pulsars originates from relativistic charged particles streaming along the curved magnetic field lines, the physical understanding of various observed phenomena and properties, e.g. pulse-nulling, variety of subpulse drifting, polarization mode changing, profile mode switching, origin of multiple emission cones, giant pulse emission, notches in the average profiles, etc., is still far from complete. The work presented in Part I and II of this thesis makes use of present understanding of the phenomenon of subpulse drifting to address the origin of radio emission in multiple cones and for tomographic studies of the pulsar polar emission regions. In the last part, we have presented our searches for dispersed (periodic as well as transient) signals in the direction of several radio-quiet gamma-ray pulsars at very low frequencies.

Part I: Origin of Radio Emission in Multiple Cones

In the qualitative framework of the *carousel model* (Ruderman & Sutherland, 1975), the coherent modulation in a subpulse sequence can be mapped back to the underlying pattern of sub-beams (see, for example, Deshpande & Rankin, 1999). However, the completeness with which the underlying configuration of sub-beams can be sampled depends on how close our line of sight approaches the magnetic axis. The bright pulsar B1237+25 with its special viewing geometry, where the sight-line traverses almost through the magnetic axis, provides an excellent opportunity to map and study the underlying patterns across the full transverse slice of its polar emission region. In Chapter 2, we presented our analysis on a number of pulse-sequences from this star to map, and study any relationship between, the underlying patterns responsible for the emission in two pairs of presumed conal-components and a core-component. We summarize the results obtained from our study of B1237+25 as below:

1. The underlying carousel of sparks for this pulsar appears to lack stability over long durations, even when the pulsar remains in the same emission mode. Our study of smaller length sub-sequences revealed low frequency modulations which could be associated to carousel rotation. The deduced circulation period appears, however, to vary over a large range (about 18 to 34 times the pulsar spin period).
2. Even for the shorter sub-sequences, the sweep of the modulation phase across the pulse longitudes deviates significantly from that predicted by the carousel model. Unless these deviations have significant contributions from pulse-nulling, mode-changing and/or inherent irregularities in the carousel on time-scales much lesser than the lengths of our individual sub-sequences, they pose a serious challenge to the widely accepted standard carousel model.
3. The emission patterns corresponding to the outer and the inner cones are found to be significantly correlated with each other, implying that the origin of emission in the two cones share a common seed pattern of sparks. This result is consistent with the same radio frequency emission in the two cones correspond to two different altitudes, but originating from a common seed pattern of sparks.
4. Interestingly, the emission patterns corresponding to the outer and the inner cones are found to be offset from each other, consistently across various sub-sequences, by about 10° in magnetic azimuth¹. This offset between the patterns at two different emission altitudes indicates certainly a twist in the emission columns, and most likely in the magnetic field geometry.
5. The core component also seems to share its origin with the conal counterparts, contrary to common belief that they are qualitative distinct emission components. Presence of a compact, diffuse and *further-in* carousel of sub-beams is consistent with the observed modulation in the core component of this pulsar. The featureless spectrum observed for many core-single pulsars can be explained readily when the diffuse pattern approaches uniformity.

While our study has revealed that the two emission cones share their origin to a common seed pattern of sparks, the different spectral properties of emission in the two cones, in light of this new connection, are yet to be understood. The emission altitude of the inner cone does not appear to evolve with frequency, as against the clear radius-to-frequency mapping manifested by the outer cone (Mitra & Rankin, 2002). Investigations of the correlation between the emission patterns of the two cones at multiple frequencies, preferably simultaneously, would help in understanding the near constancy of the emission altitude and the origin of the inner cone. Our simultaneous multi-

¹The observed offset does not have its origin in complexity of the orthogonal polarization modes.

frequency observations of this pulsar, carried out using the multi-band receiver with the Green Bank Telescope, pave the way for studying these aspects.

An incidental, but important, result of our study is that the modulation-phase variation as a function of the pulse longitude has *not* been found in agreement with that expected from the standard carousel model (Ruderman & Sutherland, 1975). There also have been difficulties in explaining the unusual subpulse modulation-phase envelope of B0320+39, in the standard hypothesis of a rotating carousel (Edwards *et al.*, 2003). Although the deviations from the expected phase envelope need to be assessed more carefully in light of possible perturbations to the carousel rotation due to nulling, mode-changing etc., there are several other related phenomena, e.g., observed asymmetry in the average profiles (in component locations as well as their amplitudes), multiple drift rates, variable separation between consecutive sub-pulses (i.e., variable P_2), phase-locked modulation between the main and the inter-pulse, etc., where the carousel model has lacked in providing an internally consistent explanation. Motivated by these aspects, one of our main objectives in the near future is to *redescribe* the subpulse modulation phenomenon in a way that is internally-consistent with the observed variety in modulation and the consequent observable effects in the average profiles. Consistency with several other phenomena (e.g. nulling, mode-changing etc.), which appear as intrinsic to the emission mechanism as the subpulse modulation, would be desirable in such a redescription.

Part II: Tomography of the Pulsar Magnetosphere: Development of a Multi-band Receiver

Radius-to-frequency mapping (Cordes, 1978) in pulsars suggests that the emission at higher frequencies originates closer to the star’s surface than that at lower frequencies (Komesaroff, 1970; Cordes, 1978). Hence, simultaneous polar emission mapping at multiple frequencies would essentially reconstruct emission details in multiple transverse slices of the radio emission cone at the corresponding emission altitudes, providing a “tomograph” of the polar emission region. Such tomographic studies would reveal not only the evolution of sub-beams across the magnetosphere but can also provide much needed clues about the generation of the sub-beam patterns, and their possible connection with the profile/polarization mode changes observed in various pulsars. Simultaneous multi-frequency observations are usually carried out by simultaneously using several telescopes, each operating at different frequency. However, many technical constraints and difficulties encountered in practice, some of which are discussed in Chapter 3, fail to render the desired advantages of such observations. A superior and optimum alternative is to use a suitable receiver system, which can cater to simultaneous sampling of a number of pre-selected frequency bands, with a large aperture telescope. In Chapter 4, we have presented design and development of such a unique receiver — RRI-GBT multi-band receiver (MBR). Main features of the MBR include:

1. The MBR is a self-contained receiver system which includes a suitable feed, broadband front-end, parallel analog and digital receiver pipelines, along with appropriate monitoring, synchronization and data recording systems.
2. When used with a large aperture, the MBR facilitates sensitive observations, with high time and spectral resolution, simultaneously in 10 discrete frequency bands sampling a wide spectral span (100 MHz–1500 MHz) in a nearly log-periodic fashion. The raw voltage time sequences corresponding to each of the two linear polarization channels for each of the 10 spectral bands are simultaneously recorded, each sampling a bandwidth of 16 MHz at the Nyquist rate.
3. The dual-polarization multi-band feed, a key part of the MBR, is designed to have good responses only over the 10 discrete bands pre-selected as relatively RFI-free, and hence provides preliminary immunity against RFI. The frequency bands known to be severely affected by RFI are filtered out explicitly, soon after the signals from the feed are pre-amplified.
4. The MBR also offers significant tunability of the center frequencies of each of the 16-MHz wide sub-bands separately, within the spectral spans of respective bands.
5. Once the wide-band RF signal is split into 10 fixed sub-bands, the 10 signals are processed through very similar high gain chains. Similarity of the sub-band receiver chains provides desired compatibility, in addition to an easy inter-changeability of these units, if required, and an overall modularity to the system.
6. Quasi-real-time monitoring of spectra, as well as total power time sequences, is also facilitated.

The MBR was successfully built, and used with the 110 meter Green Bank Telescope to conduct test observations on a few bright continuum sources, and about 20 hours of observations on a number of bright pulsars. Beam-widths corresponding to the two polarizations, estimated simultaneously in all the 10 bands from a slew scan across Cas-A, indicate that the multi-band feed illuminated the GBT dish uniformly across the frequency, and the illumination efficiency is estimated to be about 75%. Using the pulsar observations, we have presented in Chapter 5, a preliminary tomograph of the polar emission region of B0809+74, and a study of the spectral evolution of emission altitudes and flux density of B0329+54.

Although the MBR system design is optimized for tomographic studies of pulsar polar emission regions, simultaneous multi-frequency observations with such a system offer particular advantages in fast transient searches. The MBR is also suitable for several other astronomical investigations, e.g., studying the spectral evolution of average properties of pulsars and propagation effects, single-dish continuum studies and surveys/studies of recombination lines.

Part III: Searches for Decameter-wavelength Counterparts of Radio-quiet Gamma-ray Pulsars

Despite deep radio follow-up searches, a significant fraction of the known gamma-ray pulsar population has remained undetected. One of the possible explanations for the apparent absence of radio emission from these pulsars — known as “radio-quiet” gamma-ray pulsars — is that their narrow radio beams may be missing the line of sight towards earth (Brazier & Johnston, 1999). The radius-to-frequency mapping in radio pulsars suggests that the emission beam becomes wider at low radio frequencies, increasing the probability of our line of sight intercepting the radio beam. However, all of the previous deep searches were carried out at higher radio frequencies, and the lower frequency domain ($\lesssim 100$ MHz) had remained relatively unexplored. Given the widening of emission beam, follow-up searches of these pulsars at low radio frequencies could also be revealing. With this view, we searched for pulsed emission along the direction of several of these gamma-ray pulsars, using the archival data of the pulsar/transient survey as well as extensive follow-up and new observations at 34 MHz with the Gauribidanur telescope (Chapter 6 and 7). Highlights of our searches, and results obtained therefrom, are:

1. We searched for decameter wavelength counterparts of a total of 16 *radio-quiet* gamma-ray pulsars. Archival data were used to search for counterparts of 17 gamma-ray pulsars (3 of which are already known to have radio counterparts from searches at higher frequencies), while new extensive observations were carried out in the direction of 10 gamma-ray pulsars. Eight of the target pulsars were common to both, the archival and the new observations.
2. Time-aligning and combining of observations from different epochs allowed us to carry out deeper searches for signals at the expected periodicities of the gamma-ray pulsars. Despite the large background sky-temperature at decameter wavelengths, the minimum detectable flux density in our deep searches are comparable with those from previous searches at higher frequencies, when scaled using a spectral index of -2.0 and assuming no turn-over in the spectrum.
3. A possible detection of periodic radio pulses from J1732–3131 was made, using the archival data, at a dispersion measure (DM) of 15.44 ± 0.32 pc/cc. We also detected 10 individual bright pulses in the same observing session, although marginally above the detection threshold, at a DM consistent with that associated with the periodic signal. The apparent brightness of these single pulses, and similarity of their apparent distribution in pulse-longitude with that of giant pulses in J0218+4232, suggest that these might be giant pulses. Our DM-based distance estimate, using Cordes & Lazio electron density model (2002), matches well with earlier estimates based on gamma-ray emission efficiency.

4. In our follow-up deep searches, we could not detect any readily apparent pulsed radio signal (neither periodic nor single pulses) from J1732–3131, i.e., above a detection threshold of 8σ . However, when we time-aligned and co-added data from observing sessions at 21 different epochs, and dedispersed using the DM estimated from the candidate detection, the average profile shape is found to be completely consistent with that from the candidate detection. Finding a matching profile shape after 10 years of the original detection suggests that the signal is unlikely to be due to RFI or a mere manifestation of random noise.
5. In a couple of the observing sessions towards the telescope pointing direction of RA=06:34:30, DEC=10°, we detected a few ultra-bright pulses at two different DMs of about 2 pc/cc and 3.3 pc/cc, respectively. However, when dedispersed at the DMs suggested by the bright single pulses, no significant signal was found at the expected periodicities of our target pulsars J0633+0632 and J0633+1746, which would be in the telescope beam centered at above coordinates. Energies of these strong pulses in the two observing sessions are comparable to typical energies of giant pulses from the Crab pulsar at decameter wavelengths.
6. No significant pulsed signal (periodic or transient), above a detection threshold of 8σ , was found towards the directions of other selected radio-quiet gamma-ray pulsars. However, our searches have provided useful upper limits on the decameter-wavelength flux densities of these pulsars.

Non-detection of pulsed radio emission from a majority of our target pulsars, despite the sensitive set-up at a low radio frequency, indicate that a large fraction of our sample may indeed be radio-quiet, consistent with the predictions of “fan-beam outer magnetosphere” models for gamma-rays *together* with “narrow beam polar cap” models for the radio emission.

As a natural next step, we plan to observe, and search for radio counterparts of, several other *radio-quiet* gamma-ray pulsars in the second phase of our *deep-search* observing program. Also, the enhancement in sensitivity obtained by combining multi-epoch observations enables detection and study of larger number of radio pulsars at such low frequencies. Detailed studies of some important aspects of the radio emission from pulsars, e.g., changes in shape of the average pulse profile components, “radius-to-frequency mapping” of the emission, long term flux density variations, etc., are still lacking at very low frequencies. We plan to pursue some of these investigations in the near future, in addition to the studies of the intervening medium properties (e.g., interstellar scattering) at decameter wavelengths, with our sensitive set-up.

Since the dipole array is phased using the phase-gradients, instead of the delay gradients, the usable bandwidth is somewhat limited. However, test observations of B0834+06 have shown that bandwidth of about 2.5–3 MHz is still usable. To benefit from the available bandwidth, and the sensitivity obtained therefrom, a new receiver system — mini-Portable Pulsar Receiver (MPPR)

— that enables sampling a bandwidth of about 5 MHz at Nyquist rate (a single receiver pipe-line of the MBR, used with a 5 MHz filter and corresponding modifications) has been set up. This new receiver provides a more sensitive set-up for potential low frequency studies using the Gauribidanur telescope.

Given the large collecting area, the Gauribidanur radio telescope is a sensitive instrument also for searching new radio pulsars and transients. However, its large beam-width (especially in declination) results in correspondingly large uncertainties in the sky position of a new detection, limiting its usability for such surveys. A possible construction of a few groups with large separations in the north-south direction could improve the telescope's capability in this regard, and make the Gauribidanur radio telescope a more suitable and useful instrument for pulsar/transient searches at decameter wavelengths.

Appendix A

Emission geometry: Formal derivation of a few useful formulae

A schematic view of the geometry of pulsar emission, along with conventional notations of various angular quantities involved, is shown in Figure A.1. The magnetic inclination angle with respect to the spin axis is denoted by α . Observer's sight-line traversal is shown by the arc passing through the points A and B. The sight-line impact angle is denoted by β . The pulse longitude ϕ is measured with respect to the longitude at which observer's line of sight cuts the fiducial plane — the plane containing the rotation and magnetic axes. Similarly, the magnetic azimuth angle (χ) is also referred with respect to that at the fiducial plane. The polarization position angle (ψ) is measured with respect to the instantaneous projected direction of the magnetic axis, as shown in the figure. We will use these notations and the geometrical picture as in Figure A.1, to derive a few of the frequently-used expressions.

A.1 Polarization position angle

We shall follow the convention of denoting the vertex (corner) angles by capital letters (e.g., M), and the spherical triangle sides opposite to the vertex angles by the corresponding small letters (e.g., m). Note that the sides of a spherical triangle are given *not* by their length, but by the corresponding arc angle subtended at the center of the sphere. In Figure A.1, consider the spherical triangle PMA. Using the cosine formula, we have :

$$\cos a = \cos p \cos m + \sin p \sin m \cos A \tag{A.1}$$

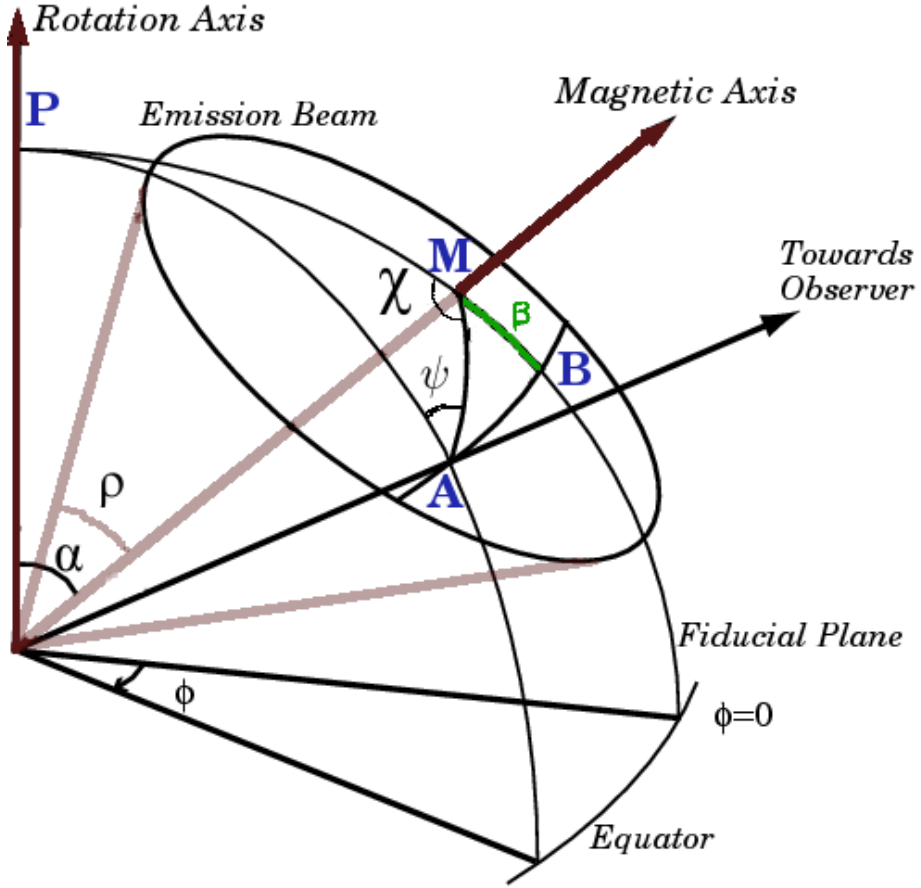


Figure A.1: A schematic view of the pulsar emission geometry.

Or,

$$\cos \psi = \frac{\cos \alpha - \cos p \cos \zeta}{\sin p \sin \zeta} \quad (\text{A.2})$$

where, $\zeta = \alpha + \beta$. Using the sine formula

$$\frac{\sin a}{\sin A} = \frac{\sin p}{\sin P} = \frac{\sin m}{\sin M}, \quad (\text{A.3})$$

we have expression for $\sin p$ as

$$\sin p = \frac{\sin \alpha \sin \phi}{\sin \psi} \quad (\text{A.4})$$

Also, using the cosine formula, we have expression for $\cos p$ as

$$\cos p = \cos \alpha \cos \zeta + \sin \alpha \sin \zeta \cos \phi \quad (\text{A.5})$$

Substituting for $\sin p$ and $\cos p$ in Equation (A.2), we get the well known expression (Komesaroff, 1970) for the position angle of the linear polarization, ψ , as

$$\tan \psi = \frac{\sin \alpha \sin \phi}{\cos \alpha \sin \zeta - \sin \alpha \cos \zeta \cos \phi} \quad (\text{A.6})$$

The rate of change of the position angle with respect to the pulse longitude, i.e., $d\psi/d\phi$, is steepest at the longitude corresponding to the fiducial plane, and is given by

$$\left(\frac{d\psi}{d\phi}\right)_{\max} = \frac{\sin \alpha}{\sin \beta} \quad (\text{A.7})$$

A.2 Magnetic azimuth

The angle PMA defines the magnetic azimuth, χ , corresponding to the pulse phase, ϕ . Below, we will derive an expression for this angle.

Applying the cosine formula in the spherical triangle PMA, we have :

$$\cos m = \cos p \cos a + \sin p \sin a \cos M \quad (\text{A.8})$$

Or,

$$\cos \chi = \frac{\cos \zeta - \cos p \cos \alpha}{\sin p \sin \alpha} \quad (\text{A.9})$$

Also, using the sine formula, we have

$$\sin p = \frac{\sin \zeta \sin \phi}{\sin \chi} \quad (\text{A.10})$$

Using Eqn. A.10 and A.5 in Eq. A.9, we get the expression for magnetic azimuth as

$$\tan \chi = \frac{\sin \zeta \sin \phi}{\sin \alpha \cos \zeta - \cos \alpha \sin \zeta \cos \phi} \quad (\text{A.11})$$

A.3 Subpulse modulation phase

We shall assume that the observed subpulse modulation is due to a carousel of sparks/subbeams circulating around the magnetic axis, as envisioned by Ruderman & Sutherland (1975). The subpulse modulation phase, Θ_{sub} , as a function of pulse longitude, ϕ , consists of three terms (for example, see Edwards & Stappers, 2002):

1. *A scaled version of the magnetic azimuth:* If there are N_{sparks} uniformly distributed sparks, then the scaling factor equals N_{sparks} . Additionally, we also have to take care of the sign of the modulation phase gradient which depends on the relative direction of the pulsar rotation and the carousel circulation. We will assume this sign-factor to be q (where $q = +1$ or -1), so that the net scaling factor becomes equal to $q N_{\text{sparks}}$.

2. An additional, pulse longitude dependent phase which accounts for the carousel rotation over the course of the pulse.
3. Reference modulation phase, Θ_0 , at the reference pulse longitude, i.e., at $\phi = 0$.

So we can write expression for Θ_{sub} as

$$\Theta_{\text{sub}} = q N_{\text{sparks}} \chi + \left(\frac{P_1}{P_3} \right) \phi + \Theta_0 \quad (\text{A.12})$$

Note that we have assumed the reference pulse longitude, i.e., the longitude at the fiducial plane, to be 0. The actual modulation period, P_3 , can be expressed in terms of the observed modulation period, P_3^{obs} , and the aliasing order, n , as follows

$$\frac{P_1}{P_3} = n + \frac{P_1}{P_3^{\text{obs}}}$$

where n is an integer, and for $n = 0$, $P_3^{\text{obs}} = P_3$. Substituting for P_3 from above, and for χ from Eqn. (A.11) in to Eqn. (A.12), we get the expression for the subpulse modulation phase as a function of pulse longitude as follows

$$\Theta_{\text{sub}}(\phi) = q N_{\text{sparks}} \tan^{-1} \left[\frac{\sin \zeta \sin \phi}{\sin \alpha \cos \zeta - \cos \alpha \sin \zeta \cos \phi} \right] + \left(n + \frac{P_1}{P_3^{\text{obs}}} \right) \phi + \Theta_0 \quad (\text{A.13})$$

Appendix B

MBR system details and supplementary material

To provide a fairly complete documentation of the receiver, in the first two sections of this appendix, we present detailed block diagrams of various parts of the multi-band receiver system and the details of the control software, respectively¹. The last section provides supplementary material to the synoptic results presented in Chapter 5.

B.1 MBR hardware block diagrams

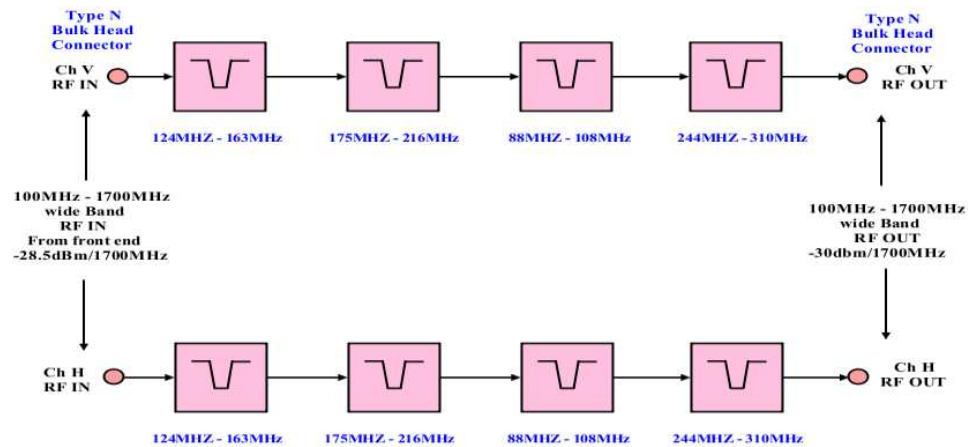


Figure B.1: Block diagram of the band-reject filter unit used in the MBR front-end.

¹Courtesy: The hardware and the software teams for providing the material in these two sections.

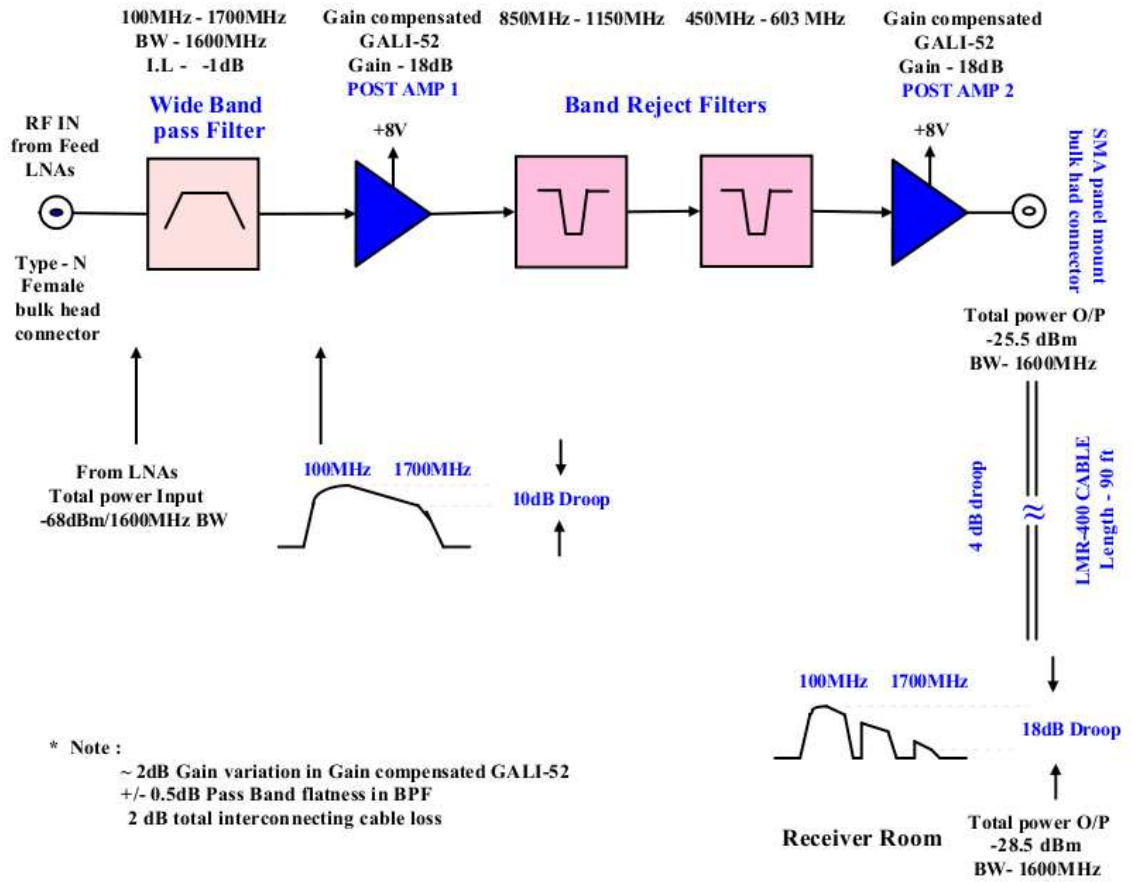


Figure B.2: Block diagram of the MBR front-end.

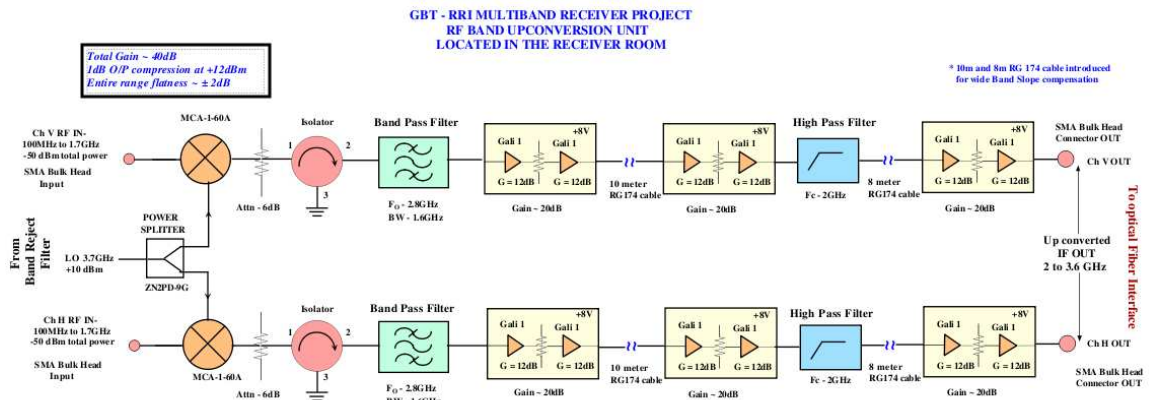


Figure B.3: Block diagram of the up-converter unit.

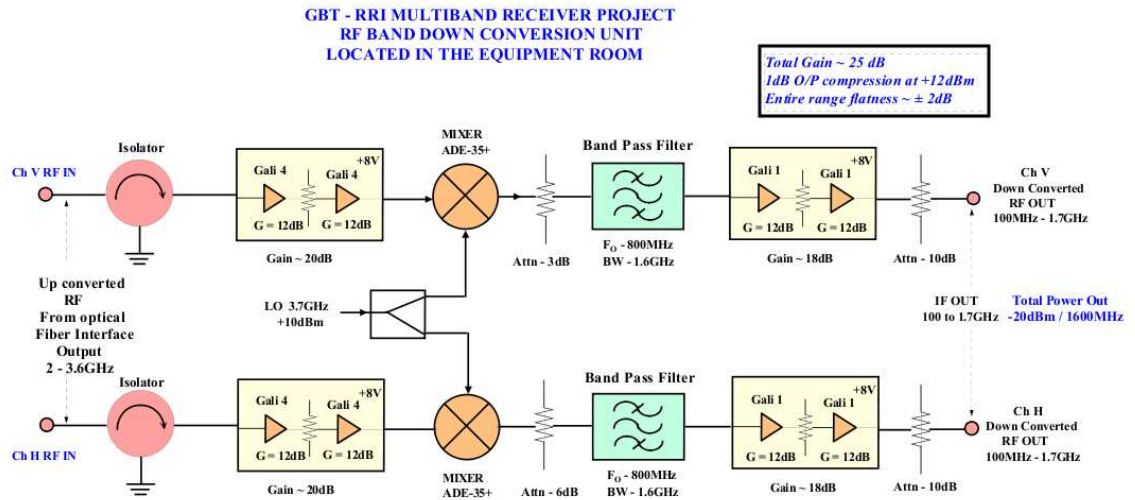


Figure B.4: Block diagram of the down-converter unit.

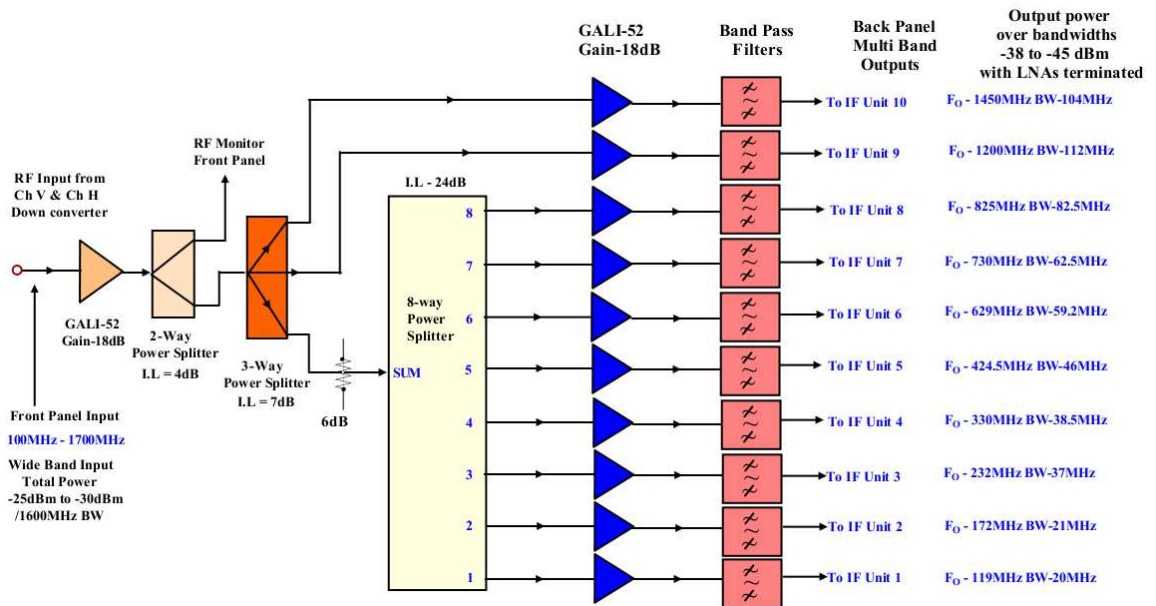


Figure B.5: Block diagram of the RF-unit.

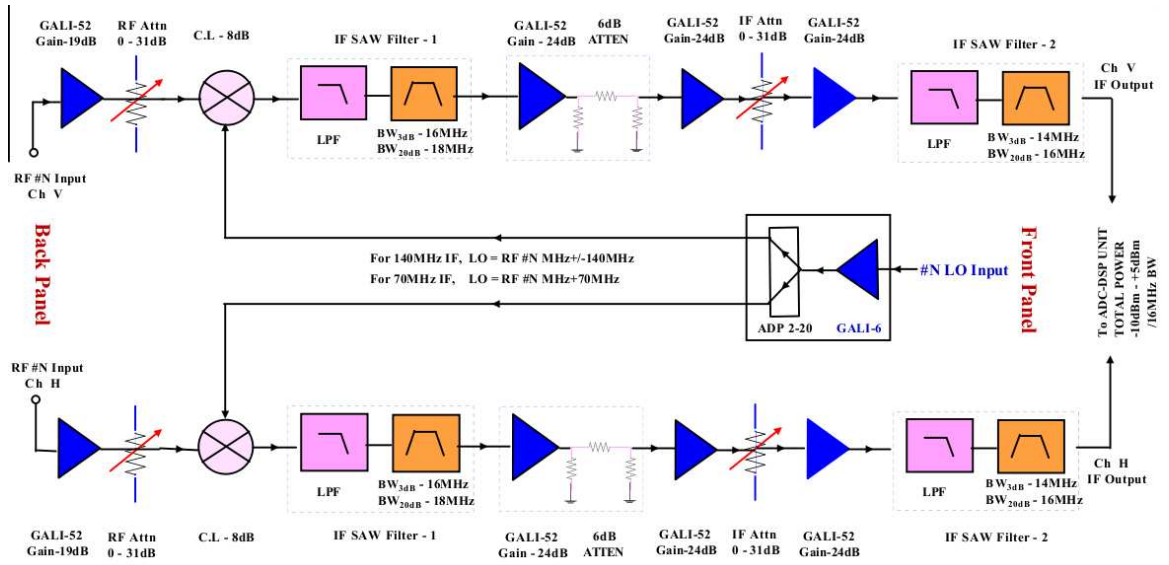


Figure B.6: Block diagram of the IF-chain.

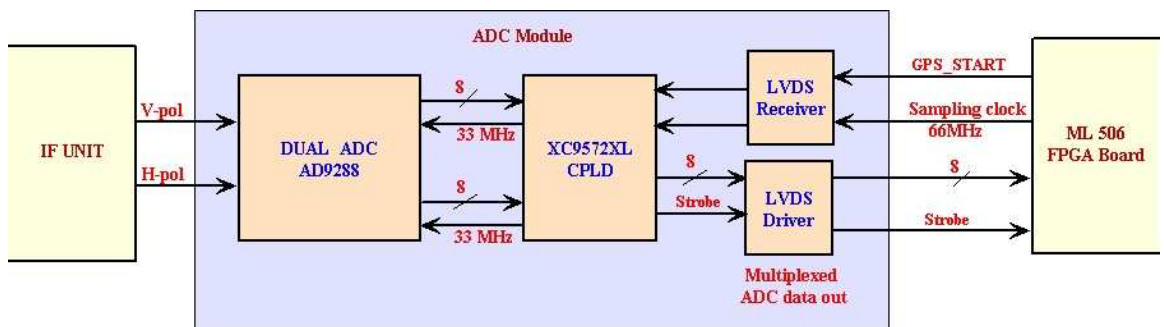


Figure B.7: Block diagram of the ADC-module.

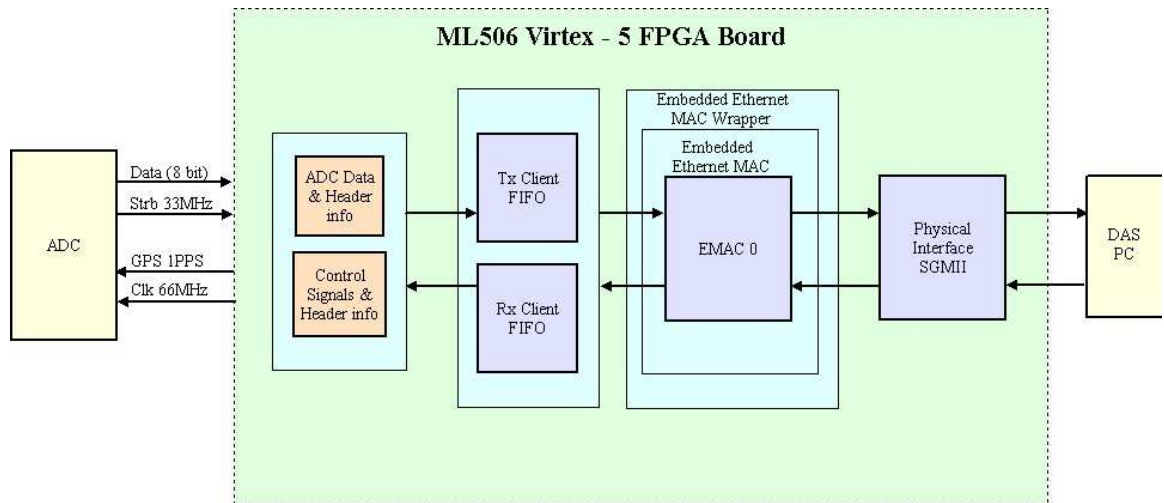


Figure B.8: Block diagram of the Virtex-5 FPGA Board.

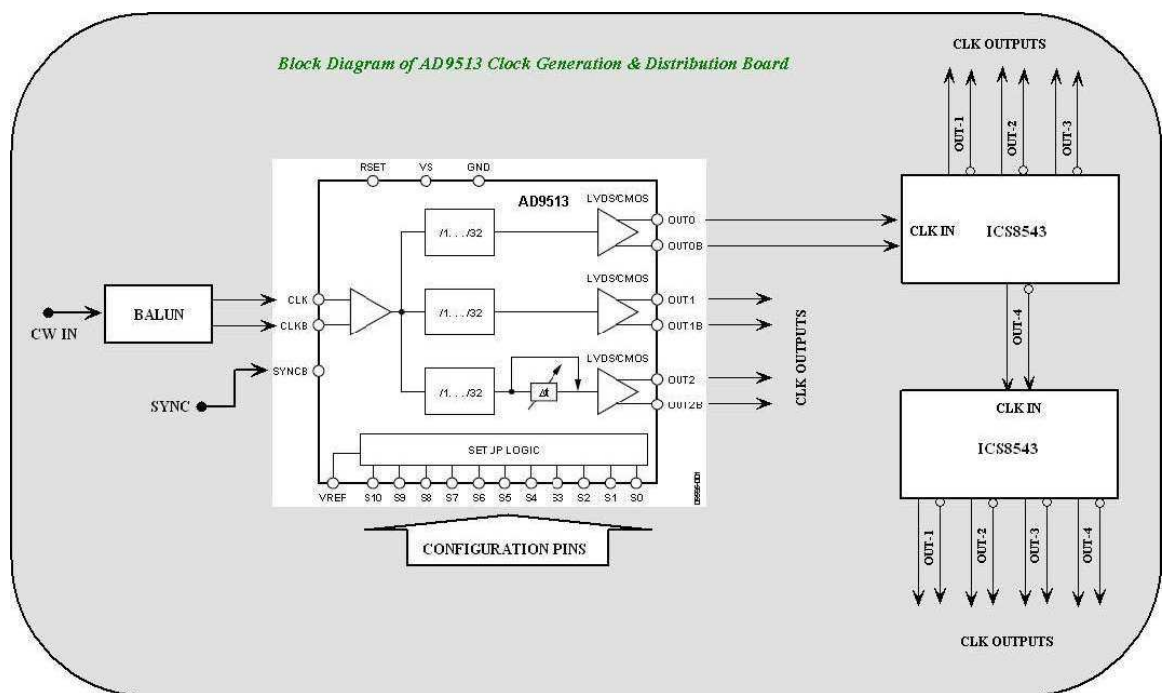


Figure B.9: Block diagram of the clock-generation and distribution board.

B.2 MBR software details

The software that runs on the MBR system is divided into three major components – commands, the M&C daemon, and the DAS daemons, the latter two running on respective machines. The M&C daemon acts as a command router – it receives user commands and dispatches them to the relevant DAS machine. The DAS daemon running on a DAS machine receives the commands intended for it, and executes them. It also returns command status information back to the M&C machine. A command is a program that works in two modes – in ‘remote mode’, the program sends a command string to the M&C daemon, and in ‘local mode’ (when given on the DAS machine) executes the task it is expected to perform. Commands include control commands and monitoring commands. The general form of a command is ‘<command> <das-id> <parameter> <value>’, where <command> can be one of three types – ‘set’, ‘get’, and ‘do’. The first two types are used to set and retrieve system settings, respectively, whereas the third type is used to perform specific tasks, such as triggering data acquisition. A command can be initiated from the GBT observation system either by executing the command binary directly, or by sending the equivalent command string to the M&C daemon over a socket connection. <das-id> is a numeric identifier specifying which DAS machine the command is intended for. A value of 0 results in the broadcasting of the command to all the 10 DAS machines. <parameter> and <value> can be, as the names imply, names of configurable parameters and their possible values. The M&C software system architecture, depicting a sample command flow, is shown in Figure B.10.

The usage syntaxes of the three types of commands discussed above, along with that of the data-acquisition command, are as following:

```
-----
mbrset[mbrget] <das-id>
    acquisition on: Pulls the FPGA ENABLE bit low (transmits data)
                  off: Pulls the FPGA ENABLE bit high (transmits zeroes)
    attenuator 1 <value>: V-RF
    attenuator 2 <value>: V-IF
    attenuator 3 <value>: H-RF
    attenuator 4 <value>: H-IF
    lofreq <value>: Sets the LO frequency
    lofreq +<value>: Increments LO frequency by <value>
    lofreq -<value>: Decrements LO frequency by <value>
    fpgareset      : Resets the FPGA board
    fpgaprogram   : Programs the FPGA board
    acqmode diag  : For FPGA to transmit counter values
    acqmode observe: For FPGA to transmit actual data
    bitpackmode 4 : 4-bit packing of data
```

```

bitpackmode 8 : 8-bit packing of data
fpgagps: Simulate sending of a single GPS pulse to the FPGA
fhist: Writes the relevant fields of the config file to the
      RF history file

mbrdo <das-id> shutdown      : Shuts down the specified DAS
      reboot                : Reboots the specified DAS
      run <command>: Runs <command> on the specified DAS (<command>
      should not contain the pipe [|] symbol)

mbracquire [options]
-h --help                Display this usage information
-d --device <dev_name>  Select the input device (default is 'eth0')
-f --files <num_files>  Set the number of 2GB files to be written
                        (default is 1)
-m --mode                Acquisition mode
                        ('obs' is 'observation' - filenames are formatted;
                        'sniff' is 'sniff' - no files are created,
                        data is just sniffed
                        [sent to the M&C machine];
                        'sniffacq' is 'sniff and acquire' - filenames
                        are formatted, and are
                        prefixed with 'sniff_',
                        and data is sniffed
                        [sent to the M&C machine];
                        'check' is 'check' - no files are created [100
                        packets are acquired and
                        slip check is performed];
                        default is 'observation')
-o --offset <offset>    In sniff modes, sets the packet offset
-k --kill                Kills the existing instance of this program

```

B.3 Synoptic results: Supplementary material

In this section, we provide the summary of our modeling the average profiles of the bright pulsar B0329+54, in the 9 frequency bands of the MBR, as a sum of individual Gaussian components. The separated emission components, modeled as individual Gaussian components, are shown along with the observed average profiles in Figure B.11. The observed and the fitted profiles, along with the fractional fit residuals, are presented in Figure B.12.

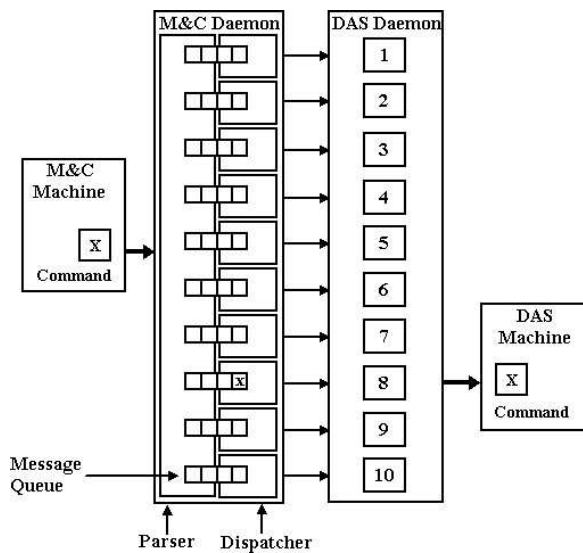


Figure B.10: Software architecture of the MBR system. Here, “X” is a command intended for DAS 8. The parser unit of the M&C daemon pushes this command into the message queue for the eighth dispatcher, which in turn sends the command over the network to the DAS daemon. The DAS daemon runs the binary corresponding to the command.

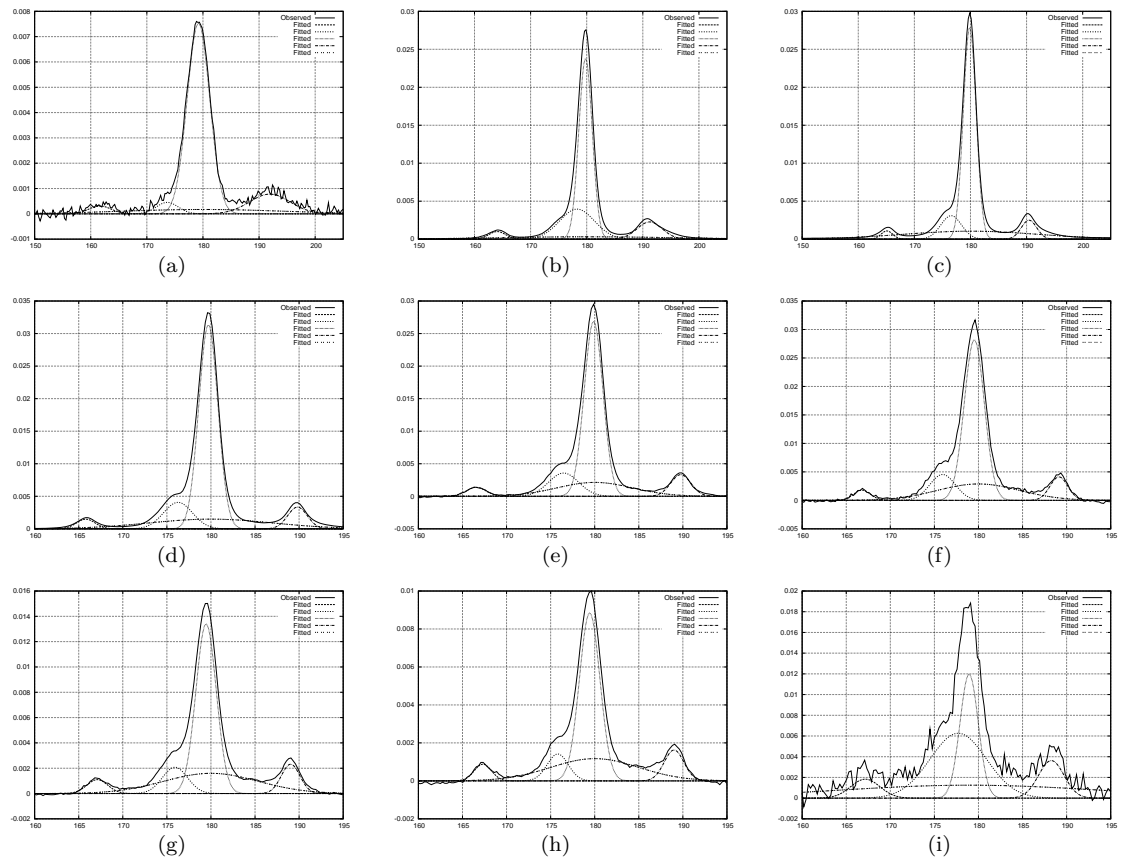


Figure B.11: The nine panels show the observed average profile (solid-line), and the fitted Gaussian components, at the 9 frequency bands.

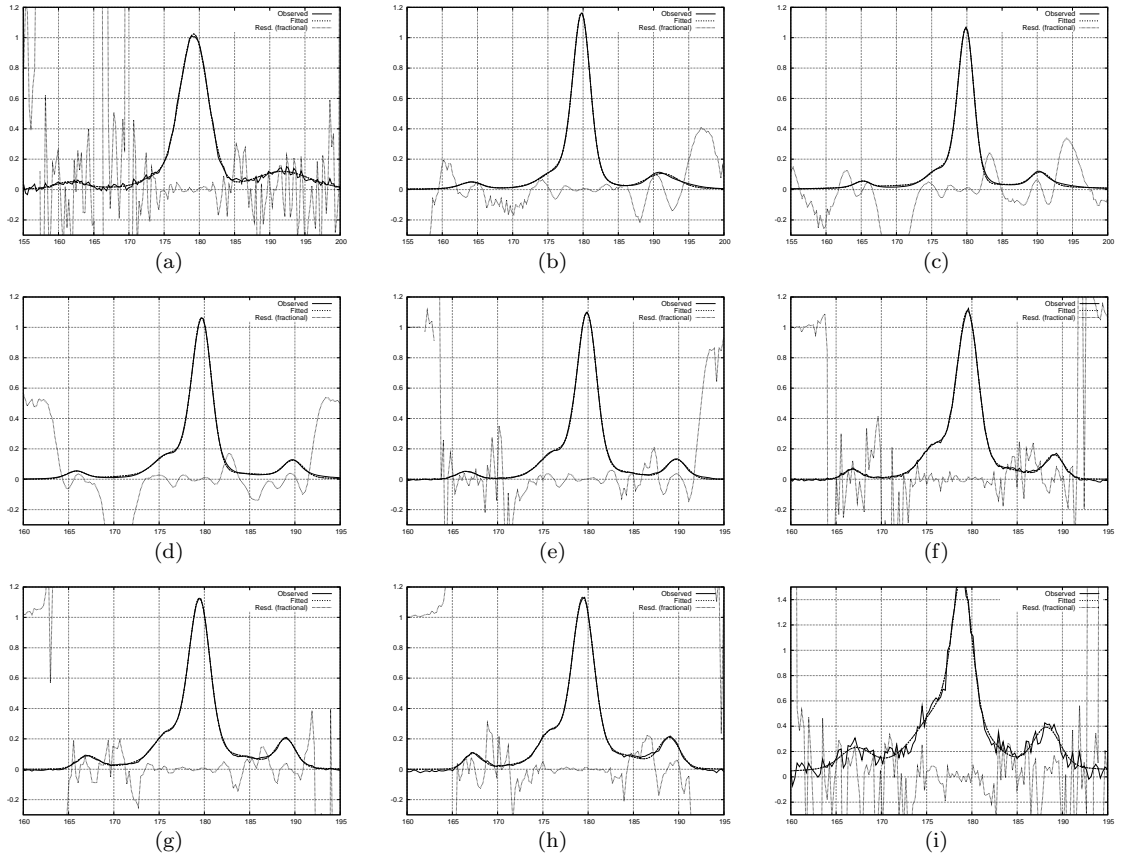


Figure B.12: The nine panels show the observed average profiles, fitted profiles and the *fractional* fit-residuals at the 9 frequency bands. In most of the cases, the observed and fitted profiles are indistinguishable from each other at this plot-scale. Well outside the pulse profile, the fractional fit-residuals would approach unity as the fitted profile approaches zero. This is apparent in some of the panels. Both, the average and the fitted profiles, are scaled by a common factor so as to bring the peak-value near unity (for ease of viewing the fractional fit-residuals).

Radio counterparts of gamma-ray pulsars: supplementary material

C.1 Profile significance measure: Figure of merit

It is important to use an appropriate quantitative figure of merit for average pulse profiles to assess the significance of a detection, specially that of a weak detection. Below we describe three significance measures, first two of which are in common use. In the following descriptions, we will assume that the distribution of noise in the average profiles follow Gaussian statistics.

1. Signal to noise ratio

Profile signal to noise ratio, $(S/N)_{\text{prof}}$, is the most commonly used measure of profile significance. Assuming the profile is represented as an array of n_{bins} phase bins, and the amplitude of the i^{th} bin is labelled as a_i , the profile signal to noise ratio is defined as:

$$(S/N)_{\text{prof}} = \frac{1}{\sigma_{\text{off}} \sqrt{W}} \sum_{i=1}^{n_{\text{bins}}} (a_i - a_{\text{ref}}) \quad (\text{C.1})$$

where a_{ref} and σ_{off} are the off-pulse mean (i.e., the baseline) and standard deviation, respectively, generally computed using only the off-pulse region. W is the equivalent width of a top-hat pulse with the same area and peak height as that of the observed profile. Hence, W is effectively the area under the observed profile divided by its peak value. The probability of chance occurrence of

a profile with $(S/N)_{\text{prof}}$ greater than a chosen $(S/N)_{\text{thresh}}$ is given by

$$\begin{aligned} \text{Probability} \left[(S/N)_{\text{prof}} > (S/N)_{\text{thresh}} \right] &= \frac{1}{\sqrt{2\pi}} \int_{(S/N)_{\text{thresh}}}^{\infty} e^{-x^2/2} dx \\ &= \frac{1}{2} \left[1 - \text{erf} \left(\frac{(S/N)_{\text{thresh}}}{\sqrt{2}} \right) \right] \end{aligned} \quad (\text{C.2})$$

where the error function $\text{erf}(x)$ can be estimated by the rational approximation (for example, see *Approximations for digital computers*, Hastings, 1955):

$$\text{erf}(x) = 1 - (a_1 t + a_2 t^2 + a_3 t^3 + a_4 t^4 + a_5 t^5) e^{-x^2} + \epsilon(x) \quad (\text{C.3})$$

where,

$$\begin{aligned} t &= \frac{1}{1 + px}, \quad |\epsilon(x)| \leq 1.5 \times 10^{-7}, \\ p &= 0.3275911, \quad a_1 = 0.254829592, \quad a_2 = -0.284496736, \\ a_3 &= 1.421413741, \quad a_4 = -1.453152027, \quad \text{and } a_5 = 1.061405429 \end{aligned}$$

Alternatively, the error function can also be solved numerically (see, for example, *Numerical recipes: The art of scientific computing* Press *et al.*, 1992).

2. Chi-squared statistics

To quantify the folding analysis of X-ray data Leahy *et al.* (1983) defined a variant of χ^2 statistic, having $(\text{nbins} - 1)$ degrees of freedom, as

$$\chi^2 = \frac{1}{\sigma_{\text{off}}^2} \sum_{i=1}^{\text{nbins}} (a_i - a_{\text{ref}})^2 \quad (\text{C.4})$$

χ^2 defined above is essentially a measure of how much a given profile deviates from pure Gaussian noise with mean a_{ref} and standard deviation σ_{off} . The probability of exceeding a given χ^2 by chance is given by

$$\text{Probability}(\chi^2) = \frac{1}{\Gamma(a)} \int_{\chi^2/2}^{\infty} e^{-t} t^{a-1} dt, \quad (\text{C.5})$$

$$\text{where, } a = (\text{nbins} - 1)/2 \quad \text{and} \quad \Gamma(a) = \int_0^{\infty} t^{a-1} e^{-t} dt$$

The above function can be integrated numerically (see, for example, *Numerical recipes: The art of scientific computing* Press *et al.*, 1992).

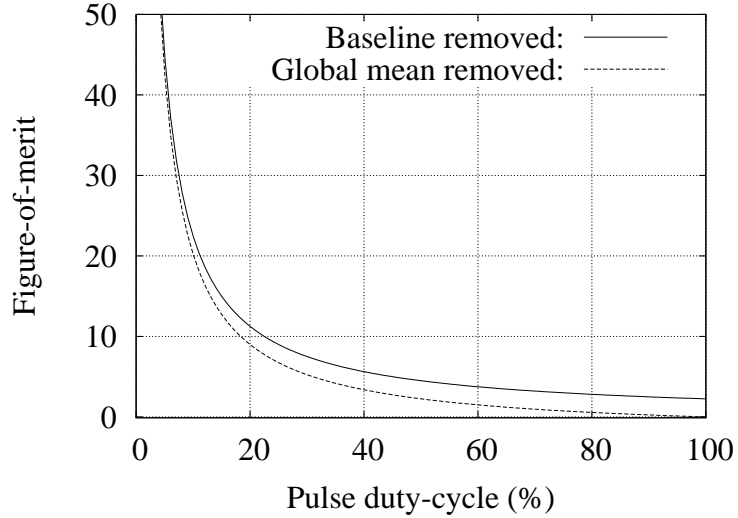


Figure C.1: Two different realizations of sum-of-squares as a function of pulse duty cycle are shown. The two realizations, represented by *solid* and *dotted* lines, use the mean computed from off-pulse region and the global mean, respectively.

3. Sum of squares

In our searches for periodic emission from selected radio-quiet gamma-ray pulsars, we have also used another alternative figure of merit — sum of squares (SSQ) — defined as

$$\text{SSQ} = \sum_{i=1}^{\text{nbins}} (a_i - a_{\text{ref}})^2 \quad (\text{C.6})$$

Note that SSQ and χ^2 are equivalent to each other, since the latter is nothing but SSQ normalized by σ_{off}^2 . It is important to compute the mean (baseline) value, a_{ref} , using only the off-pulse region. Usage of the global mean, i.e., the mean computed using all the phase-bins in the profile, worsens the figure-of-merit, specially for wider profiles. Figure C.1 shows SSQ as a function of pulse duty cycle, for a pulse of given energy, for two cases – using the off-pulse mean and that using the global mean.

C.2 Estimation of the clock drift rate

The clock drift rate was estimated by using multi-epoch observations of B0834+06. Dedispersed time sequences from this pulsar, at 49 different epochs, were used to find out the best-fit observed period. The drift rate was then estimated by comparing these best-fit period values with those predicted by the timing software TEMPO using the pulsar’s ephemeris at the corresponding

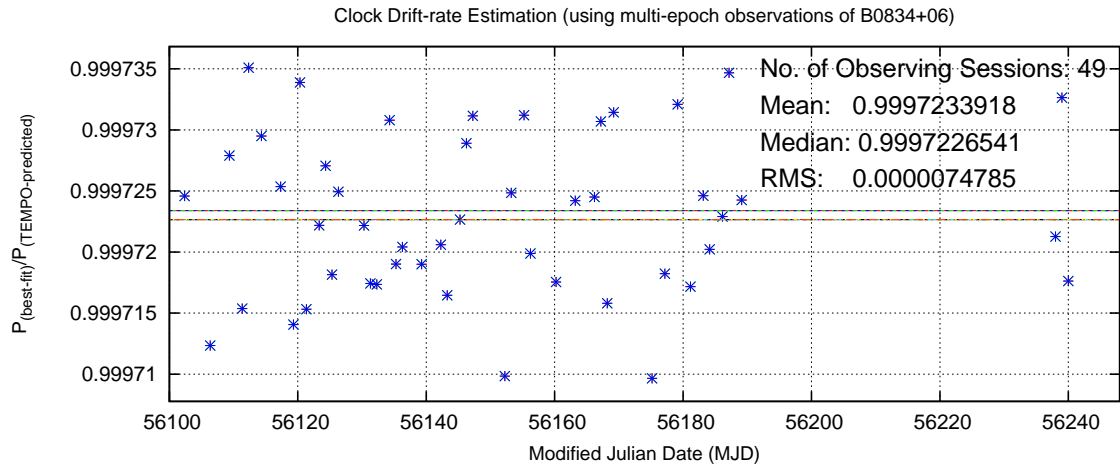


Figure C.2: Estimation of the clock drift rate using multi-epoch observations of B0834+06.

epochs. Ratios of the observed and predicted periods at various epochs are shown in Figure C.2, along with the estimated drift rates. The accuracy of the clock itself, despite the drift estimated above, is adequate for the duration of our individual observing sessions (about 30 minutes).

Bibliography

- Abdo, A. A., Ackermann, M., Ajello, M., Anderson, B., Atwood, W. B., *et al.* . 2009. Detection of 16 Gamma-Ray Pulsars Through Blind Frequency Searches Using the Fermi LAT. *Science*, **325**, 840–844.
- Abdo, A. A., Ackermann, M., Ajello, M., Baldini, L., Ballet, J., *et al.* . 2010. PSR J1907+0602: A Radio-Faint Gamma-Ray Pulsar Powering a Bright TeV Pulsar Wind Nebula. *ApJ*, **711**, 64–74.
- Ables, J. G., McConnell, D., Deshpande, A. A., & Vivekanand, M. 1997. Coherent Radiation Patterns Suggested by Single-Pulse Observations of a Millisecond Pulsar. *ApJ*, **475**, L33.
- Baars, J. W. M., Genzel, R., Pauliny-Toth, I. I. K., & Witzel, A. 1977. The absolute spectrum of CAS A - an accurate flux density scale and a set of secondary calibrators. *A&A*, **61**, 99–106.
- Backer, D. C. 1970. Peculiar Pulse Burst in PSR 1237 + 25. *Nature*, **228**, 1297–1298.
- Backer, D. C. 1973. Pulsar Fluctuation Spectra and the Generalized Drifting-Subpulse Phenomenon. *ApJ*, **182**, 245–276.
- Backer, D. C. 1976. Pulsar average wave forms and hollow-cone beam models. *ApJ*, **209**, 895–907.
- Bhattacharyya, B., Gupta, Y., & Gil, J. 2009. Exploring the remarkable subpulse drift and polarization properties of PSR B0818-41. *MNRAL*, **398**, 1435–1449.
- Bignami, G. F., & Caraveo, P. A. 1996. Geminga: Its Phenomenology, Its Fraternity, and Its Physics. *Annu. Rev. Astron. Astrophys*, **34**, 331–382.
- Brazier, K. T. S., & Johnston, S. 1999. The implications of radio-quiet neutron stars. *MNRAS*, **305**, 671–679.

- Burke-Spolaor, S., Bailes, M., Ekers, R., Macquart, J.-P., & Crawford, III, F. 2011a. Radio Bursts with Extragalactic Spectral Characteristics Show Terrestrial Origins. *ApJ*, **727**, 18.
- Burke-Spolaor, S., Bailes, M., Johnston, S., Bates, S. D., Bhat, N. D. R., *et al.* . 2011b. The High Time Resolution Universe Pulsar Survey - III. Single-pulse searches and preliminary analysis. *MNRAS*, **416**, 2465–2476.
- Camilo, F., Ray, P. S., Ransom, S. M., Burgay, M., Johnson, T. J., *et al.* . 2009. Radio Detection of LAT PSRs J1741-2054 and J2032+4127: No Longer Just Gamma-ray Pulsars. *ApJ*, **705**, 1–13.
- Cordes, J. M. 1978. Observational limits on the location of pulsar emission regions. *ApJ*, **222**, 1006–1011.
- Cordes, J. M., & Lazio, T. J. W. 2002. NE2001.I. A New Model for the Galactic Distribution of Free Electrons and its Fluctuations. *ArXiv Astrophysics e-prints*.
- Cordes, J. M., & McLaughlin, M. A. 2003. Searches for Fast Radio Transients. *ApJ*, **596**, 1142–1154.
- Deshpande, A. A. 1987. *The Detection and Processing of Pulsar Signals at Decametric Wavelengths*. Ph.D. thesis, Indian Institute of Technology, Bombay.
- Deshpande, A. A., & Radhakrishnan, V. 1992. Pulsar observations at 34.5 MHz using the Gauribidanur Telescope. *JApA*, **13**, 151–165.
- Deshpande, A. A., & Rankin, J. M. 1999. Pulsar Magnetospheric Emission Mapping: Images and Implications of Polar CAP Weather. *ApJ*, **524**, 1008–1013.
- Deshpande, A. A., & Rankin, J. M. 2001. The topology and polarization of sub-beams associated with the ‘drifting’ sub-pulse emission of pulsar B0943+10 - I. Analysis of Arecibo 430- and 111-MHz observations. *MNRAS*, **322**, 438–460.
- Deshpande, A. A., Shevgaonkar, R. K., & Sastry, Ch. V. 1989. The Decameterwave Radio Telescope at Gauribidanur: Antenna Arrays and Control System. *J.IETE*, **35**, 342–347.
- Drake, F. D., & Craft, H. D. 1968. Second Periodic Pulsation in Pulsars. *Nature*, **220**, 231–235.
- Dwarakanath, K. S., & Udaya Shankar, N. 1990. A synthesis map of the sky at 34.5 MHz. *JAE&A*, **11**, 323–410.
- Dyks, J. 2008. Altitude-dependent polarization in radio pulsars. *MNRAS*, **391**, 859–868.
- Dyks, J., & Harding, A. K. 2004. Rotational Sweepback of Magnetic Field Lines in Geometric Models of Pulsar Radio Emission. *ApJ*, **614**, 869–880.

- Dyks, J., Rudak, B., & Harding, A. K. 2004. On the Methods of Determining the Radio Emission Geometry in Pulsar Magnetospheres. *ApJ*, **607**, 939–948.
- Edwards, R. T., & Stappers, B. W. 2002. Drifting sub-pulse analysis using the two-dimensional Fourier transform. *A&A*, **393**, 733–748.
- Edwards, R. T., Stappers, B. W., & van Leeuwen, A. G. J. 2003. Unusual subpulse modulation in PSR B0320+39. *A&A*, **402**, 321–329.
- Everett, J. E., & Weisberg, J. M. 2001. Emission Beam Geometry of Selected Pulsars Derived from Average Pulse Polarization Data. *ApJ*, **553**, 341–357.
- Fishman, G. J., Harnden, Jr., F. R., & Haymes, R. C. 1969a. Observation of Pulsed Hard X-Radiation from NP 0532 from 1967 Data. *ApJ*, **156**, L107.
- Fishman, G. J., Harnden, Jr., F. R., Johnson, III, W. N., & Haymes, R. C. 1969b. The Period and Hard-X Spectrum of NP 0532 IN 1967. *ApJ*, **158**, L61.
- Gangadhara, R. T., & Gupta, Y. 2001. Understanding the Radio Emission Geometry of PSR B0329+54. *ApJ*, **555**, 31–39.
- Gil, J. A., & Kijak, J. 1993. Period Dependence of Radio Emission Altitudes in the Pulsar Magnetosphere. *A&A*, **273**, 563–569.
- Gil, J. A., & Sendyk, M. 2000. Spark Model for Pulsar Radiation Modulation Patterns. *ApJ*, **541**, 351–366.
- Gil, J. A., Kijak, J., & Seiradakis, J. H. 1993. On the Two-Dimensional Structure of Pulsar Beams. *A&A*, **272**, 268.
- Goldsmith, P. F., Pandian, J. D., & Deshpande, A. A. 2008. A Search for 6.7 GHz Methanol Masers in M33. *ApJ*, **680**, 1132–1136.
- Gould, D. M., & Lyne, A. G. 1998. Multifrequency polarimetry of 300 radio pulsars. *MNRAS*, **301**, 235–260.
- Gupta, Y., & Gangadhara, R. T. 2003. Understanding the Radio Emission Geometry of Multiple-Component Radio Pulsars from Retardation and Aberration Effects. *ApJ*, **584**, 418–426.
- Hankins, T. H., Kern, J. S., Weatherall, J. C., & Eilek, J. A. 2003. Nanosecond radio bursts from strong plasma turbulence in the Crab pulsar. *Nature*, **422**, 141–143.
- Hastings, C. 1955. *Approximations for digital computers*.

- Hewish, A., Bell, S. J., Pilkington, J. D. H., Scott, P. F., & Collins, R. A. 1968. Observation of a Rapidly Pulsating Radio Source. *Nature*, **217**, 709–713.
- Issur, N. H. 2002. The Pulsar Observing System and Data Analysis Procedure Used at MRT. *Ap & SS*, **282**, 77–85.
- Jouteux, S., Ramachandran, R., Stappers, B. W., Jonker, P. G., & van der Klis, M. 2002. Searching for pulsars in close circular binary systems. *A&A*, **384**, 532–544.
- Kijak, J., & Gil, J. 1997. Radio emission altitudes in pulsar magnetospheres. *MNRAS*, **288**, 631–637.
- Knight, H. S., Bailes, M., Manchester, R. N., Ord, S. M., & Jacoby, B. A. 2006. Green Bank Telescope Studies of Giant Pulses from Millisecond Pulsars. *ApJ*, **640**, 941–949.
- Komesaroff, M. M. 1970. Possible Mechanism for the Pulsar Radio Emission. *Nature*, **225**, 612–614.
- Kramer, M., Xilouris, K. M., Lorimer, D. R., Doroshenko, O., Jessner, A., *et al.* . 1998. The Characteristics of Millisecond Pulsar Emission. I. Spectra, Pulse Shapes, and the Beaming Fraction. *ApJ*, **501**, 270.
- Kramer, M., Karastergiou, A., Gupta, Y., Johnston, S., Bhat, N. D. R., *et al.* . 2003. Simultaneous single-pulse observations of radio pulsars. IV. Flux density spectra of individual pulses. *A&A*, **407**, 655–668.
- Kuzmin, A. D., Izvekova, V. A., Shitov, Y. P., Sieber, W., Jessner, A., *et al.* . 1998. Catalogue of time aligned profiles of 56 pulsars at frequencies between 102 and 10500 MHz. *A&AS*, **127**, 355–366.
- Lange, C., Kramer, M., Wielebinski, R., & Jessner, A. 1998. Radio pulsar microstructure at 1.41 and 4.85 GHz. *A&A*, **332**, 111–120.
- Leahy, D. A., Darbro, W., Elsner, R. F., Weisskopf, M. C., Kahn, S., *et al.* . 1983. On searches for pulsed emission with application to four globular cluster X-ray sources - NGC 1851, 6441, 6624, and 6712. *ApJ*, **266**, 160–170.
- Lorimer, D. R., & Kramer, M. 2004. *Handbook of Pulsar Astronomy*.
- Lundgren, S. C., Cordes, J. M., Ulmer, M., Matz, S. M., Lomatch, S., *et al.* . 1995. Giant Pulses from the Crab Pulsar: A Joint Radio and Gamma-Ray Study. *ApJ*, **453**, 433.
- Lyne, A. G., & Ashworth, M. 1983. The effect of nulls upon subpulse drift in PSRs 0809+74 and 0818-13. *MNRAS*, **204**, 519–536.

- Lyne, A. G., & Manchester, R. N. 1988. The shape of pulsar radio beams. *MNRAS*, **234**, 477–508.
- Maan, Y., & Aswathappa, H. A. 2014. Deep searches for decameter wavelength pulsed emission from radio-quiet gamma-ray pulsars. *Submitted to MNRAS*.
- Maan, Y., & Deshpande, A. A. 2008. Revisiting the rich sub-pulse patterns of B1237+25: Preliminary Results. *Pages 103–105 of: Bassa, C., Wang, Z., Cumming, A., & Kaspi, V. M. (eds), 40 Years of Pulsars: Millisecond Pulsars, Magnetars and More*. American Institute of Physics Conference Series, vol. 983.
- Maan, Y., & Deshpande, A. A. 2014. Inter-relationship between the two emission cones of B1237+25. *Submitted to ApJ*.
- Maan, Y., Amiri, S., Raja, W., & Mehta, N. 2009. Multi-Band Feeds: A Design Study. *Page 430 of: Saikia, D. J., Green, D. A., Gupta, Y., & Venturi, T. (eds), The Low-Frequency Radio Universe*. Astronomical Society of the Pacific Conference Series, vol. 407.
- Maan, Y., Aswathappa, H. A., & Deshpande, A. A. 2012. Pulsed radio emission from the Fermi-LAT pulsar J1732-3131: search and a possible detection at 34.5 MHz. *MNRAS*, **425**, 2–7.
- Maan, Y., Deshpande, A. A., Chandrashekar, V., Chennamangalam, J., Raghavendra Rao, K. B., *et al.* . 2013. RRI-GBT Multi-band Receiver: Motivation, Design, and Development. *ApJS*, **204**, 12.
- Malofeev, V. M., & Malov, I. F. 1980. Average pulsar spectra and their interpretation. *Sov. Astron.*, **24**, 54.
- Manchester, R. N., & Taylor, J. H. 1977. *Pulsars*.
- Manchester, R. N., Taylor, J. H., & Huguenin, G. R. 1975. Observations of pulsar radio emission. II - Polarization of individual pulses. *ApJ*, **196**, 83–102.
- Manchester, R. N., Hobbs, G. B., Teoh, A., & Hobbs, M. 2005. The Australia Telescope National Facility Pulsar Catalogue. *AJ*, **129**, 1993–2006.
- Maron, O., Kijak, J., Kramer, M., & Wielebinski, R. 2000. Pulsar spectra of radio emission. *A&AS*, **147**, 195–203.
- Mitra, D., & Rankin, J. M. 2002. Toward an Empirical Theory of Pulsar Emission. VII. On the Spectral Behavior of Conal Beam Radii and Emission Heights. *ApJ*, **577**, 322–336.
- Olsson, R., Kildal, P. S., & Weinreb, S. 2004. A novel low profile log-periodic ultra wideband feed for dual reflector antenna of US-SKA. *IEEE Symposium Antennas and Propagation*, **00**, 3035–3038.

- Olsson, R., Kildal, P. S., & Weinreb, S. 2005. Measurement of a 1 to 13 GHz Model of a Dual Polarized Low-profile Log-periodic Feed for US-SKA. *Proc. IEEE Antennas and Propagation Society International Symposium*, **02**, 700–703.
- Olsson, R., Kildal, P. S., & Weinreb, S. 2006. . *IEEE Trans. Ant. Prop.*, **54**, 368–375.
- Oster, L., & Sieber, W. 1976. Pulsar geometries. III - The hollow-cone model. *ApJ*, **210**, 220–229.
- Page, C. G. 1973. The drifting sub-pulse phenomenon in PSR 0809+74. *MNRAS*, **163**, 29.
- Phillips, J. A. 1992. Radio emission altitudes in the pulsar magnetosphere. *ApJ*, **385**, 282–287.
- Pletsch, H. J., Guillemot, L., Allen, B., Kramer, M., Aulbert, C., *et al.* . 2012. Discovery of Nine Gamma-Ray Pulsars in Fermi Large Area Telescope Data Using a New Blind Search Method. *ApJ*, **744**, 105.
- Popov, M. V., & Sieber, W. 1990. Correlation of pulsar radiation intensity fluctuations at various longitudes of the mean profile - Analysis of observational data. *Astronomicheskii Zhurnal (in Russian)*, **67**, 757–784.
- Popov, M. V., Kuz'min, A. D., Ul'yanov, O. M., Deshpande, A. A., Ershov, A. A., *et al.* . 2006. Instantaneous radio spectra of giant pulses from the crab pulsar from decimeter to decameter wavelengths. *Astronomy Reports*, **50**, 562–568.
- Press, W. H., Teukolsky, S. A., Vetterling, W. T., & Flannery, B. P. 1992. *Numerical recipes: The art of scientific computing*.
- Radhakrishnan, V., & Cooke, D. J. 1969. Magnetic Poles and the Polarization Structure of Pulsar Radiation. *Astrophys. Lett.*, **3**, 225.
- Ramachandran, R., Mitra, D., Deshpande, A. A., McConnell, D. M., & Ables, J. G. 1997. Measurement of scatter broadening for 27 pulsars at 327 MHz. *MNRAS*, **290**, 260–264.
- Ramachandran, R., Deshpande, A. A., & Indrani, C. 1998. Upper limits on the pulsed radio emission from the Geminga pulsar at 35 & 327 MHz. *A&A*, **339**, 787–790.
- Ramkumar, P. S., & Deshpande, A. A. 1999. Determination of Linear Polarization and Faraday Rotation of Pulsar Signals from Spectral Intensity Modulation. *Journal of Astrophysics and Astronomy*, **20**, 37–50.
- Rankin, J. M. 1983. Toward an empirical theory of pulsar emission. I Morphological taxonomy. *ApJ*, **274**, 333–368.

- Rankin, J. M. 1986. Toward an empirical theory of pulsar emission. III - Mode changing, drifting subpulses, and pulse nulling. *ApJ*, **301**, 901–922.
- Rankin, J. M. 1993. Toward an empirical theory of pulsar emission. VI - The geometry of the conal emission region. *ApJ*.
- Rankin, J. M., & Ramachandran, R. 2003. Toward an Empirical Theory of Pulsar Emission. VIII. Subbeam Circulation and the Polarization-Modal Structure of Conal Beams. *ApJ*, **590**, 411–423.
- Rankin, J. M., Suleymanova, S. A., & Deshpande, A. A. 2003. The topology and polarization of sub-beams associated with the ‘drifting’ subpulse emission of pulsar B0943 + 10 - III. Analysis of Pushchino 103/40-MHz observations. *MNRAS*, **340**, 1076–1086.
- Rankin, J. M., Ramachandran, R., & Suleymanova, S. A. 2006a. Phenomenology of pulsar B0809+74’s rotating subbeam system. I. Geometry and profile “absorption”. *A&A*.
- Rankin, J. M., Ramachandran, R., van Leeuwen, J., & Suleymanova, S. A. 2006b. Phenomenology of pulsar B0809+74’s rotating subbeam system. II. “Carousel” configuration and polarization. *A&A*.
- Ransom, S. M., Greenhill, L. J., Herrnstein, J. R., Manchester, R. N., Camilo, F., *et al.* . 2001. A Binary Millisecond Pulsar in Globular Cluster NGC 6544. *ApJ*, **546**, L25–L28.
- Ransom, S. M., Eikenberry, S. S., & Middleditch, J. 2002. Fourier Techniques for Very Long Astrophysical Time-Series Analysis. *AJ*, **124**, 1788–1809.
- Ransom, S. M., Cordes, J. M., & Eikenberry, S. S. 2003. A New Search Technique for Short Orbital Period Binary Pulsars. *ApJ*, **589**, 911–920.
- Ravi, V., Manchester, R. N., & Hobbs, G. 2010. Wide Radio Beams from γ -ray Pulsars. *ApJ*, **716**, L85–L89.
- Ray, P. S., Kerr, M., Parent, D., Abdo, A. A., Guillemot, L., *et al.* . 2011. Precise γ -ray Timing and Radio Observations of 17 Fermi γ -ray Pulsars. *ApJS*, **194**, 17.
- Ruderman, M. A., & Sutherland, P. G. 1975. Theory of pulsars - Polar caps, sparks, and coherent microwave radiation. *ApJ*, **196**, 51–72.
- Satten, Corey. 2008. Lossless Gigabit Remote Packet Capture With Linux. <http://staff.washington.edu/corey/gulp/>, *University of Washington Network Systems*, Mar.
- Saz Parkinson, P. M., Dormody, M., Ziegler, M., Ray, P. S., Abdo, A. A., *et al.* . 2010. Eight γ -ray Pulsars Discovered in Blind Frequency Searches of Fermi LAT Data. *ApJ*, **725**, 571–584.

- Seiradakis, J. H., & Wielebinski, R. 2004. Morphology and characteristics of radio pulsars. *A&A Rev.*, **12**, 239–271.
- Serylak, M., Stappers, B. W., & Weltevrede, P. 2009. S2DFS: analysis of temporal changes of drifting subpulses. *A&A*, **506**, 865–874.
- Sieber, W., & Oster, L. 1977. Further evidence for multiple-ring structure in the hollow-cone emission of radio pulsars. *A&A*, **61**, 445.
- Smith, E., Rankin, J., & Mitra, D. 2013. Core and conal component analysis of pulsar B1237+25 - II. Investigation of the segregated modes. *MNRAS*, **435**, 1984–2002.
- Smits, J. M., Mitra, D., & Kuijpers, J. 2005. Frequency dependence of the drifting subpulses of PSR B0031-07. *A&A*, **440**, 683–692.
- Srostlik, Z., & Rankin, J. M. 2005. Core and conal component analysis of pulsar B1237+25. *MNRAS*, **362**, 1121–1133.
- Taylor, J. H., & Huguenin, G. R. 1969. Two New Pulsating Radio Sources. *Nature*, **221**, 816–817.
- Toscano, M., Bailes, M., Manchester, R. N., & Sandhu, J. S. 1998. Spectra of Southern Pulsars. *ApJ*, **506**, 863–867.
- Unwin, S. C., Readhead, A. C. S., Wilkinson, P. N., & Ewing, W. S. 1978. Phase stability in the drifting subpulse pattern of PSR 0809+74. *MNRAS*, **182**, 711–721.
- van Leeuwen, A. G. J., Kouwenhoven, M. L. A., Ramachandran, R., Rankin, J. M., & Stappers, B. W. 2002. Null-induced mode changes in PSR B0809+74. *A&A*, **387**, 169–178.
- Vinyaikin, E. N. 2007. Evolution of the radio spectrum of Cassiopeia A from long-term observations. Observations at 290 and 927 MHz. *Astronomy Reports*, **51**, 87–96.
- Vitkevich, V. V., & Shitov, Y. P. 1970. Short Duration Pulsations of CP 0808 and Main Features of its Radio Emission in the Metre Band. *Nature*, **225**, 248–251.
- Vivekanand, M., Narayan, R., & Radhakrishnan, V. 1982. On selection effects in pulsar searches. *JAA&A*, **3**, 237–247.
- Wang, W. 2011. Possible distance indicators in gamma-ray pulsars. *Research in Astronomy and Astrophysics*, **11**, 824–832.
- Weisberg, J. M., Cordes, J. M., Lundgren, S. C., Dawson, B. R., Despotes, J. T., *et al.* . 1999. Arecibo 1418 MHz Polarimetry of 98 Pulsars: Full Stokes Profiles and Morphological Classifications. *ApJS*, **121**, 171–217.

- Weltevrede, P., Stappers, B. W., & Edwards, R. T. 2007. The subpulse modulation properties of pulsars at 92 cm and the frequency dependence of subpulse modulation. *A&A*, **469**, 607–631.
- Wright, G. A. E., & Fowler, L. A. 1981. Mode-changing and quantized subpulse drift-rates in pulsar PSR 2319+60. *A&A*, **101**, 356–361.